Università degli Studi di Firenze
Dipartimento di Fisica

Dottorato di Ricerca in Fisica - XV Ciclo

Trigger Selection of $WH \rightarrow \mu\nu b\bar{b}$ with CMS

Tesi di Dottorato di Ricerca in Fisica di

Riccardo Ranieri

Relatore: **Dott. Carlo Civinini**

Coordinatore: **Prof. Alessandro Cuccoli**

Firenze, 30 Aprile 2003

Contents

Introduction

The origin of the mass of elementary particles, whose electroweak and strong interactions are described by the Standard Model theory, is thought to be the result of the electroweak symmetry breaking mechanism, which predicts the existence of a new particle, the Higgs boson. Experimental observations have confirmed the validity of the Standard Model, but the Higgs boson itself has never been detected. It is an extremely elusive particle, because the production cross section is extremely low and, since its mass is a free parameter of the theory, it must be searched over a wide range of values. A very powerful accelerator, the Large Hadron Collider (LHC), is being constructed at the European Laboratory of Particle Physics (CERN) in Geneva, Switzerland, so as to allow a Higgs boson discovery and to search for new physics phenomena up to the TeV energy scale. Two oppositely directed proton beams will be accelerated to a total centre-of-mass energy of 14 TeV and will collide every 25 ns in correspondence of the experimental areas, where particle detectors will be placed. One of the approved LHC experiments is the Compact Muon Solenoid (CMS). The CMS innermost detector is the silicon tracker, composed by a pixel vertex detector surrounded by several layers of silicon microstrip devices. It will suffer continuously from radiation damages due to LHC particle fluence. The analysis I made on microstrip detector data points out that excellent performance is reached even when working with radiation damaged detectors.

A vital element for a successful study of interesting physics is the trigger system, which is very complex for the experiments at the hadron collider. The CMS collaboration has chosen to divide the trigger selection into two main levels: the Level-1 trigger will be able to analyse every proton-proton collision, by processing calorimeter and muon chamber information with fast programmable hardware, and the High-Level Trigger (HLT) which will process Level-1 accepted events via software running in thousands of CPU units.

Results from LEP experiments have indicated a possible existence of a light Higgs boson with mass near 116 GeV/c^2. At LHC the cleaner channel to detect such a signal is the decay $H \rightarrow \gamma\gamma$, which has a very low decay branching ratio and consequently a very low cross section. Sufficient statistics could be collected only after several years of running. A valid alternative to this channel could be the associated production $W(\rightarrow \mu\nu)H(\rightarrow b\bar{b})$, which has a higher cross section but it is difficult to trigger because overwhelmed by the more copious hadronic background. The WH channel can be used combined with the associated $t\bar{t}H$ production to complement the $H \rightarrow \gamma\gamma$ decay in searching for a possible Higgs boson signal. Unfortunately these events would be mostly discarded if charged particle track information were not available at trigger level and the event selections

were based only on the faster response of calorimeters and muon chambers.

In this framework I have studied the possibility of extensively using the CMS tracking system data during the HLT phase. I have contributed to develop a fast online track finding algorithm by studying in detail the best way to stop the track reconstruction when a sufficient resolution on several track parameters is reached, depending on the number of crossed silicon tracker layers. The online track finding algorithm is based on regional and partial track reconstruction, because tracks are fast and still efficiently reconstructed when only a limited region around the jet directions, measured by the calorimeters, is considered. The encouraging results obtained in terms of tracking efficiency have lead to build an online algorithm able to select b-physics events with jets using a fast b-tag criterion based on track impact parameter. Detailed studies on the time spent by online software have permitted to define the best online track finder combining speed with efficiency. Thus portion of the HLT bandwidth will be dedicated to the b-jet selection with tracker. This "selection stream" makes possible to exploit the potentiality of the CMS detector for what concerns the b-physics.

Furthermore, my main contribution to the CMS activities has been the study and implementation of a dedicated algorithm to trigger the $W(\rightarrow\mu\nu)H(\rightarrow b\bar{b})$ channel. Using this algorithm it is possible to quickly analyse accepted events by Level-1 trigger with one muon and two jets within the tracker acceptance. The muon is checked for isolation within the tracker, the reconstructed tracks are used to refine the calorimeter jet measurements and to apply online b-tag in order to single out b-jets from Higgs boson decay. In this way the background rate is drastically reduced while keeping most of the WH signal events. The trigger selection is performed without exceeding the maximum allowed CPU time for High-Level trigger operations.

The obtained result is very important, because before this thesis it was not thought possible to use the CMS silicon tracker during High-Level trigger and it was unconceivable to efficiently select $W(\rightarrow\mu\nu)H(\rightarrow b\bar{b})$ events at trigger level. This work has opened the way to use such a powerful detector, as the tracker is, in a context of paramount importance such as the trigger system. In a similar way also $t\bar{t}H$ events can be selected and the Higgs boson searches can be performed in the low mass region even during the initial period of LHC operations.

Part I

Theoretical and Experimental Framework

Chapter 1

Standard Model of Electroweak Interactions

In this chapter the basic concepts of electroweak unification theory are introduced together with the lagrangian description of elementary particle interactions. The Standard Model is a Quantum Field Theory based on a local $\mathrm{SU(3)_c} \otimes \mathrm{SU(2)_L} \otimes \mathrm{U(1)_Y}$ gauge symmetry. Starting from the gauge symmetry $\mathrm{SU(2)_L} \otimes \mathrm{U(1)_Y}$ and the spontaneous symmetry breaking mechanism, gauge bosons are defined ($\mathrm{W^+}$, $\mathrm{W^-}$ and Z for weak interactions and the photon γ for electromagnetic interaction) and a new particle is introduced in the theory, the Higgs boson. The gauge symmetry can be extended to $\mathrm{SU(3)_c} \otimes \mathrm{SU(2)_L} \otimes \mathrm{U(1)_Y}$ including the strong interactions related to the $\mathrm{SU(3)_c}$ colour symmetry and mediated by eight coloured massless gluons. In the last part of the chapter, the generation of boson and fermion masses will be described as couplings to the Higgs field. The theoretical introduction ends with the review of Standard Model Higgs boson decay modes and constraints on the value of the mass.

In this work the natural units are used and either in formulæ or in experimental results it is implicitly assumed, if it is not stated otherwise, $\hbar$=c=1.

The values of the constants are [1] $\hbar \equiv h/2\pi = 6.582\ 118\ 89(26) \times 10^{-22}$ MeV s and $\mathrm{c} = 299\ 792\ 458\ \mathrm{m\,s^{-1}}$. A useful conversion constant is $\hbar\mathrm{c} = 197.326\ 960\ 2(77)$ MeV fm.

1.1 Elementary Particles

In the Standard Model the elementary spin-$\frac{1}{2}$ fermions are the leptons, the quarks and their anti-particles. They are classified in three families (generations):

$$\begin{pmatrix} \nu_{\mathrm{e}} \\ \mathrm{e} \end{pmatrix} \quad \begin{pmatrix} \nu_{\mu} \\ \mu \end{pmatrix} \quad \begin{pmatrix} \nu_{\tau} \\ \tau \end{pmatrix}$$

$$\begin{pmatrix} \mathrm{u} \\ \mathrm{d} \end{pmatrix} \quad \begin{pmatrix} \mathrm{c} \\ \mathrm{s} \end{pmatrix} \quad \begin{pmatrix} \mathrm{t} \\ \mathrm{b} \end{pmatrix}$$

The matter consists of leptons and hadrons, the latter are divided into mesons (made up with one quark and one anti-quark) and baryons (made up with combinations of three quarks).

All the elements belonging to the three families have been directly or indirectly observed and no experimental evidence of the existence of a fourth generation is provided.

Elementary particles interact with each other via the four fundamental interactions of Nature, which are mediated by bosons. The four forces and the respective force carriers are:

Gravity graviton G

Strong 8 gluons g

Weak W^{+}, W^{-}, Z

Electromagnetic photon γ

The weak and electromagnetic forces are two aspects originated from the same source, the electroweak interaction.

1.2 Electromagnetic and weak interaction unification

1.2.1 Helicity states

The study of the phenomenology of weak interactions, the only parity violating interactions, has driven S.L. Glashow [2], A. Salam [3] and S. Weinberg [4] in 1967[1] to formulate

[1]Nobel Prizes in Physics 1979 *"for their contributions to the theory of the unified weak and electromagnetic interaction between elementary particles, including inter alia the prediction of the weak neutral current"*.

a theory based on a $\mathrm{SU}(2) \otimes \mathrm{U}(1)$ gauge invariant lagrangian. This hypothesis implies the impossibility to include in the lagrangian mass terms for the fermion fields, as a consequence the helicity is a good quantum number. In this way, Dirac spinors are introduced with well defined helicity, right-handed (R) or left-handed (L). For the lepton families, L_L and L_R states are defined by Eq. 1.1 and 1.2 respectively:

$$\mathrm{L}_L = \begin{pmatrix} \nu_\ell \\ \ell \end{pmatrix}_L \tag{1.1}$$

$$\mathrm{L}_R = \begin{pmatrix} \ell \end{pmatrix}_R \tag{1.2}$$

with $\ell = (\mathrm{e}, \mu, \tau)$.

The right-handed neutrino $(\nu_\ell)_R$ singlet is not included in the theory because in principle neutrinos are massless and have negative helicity from experiment, being left-handed [5]. For the quark families the definition of the helicity states is the same, the only difference resides in the right-handed singlets, that are two, one per each quark of the generation.

Interactions are described via weak charged currents ("V−A" theory) and two new quantum numbers make easier the representation of helicity states within $\mathrm{SU}(2)_\mathrm{L} \otimes \mathrm{U}(1)_\mathrm{Y}$ gauge theory. They are the *Weak Isospin* T (with third axis projection T_3) and the *Weak Hypercharge* Y, defined by Eq. 1.3:

$$Y = 2(Q_{em} - T_3) \tag{1.3}$$

where Q_{em} is the electric charge in units of elementary charge[2] e. In Tab. 1.1 the values of the previously introduced quantum numbers are summarized.

From this point of view, for the lepton states it is clear the notation

$$\mathrm{L}_L \in (2, -1) \tag{1.4}$$

$$\mathrm{L}_R \in (1, -2) \tag{1.5}$$

where the first number points out the dimension of the representation of the SU(2) group and the second number the value of the hypercharge, connected with the U(1) group representation.

[2] $e = 1.602\ 176\ 462(63) \times 10^{-19}$ C [1] is the absolute value of the electric charge of the electron, whose charge value is -e.

Fermions	Quantum Numbers			
	Q_{em}	T	T_3	Y
$(\nu_\ell)_L$	0	$\frac{1}{2}$	$+\frac{1}{2}$	-1
$(\ell)_L$	-1	$\frac{1}{2}$	$-\frac{1}{2}$	-1
$(\ell)_R$	-1	0	0	-2
$(u)_L$	$+\frac{2}{3}$	$\frac{1}{2}$	$+\frac{1}{2}$	$+\frac{1}{3}$
$(d)_L$	$-\frac{1}{3}$	$\frac{1}{2}$	$-\frac{1}{2}$	$+\frac{1}{3}$
$(u)_R$	$+\frac{2}{3}$	0	0	$+\frac{4}{3}$
$(d)_R$	$-\frac{1}{3}$	0	0	$-\frac{2}{3}$

Table 1.1: *Quantum numbers of lepton (ℓ=e, μ, τ) and quark ($[u,d]$=[u, d], [c, s], [t, b]) helicity states: electric charge Q_{em} in unit of e, weak isospin T with third axis projection T_3 and weak hypercharge Y.*

1.2.2 Electroweak sector

In absence of gauge interactions, the electroweak lagrangian $\mathcal{L}_{EW}^{lepton}$ is

$$\mathcal{L}_{EW}^{lepton} = i\sum_{i=1}^{3}\left(\mathrm{L}_L^{\dagger i}\overline{\sigma}^\mu\partial_\mu\mathrm{L}_L^i + \mathrm{L}_R^{\dagger i}\sigma^\mu\partial_\mu\mathrm{L}_R^i\right) \tag{1.6}$$

with $\sigma^\mu = (1,\vec{\sigma})$, $\overline{\sigma}^\mu = (1,-\vec{\sigma})$ and $\vec{\sigma} = (\sigma^1,\sigma^2,\sigma^3)$ the Pauli matrices. The index i runs over the three lepton families.

The local $\mathrm{SU(2)_L}\otimes\mathrm{U(1)_Y}$ gauge invariance is obtained by replacing the partial derivative with the covariant derivative

$$\mathcal{D}_\mu = \partial_\mu + i\frac{g'}{2}(Y)Y_\mu + ig\frac{\vec{\tau}}{2}\cdot\vec{W}_\mu \tag{1.7}$$

being Y the hypercharge of the lepton field and $\vec{W}^\mu$ and Y^μ the vector boson fields associated to the $\mathrm{SU(2)_L}\otimes\mathrm{U(1)_Y}$ gauge symmetry with couplings g and g'. The kinetic terms of gauge fields

$$\mathcal{L}_{EW}^{boson} = -\frac{1}{4}\vec{W}_{\mu\nu}\cdot\vec{W}^{\mu\nu} - \frac{1}{4}B_{\mu\nu}B^{\mu\nu} \tag{1.8}$$

with

$$\vec{W}_{\mu\nu} = \partial_\mu\vec{W}_\nu - \partial_\nu\vec{W}_\mu + g\left(\vec{W}_\mu\times\vec{W}_\nu\right) \tag{1.9}$$

$$B_{\mu\nu} = \partial_\mu Y_\nu - \partial_\nu Y_\mu \tag{1.10}$$

are added to complete the invariant-by-construction $\mathrm{SU(2)_L} \otimes \mathrm{U(1)_Y}$ lagrangian.

Lagrangians 1.6 and 1.8 with substitution 1.7 describe massless gauge bosons and fermions. Requiring massless gauge bosons is usual in gauge theories, while a mass term for fermion fields f

$$-m_f \overline{f} f = -m_f \left(\overline{f}_R f_L + \overline{f}_L f_R \right) \tag{1.11}$$

manifestly violates gauge invariance because f_L and f_R are members of a SU(2) doublet and singlet respectively.

1.2.3 Quark sector

The left-handed components of the quarks are arranged into $Y = +\frac{1}{3}$ isospin doublets

$$\mathrm{Q}_L = \begin{pmatrix} \mathrm{U}_L \\ \mathrm{D}_L \end{pmatrix} \in \left(2, +\tfrac{1}{3}\right) \tag{1.12}$$

and the right-handed into singlets

$$\begin{aligned} \mathrm{U}_R &\in \left(1, +\tfrac{4}{3}\right) \\ \mathrm{D}_R &\in \left(1, -\tfrac{2}{3}\right) \end{aligned} \tag{1.13}$$

where U and D are combinations of the mass eigenstates $u^i = \{\mathrm{u}, \mathrm{c}, \mathrm{t}\}$ and $d^i = \{\mathrm{d}, \mathrm{s}, \mathrm{b}\}$:

$$\mathrm{U}^i_{L,R} = \textstyle\sum_{j=1}^{3} X(\mathrm{U})^{ij}_{L,R} u^j_{L,R} \qquad \mathrm{D}^i_{L,R} = \textstyle\sum_{j=1}^{3} X(\mathrm{D})^{ij}_{L,R} d^j_{L,R} \tag{1.14}$$

The $X(\mathrm{U}, \mathrm{D})_{L,R}$ are 3×3 unitary matrices related to the Cabibbo-Kobayashi-Maskawa quark mixing matrix [6]. In analogy with the leptonic case, the quark electroweak lagrangian is

$$\mathcal{L}^{quark}_{EW} = i \sum_{i=1}^{3} \left(\mathrm{Q}^{\dagger i}_L \overline{\sigma}^\mu \mathcal{D}_\mu \mathrm{Q}^i_L + \mathrm{U}^{\dagger i}_R \sigma^\mu \mathcal{D}_\mu \mathrm{U}^i_R + \mathrm{D}^{\dagger i}_R \sigma^\mu \mathcal{D}_\mu \mathrm{D}^i_R \right) \tag{1.15}$$

with $\mathcal{D}^\mu$ from Eq. 1.7.

The Weinberg model is extended to a gauge field theory $\mathrm{SU(3)_c} \otimes \mathrm{SU(2)_L} \otimes \mathrm{U(1)_Y}$ including the strong interactions between hadrons, called quantum chromodynamics (QCD).

The QCD charge is represented by the colour *red*, *green* or *blue* that any quark carries and exchanges through eight different bi-coloured massless gluons g [7]. The colour interaction is represented by

$$\mathcal{L}_{QCD} = -g_s \sum_{i,j,k} \left(\overline{q}^k_i \gamma^\mu \mathcal{T}^{ij}_a q^k_j \right) G^a_\mu - \frac{1}{4} G^a_{\mu\nu} G^{\mu\nu}_a \tag{1.16}$$

and it is composed with the gluon kinetic term

$$G^a_{\mu\nu} = \partial_\mu \mathcal{A}^a_\mu - \partial_\nu \mathcal{A}^a_\nu + g_s f_{abc} \mathcal{A}^b_\mu \mathcal{A}^c_\nu \tag{1.17}$$

and the interaction between the gluon fields and quarks, where g_s is the QCD coupling constant and γ^μ the Dirac matrices, $\mathcal{T}^a_{ij}$ ($a=1, ..., 8$) are the $\mathrm{SU(3)_c}$ colour matrices and f_{abc} the colour structure constant; q^k_i are the Dirac spinors associated with the i-coloured k-type quark fields and $\mathcal{A}^a_\mu(x)$ are the eight Yang-Mills gluon fields. The Feynman rules [8] are derived from Eq. 1.16 and differently from quantum electrodynamics (QED), in QCD the vector bosons carry colour charge and hence it is possible the interaction between two or more gluons.

1.2.4 Spontaneous symmetry breaking

The spontaneous symmetry breaking of a local SU(2) gauge theory was at first introduced by P.W. Higgs [9]. He theorized a new complex field with mass μ and two components (Higgs doublet) together with an appropriate potential. The interaction term between the Higgs field, expanded around its vacuum expectation value, and the SU(2) gauge fields is the responsible of mass terms of the three gauge field components. In Appendix A it is described more in detail how it works.

The purpose of this procedure is to dress the weak vector bosons with mass and at the same time to keep the photon, carrier of electromagnetic interaction, massless. Strictly speaking, the symmetries to be broken are $\mathrm{SU(2)_L}$ and $\mathrm{U(1)_Y}$, but *not* the internal symmetry $\mathrm{U(1)}_{em}$, since the requirement of the theory is a massless photon.

The choice of the suitable Higgs field was made in 1967 by S. Weinberg [4], who inserted a complex doublet $\phi \in (2, +1)$, as

$$\phi = \begin{pmatrix} \phi^+ \\ \phi^0 \end{pmatrix} \tag{1.18}$$

in the $\mathrm{SU(2)_L} \otimes \mathrm{U(1)_Y}$ invariant lagrangian

$$\mathcal{L}_{Higgs} = \left[\left(i\partial_\mu - g\frac{\vec{\tau}}{2} \cdot \vec{W}_\mu - \frac{g'}{2}(+1)B_\mu \right) \phi \right]^\dagger \cdot \left[\left(i\partial^\mu - g\frac{\vec{\tau}}{2} \cdot \vec{W}^\mu - \frac{g'}{2}(+1)B^\mu \right) \phi \right] - V(\phi) \tag{1.19}$$

The Higgs potential is quartic

$$V(\phi) = \mu^2 \left(\phi^\dagger \phi \right) + \lambda \left(\phi^\dagger \phi \right)^2 = \mu^2 |\phi|^2 + \lambda |\phi|^4 \tag{1.20}$$

with a complex mass term $\mu^2 < 0$ and a positive quartic coupling $\lambda > 0$. No higher order auto-interaction terms than the quartic one $|\phi|^4$ appear in the expression 1.20 of the Higgs potential to guarantee the renormalizability of the theory [10].

The suitable Higgs field vacuum expectation value for keeping the photon mass null is

$$\phi_0 = \frac{1}{\sqrt{2}} \begin{pmatrix} 0 \\ v \end{pmatrix} \tag{1.21}$$

because it has the right quantum numbers: $T=\frac{1}{2}$, $T_3=-\frac{1}{2}$, $Y=+1$, especially $\frac{1}{2}Y+T_3=Q_{em}=0$ (see Eq. 1.3) to preserve $\mathrm{U}(1)_{em}$ invariance[3].

The mass terms in Eq. 1.19 can be written as

$$\begin{aligned} \mathcal{L}^{boson}_{mass} = & \frac{1}{8}g^2v^2\left[\left(W^1_\mu\right)^2+\left(W^2_\mu\right)^2\right]+ \\ & + \frac{1}{8}v^2\left(g'B_\mu - gW^3_\mu\right)\left(g'B^\mu - gW^{3\mu}\right) \end{aligned} \tag{1.22}$$

where two terms are explicitly expressed.

The first term can be modified by the substitution

$$W^\pm = \frac{W^1 \mp iW^2}{\sqrt{2}} \tag{1.23}$$

and describes a complex field with mass $M_W = \frac{1}{2}gv$.

The second term of Eq. 1.22 is a rotation of the neutral components W^3_μ and B_μ ruled by the Weinberg angle[4] θ_W, defined as $\tan\theta_W = \frac{g'}{g}$:

$$\begin{pmatrix} A_\mu \\ Z_\mu \end{pmatrix} = \begin{pmatrix} \cos\theta_W & \sin\theta_W \\ -\sin\theta_W & \cos\theta_W \end{pmatrix} \begin{pmatrix} B_\mu \\ W^3_\mu \end{pmatrix} \tag{1.24}$$

The first field represents the Z boson associated to the mass term of Eq. 1.22, while the second is the photon field, which remains massless because it does not interact with the Higgs field.

In this framework, the masses[5] and couplings are related to g, g' and v:

$$M_W = \frac{1}{2}gv \tag{1.25}$$

$$\frac{M_W}{M_Z} = \cos\theta_W \tag{1.26}$$

[3]The generator of $\mathrm{U}(1)_{em}$ group is the electric charge $Q = Q_{em} = T_3 + \frac{Y}{2}$ (Eq. 1.3), therefore $Q\phi_0 = 0$ and the local invariance is guaranteed: $\phi_0 \to \phi'_0 = e^{i\alpha(x)Q}\phi_0 = \phi_0 \ \ \forall\alpha(x)$.

[4]The measured value of the weak mixing angle is $\sin^2\theta_W = 0.23113(15)$ [1].

[5]Measured value of gauge boson masses and widths [1]:
M_W=80.423±0.039 GeV/c^2, Γ_W=2.118±0.042 GeV;
M_Z=91.1876±0.0021 GeV/c^2, Γ_Z=2.4952±0.0023 GeV;
$M_\gamma < 2\times10^{-16}$ eV/c^2 @ 95% CL.

$$M_A = 0 \tag{1.27}$$

and the elementary charge is

$$\frac{1}{e^2} = \frac{1}{g^2} + \frac{1}{g'^2} \tag{1.28}$$

The Higgs parameter v is related to the Fermi constant[6]:

$$v^2 = \frac{1}{\sqrt{2}G_F} \simeq (246 \text{ GeV})^2 \tag{1.29}$$

1.3 Higgs Sector

1.3.1 Interaction vertices

The expression of Higgs field expanded near the vacuum expectation value of Eq. 1.21

$$\phi(x) = \frac{1}{\sqrt{2}} \begin{pmatrix} 0 \\ v + h(x) \end{pmatrix} \tag{1.30}$$

gives rise, if inserted into lagrangian 1.19, to a new particle with mass $m_h = \sqrt{-2\mu^2}$ (see Appendix A keeping in mind that $\mu^2 < 0$). The interactions of this particle, the Higgs boson, are studied extracting from lagrangian 1.19 the interaction vertices (at tree level)

$$hW^+W^- \longrightarrow igM_W \tag{1.31}$$

$$hhW^+W^- \longrightarrow \frac{1}{4}ig^2 \tag{1.32}$$

$$hZZ \longrightarrow \frac{1}{2}\frac{ig}{\cos\theta_W}M_Z \tag{1.33}$$

$$hhZZ \longrightarrow \frac{1}{8}\frac{ig^2}{\cos^2\theta_W} \tag{1.34}$$

which are used to calculate invariant amplitudes and then cross sections with the usual Feynman rules [8].

[6]The Fermi constant, whose value is $\frac{G_F}{(\hbar c)^3}$=1.166 39(1)$\times 10^{-5}$ GeV^{-2} [1], was introduced by Fermi himself to represent the coupling constant assigned to the weak interaction vertex in a theory with punctual interactions, not mediated by vector bosons. It is measured very accurately from the charged current muon decay $\mu^- \to e^- \bar{\nu}_e \nu_\mu$, that occurs through W emission.

1.3.2 Fermion masses

The importance of Weinberg's choice of Eq. 1.21 for the Higgs field resides also in another basic aspect of the electroweak theory. Higgs field alone is suitable to generate the masses of all the fermion fields without symmetry violating terms. This can be done via a Yukawa coupling G_f, the lagrangian being expressed in the more general form of Eq. 1.35:

$$\mathcal{L}_{mass}^{fermion} = -G_f[\overline{L}\phi R + \overline{R}\phi^\dagger L] \tag{1.35}$$

For a lepton family, Eq. 1.35 becomes

$$\mathcal{L}_{mass}^{lepton} = -G_\ell[\overline{\mathrm{L}}_L\phi \mathrm{L}_R + \overline{\mathrm{L}}_R\phi^\dagger \mathrm{L}_L] \tag{1.36}$$

which can be divided in two terms using the expression of $\phi(x)$ (Eq. 1.30) and the definitions of L_L (Eq. 1.1) and L_R (Eq. 1.2):

$$\mathcal{L}_{mass}^{lepton} = -\frac{G_\ell v}{\sqrt{2}}\left(\overline{\ell}_L\ell_R + \overline{\ell}_R\ell_L\right) - \frac{G_\ell}{\sqrt{2}}\left(\overline{\ell}_L\ell_R + \overline{\ell}_R\ell_L\right)h(x) \tag{1.37}$$

with G_ℓ Yukawa coupling constant of the lepton family.

The expression of the charged lepton mass m_ℓ is straightforward:

$$m_\ell = \frac{G_\ell v}{\sqrt{2}} \tag{1.38}$$

and with Eq. 1.25 leads to

$$\mathcal{L}_{mass}^{lepton} = -m_\ell\overline{\ell}\ell - \frac{1}{2}g\frac{m_\ell}{M_W}\overline{\ell}\ell h(x) \tag{1.39}$$

Being G_ℓ an arbitrary parameter, the mass of the charged lepton ℓ (e, μ or τ) can not be predicted by the theory and its measurement[7] only fixes the value of G_ℓ.

The second term of Eq. 1.39 represents the vertex of interaction between the Higgs boson and the $\ell^+\ell^-$ pair (or, more in general, any fermion–anti-fermion $f\bar{f}$ pair):

$$h\overline{f}f \longrightarrow -\frac{1}{2}ig\frac{m_f}{M_W} \tag{1.40}$$

The proportionality of the interaction strength to the fermion mass is a prediction of the theory; interactions with lighter fermions are disfavoured, since the vertex coupling depends on the ratio $\frac{m_f}{M_W}$.

[7] Measured value of charged lepton masses [1]:
m_e=0.510 998 902(21) MeV/c^2, m_μ=105.658 357(5) MeV/c^2, m_τ=1776.99$^{+0.29}_{-0.26}$ MeV/c^2.

1.4 Higgs Decays

The Standard Model is extremely predictive in the Higgs sector, because all couplings, decay widths and production cross sections are given in terms of the unknown Higgs boson mass, being the other parameters experimentally measured. Starting from Eq. 1.40 and Eq. 1.31 - 1.34, the partial decay widths, and hence the total decay width, are calculated. In Fig. 1.2 the Standard Model Higgs boson H decay branching ratios are reported as a function of the mass for a large range of values, from 50 GeV/c^2 to 1 TeV/c^2 [11, 12]. All the curves are obtained with the program HDECAY [13], which includes also higher order radiative corrections.

The total decay width is shown in Fig. 1.1. Below m_{H}=150 GeV/c^2 the Higgs boson resonance is quite narrow, reflecting the weak coupling to the lighter fermions, with $\Gamma_{\mathrm{H}} < 10$ MeV. In this mass region, the Higgs boson width is too narrow to be experimentally resolved. As soon as the WW* and ZZ* channels become accessible, the width increases rapidly to $\Gamma_{\mathrm{H}} \simeq 1$ GeV at m_{H} near 200 GeV/c^2.

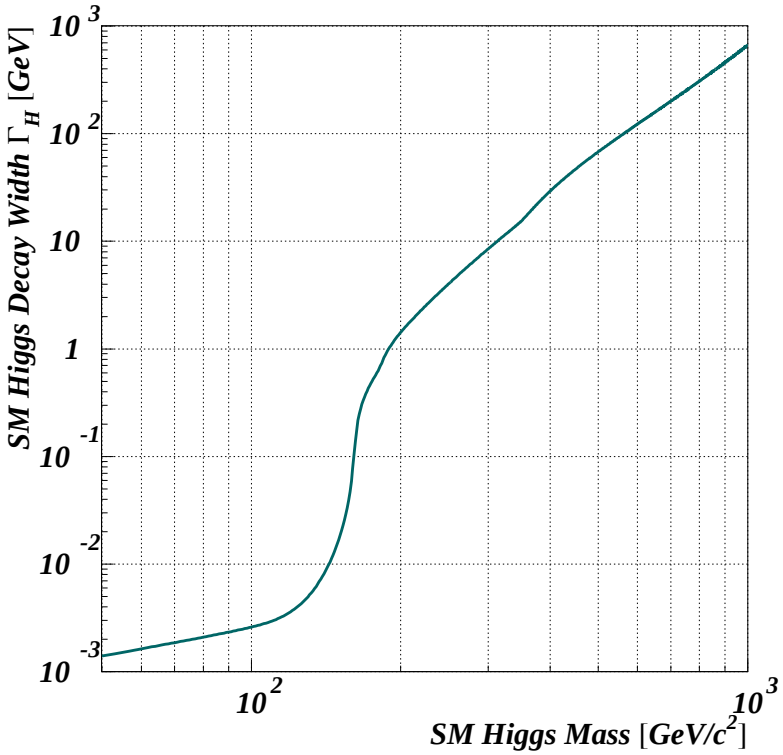

Figure 1.1: *Total decay width Γ_{H} of Standard Model Higgs boson as a function of the mass.*

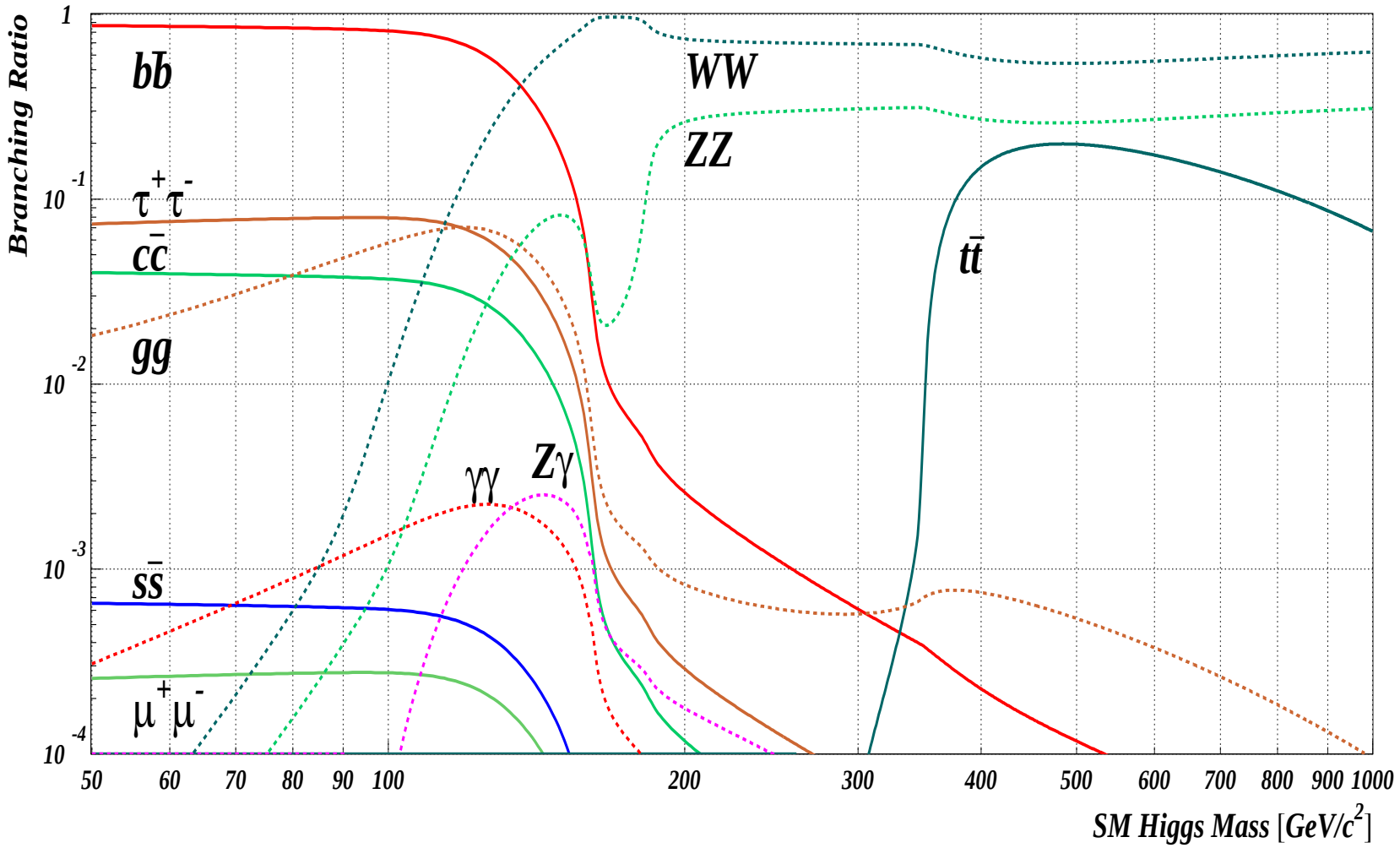

Figure 1.2: *Decay branching ratios of the Standard Model Higgs boson as a function of the mass. Decays into fermion–anti-fermion pairs are represented by solid lines, decays into gauge boson pairs by dashed lines.*

1.5 Limits on Higgs boson mass

The mass of the Higgs boson is a free parameter for the theory, which *a priori* could assume every conceivable value. Beyond the mere fact of its existence, however, there are some indications to assign boundaries to the expected mass of the Higgs, either on pure theoretical bases or according to the experimental results, which up to now have not confirmed the existence of this elusive particle.

1.5.1 Theoretical limits

The consistency of the Standard Model picture limits the allowed mass range of the Higgs boson. The tighter theoretical constraints come from one-loop matching conditions relating the particle couplings to their masses [11, 14]. The allowed upper and lower bounds are shown in Fig. 1.3 as a function of the cutoff parameter Λ at which the Standard Model is replaced by a higher energy theory. The region above the upper curve is forbidden because the quartic coupling of Higgs potential is infinite (*triviality*). The region below the lower curve is not permitted because the quartic coupling becomes negative and the potential is unbounded from below (*vacuum stability*). The shaded areas reflect the theoretical uncertainties in the determination of the Higgs boson mass bounds. If the validity of the Standard Model is assumed up to Planck scale $\Lambda \sim 10^{19}$ GeV, the allowed Higgs mass range is between 130 and 190 GeV/c^2. Conversely, a possible discovery of the Standard Model Higgs boson outside this mass range would be an hint of the presence of a new theory above a certain energy scale.

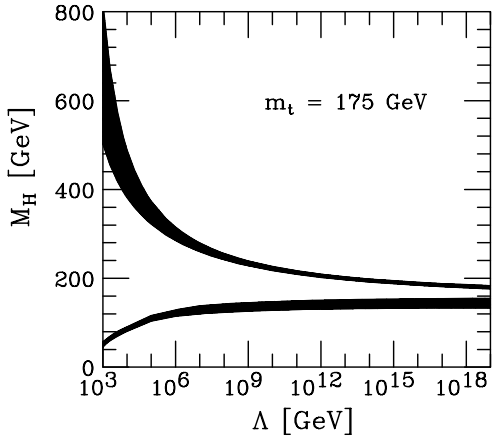

Figure 1.3: *Theoretical limits on Standard Model Higgs boson mass. The allowed region, as a function of the energy scale Λ at which the Standard Model breaks down, is between the two curves, obtained assuming $m_t = 175$ GeV/c^2 and $\alpha_s(m_Z) = 0.118$ [14].*

1.5.2 Experimental limits

The more constraining limits on the mass of the Higgs particle are given by the experimental searches. The search for the Higgs boson is divided into two parallel lines: the direct searches at leptonic or hadronic colliders and the indirect searches, which rely upon several measured parameters to check for internal consistency of the proposed model.

Indirect searches and constraints on Standard Model

The measurable value of the Standard Model observables is affected by electroweak radiative corrections, in which the Higgs particle enters into one loop. The precision of electroweak measurements has reached such a sensibility to probe the corrections to tree-level expectation values given by higher order loops. It is demonstrated that at one loop all electroweak parameters have at most logarithmic dependence on m_{H} [15], this behaviour is summarized by the *screening theorem* [16]. In general, electroweak radiative corrections involving Higgs boson loops assume the form

$$g^2 \left(\log \frac{m_{\mathrm{H}}}{m_{\mathrm{W}}} + g^2 \frac{m_{\mathrm{H}}^2}{m_{\mathrm{W}}^2} \cdots \right) \tag{1.41}$$

with the quadratic term always screened by an additional power of g with respect to the logarithmic term, resulting in a mild contribution to the total correction. Corrections due to top quark loops are stronger, depending at leading order on $(m_{\mathrm{t}}/m_{\mathrm{W}})^2$ and gave the input for the discovery of the top quark at FermiLab [17].

Using the measurements listed in [18], several Standard Model fits are made with model predictions calculated with TOPAZ0 [19] and ZFITTER [20] and χ^2 minimization performed by the MINUIT [21] program. Results from experiments all over the world but mainly from LEP [22] are fitted to obtain the best constraints on m_{H}. The results of the global fit are reported in Tab. 1.2 In Fig. 1.4 on page 18 the observed value of $\Delta\chi^2 = \chi^2 - \chi^2_{min}$ as a function of m_{H} is shown. The solid curve corresponds to the result of Tab. 1.2, the shaded bands represent the uncertainty in the calculation due to neglected higher-order corrections. The 95% confidence level upper limit on m_{H} is

$$m_{\mathrm{H}} < 193 \text{ GeV/c}^2 \tag{1.42}$$

The lower limit obtained from direct searches is not taken into account in determining it. The limit 1.42 is model-dependent, being calculated from loop corrections, that could be circumvented by some new physics contributions. This limit is well-grounded only within the Standard Model theory and has always to be confirmed by the direct observation of the expected Higgs boson phenomena.

m_{t} [GeV/c^2]	$174.3^{+4.5}_{-4.3}$
m_{H} [GeV/c^2]	81^{+52}_{-33}
$\log\left(m_{\mathrm{H}}/[\,\mathrm{GeV/c^2}]\right)$	$1.91^{+0.22}_{-0.23}$
$\alpha_s(m_{\mathrm{Z}}^2)$	0.1183±0.0027
χ^2/d.o.f.	29.7/15 (1.3%)
$\sin^2\theta_W$	0.22272±0.00036
m_{W} [GeV/c^2]	80.394±0.019

Table 1.2: *Results of the electroweak fit to all data summarized in [18]. Since the sensitivity to m_{H} is logarithmic, both m_{H} and $\log(m_{\mathrm{H}})$ are quoted.*

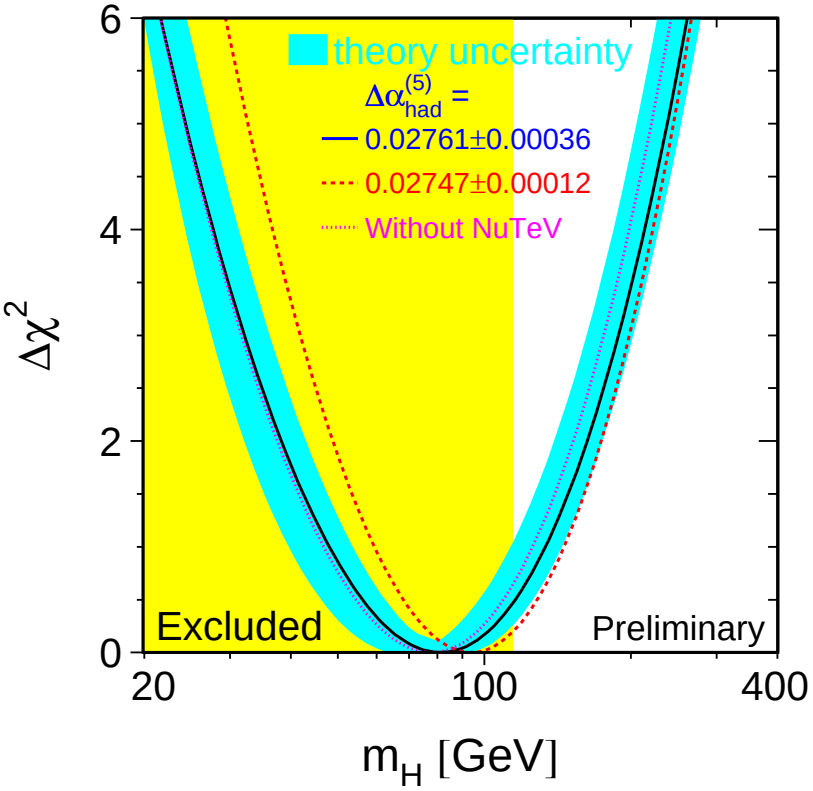

Figure 1.4: *Observed value of $\Delta\chi^2 = \chi^2 - \chi^2_{min}$ as a function of Higgs mass m_{H}. The line is the result of the electroweak fit using all data [18], the band represents the uncertainty due to neglecting higher order corrections. The vertical band is the region excluded by direct searches.*

Direct searches

No conclusive evidence for the Higgs existence comes from LEP2 searches [23].

The four collaborations ALEPH [24], DELPHI [25], L3 [26] and OPAL [27] have collected 2 461 pb^{-1} of $\mathrm{e^+e^-}$ collision data at centre-of-mass energies $\sqrt{s}$ between 189 and 209 GeV. At LEP, the Standard Model Higgs boson is expected to be produced mainly in association with a Z boson, through a process called *Higgsstrahlung*. Small contributions are from the t-channel WW and ZZ fusion processes with Higgs particle production together with a pair of neutrinos or electrons respectively.

According to Fig. 1.2 on page 15, the accessible Higgs particles ($m_\mathrm{H} \simeq \sqrt{s} - m_\mathrm{Z}$) decay predominantly into $\mathrm{b\bar{b}}$ pairs, hence the final-state topologies are determined by the decay properties of the associated Z boson. The searched final states are:

four-jet $\mathrm{e^+e^-}\to\mathrm{H}(\to\mathrm{b\bar{b}})\mathrm{Z}(\to\mathrm{q\bar{q}})$

missing energy $\mathrm{e^+e^-}\to\mathrm{H}(\to\mathrm{b\bar{b}})\mathrm{Z}(\to\nu_\ell\bar{\nu}_\ell)$ $(\ell = \mathrm{e}, \mu, \tau)$

leptonic $\mathrm{e^+e^-}\to\mathrm{H}(\to\mathrm{b\bar{b}})\mathrm{Z}(\to\ell^+\ell^-)$ $(\ell = \mathrm{e}, \mu)$

tauonic $\mathrm{e^+e^-}\to\mathrm{H}(\to\mathrm{b\bar{b}})\mathrm{Z}(\to\tau^+\tau^-)$ or $\mathrm{e^+e^-}\to\mathrm{H}(\to\tau^+\tau^-)\mathrm{Z}(\to\mathrm{q\bar{q}})$

Inputs from the four experiments are provided for all the channels and are combined together to define a variable, which is sensitive to the signal-to-background ratio: the log-likelihood test statistics $-2\ln(Q)$ [23]. The measured value of the test statistics as a function of the test-mass m_H is shown in Fig. 1.5 on page 20 with the expected curves for the background only and signal+background hypotheses. A broad minimum on the observed curve extends from $m_\mathrm{H} = 115$ GeV/c^2 to 118 GeV/c^2 and intersects the expected signal+background curve at m_H close to 116 GeV/c^2, 1.74 standard deviations away from the background hypothesis. The favoured interpretation of this observation is the signal of a Standard Model Higgs boson within this mass range [23]. The signal-like behaviour mainly originates from the four-jet ALEPH data [28].

The lower limit on Higgs boson mass is [23]

$$m_\mathrm{H} > 114.4 \text{ GeV/c}^2 \tag{1.43}$$

at 95% Confidence Level, well below the value indicated by the excess of signal-like events near $m_\mathrm{H} = 116$ GeV/c^2.

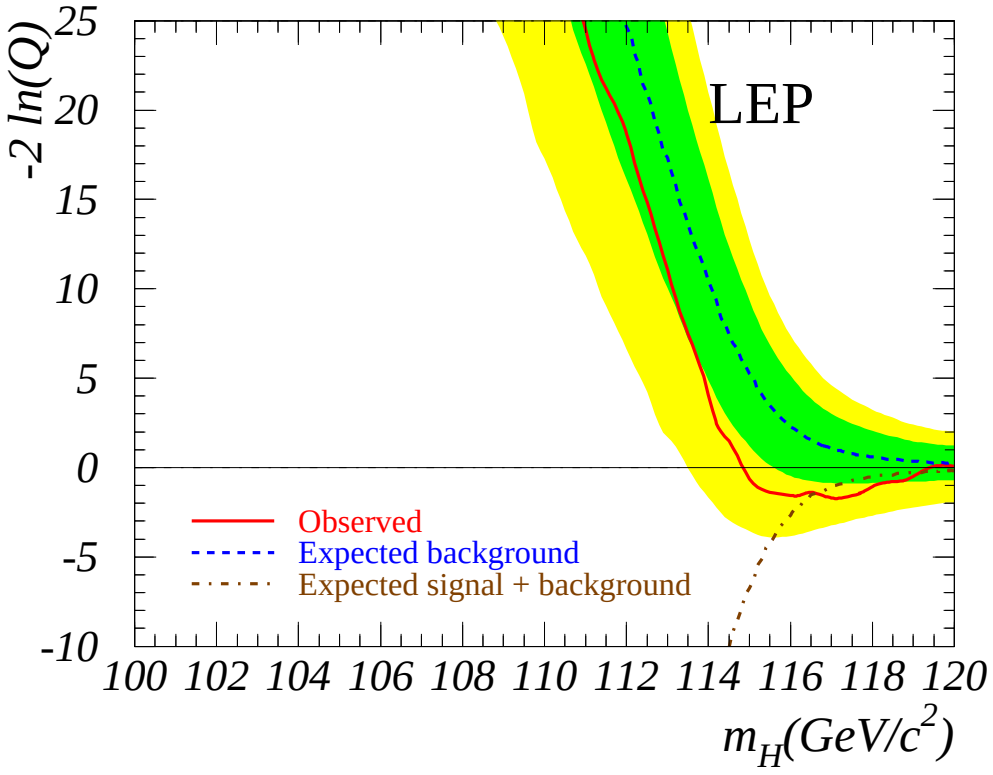

Figure 1.5: *Observed and expected behaviour of test-statistics* $-2\ln(Q)$ *as a function of the test-mass* m_{H}*, obtained combining the data of the four LEP experiments [23]. The solid line is the observed curve, the dashed (dot-dashed) is the median expectation in the hypothesis of background only (signal+background). The two shaded areas are the 68% and 95% probability bands around the median background expectation.*

Chapter 2

Standard Model Higgs physics at Large Hadron Collider

In this chapter, the phenomenology of Higgs physics at Large Hadron Collider (LHC) is reviewed. The mechanisms of Higgs production in 14 TeV centre-of-mass energy pp collisions and the search strategies for different mass regions are described. In pp collisions a lot of particle are created, hence the Higgs boson is also searched in association with other particles, whose decays are well detectable and can be more easily singled out.

2.1 Higgs production in hadronic interactions

The search for the Higgs boson is one of the main goals of LHC [29], hence the precise knowledge of production cross sections in pp collisions at centre-of-mass energy $\sqrt{s}=14$ TeV is an important prerequisite to define a discovery strategy. There is not a single production mechanism or decay channel that dominates the whole accessible mass range from 100 GeV/c^2 to 1 TeV/c^2, rather there exist several scenarios that excel depending on m_{H}. The production mechanisms leading to detectable cross sections at LHC have the common feature of Higgs coupling to heavier particles ($\mathrm{W}^{\pm}$, Z and t) and are:

- gluon-gluon fusion [30, 31]
- WW, ZZ fusion [32]
- associated production with W or Z bosons [33]
- associated production with $\mathrm{b\bar{b}}$ or $\mathrm{t\bar{t}}$ pairs [34]

All these processes are known with some uncertainties, as the lack of precise knowledge of gluon distribution inside proton or effect of higher-order perturbative QCD corrections, although none of these is particularly large. In Fig. 2.1 the cross sections for the main production processes at LHC as a function of m_{H} are shown. The gluon fusion is largely the most important, but the associated production with $\mathrm{W}^{\pm}$ or $\mathrm{t\bar{t}}$ can be used in experimental searches to reject the background in a more efficient way.

2.2 Searches for SM Higgs Boson at LHC

Fully hadronic events are the most copious final states from Higgs decays. These decays can not easily resolved when merged in QCD background, therefore topologies with leptons or photons are preferred, even if they have a smaller branching ratio. Furthermore the associated production with a leptonically decaying particle is searched for, despite a smaller cross section.

The different search strategies depend also on the Higgs boson mass range. According to the Higgs boson decay mode curves of Fig. 1.2 on page 15, three regions of m_{H} are defined:

Low Mass Region $\mathbf{m_H \lesssim 130\ GeV/c^2}$ the $\mathrm{b\bar{b}}$ decay mode dominates.

Intermediate Mass Region $\mathbf{130\ GeV/c^2 \lesssim m_H \lesssim 2m_Z}$ the $\mathrm{b\bar{b}}$ decay decreases with increasing $\mathrm{H \to VV^*}$ ($\mathrm{V = W^{\pm}}$ or Z).

High Mass Region $\mathbf{m_H \gtrsim 2m_Z}$ the Higgs boson decays mainly into *on-shell* $\mathrm{W^+W^-}$ or ZZ pairs.

In the next sections it will be described how the search puzzle should be solved in all the three mass regions.

2.2.1 Low Mass Region

This region is the most probable to find Higgs boson in, as indicated by theoretical and experimental limits (see Sec. 1.5.2), but it is nevertheless the harder to be explored at LHC. The $\mathrm{b\bar{b}}$ decay mode is the dominant one by more than one order of magnitude. Inclusive Higgs boson production followed by $\mathrm{H \to b\bar{b}}$ decay has a relatively large cross section (28 pb for $m_{\mathrm{H}} = 115\ \mathrm{GeV/c^2}$) but it is almost impossible to exploit the $\mathrm{H \to b\bar{b}}$ decay into overwhelming QCD background, since the total $\mathrm{b\bar{b}}$ cross section at LHC is more than six order of magnitude higher than the expected signal. This is the reason

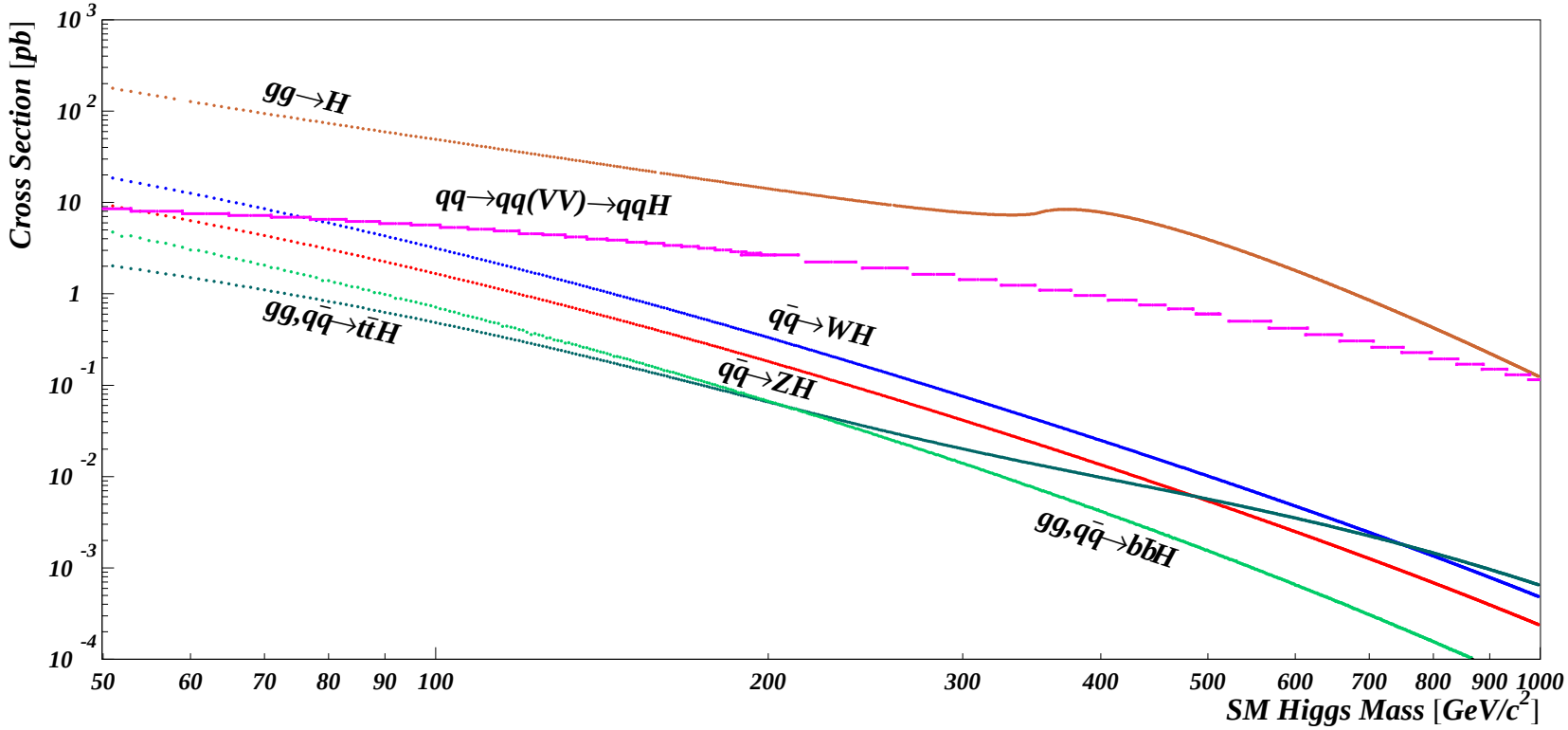

Figure 2.1: *Higgs production cross sections in* $\sqrt{s}=14$ TeV pp *collisions at LHC: gluon fusion [30, 31]* $gg \to H$, *vector boson fusion [32]* $qq \to qqVV \to qqH$ *(*$V = W$ *or* Z*), associated production [33, 34]* $W^{\pm}H$, ZH, $t\bar{t}H$ *and* $b\bar{b}H$. *All these processes but* $t\bar{t}H$ *and* $b\bar{b}H$ *are calculated at higher order of QCD corrections.*

of the importance of the search for the associated production $t\bar{t}H$, $W^{\pm}H$ or ZH with the $H \to b\bar{b}$ decay followed by the leptonic decay of the accompanying particle. For a 115 GeV/c^2 Higgs boson mass, the WH cross section is about 2 pb, but nevertheless this kind of events can be efficiently extracted from the background by identifying the isolated charged lepton (e, μ) originated from the W decay. This thesis is focused on the online selection of the WH production and decay represented in Fig. 2.2, selected with $W \to \mu\nu_\mu$ identification followed by b-tagging. The development of a trigger algorithm for the CMS experiment at LHC to select this process is the final goal.

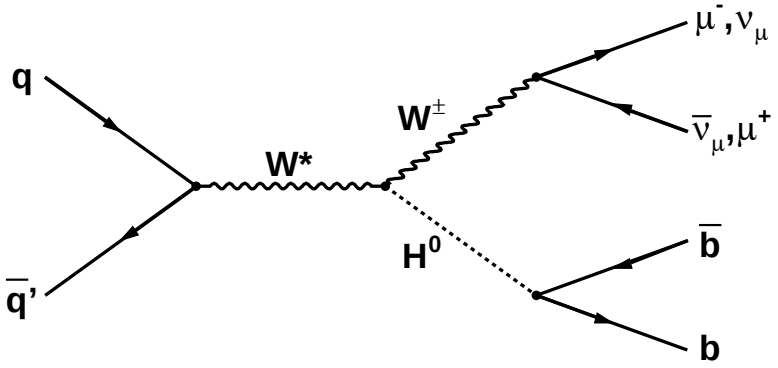

Figure 2.2: *Feynman diagram for $q\bar{q}' \to W^* \to W(\to \mu\nu_\mu)H(\to b\bar{b})$ process at tree-level.*

The second decay channel $H \to \tau^+\tau^-$ is hopeless to be studied, because it is overwhelmed by $t\bar{t}$ and Drell-Yan $\tau^+\tau^-$ pair production.

A cleaner channel should be the decay $H \to \gamma\gamma$, but it has a very small cross section, $\sigma(gg \to H) \cdot Br(H \to \gamma\gamma)$=38.1 pb·0.2 $\times 10^{-2}$ = 76 fb for a 115 GeV/c^2 Higgs boson mass. The background for this channel comes from $\pi^0 \to \gamma\gamma$ decays with the two photons too close to, faking a single energetic γ. Anyway the signal-to-background ratio is 10^{-2}, this is the reason why this channel is much more attractive than the $b\bar{b}$ channel. The two photon decay can be searched for also in association with a leptonic $t\bar{t}$ or $W^{\pm}$ decay making this channel the most clear at LHC if the Higgs mass were less than 150 GeV/c^2. Of course an electromagnetic calorimeter with excellent performance is required to enhance the signal-to-background ratio for this channel.

2.2.2 Intermediate Mass Region

The most promising channels are $gg \to H \to WW^* \to \ell^+\nu_\ell\ell'^-\bar{\nu}_{\ell'}$ or $gg \to H \to ZZ^* \to \ell^+\ell^-\ell'^+\ell'^-$, with ℓ, ℓ' = e or μ. The WW^* decay mode has to be extracted from a background mainly due to $qq \to WW$ continuum or $t\bar{t} \to bW^+\bar{b}W^-$ and $W^{\pm}t(b)$ associated production.

The fully leptonic decay H→ZZ*→4ℓ has the cleanest experimental signature, particularly in the four-muon channel. The signal selection is based on the identification of two opposite charged lepton pairs coming from a common vertex. The invariant mass of one of the two pairs should be compatible with m_{Z}. The main irreducible background is continuum ZZ* production $q\bar{q}$→ZZ*→4ℓ together with reducible background t$\bar{\mathrm{t}}$→4ℓ + X and Zb$\bar{\mathrm{b}}$→4ℓ + X. In the first case leptons come from t→Wb decay followed by W→$\ell\nu_\ell$ and semileptonic b decay, in the second case two leptons are from Z→$\ell\bar{\ell}$ and the other two from b quark decay chains.

2.2.3 High Mass Region

The predominant decay channels are H→$\mathrm{W}^+\mathrm{W}^-$ and H→ZZ with both vector bosons *on-shell*. The $\mathrm{H}\to\mathrm{ZZ}\to 4\ell$ channel has a smaller $q\bar{q}\to\mathrm{ZZ}\to 4\ell$ background than in the intermediate mass region, the selection of the signal being facilitated by requiring both $\ell^+\ell^-$ pair invariant masses close to m_{Z}. Furthermore, the intrinsic Higgs width Γ_{H}, shown in Fig. 1.1 on page 14, is larger than the achievable experimental mass resolution, therefore the detector performance is not critical. For all these reasons, the H→ZZ→4ℓ channel is a *gold-plated* Higgs boson signature at LHC.

For very large masses, $m_H > 600$ GeV/c^2, other decay modes are used to supplement H→ZZ→4ℓ, because the production cross section decreases significantly and the resonance peak of the four leptons becomes too broad ($\Gamma_{\mathrm{H}} = 665$ GeV at $m_{\mathrm{H}} = 1$ TeV/c^2) and will no longer be visible. There are exploited the following decays of associated vector bosons: H→Z(→$\ell^+\ell^-$)Z(→$\nu_{\ell'}\bar{\nu}_{\ell'}$) or H→Z(→$\ell^+\ell^-$)Z(→$q\bar{q}$) and H→W(→$\ell\nu_\ell$)W(→$q\bar{q}'$), whose vector boson hadronic decay has a greater branching ratio than the pure leptonic ones. The main background is from ZZ, ZW, WW and W(Z)q and if neutrinos appear in the final states a high missing transverse energy will be the relevant signatures of the event.

The list of the most suitable signatures for Higgs searches at LHC is shown in Fig. 2.3 with the corresponding mass ranges. The task of the work that will be described in the next chapters is to realize an algorithm to select during the online data taking the most difficult low mass channel with muons and b quarks, as $q\bar{q}'$→W*→W(→$\mu\nu_\mu$)H(→b$\bar{\mathrm{b}}$), which presently is considered hardly impossible to be triggered at LHC and stored permanently for the offline analysis.

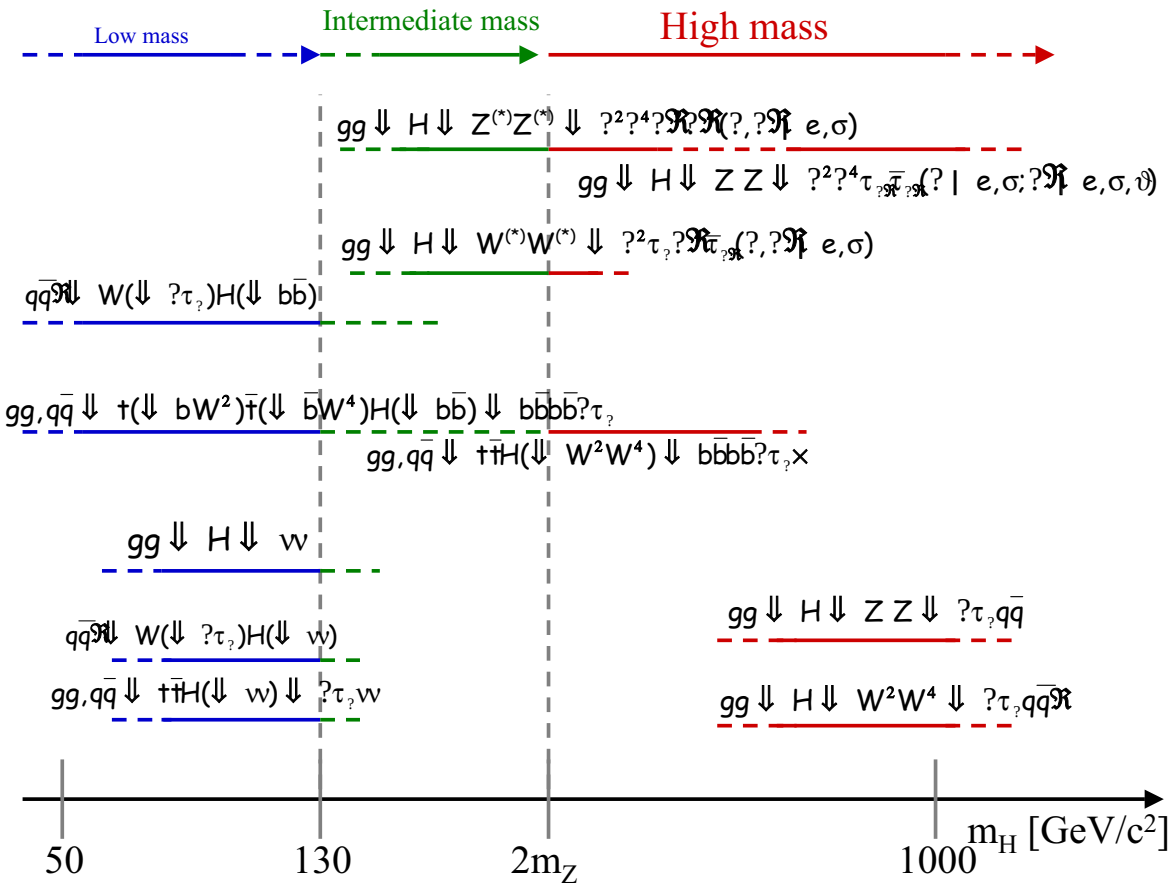

Figure 2.3: *Most useful experimental signatures for Higgs search at LHC and corresponding mass ranges.*

Chapter 3

The CMS experiment at LHC

The new frontiers of particle physics are the searches for extremely elusive particles, which are produced in processes with very low cross sections, the *femtobarn* being the natural unit. The leptonic colliders are no more suitable to explore the boundaries of particle physics, higher energies and larger luminosities are needed and presently only hadron colliders have the technologies to provide them on earth. Despite the production of a lot of low energetic particles resulting in a not clean environment if compared to a leptonic interaction, a proton-proton collider offers the possibility to span over a wider energy spectrum that can be explored simultaneously and permits to reach higher production rates. These are the motivations of the CERN choice for the Large Hadron Collider (LHC) with the related experiments, as the one I am involved in which is described in this chapter: the Compact Muon Solenoid (CMS).

3.1 The Large Hadron Collider

3.1.1 The Accelerator

The Large Hadron Collider LHC [29] will be the most powerful hadron collider running in the next two decades. It is under construction in the already existing LEP [22] tunnel at CERN laboratories in Geneva, Switzerland. The Large Electron-Positron collider LEP has accelerated e^+e^- beams from August 13^{th} 1989 to November 2^{nd} 2000 with centre-of-mass energies from the Z peak $\sqrt{s}=91$ GeV (LEP1) to the W^+W^- threshold ($\sqrt{s}=161$ GeV) and up to the over-designed $\sqrt{s}=210$ GeV (LEP2). It was a circular accelerator, sited about 100 m depth underground between the French-Swiss border. The new accelerator LHC will produce collisions between proton beams with $\sqrt{s}=14$ TeV, world record for a collider. It is planned to produce the first collision on April 2007

and start the physics programme from August 2007. To reach such an energy, proton beams will be accelerated by existing CERN facilities of Fig. 3.1, which will be upgraded. Protons will be accelerated and brought up to 50 MeV by a linear accelerator LINAC. A Booster raises the beam energy up to 1.4 GeV injecting proton beams into the old

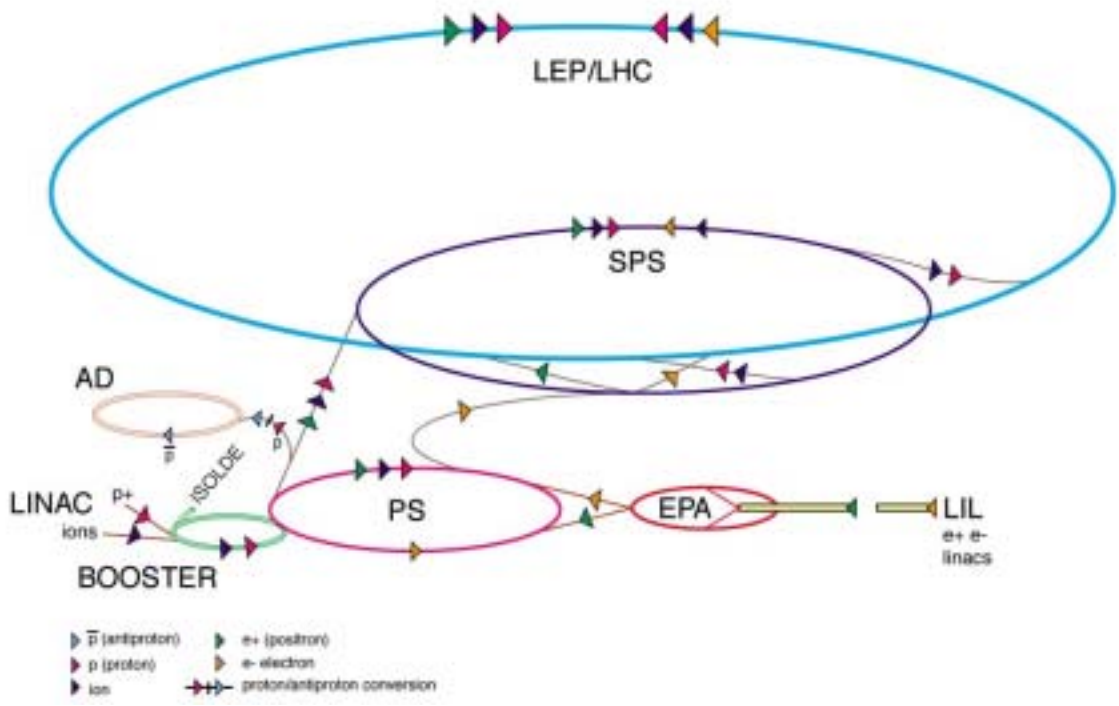

Figure 3.1: *Overview of the accelerator complex at CERN. The LEP* e^+ *and* e^- *trajectories and LHC* pp *and* Pb-Pb *trajectories are indicated.*

circular accelerator PS[1]. The 25 GeV energy beams extracted from PS are injected to a bigger circular accelerator SPS[2], which introduces 450 GeV proton beams into the LHC ring. The tunnel of LHC is a 26.659 km circumference, composed with 8 curvilinear sections (2.840 km) and 8 rectilinear sections, where the beams collide. The accelerating power of LHC is limited by the bending magnetic field needed to keep the beams circulating in the tunnel, that is

$$p[\,\mathrm{GeV/c}] = 0.3 \cdot B[\mathrm{T}] \cdot \rho[\mathrm{m}] \tag{3.1}$$

with B magnetic field supplied to maintain p momentum particles in a circular orbit with radius ρ. The choice of 7 TeV beam energy is forced by the maximum achievable

[1]Proton Synchrotron.
[2]Super Proton Synchrotron.

magnetic fields and depends on the radius $\rho = 4.3$ km of the pre-existent accelerator, resulting in $B = 5.4$ T. For the collisions will occur between particles of the same kind, a unique magnetic field is required to accelerate the proton beams in opposite directions and the two beam pipes will be inserted into a single cryostatic structure with the superconducting magnets and the corresponding coils. A sketch of the LHC cryodipole is painted in Fig. 3.2. Moreover, the machine can not be completely filled with magnets, hence in the curvilinear sections 1 232 main dipoles operating at 1.9 K and generating a magnetic field up to 8.33 T will be used to steer the particles into curvilinear trajectories together with 386 quadrupoles, 360 sextupoles and 336 octupoles for stability control. In the linear segments, 400 MHz superconducting radiofrequency cavities will provide the boost and supply energy losses with electric fields ranging from 3 $\mathrm{MV\,m^{-1}}$ at injection to 16 $\mathrm{MV\,m^{-1}}$. In Tab. 3.1 the main design parameters of LHC are listed. At LHC there will be accelerated also heavy ions with total energy up to 2.76 ATeV in $\mathrm{Pb-Pb}$ collisions.

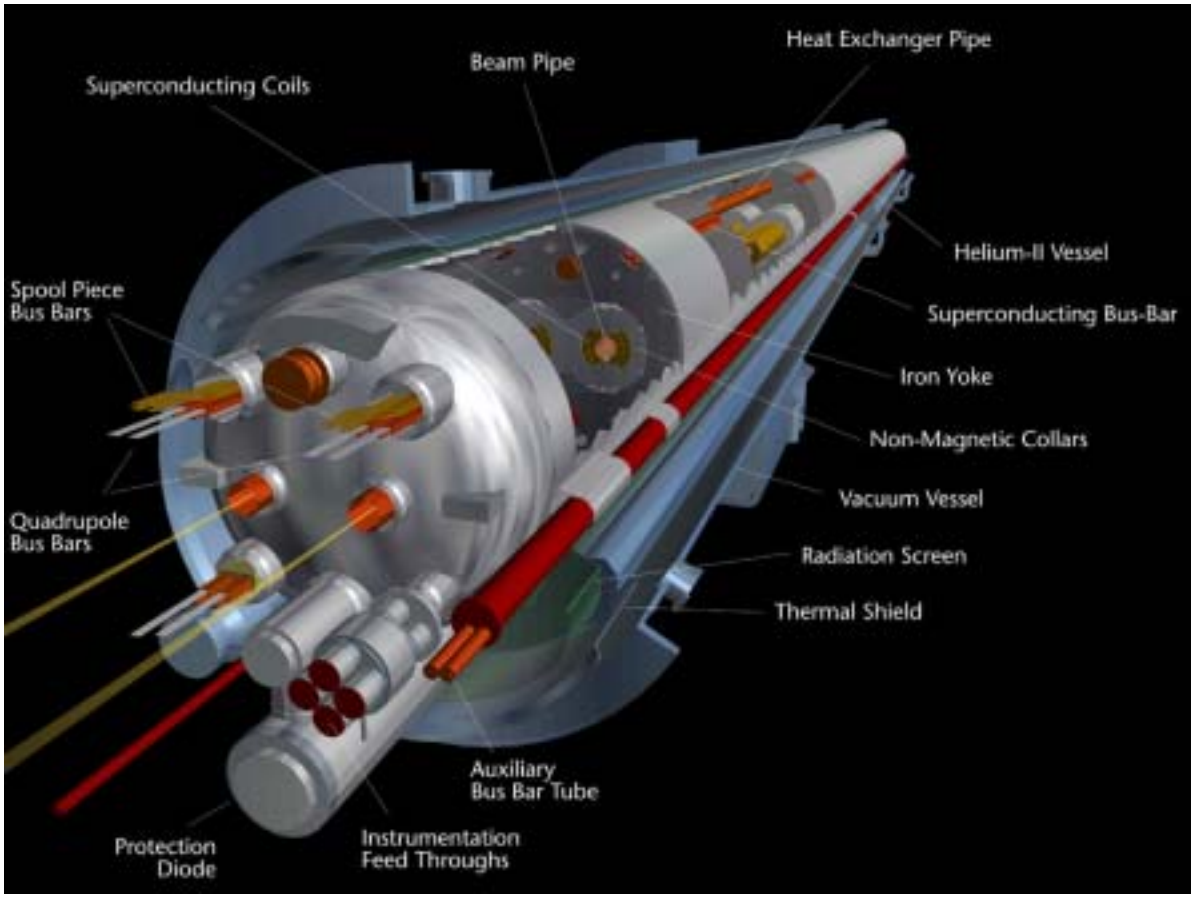

Figure 3.2: *The* 15 m *long LHC cryodipole. The coil inner diameter is* 55 mm.

Circumference	26.659 km	
Maximum Dipole field	8.33 T	
Magnetic Temperature	1.9 K	
	p − p	$^{82}_{208}$Pb-$^{82}_{208}$Pb
Beam energy at injection	450 GeV	73.8 TeV
Beam energy at collision	7 TeV	574 TeV(2.76 ATeV)
Maximum Luminosity	1×10^{34} cm^{-2}s^{-1}	2×10^{27} cm^{-2}s^{-1}
Number of Bunches	2 808	608
Bunch spacing	7.48 cm	5.3 cm
Bunch separation	24.95 ns	124.75 ns
Number of particles per bunch	1.1×10^{11}	8×10^{7}
Total crossing angle	300 μrad	$<$100 μrad
Bunch Length (r.m.s.)	7.5 cm	7.5 cm
Transverse beam size at Impact Point	15 μm	15 μm
Luminosity lifetime	10 h	4.2 h
Filling time per ring	4.3 min	9.8 min
Energy loss per turn	7 keV	
Total radiated power per beam	3.8 kW	
Stored energy per beam	350 MJ	

Table 3.1: *Technical parameters of LHC.*

An important parameter to characterize the performance of a collider is the luminosity $\mathcal{L}$, a quantity completely determined by the colliding beam properties. With a small crossing angle between the beams, composed with gaussian-shaped bunches, LHC luminosity $\mathcal{L}$ is expressed as [35]

$$\mathcal{L} = F\frac{\upsilon n_b N_1 N_2}{4\pi\sigma_x\sigma_y} \tag{3.2}$$

where υ is the revolution frequency of the n_b bunches, $F=0.9$ is a correction factor due to non-zero crossing angle (lower than 300 μrad), N_1 and N_2 number of protons in the two colliding bunches, σ_x and σ_y the beam profiles in horizontal (bend) and vertical directions at the interaction point. A realistic scenario foresees a three-year initial period at "low luminosity" $\mathcal{L}=2\times10^{33}$ cm^{-2}s^{-1}, after which it will be gradually reached the planned "high luminosity" value of 10^{34} cm^{-2}s^{-1} for pp collisions. To achieve this unprecedented value, the two beams will contain 2 808 closely-spaced bunches filled with an average of 1.1×10^{11} protons each and will collide every 25 ns. In case of lead-lead collisions,

the designed luminosity is about 10^{27} cm^{-2}s^{-1}. This performance can be obtained also because the two proton beams will be very collimated, with an estimated spread of the beam spot $\sigma_x \simeq \sigma_y \simeq 15$ μm in the plane perpendicular to the beam direction. The uncertainty on the collision point position along the beam axis is about 7.5 cm around the nominal point.

The number of interactions N_i corresponding to the process "i" with cross section σ_i can be written as

$$N_i = \sigma_i \int \mathcal{L} dt \tag{3.3}$$

where the integration is performed upon the running time of the machine with luminosity $\mathcal{L}$. The expression $\int\mathcal{L}$ is referred to as *Integral Luminosity* and it is measured in *inverse barn* (b^{-1}), 1 b=10^{-24} cm^2. An integrated luminosity of 20 fb^{-1} per year in the first three years at low luminosity for a total of 60 fb^{-1} should be collected. The second phase at high luminosity will last at least five years for a total amount of 500 fb^{-1} of data.

Four detectors will be installed in the caverns around the collision points, shown in Fig. 3.3; two of them are multi-purpose experiments, ATLAS [36] and CMS [37], the other two are dedicated experiments, one to heavy ion physics, ALICE [38], and the other to b quark physics and precision measurements of CP violation, LHCb [39].

3.1.2 Phenomenology of proton-proton collisions

Unless leptons, protons are not elementary particles, but are composed with partons: three valence quarks (uud) surrounded by a "sea" of quarks and gluons continuously produced mainly by gluon radiation from valence quarks followed by gluon splitting $g \rightarrow q\bar{q}$. When two protons collide at energies higher than the mass[3], the interaction involves generally two of the constituent partons. In Fig. 3.4 it is represented the interaction of the two hadron beams A and B, that takes place between partons a and b leaving the remaining partons untouched.

The inelastic interactions belong to two classes:

- Large distance collisions between the two incoming protons, where only a small momentum is transferred during the interaction. They are soft collisions with production of particles with large longitudinal momentum and small transverse momentum $p_T \simeq 500$ MeV/c. The scattering at large angle is suppressed, most of the particles escaping detection along the beam pipe. This kind of processes is referred to as *Minimum Bias* and represents the majority of pp collisions.

[3] m_p=938.272 00(4) MeV/c^2 [1].

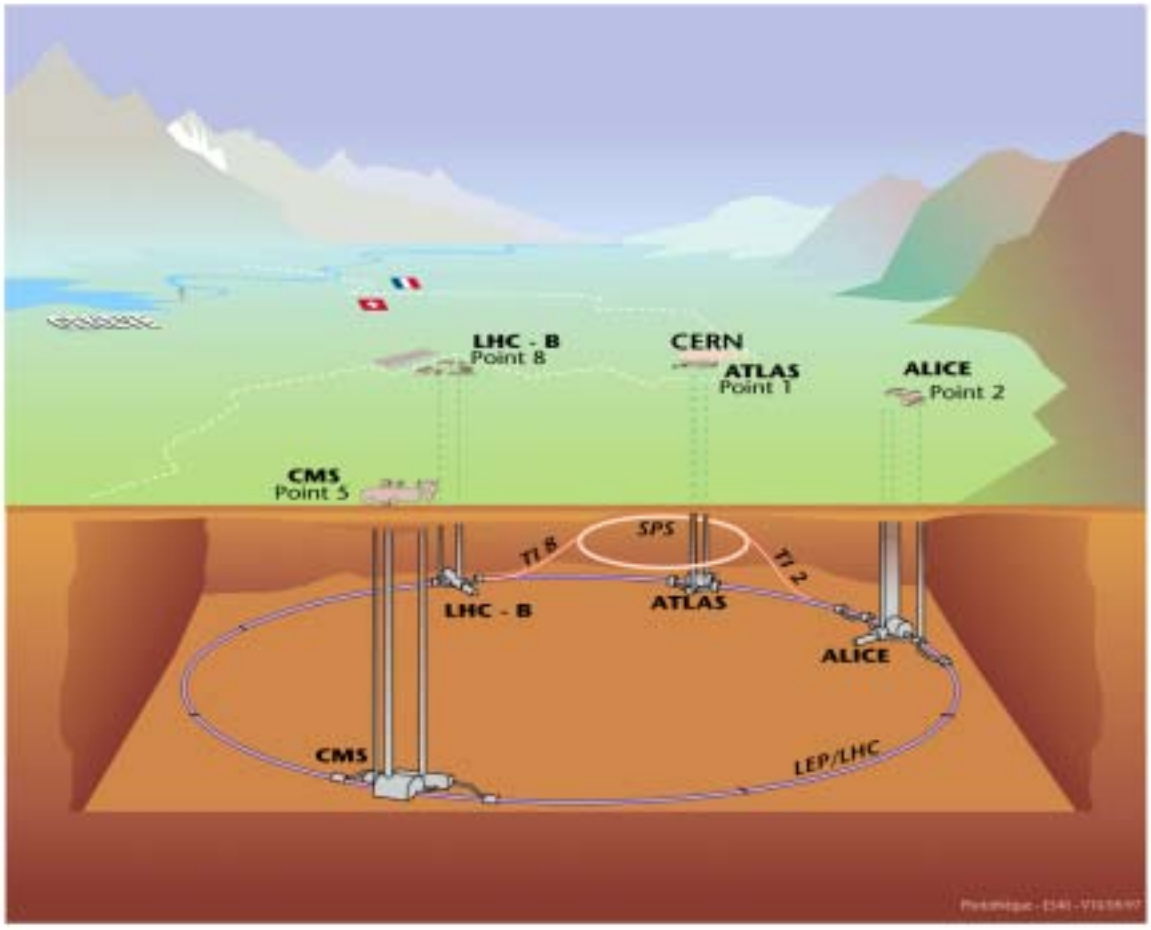

Figure 3.3: *Map of LHC and related experiments.*

- A monoenergetic proton beam can be thought as a beam of partons (quarks, gluons) with a wide energy band. Occasionally, head-on collisions occur at small distances between parton a from the first beam and parton b from the second. In this hard scattering there is a larger transferred momentum than in Minimum Bias and massive particles could be created, with higher p_{T} and large angles with respect to the beam line. These are the interesting physics events, but unfortunately they are rare. For example, the inclusive W (Z) production cross section is [40] 140 nb (43 nb) and assuming the total inelastic pp cross section at $\sqrt{s}=14$ TeV to be $\sigma_{in}^{\mathrm{pp}}=55$ mb, the result is that it occurs only every about 2 millions (8 millions) pp interactions.

Another important aspect of pp collisions is the impossibility to define *a priori* the centre-of-mass energy of the interaction. As can be seen in Fig. 3.4, only a fraction

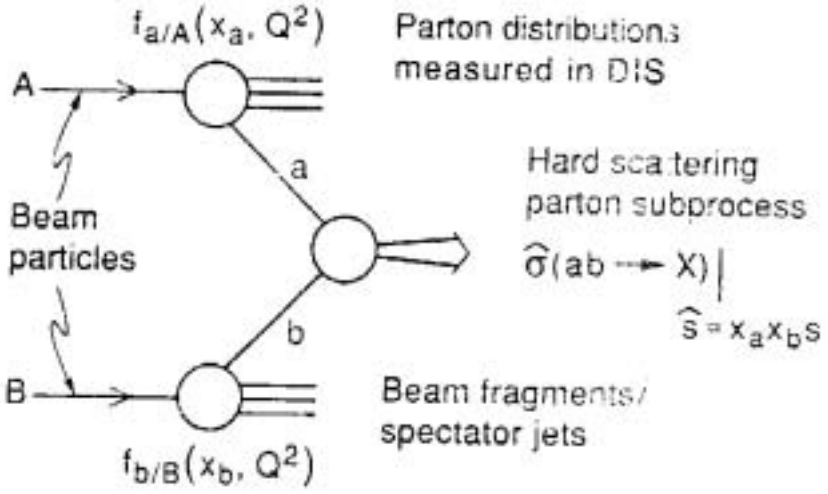

Figure 3.4: *Schematic picture of hadron-hadron collisions.*

$0 < x_a(x_b) < 1$ of the A (B) beam momentum is carried away by the interacting parton. In general the two fractions x_a and x_b are different and this fact leads to two important consequences: the energy available for each interaction of the di-parton system $\sqrt{\hat{s}} = \sqrt{x_a x_b s}$ varies from event to event, thus giving the possibility to explore a wide energy range, and the effective centre of mass is boosted along the beam direction, hence invariant variables for boosts along the beam direction are preferred to describe the dynamics of these interactions. The initial state constraints present in LEP-like colliders are no longer usable, at least the longitudinal ones.

The total cross section for a generic hard interaction can be written as

$$\sigma = \sum_{a,b} \int dx_a dx_b f_a(x_a, Q^2) f_b(x_b, Q^2) \hat{\sigma}(x_a, x_b) \tag{3.4}$$

where the sum is performed over all the partons a and b of the two protons, $f_a(x_a, Q^2)$ ($f_b(x_b, Q^2)$) is the probability of finding a parton carrying a fraction x_a (x_b) of the proton momentum with exchanged four-momentum Q^2 during the interaction (the Parton Density Functions [41] represented in Fig. 3.5) and $\hat{\sigma}(x_a, x_b)$ cross section for the elementary interaction between partons a and b.

The dynamics described above has not a motionless centre of mass in the LHC reference frame, but on average there is a boost along the direction of the two beams. For this reason, boost invariant quantities has to be defined to characterize the event. The more important are the transverse momentum p_{T}, defined as the magnitude of the projection of the momentum $\vec{p}$ on a plane perpendicular to the beam axis, and the

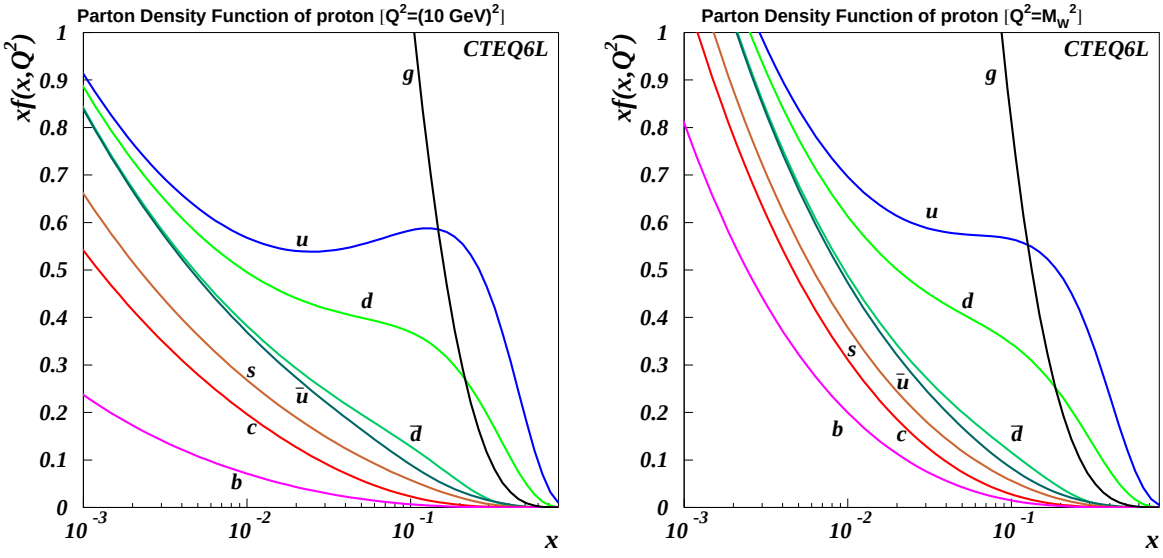

(a) (b)

Figure 3.5: *Parton Density Function [41] for a proton with* $Q^2 = (10\ \mathrm{GeV})^2$ *(a) and* $Q^2 = M_{\mathrm{W}}^2$ *(b).*

rapidity

$$y = \frac{1}{2} \ln \frac{E + p_z}{E - p_z} = \tanh^{-1} \left(\frac{p_z}{E} \right) \tag{3.5}$$

with E energy and p_z projection of the momentum of the particle along the beam axis. Under a boost in the z direction with velocity β, $y \to y - \tanh^{-1} \beta$ and hence the rapidity distribution $\frac{dN}{dy}$ is invariant. In the ultrarelativistic approximation $\frac{m}{|\vec{p}|} \ll 1$, the rapidity may be expanded to obtain

$$y = \frac{1}{2} \ln \left[\frac{1 + \cos\theta + \frac{1}{2} \left(\frac{m}{|\vec{p}|} \right)^2 + o\left(\left(\frac{m}{|\vec{p}|} \right)^2 \right)}{1 - \cos\theta + \frac{1}{2} \left(\frac{m}{|\vec{p}|} \right)^2 + o\left(\left(\frac{m}{|\vec{p}|} \right)^2 \right)} \right] \simeq -\ln \tan \left(\frac{\theta}{2} \right) \equiv \eta \tag{3.6}$$

with $\cos\theta = \frac{p_z}{|\vec{p}|}$. The Eq. 3.6 defines the pseudorapidity η, approximately equal to y if $\frac{m}{|\vec{p}|} \ll 1$ and $\theta \gg \frac{1}{\gamma}$ and in any case measurable when either the mass or the momentum of a particle are unknown.

Thus the invariant differential cross section can be expressed as

$$E \frac{d^3\sigma}{d^3\vec{p}} \Rightarrow \frac{d^2\sigma}{\pi dy\, d(p_{\mathrm{T}}^2)} \simeq \frac{d^2\sigma}{\pi d\eta\, d(p_{\mathrm{T}}^2)} \tag{3.7}$$

using $\frac{dy}{dp_z} = \frac{1}{E}$ and integrating over the azimuthal angle $\phi \in [0, 2\pi)$.

3.1.3 Experimental Challenges

The event rate R_i is defined as the number of events per unit of time occurring with cross section σ_i and can be extracted by deriving with respect of time Eq. 3.3:

$$\frac{dN_i}{dt} = R_i = \sigma_i \cdot \mathcal{L} \tag{3.8}$$

It is proportional to the cross section σ_i with the proportionality constant given by the luminosity $\mathcal{L}$, which depends only on the machine parameters and *not* on the physical process i. In Eq. 3.8 it is indicated how to achieve the highest statistics for a given process i: it can be acted either on the luminosity or in the collision energy that maximizes the cross section. In Fig. 3.6 the cross sections for various processes that will be studied at LHC are shown as a function of the proton-proton energy of the centre of mass $\sqrt{s}$. The indication that can be argued to raise the statistics is to push to the limit the beam energy, because the inclusive Higgs boson cross section grows rapidly with $\sqrt{s}$ while the total inelastic pp cross section remains approximately constant. The extrapolated inelastic pp cross section at $\sqrt{s}=14$ TeV is $\sigma_{in}^{\mathrm{pp}}=55$ mb, therefore from Eq. 3.8 the total rate is estimated to be 5.5×10^8 ev s^{-1} (1.1×10^8 ev s^{-1}) at high (low) luminosity $\mathcal{L}=10^7$ mb^{-1}s^{-1} ($\mathcal{L}=2\times10^6$ mb^{-1}s^{-1}). The total number of inelastic pp interactions at each bunch crossing $\mathcal{N}_{int}$ can be estimated from Eq. 3.9:

$$\mathcal{N}_{int} = \frac{R}{f(1-e)} = \frac{\sigma_{in}^{\mathrm{pp}} \cdot \mathcal{L}}{f(1-e)} \tag{3.9}$$

where the beam collision frequency f is equal to $\frac{1}{25\ \mathrm{ns}}=40$ MHz and e=20% is the fraction of empty bunch crossings. From Eq. 3.9 it results that an average of 17.2 (3.4) inelastic interactions will occur per each bunch crossing at high (low) luminosity. This causes a very hostile environment, every soft collision will produce on average seven charged particles in the central pseudorapidity region with a mean transverse momentum $p_{\mathrm{T}}=0.5$ GeV/c and 8.3 primary photons per unit of pseudorapidity. The distribution of the charged particles from Minimum Bias is almost flat in the region of η between -6 and $+6$, as it is shown in Fig 3.7a. The consequence of this dense particle environment (both in space and time) is the highly demanding requirement for the LHC experiments: they have to be finely space-segmented detectors and have high time resolution. According to Eq. 3.9, a way to reduce the Minimum Bias interactions keeping $\mathcal{L}$ constant is to increase the collision frequency reducing the number of particles per bunches (see also Eq. 3.2), as a consequence the detectors are demanded to have very fast timing performance to separate signals from different bunch crossings, reducing the *pile-up* of near-by events.

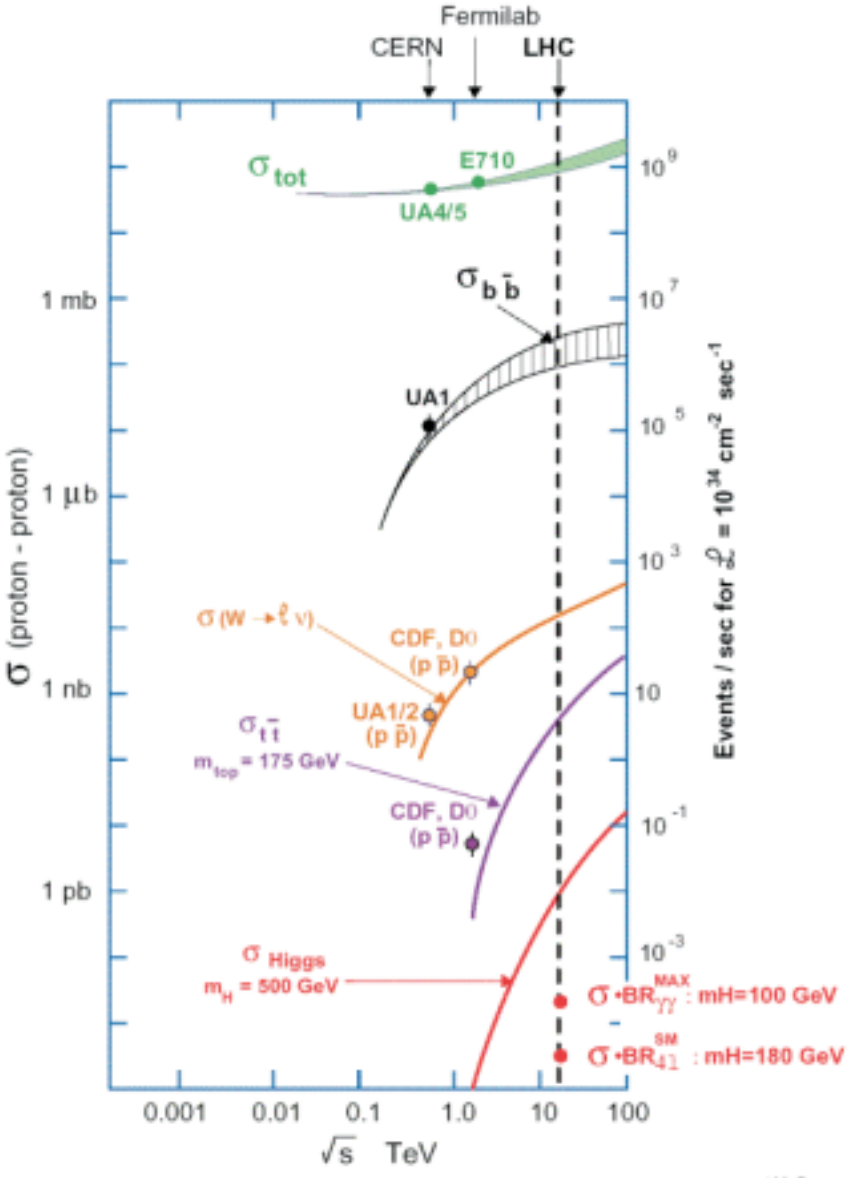

Figure 3.6: *Cross section σ of proton-proton collisions as a function of the center of mass energy $\sqrt{s}$ (*TeV*).*

3.2 The CMS Experiment

The Compact Muon Solenoid experiment, CMS [37], is a general purpose detector which will operate at LHC. The main feature of CMS is the 4 T superconducting solenoid that permits a compact design of the detector with a strong magnetic field. The design priorities fulfilled by the CMS project [42] are a redundant muon system, a good electromagnetic calorimeter and a high quality tracking system.

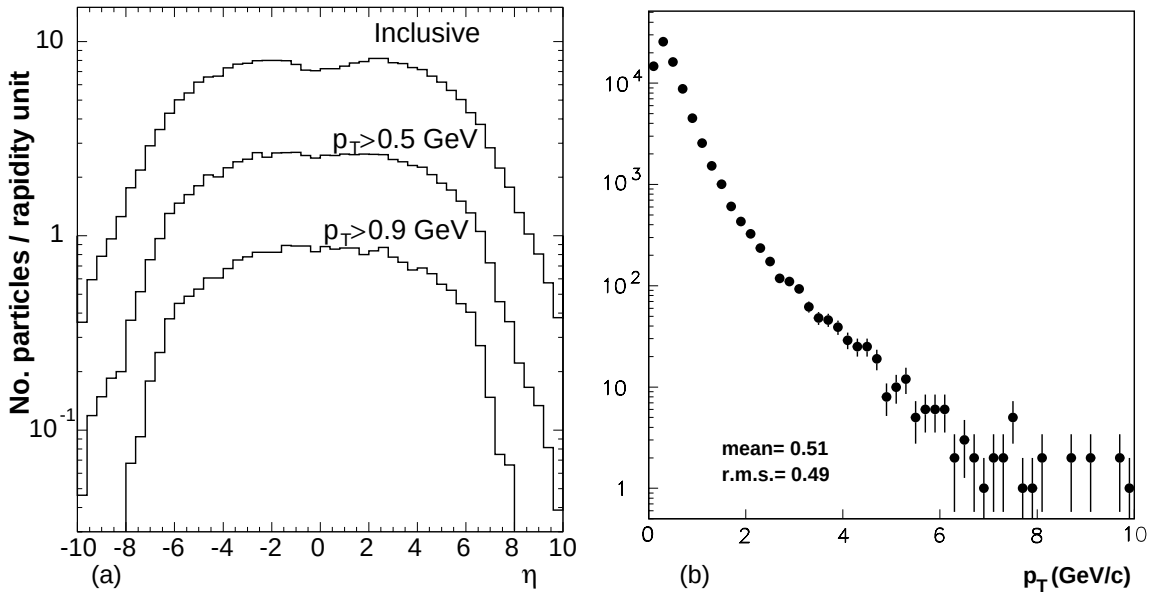

Figure 3.7: *Pseudorapidity η (a) and transverse momentum p_{T} (b) distributions of charged particles per Minimum Bias event.*

The structure of CMS is typical of a general purpose experiment designed for a collider: several cylindrical layers coaxial to the beam direction, referred to as *barrel* layers, closed at both ends by detector disks orthogonal to the beam pipe, the *endcaps*, to ensure detector hermeticity. In Fig. 3.8 a schematic view of CMS is drawn pointing out the cylindrical symmetry of the experiment, which has a full length of 21.6 m, a diameter of 15 m and reaches a total weight of 12 500 t.

The natural coordinate frame used to describe the detector geometry is a right-handed cartesian system with the x axis pointing to the centre of LHC ring, the z axis coincident with the CMS cylinder axis and the y axis directed almost upwards[4] along the vertical. The cylindrical symmetry of CMS design and the invariant description of pp physics drive to use a pseudo-angular reference frame, given by the triplet (r, φ, η), with r distance from z axis, φ azimuthal coordinate with respect to x axis and pseudorapidity η defined by Eq. 3.6.

In this reference frame it is easy to describe the CMS subdetectors, that are installed radially from inside out and represented in detail in Fig. 3.9 on page 39 and 3.10 on page 40:

[4]Since the beams are 1.23% inclined with respect to a plane perpendicular to the direction of the gravity force vector, the y axis is not exactly parallel to the vertical.

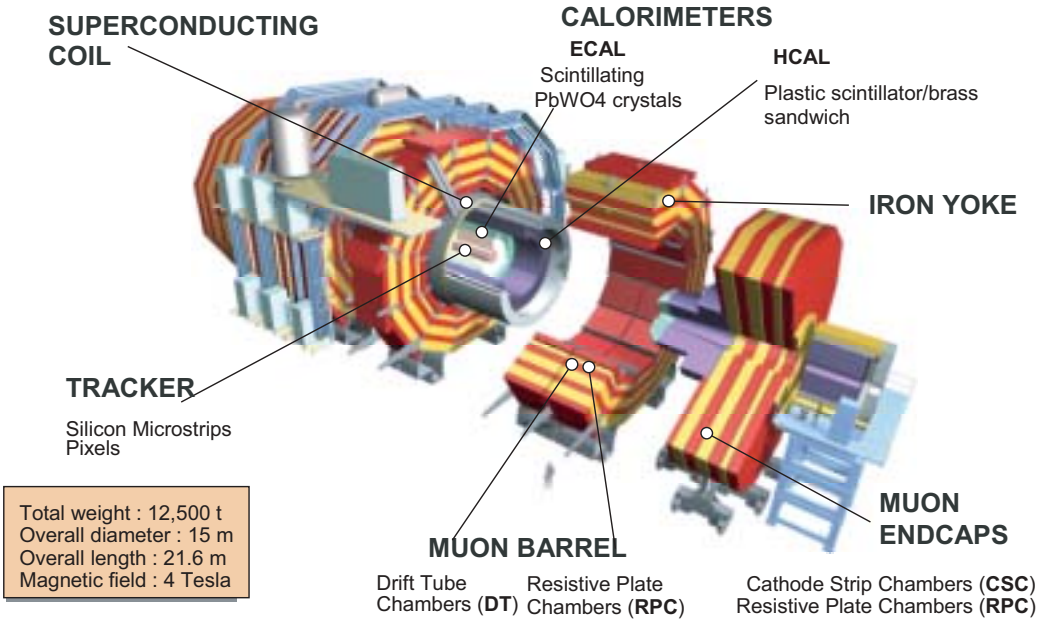

Figure 3.8: *Schematic picture of CMS experiment at LHC.*

– **Tracker** $r < 1.2$ m $|\eta| < 2.5$ Silicon pixel vertex detector plus 198 m^2 active area of Silicon microstrip detectors to reconstruct charged particle tracks and individuate primary and secondary vertices.

– **ECAL** $1.2\text{ m} < r < 1.8\text{ m}$ $|\eta| < 3$ electromagnetic calorimeter to precisely measure electrons and photons, composed by $PbWO_4$ scintillating crystals and a forward preshower detector.

– **HCAL** $1.8\text{ m} < r < 2.9\text{ m}$ $|\eta| < 5$ hadron calorimeter system for jet position and transverse energy measurements, extended in the forward region $3 < |\eta| < 5$ with a very forward calorimeter (HF).

– **Magnet Coil** $2.9\text{ m} < r < 3.8\text{ m}$ $|\eta| < 1.5$ the magnet, large enough to accommodate most of the calorimeters and the inner tracker, with a 4 T longitudinal magnetic field supplied by a superconducting solenoid.

– **Muon System** $4.0\text{ m} < r < 7.4\text{ m}$ $|\eta| < 2.4$ muon chambers merged inside the magnet yoke to detect and reconstruct muon tracks, composed by Drift Tubes (DT) in the barrel and Cathode Strip Chambers (CSC) in the endcaps and complemented overall up to $|\eta| < 2.1$ by Resistive Plate Chambers (RPC).

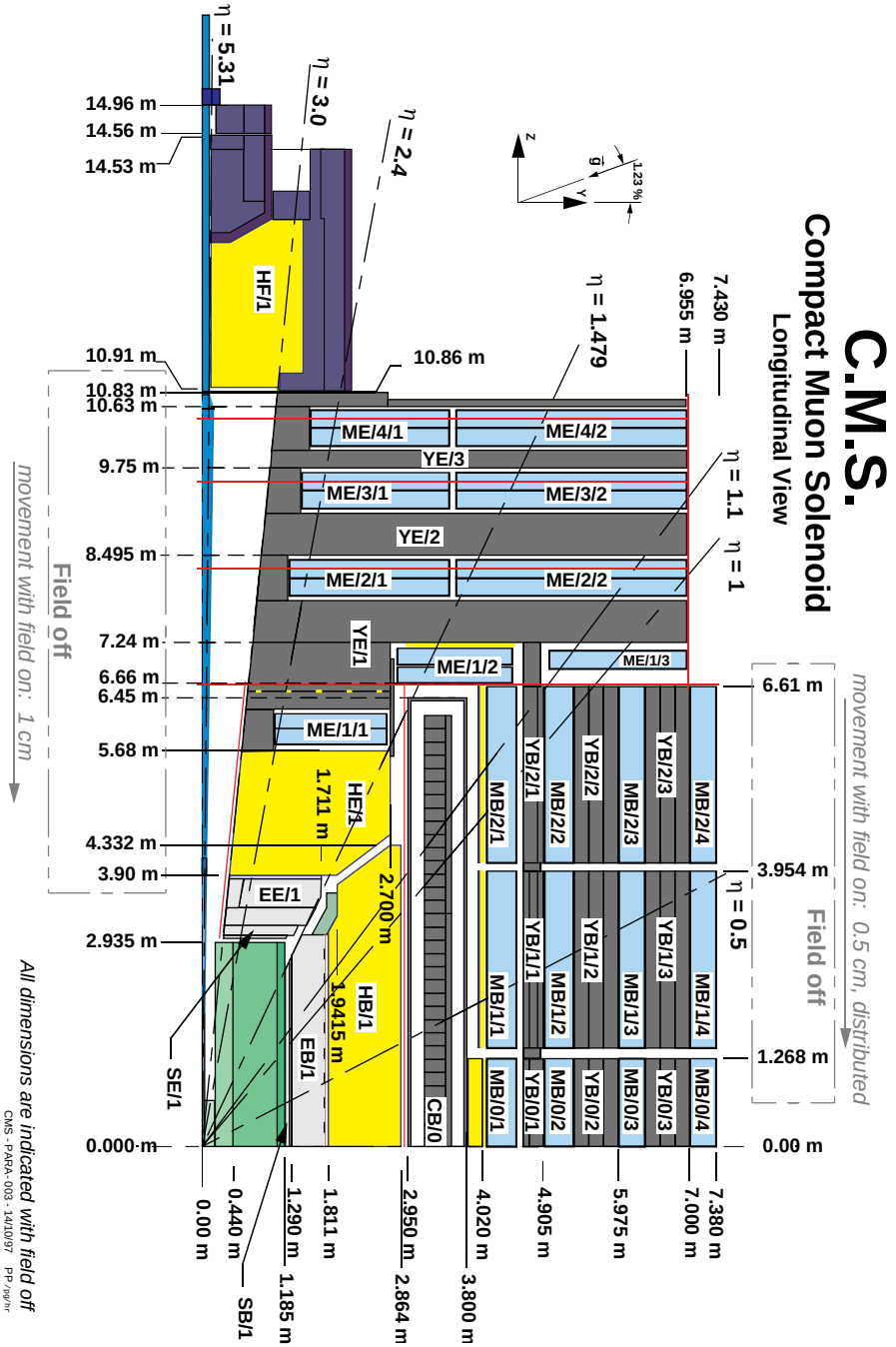

Figure 3.9: *Longitudinal view of a quarter of CMS experiment. Detectors and non-sensitive volumes are indicated by two-letter code: the first letter indicates the subdetector (S=Silicon tracker, E=Electromagnetic calorimeter, H=Hadron calorimeter, C=magnet Coil, Y=magnet iron Yoke, M=Muon chambers), the second letter refers to the position (B=Barrel, E=Endcap, F=Forward region).*

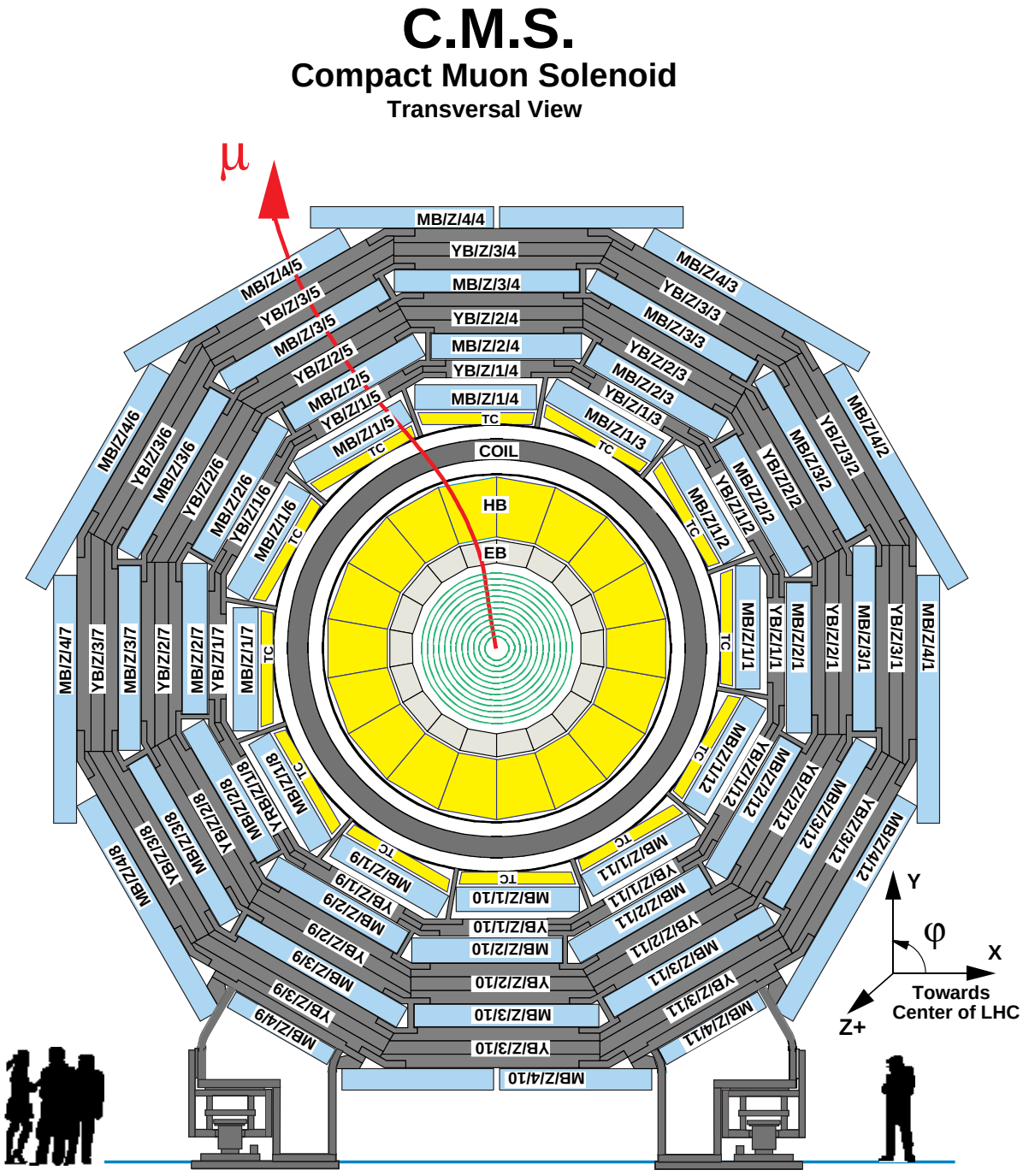

Figure 3.10: *Transversal view of the barrel region of CMS. Barrel wheels are identified with the same two-letter code of Fig. 3.9 and numbered along z direction as $z = -2, -1, 0, +1, +2$.*

3.2.1 The Magnet

The CMS magnet [43] is a 13 m long superconducting solenoid with a diameter of 5.9 m. It provides an inner uniform 4 T magnetic field, whose properties are summarized in Tab. 3.2, to permit precise measurements of charged particles transverse momentum with a large bending power.

Magnetic induction at impact point	4.0 T
Peak magnetic induction on the conductor	4.6 T
Coil length	12.48 m
Stored energy	2.70×10^9 J
Magnetomotive force	42.24×10^6 At
Magnetic radial pressure	6.47×10^6 Pa
Axial compressive force at mid plane	148×10^6 N

Table 3.2: *Main parameters of the CMS magnet.*

The conductor consists of three concentric parts: a central flat superconducting cable, an high purity aluminium stabilizer and an external aluminium-alloy to reinforce the sheath. The superconducting cable is a Rutherford type with 40 NiTb strands and is kept cooled by a liquid helium cryogenic system. The magnetic flux is closed in a loop via a 1.8 m thick saturated iron yoke, instrumented with four muon stations.

The coil accommodates the tracking system and most of the calorimeters and it is also a supporting structure for the inner part of the apparatus, because it is the main element in term of size, weight and, mostly, structural rigidity.

3.2.2 The Tracker

The silicon tracker [44] is the inner detector of CMS. It is the closest to the interaction point and represents an essential detector to address the multiplicity of LHC physics goals. It extends in the region $|\eta| < 2.5$, $r < 120$ cm, $|z| < 270$ cm and it is completely based on semiconductor detectors made of silicon covering the largest ever-designed Si detector surface of 198 m^2. Using the tracker, vertices and charged particle tracks have to be reconstructed in the highly congested LHC environment. To better solve the pattern recognition problem, the tracker is designed to fulfil two basic properties: low cell occupancy and large hit redundancy. For these reasons it is structured in an inner silicon pixel detector surrounded by several layers of silicon microstrip detectors of different size and pitch between the strips. The low occupancy is obtained by working

with high granularity detectors, mainly the ones closer to the interaction point because they have to cope with higher particle fluxes, and fast primary charge collection, obtained with thin detectors and overdepleting the silicon bulks. The redundancy is guaranteed by the overall design of Fig. 3.11, which allows many measured points per track within an acceptable material budget not to impairing too much the electromagnetic calorimeter performance. In this way an average of 12-14 points (*hits*) per track are guaranteed to

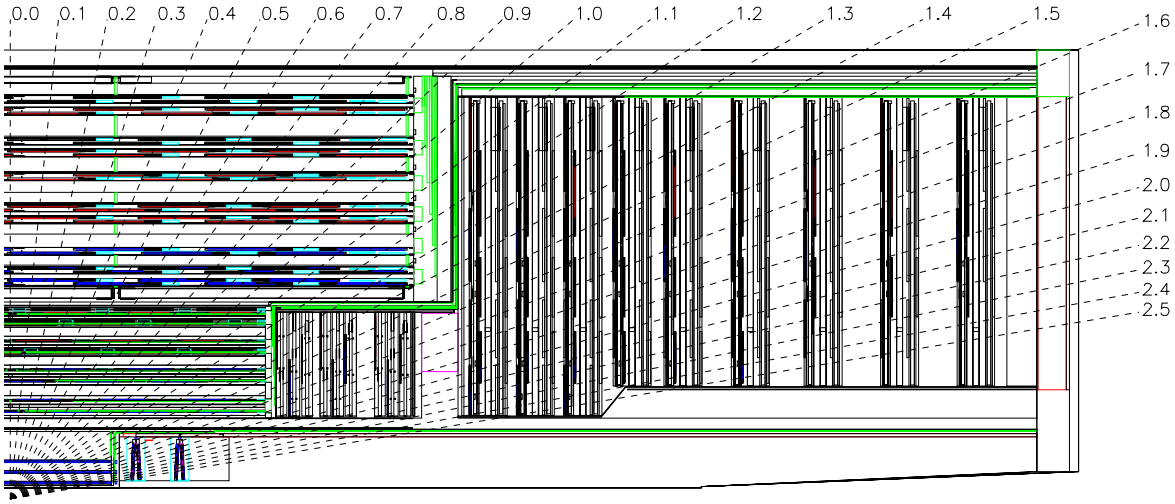

Figure 3.11: *Schematic view of a quarter of the CMS silicon tracker comprehensive of the supporting structures, cables and services.*

permit a high tracking efficiency and a low rate (10^{-3} or less) of fake tracks, which are reconstructed tracks not corresponding to any real track.

A consequence of high particle density is the radiation damage of the silicon sensors, mainly around the collision area of the proton beams. Another source of radiation is the high flux in the tracking volume due to backscattering of neutrons evaporated from nuclear interactions in the material of the electromagnetic calorimeter. To contrast the malfunctioning caused by the radiation damage, both pixel and microstrips detectors have to be kept cold at a working temperature of -10^{o} C for the whole tracker volume, except during limited maintenance periods, when they can be "warmed" up to 0^{o} C.

The physics requirements the CMS tracker has to satisfy are:

- Isolated lepton track reconstruction: the efficiency is expected to be close to 100% in $|\eta| < 2.0$ from simulation of single muons within tracker, as shown in Fig. 3.12.
- Good lepton momentum resolution: $\frac{\sigma(p_{\mathrm{T}})}{p_{\mathrm{T}}} < 4\%$ within $|\eta| < 2.0$ for single muons with different transverse momenta, as shown in simulation of Fig. 3.13.

- Tagging and reconstruction of b-jets , fundamental requirement for new physics studies ($H \rightarrow b\bar{b}$) and for top quark physics or CP violation.

- Several material budget constraints are required for cables and active layers to minimize electron bremsstrahlung and hadronic interactions not to affect tracking performance and at the same time to fully exploit the electromagnetic calorimeter for $H \rightarrow \gamma\gamma$ decays. In Fig. 3.14 on page 44 both the total radiation length[5] X and nuclear interaction length[6] λ for the tracker material as a function of pseudorapidity are reported. With this configuration, about 50% of the times both photons from Higgs boson decay traverse the tracker without converting. The material budget is higher in the transition region between barrel and endcap ($1 < |\eta| < 2$) due to cables and services that connect the tracker modules to the outside system.

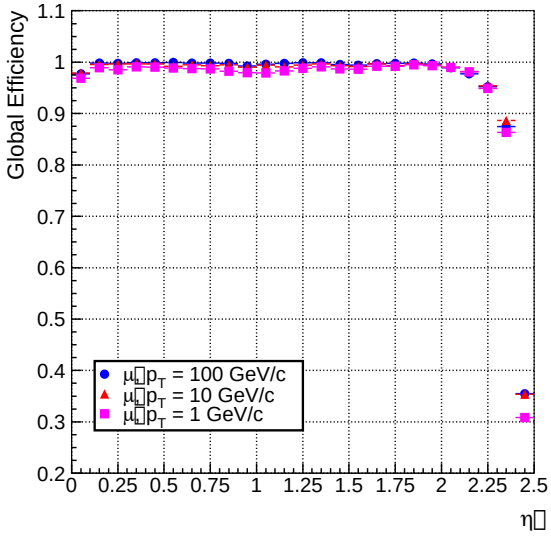

Figure 3.12: *Global track reconstruction efficiency for single muons.*

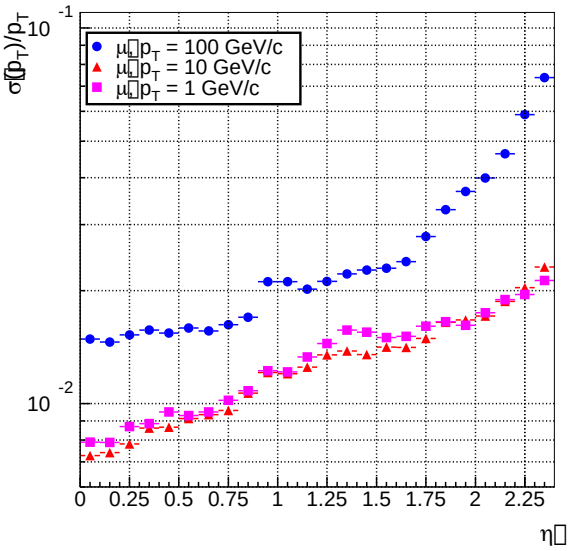

Figure 3.13: *Single muon track transverse momentum resolution.*

In Chapter 4 the silicon tracker is described more in detail and some results on the performance of the microstrip detectors as measured during test beams are summarized.

[5]The radiation length X_0 is defined as the distance over which an high energy electron loses on average all but $1/e$ of its energy within a material.

[6]The nuclear interaction length λ_0 is the mean free path for a hadron before having a nuclear interaction inside a material.

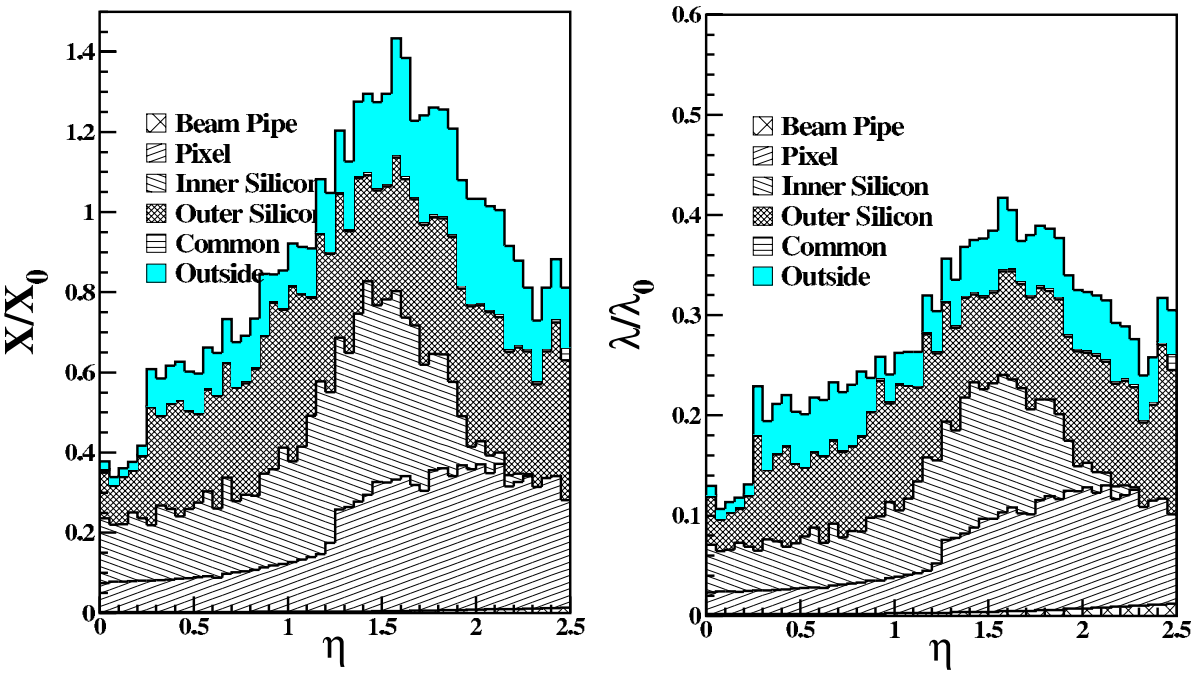

Figure 3.14: *Material budget as a function of η for different tracker subunits: material thickness in units of radiation length X_0 (left) and in units of interaction length λ_0 (right).*

3.2.3 The Electromagnetic Calorimeter

A high performance electromagnetic calorimeter is a fundamental requirement for any general purpose LHC experiment for precise measurements on electrons and photons. The design of CMS ECAL [45] has been prompted by the possibility to observe the decay of a light Higgs boson into a couple of photons. Since in the region $m_H < 140$ GeV/c^2 the intrinsic Higgs width Γ_H is less than 100 MeV, the $\gamma\gamma$ invariant mass resolution is dominated by experimental resolution, which should be of the order of 1% to enhance the significance of a possible signal.

The CMS collaboration has chosen a homogeneous calorimeter composed with finely segmented crystals of lead tungstate ($PbWO_4$), which is a radiation resistant and chemically inert scintillator suited to work in the LHC high dose environment (from 0.18 Gy/h at $|\eta| = 0$ to 6.5 Gy/h at $|\eta| = 2.6$ at high luminosity). Moreover, the lead tungstate has also a short scintillation decay time $\tau = 10$ ns that allows to collect 85% of the light in the 25 ns interval between two pp collisions. The small Molière radius[7] of 21.9 mm

[7]The Molière radius is the transversal dimension length scale of an electromagnetic shower evolving within a calorimeter.

and radiation length $X_0 = 8.9$ mm permit the shower containment in a limited space resulting in a compact calorimeter design. Figure 3.15 shows a longitudinal view of a quarter of the electromagnetic calorimeter: it is organized in a barrel region $|\eta| < 1.48$ and a forward region to cover the pseudorapidity area below 3.0.

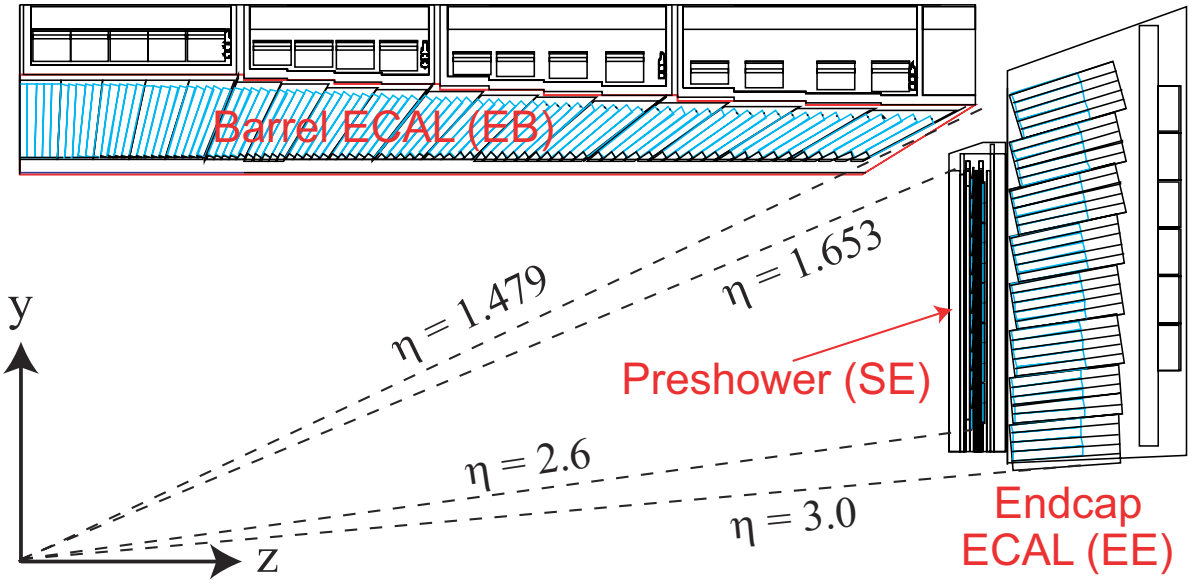

Figure 3.15: *Longitudinal view of a quadrant of CMS electromagnetic calorimeter.*

It is composed by 61 200 crystals in the barrel region and 21 528 in the endcaps grouped in 36 supermodules. The crystals have trapezoidal shape with squared front faces and are slightly different in the two regions: in the barrel they are 230 mm long with a total radiation length $X = 25.8X_0$ and 22×22 mm^2 front section, equal to the Molière radius. The granularity is $\Delta\eta \times \Delta\varphi = 0.0175 \times 0.0175$, high enough to efficient π^0-γ separation. The collection of light is performed with silicon avalanche photodiodes (APD), which are able to operate inside a high magnetic field and can address the low light-yield of the crystals.

In the endcaps, the crystals have 24.7×24.7 mm^2 square front sections and smaller length (220 mm) and hence a smaller radiation length $X/X_0 = 24.7$, because in front of the endcaps a preshower with $X = 3X_0$ in the two regions $1.65 < |\eta| < 2.6$ is foreseen. Each preshower is composed with two lead radiators and two planes of silicon microstrips to increase the π^0 rejection power in the highly irradiated forward regions, which are affected also by the decreasing of the performance due to the increasing granularity at higher $|\eta|$, with a maximum value of $\Delta\eta \times \Delta\varphi = 0.05 \times 0.05$ in the very forward crystals. The higher irradiation levels would also induce too high leakage currents in APDs,

therefore the forward crystals are read by vacuum photo-triodes (VPT).

In the range $25 < E[\mathrm{GeV}] < 500$, which is valid for $\mathrm{H} \rightarrow \gamma\gamma$ decay, the electromagnetic energy resolution σ_E can be expressed as the squared sum of three independent terms:

$$\left(\frac{\sigma_E}{E}\right)^2 = \left(\frac{a}{\sqrt{E[\mathrm{GeV}]}}\right)^2 + \left(\frac{\sigma_N}{E[\mathrm{GeV}]}\right)^2 + c^2 \tag{3.10}$$

where the first term $\frac{a}{\sqrt{E}}$ is referred to as stochastic term and parameterizes the effects of fluctuations in photo-statistics and shower containment. The second term $\frac{\sigma_N}{E}$ is due to electric noise and pile-up (the shaping time of the preamplifiers is chosen to be 40 ns) and c is a constant term. The contributions to the energy resolution are represented in Fig. 3.16, the "Intrinsic" curve includes the shower containment and the constant term c. The values of the three constants a, σ_N and c have been measured in test beams and are reported in Tab. 3.3.

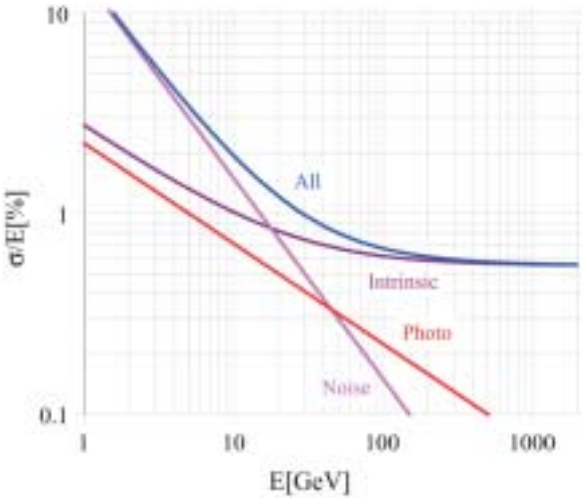

Figure 3.16: *Different contributions of energy resolution of CMS electromagnetic calorimeter.*

	barrel	endcap
a	2.7%	5.7%
σ_N	155 MeV	200 MeV
c	0.55%	0.55%

Table 3.3: *Contributions of energy resolution of* $PbWO_4$ *crystals measured on several test beams.*

At the beginning of data taking it is foreseen a staged ECAL without endcaps and only preshowers in the forward regions. This scenario is caused by the longer time scale for construction and crystal calibration, but it seems not to affect too much the resolution on di-jet invariant mass and transverse energy measurements [46]. This configuration is used also in the analysis described in this thesis.

3.2.4 The Hadron Calorimeter

The hadron calorimeter is used together with the electromagnetic one to measure the energy and direction of jets, the transverse energy E_{T} and the imbalance of transverse energy, or missing transverse energy, E_{T}^{miss}. To fulfil these requirements, it has to be thick enough to contain the whole hadron shower and have high hermeticity. Since it is placed inside the magnet, it can not be made with ferromagnetic materials.

The CMS HCAL [47] is a sampling calorimeter with 3.7 mm thick active layers of plastic scintillators alternated with 5 cm thick brass plate absorbers. The signal is readout with wavelength-shift fibres. The granularity $\Delta\eta\times\Delta\varphi = 0.087\times0.087$ is fine enough to allow an efficient di-jet separation.

It is subdivided, as it can be seen in Fig. 3.17, into barrel ($|\eta| < 1.4$) and endcap ($1.4 < |\eta| < 3.0$) with an overall thickness from 8.9 to 10 interaction lengths λ_0 respectively. Since the barrel part of the calorimeter is not sufficiently thick to contain all the energy of highly energetic showers, an additional "tail-catcher" of scintillators tiles outside the magnet is located.

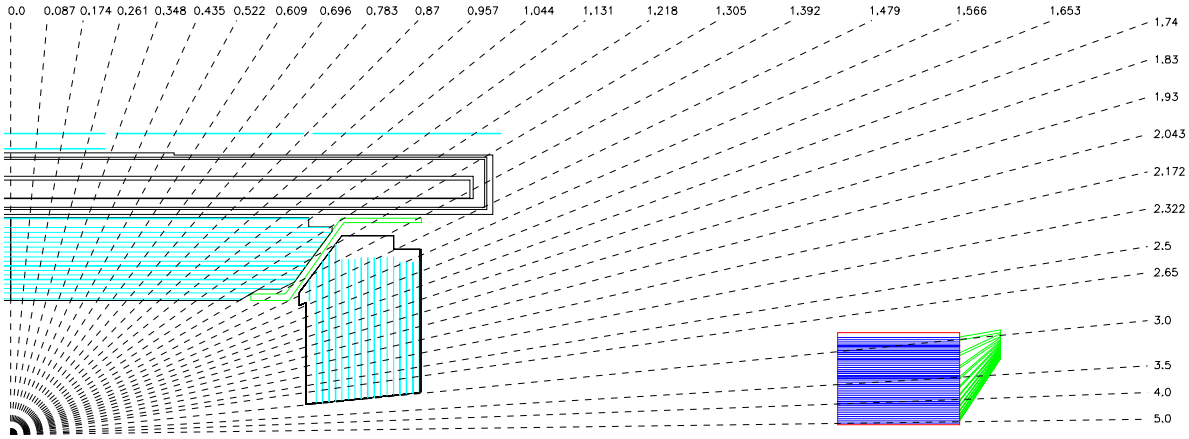

Figure 3.17: *Longitudinal view of a quarter of CMS hadron calorimeter, subdivided into barrel and endcap HCAL, placed inside the magnetic coil, the outer barrel "tail-catcher" and the very forward calorimeter HF, sited outside the magnet.*

To improve the pseudorapidity coverage from $|\eta| = 3$ to $|\eta| = 5$, a very forward calorimeter (HF) is placed outside the magnet yoke, ± 11 m away along the beam direction from the nominal interaction point. It is another sampling calorimeter with active elements made of quartz fibres parallel to the beam interleaved into steel plate absorbers. The active elements, whose granularity is $\Delta\eta \times \Delta\varphi = 0.17 \times 0.1745$, are sensitive to Čerenkov light and are readout with photomultiplier tubes. With this configuration the complex of CMS hadron calorimeter has an overall depth of more than $11\lambda_0$ over the full $|\eta| < 5$ coverage.

The energy resolution combined with ECAL measurements is

$$\frac{\sigma_E}{E} = \frac{100\%}{\sqrt{E[\mathrm{GeV}]}} \oplus 4.5\% \tag{3.11}$$

and it is expected to sensibly degrade around $|\eta| = 1.4$, where there will be installed services and cables resulting in a higher amount of inactive material.

The performance of the very forward calorimeter

$$\begin{aligned} \left(\tfrac{\sigma_E}{E}\right)^{had} &= \tfrac{182\%}{\sqrt{E[\mathrm{GeV}]}} \oplus 9\% \\ \left(\tfrac{\sigma_E}{E}\right)^{e} &= \tfrac{138\%}{\sqrt{E[\mathrm{GeV}]}} \oplus 5\% \end{aligned} \tag{3.12}$$

is sufficient both for hadrons and electrons to improve the missing transverse energy resolution to the desired level.

3.2.5 The Muon System

The muon system [48] is placed outside the magnet, embedded in the iron return yoke to make the full use of the 1.8 T magnetic return flux. It plays an essential rôle in the CMS trigger system, because high p_{T} muons are clear signatures of many physics processes. The main goal of this system is to identify muons and measure, when combined with the tracker, their transverse momentum p_{T}, but nevertheless it is used also to precise time measurement of the bunch crossing [49].

It is organized into three independent subsystems shown in Fig. 3.18: in the barrel, where the track occupancy is relatively low (<10 Hz/cm^2), drift tubes (DT) detectors are installed, while in the endcaps cathode strip chambers (CSC) are favoured to work with higher particle rates (>100 Hz/cm^2) and a larger residual magnetic field within the yoke plates. These two subsystems cover the $|\eta| < 2.4$ region and are arranged in a multi-layer structure to efficiently reject single hits produced by low range particles. In

the region $|\eta| < 2.1$ redundancy is provided by resistive plate chambers (RPC), which have a limited spatial resolution, but a faster response and excellent time resolution, less than 3 ns. They are used mainly to unambiguous bunch crossing identification and also to complement the DT+CSC measurement of p_{T} during the trigger period, because RPCs can be finely segmented since they do not demand a costly readout system.

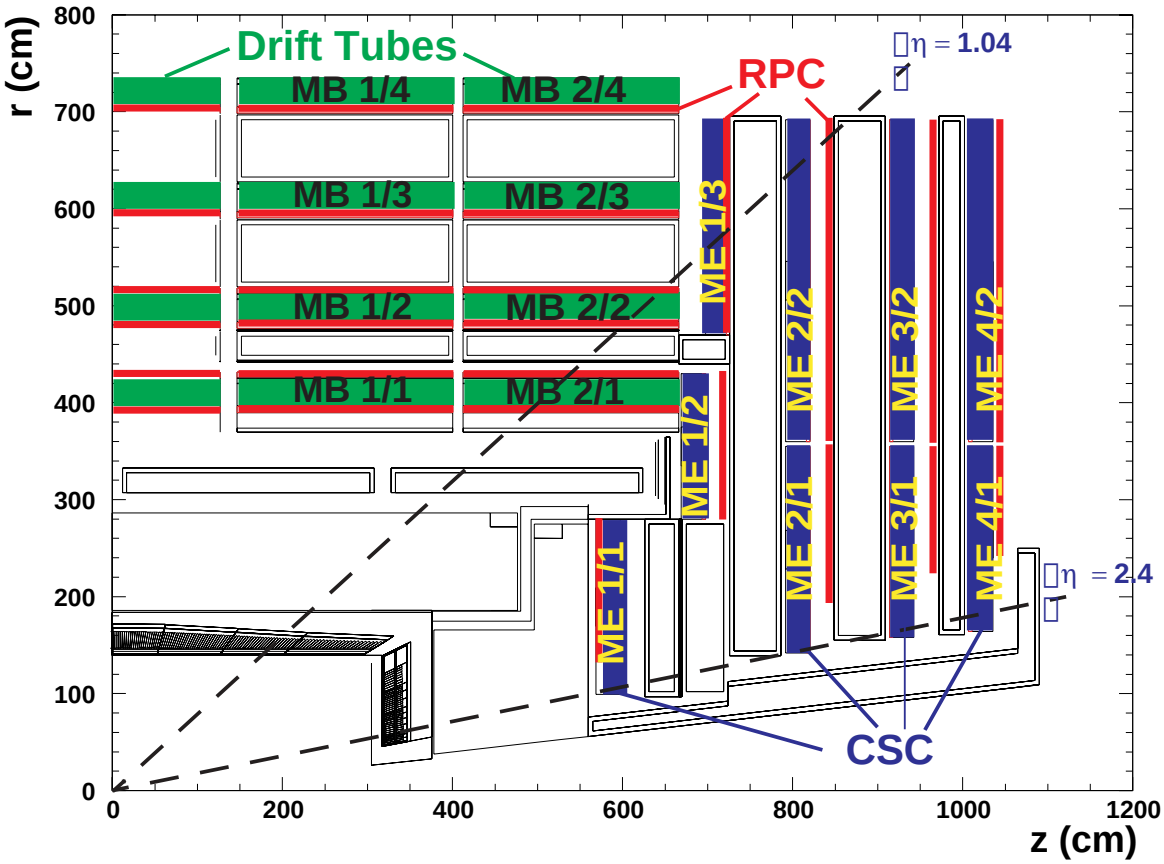

Figure 3.18: *Longitudinal view of a quarter of the muon system, subdivided into barrel with drift tubes (DT) and resistive plate chambers (RPC) and endcap with cathode strip chambers (CSC) and RPCs.*

Drift Tubes are composed with parallel aluminium plates insulated from perpendicular "I" shaped aluminium cathodes by polycarbonate plastic profile. The anodes are 50 µm diameter stainless steel wires placed between the "I" cathodes. The internal volume is filled with a binary mixture of 80% Ar and 20% CO_2 at atmospheric pressure, because this gas is non-flammable and can be safely used in underground operations in large volumes, as required in CMS. The resolution is about 100 µm both in $r\varphi$ and rz views.

Cathode Strip Chambers are composed with arrays of anode wires between pair of cathode planes, segmented into strips perpendicular to the wires. Gaps are filled with a gas mixture of 30% Ar, 50% CO_2 and 20% CF_4. The interpolation of the signal of neighbouring strips allows a precise spatial measurement of the φ coordinate with 50 μm resolution.

Resistive Plate Chambers are made of planes of a phenolic resin (bakelite) with a bulk resistivity of $10^{10} \div 10^{11}\ \Omega\,\mathrm{cm}$, separated from aluminium strips by an insulating film. The gaps are filled with a non-flammable gas mixture of 94.5% freon ($C_2H_2F_4$) and 4.5% isobutane (i-C_4H_{10}), which operates in "avalanche" mode to sustain the high rates.

3.2.6 The Trigger system

It is unconceivable to store on tape all the information about the 40 MHz rate pp collisions, practical and technical difficulties impose a limit of about 100 Hz in the acceptable rate of permanently stored data. Furthermore the rate of interesting events is considerably small, with exception of inclusive b physics, as it is shown in Fig. 3.6 on page 36, hence a trigger system is built up with the twofold task to reject a factor $4{\times}10^5$ of the collisions and to select in a short time the interesting physics events with high efficiency.

The decision on storing data from LHC collisions belongs to the trigger system, which at CMS is subdivided in two main entities, according to the picture of Fig. 3.19. Every trigger decision is taken in steps of increasing refinement using a part even more bigger of the available subdetector data. In the Level-1 trigger a dedicated hardware is used to reduce at minimum the dead time and to take a very fast accept/reject decision to cut down from 40 MHz to almost 100 kHz the data rate. In case of positive decision data are temporarily stored and passed to the High-Level Trigger (HLT) system. The High-Level trigger relies on commercial processors, organized in a farm of personal computers (PC). Many dedicated software algorithms will run to select events on physics basis and will represent the first step of physics analysis selection. Using a parallel processing scheme as much as 100 kHz of events can be processed, 500 ms/ev being the estimated maximum allowed processing time on a single CPU.

Level-1 Trigger

The Level-1 trigger selection is based exclusively on calorimeter and muon chamber information, processed with hardware logical circuits [50], though with coarse granular-

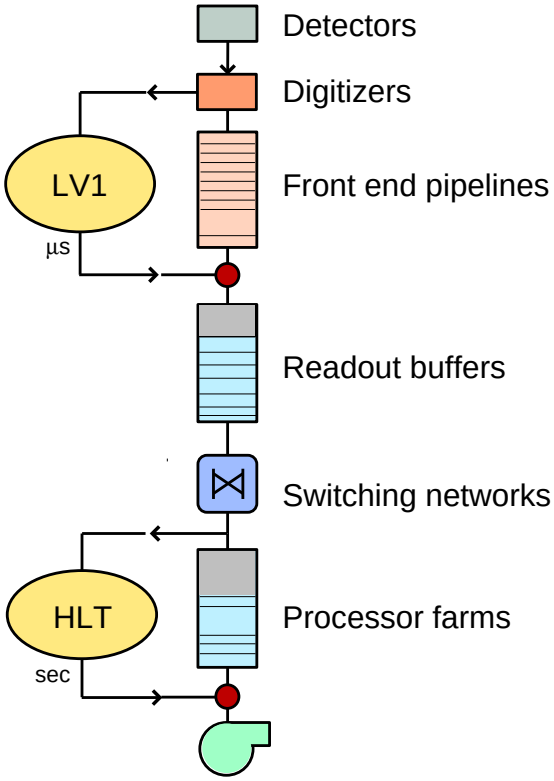

Figure 3.19: *Data flow in the CMS Trigger/DAQ system. The software-based High-Level Trigger (HLT) filters via the Data Acquisition system (DAQ) the events passing hardware-based Level-1 trigger (LV1). Time axis goes from upside down.*

ity. The Level-1 trigger system is required to be capable to process every 40 MHz pp collision and reduce to 100 kHz the data rate to pass to the HLT. At LHC startup the CMS Level-1 output rate will be reduced to only 50 kHz for low luminosity and it will be raised to the designed 100 kHz at full LHC luminosity. Only one third of the bandwidth, 16 kHz (33.5 kHz) at low (high) luminosity, is allocated to the Level-1 selections, while the rest is used as a safety margin for preventing miscalculations of the expected rates due to uncertainties in simulation of physics processes or not well known extrapolated values of cross sections. As soon as CMS will start its programme, selection thresholds will be adjusted to fully exploit the available trigger bandwidth.

The two elements of the Level-1 trigger, calorimetry and muon system, work in parallel and analyse the data locally, combine the information and produce the output passed to the Data Acquisition system (DAQ), as in the scheme of Fig. 3.20. The calorimetric information is synthetized into calorimetric *towers* by individual Trigger Primitive Generator (TPG) circuits for ECAL, HCAL and HF. The towers are clusters

of signals and are sent to the Regional Calorimeter Trigger (RCT), which combines the tower information to reconstruct jets, and leptons/photons. All these objects have a raw measurement of energy and position and are collected by the Global Calorimeter Trigger (GCT).

The Level-1 calorimetric trigger also provides a map of inactive calorimeter regions to improve the isolation of the muons, which are reconstructed in the meantime independently by the two muon subsystems, RPC and DT+CSC. The reconstructed muon segments are combined together by the Global Muon Trigger (GMT), implemented with a programmable logic. The GMT resolves ambiguities and uses inactive calorimetric regions to remove fakes and finally passes the Level-1 muon candidates to the Global Trigger.

The information of GCT and GMT passed to the Global Trigger (GT) is combined to provide a first estimation of the missing transverse energy E_{T}^{miss} and determine some regions where the HLT should focus on.

The Level-1 trigger table 3.4 (3.5) for 16 kHz (33.5 kHz) output at low (high) luminosity is obtained [51] selecting events with one or more reconstructed physics object candidates (jets, leptons, E_{T}^{miss}) above a certain fixed threshold. The tables give the generator-level E_{T} or p_{T} where the cut on the reconstructed objects gives the 95% efficiency for the generator-level value, once the output rate is fixed. Data are forwarded to the DAQ and processed by the High-Level trigger system. An amount of about 1 kHz

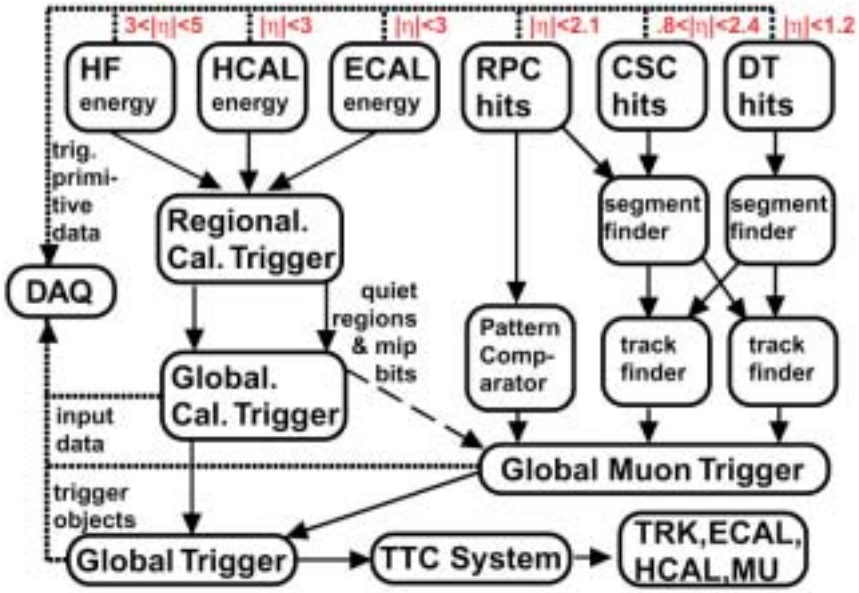

Figure 3.20: *Overview of CMS Level-1 trigger.*

is left for calibration and monitoring purposes with random triggers to obtain a uniform sample of Minimum Bias events.

The maximum time for the Level-1 to spend does not correspond to the 25 ns bunch crossing period, but it is higher because the Level-1 signals are locally stored (at front-end level) into pipelines, which can contain hundreds of bunch crossings. The trigger time limit is given by the amount of data from the silicon tracker and the preshower front-end buffers, which has to be stored during Level-1 stream and in case read after a Level-1 accept. The decision time for the Level-1 logical circuits is about 1 μs excluding unavoidable signal propagation delays. The Level-1 accept signals and raw readout data are sent to a PC farm through a temporary storage buffer.

High-Level Trigger

The High-Level trigger [51] selection (HLT) is realized with a software running on a farm of commercial processors. The goal of HLT is to reduce the Level-1 output rate to 100 Hz mass storage with dedicated "fast" algorithms. The Level-1 measurement of jets, leptons and photons are refined through intermediate steps, divided into logical levels (Level-2, Level-2.5, Level-3) with somewhat arbitrary classifications depending on the peculiar algorithms of each subdetector. There will be algorithms to reconstruct better the raw Level-1 physics objects together with streams dedicated to particular physics channel identification, for instance related to b physics [52, 53], selected with including the information of other subdetectors. The pixel *hits* are available together with tracker signals after zero-suppression, hence primary vertex reconstruction and track finding should be possible and algorithms similar to the offline ones will run online too.

The output rate of 100 Hz data to be stored on disks is subdivided into different topologies, listed in Tab. 3.6 for the initial period at low luminosity. Some selections follow the Level-1 trigger scheme and others, as the inclusive b-jet selection or the *"other events"* of the last line, regard HLT dedicated algorithms, which make use of b-tagging techniques and conditional track finding within silicon tracker. In Sec. 6.4 an online selection using tracks for inclusive b-jet events will be described, while a more specific algorithm to select events with one isolated muon and two b-jets for the study of the discovery channel $W(\rightarrow \mu\nu_\mu)H(\rightarrow b\bar{b})$ will be extensively reviewed in Part III of this thesis. The low luminosity Level-1 trigger rate when requiring one muon and jets will be also presented. A "μ AND jet" combined selection is not foreseen in Tab. 3.4, but with only 0.5 kHz expected rate, events with one muon and two central jets can be selected at Level-1. The estimated HLT selection efficiency for some interesting channels is listed in Tab. 3.7.

Trigger	Threshold [GeV or GeV/c]	Expected Rate [kHz]	Cumulative Rate [kHz]
Inclusive isolated e/γ	29	3.3	3.3
ee/$\gamma\gamma$	17	1.3	4.3
Inclusive μ	14	2.7	7.0
$\mu\mu$	3	0.9	7.9
Single τ-jet	86	2.2	10.1
Two τ-jets	59	1.0	10.9
1 jet	177	1.0	11.4
3 jets OR 4 jets	86,70	2.0	12.5
1 jet AND E_{T}^{miss}	88$\otimes$46	2.3	14.3
e AND jet	21$\otimes$45	0.8	15.1
Minimum Bias (calibration)		0.9	16.0
Total			16.0

Table 3.4: *Level-1 trigger table at low luminosity. Thresholds correspond to values at 95% efficiency [51].*

Trigger	Threshold [GeV or GeV/c]	Expected Rate [kHz]	Cumulative Rate [kHz]
Inclusive isolated e/γ	34	6.5	6.5
ee/$\gamma\gamma$	19	3.3	9.4
Inclusive μ	20	6.2	15.6
$\mu\mu$	5	1.7	17.3
Single τ-jet	101	5.3	22.6
Two τ-jets	67	3.6	25.0
1 jet	250	1.0	25.6
3 jets OR 4 jets	110,95	2.0	26.7
1 jet AND E_{T}^{miss}	113$\otimes$70	4.5	30.4
e AND jet	25$\otimes$52	1.3	31.7
μ AND jet	15$\otimes$40	0.8	32.5
Minimum Bias (calibration)		1.0	33.5
Total			33.5

Table 3.5: *Level-1 trigger table at high luminosity. Thresholds correspond to values at 95% efficiency [51].*

Trigger	Threshold [GeV or GeV/c]	Expected Rate [Hz]	Cumulative Rate [Hz]
Inclusive e	29	33	33
ee	17	1	34
Inclusive γ	80	4	38
$\gamma\gamma$	40$\otimes$25	5	43
Inclusive μ	19	25	68
$\mu\mu$	7	4	72
Inclusive τ-jets	86	3	75
Two τ-jets	59	1	76
1 jet AND E_{T}^{miss}	180$\otimes$123	5	81
1 jet OR 3 jet OR 4 jet	657,247,113	9	89
e AND jet	19$\otimes$52	1	90
Inclusive b-jets	237	5	95
Calibration and other events (10%)		10	105
Total			105

Table 3.6: *High-Level trigger table at low luminosity. The thresholds correspond to the values of E_{T} or p_{T} with 95% efficiency (90% efficiency for muons) [51].*

Channel	Efficiency
H(115 GeV/c^2)$\rightarrowtail\gamma\gamma$	77%
H(160 GeV/c^2)$\rightarrowtail$WW*	92%
H$\rightarrow$ZZ$\rightarrow 4\mu$	92%
A/H(200 GeV/c^2)$\rightarrowtail 2\tau$	45%
SUSY (0.5 TeV/c^2 s-particles)	60%
$\mathrm{R_p}$-violation SUSY	20%
W$\rightarrow$eν_{e}	67%
W$\rightarrow\mu\nu_\mu$	69%
t$\bar{\mathrm{t}}\rightarrow\mu + X$	72%

Table 3.7: *Performance of HLT selection at low luminosity after applying the cuts listed in Tab. 3.6.*

The HLT system will receive, on average, an event every 10 μs from Level-1 selection and has to reduce by a factor 1000 the amount of data. Each recorded event has an average size of 1 MB. The DAQ system must provide the means to feed data from the front-ends to the PC farm at a sustained bandwidth up to 100 kHz·1 MB=100 GB s^{-1}.

The number of CPUs needed by the CMS PC farm to sustain the input rate and select the 100 Hz to store for offline analysis is calculated taking care of two factors: the evolution of network, processors and memory technologies extrapolated at the LHC startup date and the required CPU time for the selection of each physics object during HLT calculations. For this reason it was decided to compute the time performance of the algorithms using the benchmark unit SpecInt95, abbreviated si95 [54].

In practice what is done is to compute timing performance by normalizing the results to the speed of a 1 GHz CPU Pentium III processor [55], whose power rating corresponds to 41 si95.

The time spent on average to process one event passing Level-1 trigger during HLT is roughly 300 ms and it is obtained weighting the CPU needs of the algorithms with the frequency of their application, which is the Level-1 trigger rate of the corresponding channel. The summary of CPU time for the various selections is shown in Tab. 3.8.

Physics Object	CPU time per Level-1 event [ms]	Level-1 Trigger rate [kHz]	Weighted CPU time [ms]
e/γ	160	4.3	44
μ	710	3.6	164
τ	130	3.0	25
Jets AND E_{T}^{miss}	50	3.4	11
e AND jet	165	0.8	8
Inclusive b-jets	300	0.5	16

Table 3.8: *High-Level trigger selection timing at low luminosity.*

There are all the elements to calculate the required computing power at start-up with a Level-1 rate of 50 kHz. The total power required for CMS HLT is

$$5 \times 10^4 \text{ s}^{-1} \cdot 0.300 \text{ s} \cdot 41 \text{ si95} = 0.6 \times 10^6 \text{ si95} \tag{3.13}$$

and corresponds to a total of 15 000 1 GHz Pentium III CPUs, which have to be instrumented with CMS HLT software. By the time of LHC running the evolution of technologies should produce new and more powerful computing and networking elements. For this reason the CMS DAQ system is modular and even if each part of the

architecture and functionalities is well defined, there is the possibility to change some elements without affecting the rest. According to this picture the value of the common CPU processor speed is estimated with a large uncertainty (a self-confident 50%) using Moore's Law[8], which states that the trend of increasing CPU power is roughly a factor 2 every 1.5 years. Counting 3 such periods from now to the assembling of CMS farm, a factor 8 more powerful CPUs will be available. This means that at CMS start-up about 2 000 CPUs in 1 000 dual-processors PCs have to be bought and installed in the farm. Furthermore, the average time needed to process an event will be reduced by the same factor 8 being roughly 40 ms, but it is foreseen that some events could require up to 1 s. A benchmark time for HLT studies has been fixed to about 500 ms on average, if using a 1 GHz Pentium III CPU. During this time interval the data are stored in random-access memories and if an event passes the High-Level trigger selection, it is stored and is available for offline analyses.

Assuming a total time of 20 hours data taking per day, a total disk space of 10 TB per day will be filled at full luminosity. The nominal parameters of the data acquisition system are summarized in Tab. 3.9.

Parameter	Value
Level-1 Trigger rate	100 kHz
Event size	1 MB
Event Builder bandwidth	100 GB/s
Event Filter Computing Power	0.6×10^6 SI95
Data Production	10 TB/day

Table 3.9: *Nominal parameters of the CMS data acquisition system.*

[8]Definition taken from *"The Jargon Dictionary"* [56]:

Moore's Law The observation that the logic density of silicon integrated circuits has closely followed the curve (bits per square inch) = $2^{(t-1962)}$ where t is time in years; that is, the amount of information storable on a given amount of silicon has roughly doubled every year since the technology was invented. This relation, first uttered in 1964 by semiconductor engineer Gordon Moore (who co-founded Intel four years later) held until the late 1970s, at which point the doubling period slowed to 18 months. The doubling period remained at that value through time of writing (late 1999). Moore's Law is apparently self-fulfilling. The implication is that somebody, somewhere is going to be able to build a better chip than you if you rest on your laurels, so you'd better start pushing hard on the problem. See also Parkinson's Law of Data and Gates's Law.

Chapter 4

The CMS Tracker

In this chapter the CMS silicon tracker [44] is described in detail. The construction and use of such a detector in a LHC environment represents an important effort both for experimental physics and engineering points of view. The huge amount of detector units (modules) to produce, test and assemble is astonishing and involves hundreds of people from several worldwide institutes. A large number of tests were done to study the performance of different silicon detectors and minimize the effect due to the exploitation of this detector in the harsh radiation environment present in an LHC experiment. In this context, I analysed data collected during July and August 2000 test beams at CERN facilities on not irradiated and irradiated silicon microstrip detectors respectively. The most important results are discussed in the last part of this chapter.

4.1 The Pixel vertex detector

The pixel detector of Fig. 4.1 is a fundamental device for b-tagging studies and impact parameter measurements. It has also paramount importance as a starting point in reconstructing charged particle tracks. It covers the region $|\eta| < 2.4$ and it is organized into three 53 cm long barrel layers, positioned at $r = 4.4$, 7.3 and 10.2 cm, and two disks per each side, placed at $z = \pm 34.5$ cm and ± 46.5 cm covering radii between 6 and 15 cm to guarantee at least two crossed layers per track. At high luminosity conditions, the inner barrel layer will be substituted by an outer layer placed at $r = 13$ cm to improve resolution and limit radiation damages.

Each layer is composed with modular detector units, containing a 250 μm thin-segmented sensor plate with highly integrated readout chips connected to each pixel using bump-bonding technique [57]. A scheme of a pixel detector unit is shown in Fig. 4.2. Since both $r\varphi$ and z coordinates are important for vertex finding and impact

parameter resolution, a square pixel shape has been chosen to optimize both measurements. The pixels have a size of 150×150 μm^2 and are combined with analog signal readout to profit of charge sharing effects among pixels and improve position resolution by interpolation.

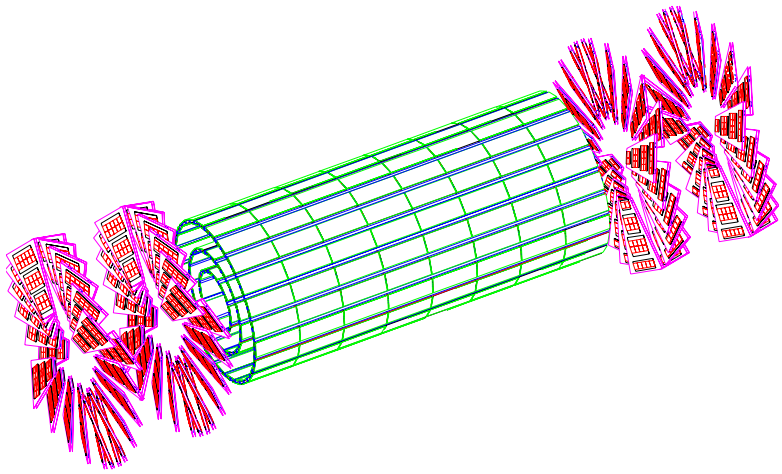

Figure 4.1: *Perspective view of the CMS pixel system in the high luminosity configuration.*

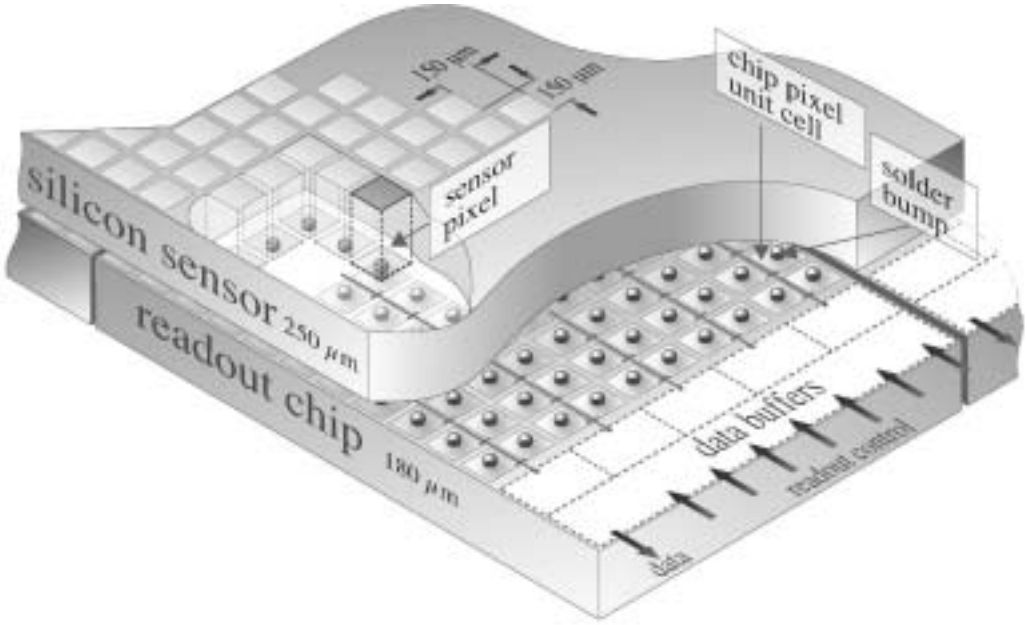

Figure 4.2: *Schematic view of a pixel detector unit.*

The charge sharing between pixels is due to the Lorentz drift of charge carriers, which is about 32° for electrons in a 4 T magnetic field, three times wider than for the holes. Therefore initial n-type substrate sensors are chosen to collect electron signals on n^+ implants, which in turn are more radiation hard. However it can not be avoided that in the barrel layers with $r < 10$ cm the pixel and readout chip lifetime is reduced by hostile radiation environment below CMS lifetime. Hence the layer at $r = 7.3$ cm should be replaced after six or seven years of operations.

In the barrel the pixels are tilted to induce significant charge sharing between neighbouring implants in $r\varphi$ plane improving the intrinsic *hit* resolution down to 10-15 μm, far below the 150 μm width of each n^+ implant, with the mechanism drawn in Fig. 4.3. Charge sharing is present also along z direction for inclined tracks leading to a similar resolution.

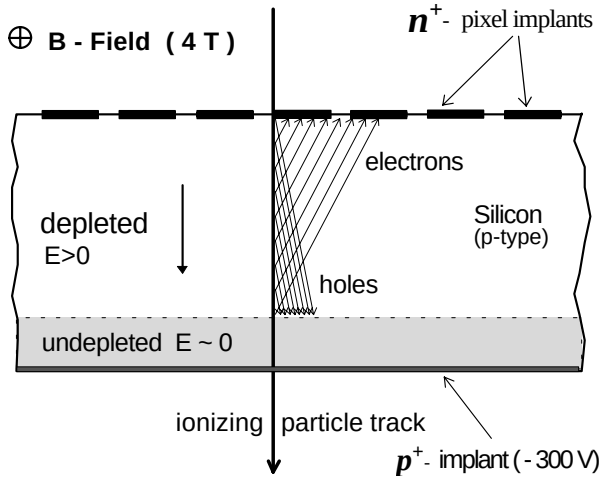

Figure 4.3: *Charge sharing induced by Lorentz drift. After bulk type inversion the detector depletes from the n-pixel side. With increasing radiation dose the detector cannot be fully depleted and the charge collected is reduced [44].*

The detectors placed on the disks are rotated with an angle of 20° around the central radial axis to benefit of charge sharing improved both in r and $r\varphi$ directions by induced Lorentz effects. Despite a Lorentz angle reduced with respect to the barrel case, the resolution in r and $r\varphi$ is expected to be 15 μm at CMS start and degrading to 20 μm when radiation damages arise.

Each pixel signal is read by a Pixel Unit Cell (PUC) bump-bounded directly to the pixel module. The PUC is integrated on the readout chip, which attends to 52 columns and 80 rows for a total of 4 160 pixels. Since the number of channels is very high (44 millions), zero-suppression is mandatory to reduce the huge data volume down to a

reasonable size. Each PUC is equipped with an analog circuit, which provides a logical positive output if the collected signal exceeds a tunable threshold. To reduce the number of channels to readout, two near-by PUC columns are read by one circuit placed in the periphery. The analog signals are temporarily stored into dedicated pipelines and on positive Level-1 trigger decision are transmitted through optical fibres to the front-end driver in the counting room.

To reduce costs it was envisaged the possibility of staging the pixel detector during the low luminosity data taking with only two barrel layers, keeping the innermost at $r = 4.4$ cm, and only one disk per each endcap region at $z = \pm 34.5$ cm. The study of WH trigger at low luminosity, described in Part III, has been performed under these operating conditions. The good results obtained under this difficult mode of operation could only lead to improvements if an additional pixel layer were foreseen.

4.2 The Silicon Strip Tracker

The outer part of the tracker is made with layers of silicon microstrip detectors. The detector unit is the *module*, which is made with one or two sensors glued on a carbon fibre mechanical support together with the readout electronics. The sensor is a n-type phosphorus doped substrate with p^+ implant strips, as shown in Fig. 4.4. The p^+-n junction is reversely biased by applying a positive voltage (hundreds of Volts) to the n side keeping the strips at ground. In such a way the region between the junction and the backplane is completely depleted of free charge carriers, with exception of the thermally created ones. When an ionizing particle passes through the silicon, it interacts in the bulk creating electron-hole pairs (e/h) which drift in the electric field towards the backplane and the p^+ implants respectively. The mean energy required to create a e/h pair in silicon is 3.6 eV, therefore a minimum ionizing particle (*mip*) with an average energy loss per path length of 390 eV/μm should create 32 500 e/h pairs passing through a 300 μm thick sensor. Since the energy loss distribution is Landau shaped, the most probable value, being about 288 eV/μm, differs from the average. For this reason it is preferred to quote the most probable value of e/h pairs produced by a *mip*, which is 24 000 in a 300 μm sensor and represents a rough estimate of the charge to collect.

Some arrangements are made to permit a better working of the device. The n^+ implant backplane forms an ohmic contact and avoid charge injection into the bulk from the connected aluminium layer. On the opposite side the active area is surrounded by two p^+ implants. The inner is a *bias ring* and is used to uniformly bias the strips through 1.5 MΩ polysilicon resistors, the outer is a *guard ring* and limits the dark current

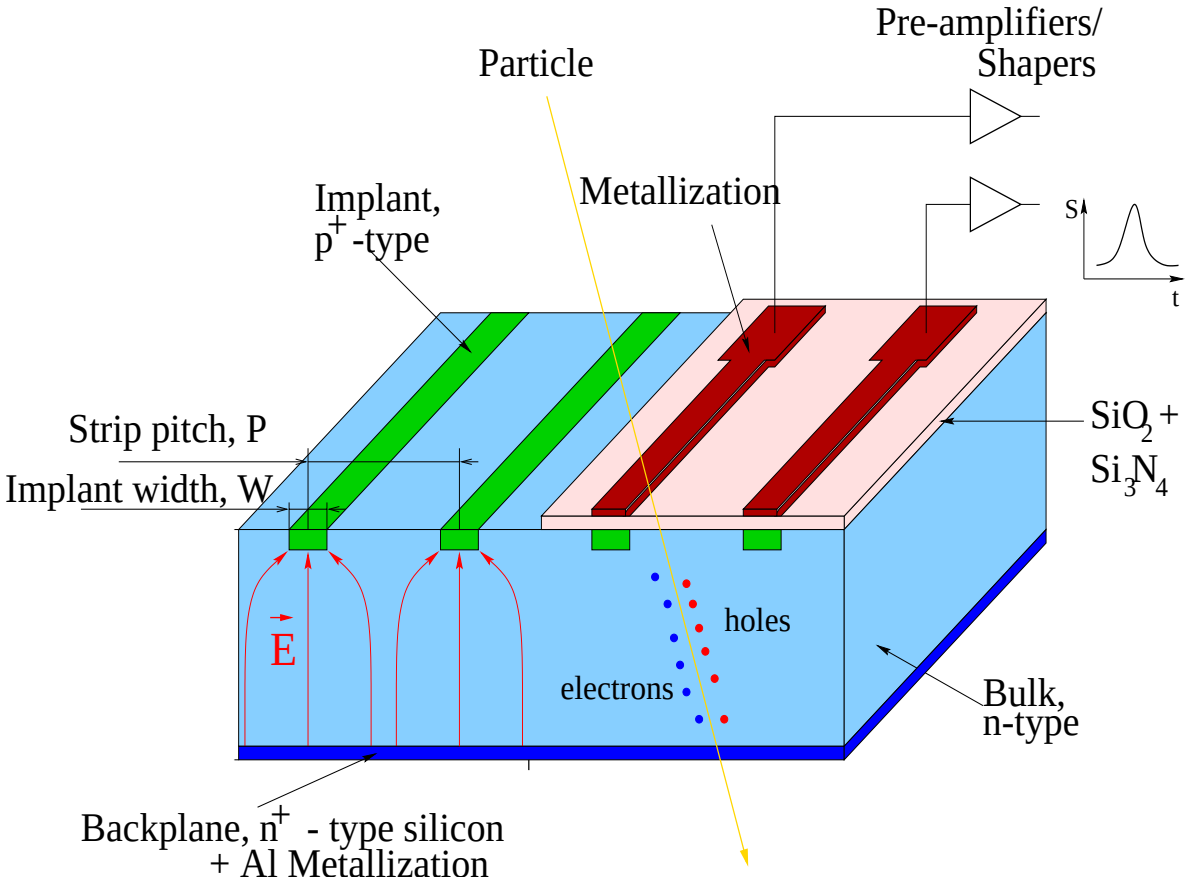

Figure 4.4: *Principle of operation of a silicon microstrip detector.*

contribution from sensor bounds. At the detector edges, n^+ implants are placed to limit charge injection from the regions damaged by the cut on the wafer. Insulating capacitor layers of dielectrics (SiO_2, Si_3N_4) are grown between the p^+ implants and the aluminium strip electrodes to decouple the readout electronics from the detector leakage current.

The strips are bonded to an array of readout chips APV25 [58] housed on a thin hybrid circuit. The analog signal of each strip is transmitted to ADCs located in the counting room via optical links. With these microstrip sensors it is possible to measure one coordinate, interpolating the crossing position by means of charge sharing between adjacent strips. A configuration to allow the bidimensional measurement of coordinates is realized gluing two detectors back-to-back with 100 mrad tilted strip directions. This

configuration is referred to as *stereo* or double-sided and is preferred to the pixel segmentation, although the resolution is worse, because the number of readout channels is less. The *hit* ambiguities present in this detector configuration are resolved at track reconstruction level.

The silicon strip tracker covers a tracking volume up to $r = 1.1$ m with a length of 5.4 m and is divided in three parts:

inner tracker 4 barrel layers (Tracker Inner Barrel=TIB)
3 disks per endcap (Tracker Inner Disks=TID)

outer tracker 6 barrel layers (Tracker Outer Barrel=TOB)

tracker endcaps 9 disks per endcap (Tracker End-Cap=TEC)

The TIB has four layers assembled in shells; the two innermost layers host double-sided detectors, pointed out in blue in Fig. 4.5. The two TIDs, each one made of three small disks, complement the TIB region. The outer barrel structure (TOB) consists of six concentric layers, also in this case the two innermost are double-sided. The TEC modules are mounted on nine disks on both side of barrel. The detectors of ring 1, 2 and 5 are made of double-sided modules, all of them have a trapezoidal shape to follow the ring geometry [59]. The main difference between the inner and the outer tracker is the thickness and dimensions of the silicon modules. The inner tracker is made with *thin* sensors with 320 μm thickness, 117 mm long strips of 64 mm total width. The outermost modules have *thick* sensors, the bulk thickness being 500 μm, with 190 mm long strips,

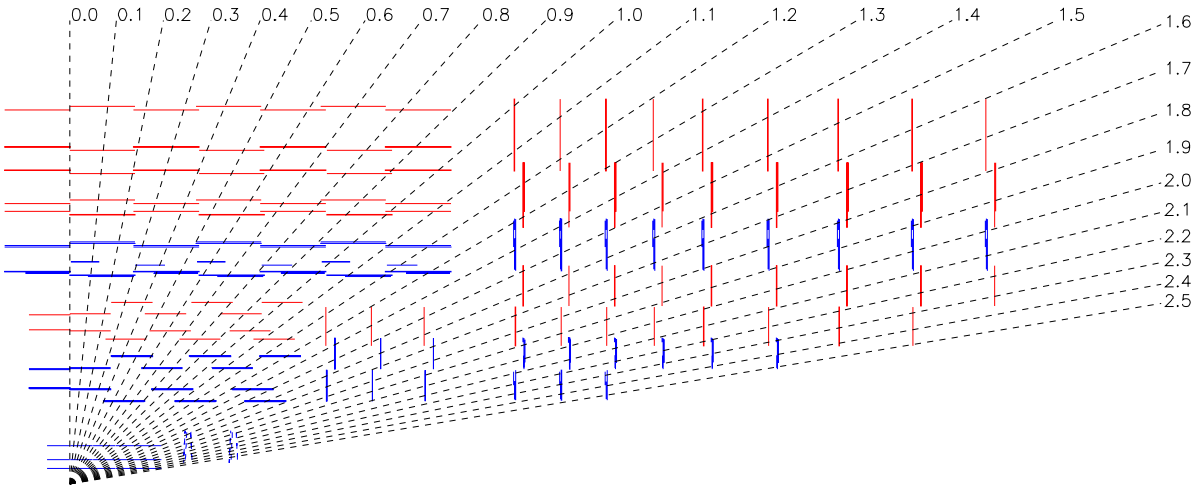

Figure 4.5: *View of a quarter of the silicon tracker in rz plane. Red lines represent single-sided module layers, blue lines stereo module layers.*

because the occupancy is lower, and total width of 96 mm. The layer thickness permits to collect a larger signal to compensate the higher noise due to longer strips. Moreover, this size reduces both the front-end electronic channels and the sensor costs, because 500 μm thick sensors are produced by 6" wafer commercial lines in a cheapest way. The TEC modules are divided in two categories: thick substrates for the outermost three rings, thin for the rest. In Tab. 4.1 the thickness and distance between two adjacent strips (the "pitch") for the tracker sensors are reported. The shape of the modules is rectangular in the barrel with the strips parallel to the beam direction for φ and r coordinate measurements. The endcap modules are trapezoidal-shaped (wedge-shaped) to allow a radial strip disposition for φ and z measurements. The total number of modules is 15 148 (about 198 m^2 silicon active area), 6 052 *thin* and 9 096 *thick* for a total of 9 648 128 electronic channels (strips) to be readout in group of 128 by 73 736 APV chips [51].

Tracker	detectors	thickness [μm]	pitch [μm]
Inner Barrel (TIB)	2 724	320	81/118
Outer Barrel (TOB)	5 208	500	123/183
Inner Disks (TID)	816	300	97/128/143
Outer Disks (*thin*) (TEC)	2 512	300	96/126/128/143
Outer Disks (*thick*) (TEC)	3 888	500	143/158/183

Table 4.1: *Detector types in the silicon tracker.*

4.3 The Readout System

The strip signal is collected through the metallized strip to one of the 128 input channels of the APV chips placed on the front-end hybrid. Since the strip pitch is different from module to module and only one type of readout chip is foreseen, a *pitch adapter* is designed to connect groups of 128 strips to the input pads of the APV. The signal of each strip is read through a charge sensitive amplifier followed by a RC-CR shaper with a time constant of about 50 ns. The output voltage is sampled at 40 MHz, synchronously with the LHC bunch crossing frequency, and analog signals are stored temporarily into a pipeline. The pipeline is a 128×192 matrix of capacitor cells that can contain the output of all the 128 strips for a maximum of 192 locations, which correspond to the number of bunch crossings and amount to a total time depth of 4.8 μs. The dimension of a cell

is 30×35 μm^2 and comprises two transistors to perform the read and write operations and the 0.25 pF storage capacitor.

In case of Level-1 accept, the pulse height signals stored into the pipeline are processed by an Analog Pulse Signal Processor circuit (APSP), which performs the analysis of the signal samplings in two different scenarios:

Peak Mode the peak amplitude of the signal is obtained by the shaper output corresponding to the triggered bunch crossing.

Deconvolution Mode the triggered and the two preceding samples are weighted and combined together to effectively reduce the signal duration to one bunch crossing, at expense of increasing noise [60]. This mode of operation is the most suitable at LHC rates, especially at high luminosity, because it reduces the signal tails of adjacent bunch crossings.

When the *trigger* is sent to the APV, its output is read. The output "frame" consists of 12 digital control bits followed by 128 analog signals as output of a 20 MHz multiplexer. The total readout time is (12+128)×50 ns=7 μs, hence if two trigger signals were closer than 7 μs, the information from the APV would be lost. To avoid this potentially long APV dead time, an internal FIFO is able to temporary store up to a maximum of 31 (10) trigger "frames" when working in peak (deconvolution) mode, thus allowing to absorb the Level-1 trigger time fluctuations.

The pulse height data coming from two APVs are multiplexed onto a differential line over a short distance to a laser driver transmitting at 1300 nm wavelength. The optical transmitter conveys the analog signals through a 100 m optical link fibre to the counting room, located outside the CMS cavern. The scheme of the readout system for the CMS silicon tracker is sketched in Fig. 4.6.

Detector data are digitized by a 9 bit ADC of the Front-End Driver (FED), which also processes digital signals performing a clustering algorithm and reducing them via zero suppression.

All the readout system is controlled by the Front-End Controller (FEC), which distributes the *clock* and *trigger* to the APVs. The global Timing Trigger Command (TTC) sends the LHC machine clock and CMS Level-1 trigger through the FEC interface. The two signals are transmitted by the FEC to the front-end hybrids through a digital optical link and distributed to series of modules by some Communication and Control Units (CCU). The clock signals are locally recovered and eventually time-tuned by Phase Locked Loop chips (PLL) to reduce at minimum the phase jitter and ensure high reliability.

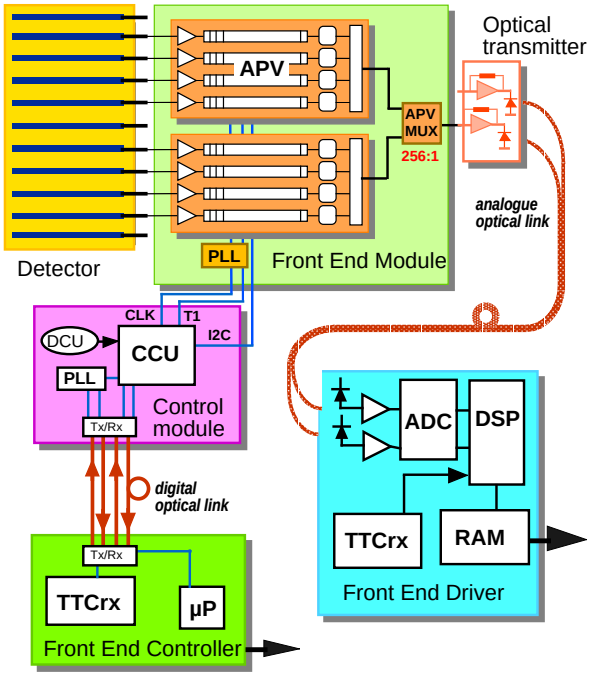

Figure 4.6: *Scheme of the readout system for the CMS silicon strip tracker.*

The design of CMS tracker readout system of Fig. 4.6 is organized to maintain analog data as long as possible basically to interpolate the strip signals and increase the resolution. This should also reduce the complexity of the front-end chips and lower the power dissipation within the tracker volume. The tracker electronics located on the detector is completely optically decoupled from the the digitizing and control systems placed in the counting room. To fully exploit this feature in keeping the noise to an acceptable level, also the power supply system (both low and high voltages) is completely floating with a high coupling impedance to the external world in the whole interesting frequency range.

4.4 Radiation damage of silicon microstrip detectors

The tracker is the CMS subdetector closer to the interaction point, hence it has to sustain the higher radiation flux, which deteriorates the modules. The radiation damage is caused not only by particles produced in primary proton-proton collisions, but also by albedo neutrons emitted from the calorimeters surrounding the tracker. Two different effects of radiation have been observed in silicon detectors: bulk damages and surface damages.

The surface damages [61] are caused by the not recombination of the e/*h* pairs created into the oxide layers of the detector surface by the crossing particles. The macroscopic consequence of this effect is the increasing of interstrip capacitance leading to a worsening of the Signal-to-Noise ratio of the device. It has been found a significant increase in the interstrip capacitance after radiation on detectors with $\langle 111 \rangle$ crystal orientation but not on sensors with $\langle 100 \rangle$ crystal orientation, which have been chosen for the tracker [62]. The interstrip capacitance can be reduced by overdepleting the junction, choosing, when possible, a working point around twice the value of the depletion voltage.

Bulk damages originate from the removal of some atoms from their regular sites on the silicon lattice [63]. A point-like defect in the lattice (*vacancy*) is created and can be considered an acceptor impurity, while the displaced atom behaves as a donor; this couple of defects is referred to as *Frenkel pair*. Various combinations and even clusters of these defects are also observed. One of the major effects of bulk damage due to radiation is the change in the effective doping concentration of the silicon crystal, which depends on the fluence of irradiating particles, the time elapsed after exposition and the absolute silicon temperature. The current passing through the junction (*dark current*) is also increased proportionally to the fluence, with the proportionality constant depending on temperature. As a result, the electronic noise contribution coming from the leakage current is enhanced. By lowering the working temperature to -10° C or less this effect is minimized. Furthermore the signal collected to the electrodes is reduced by charge trapping into the damaged bulk.

An empirical model, called *Hamburg model* [64], which is in agreement with experimental data, describes the behaviour of the effective doping concentration as a function of the fluence, the annealing time and the storage temperature. When the fluence, normalized to a 1 MeV neutron equivalent, has reached a certain value, the effective bulk donor density approaches zero. At that point, continuing the irradiation, the bulk behaves as p-type and an effective acceptor density starts to grow up. This phenomenon is called "bulk type inversion" [65] and leads to an increase of the depletion voltages for highly irradiated silicon sensors, as shown in Fig. 4.7. The polarity of reverse biasing of the device does not change after inversion, while the junction moves from the p^+ strip side to the n^+ backplane side.

The CMS collaboration choose to build the tracker with initial low resistivity n-type substrate in order to delay the type inversion and keep the detector depletion voltage as low as possible when they are heavily irradiated, as shown in Fig. 4.8 on page 70.

Irradiated detectors should work at low temperature both to minimize the dark current and the *reverse annealing* effect that increases the depletion voltage when the

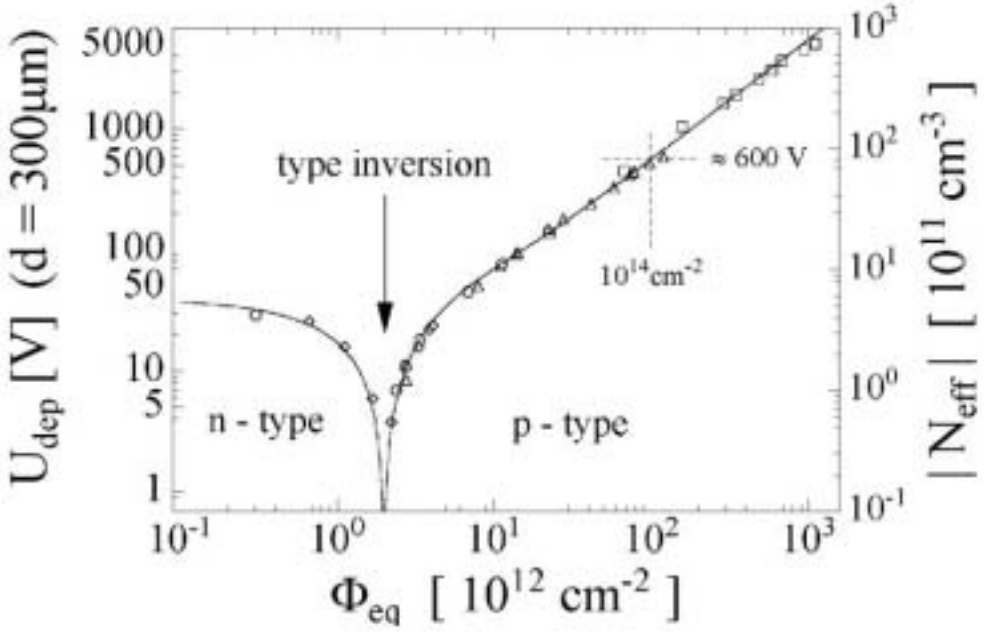

Figure 4.7: *Change in the depletion voltage respectively the absolute effective doping concentration as measured immediately after irradiation [65].*

irradiated material is kept at room temperature for a long time. Furthermore, the high bulk current present in irradiated detectors prevents the possibility to operate them through the so called mechanism of *thermal runaway*. This is a positive feedback process that induces an increase of the sensor temperature that can not be removed by the detector cooling system, and hence an increase of the current, which could not be sustained by the power supply unit. This would lead to an unstable situation making impossible to deplete the detector.

The depletion voltage V_{depl} is measured exploiting the relation linking the bulk capacitance per unit area of the p^+n junction C_b and the applied voltage V_{bias}:

$$C_b = \begin{cases} \sqrt{\frac{e\epsilon N_D}{2V_{bias}}} & V_{bias} < V_{depl} \\ \frac{\epsilon}{W_{depl}} & V_{bias} \geqslant V_{depl} \end{cases} \tag{4.1}$$

with e the elementary charge, $\epsilon = 11.9\epsilon_0 \simeq 1$ pF/cm [1] the silicon dielectric constant, N_D the bulk donor density, W_{depl} the maximum depth of the depletion layer and V_{bias} the applied voltage to the junction, or bias voltage. If C_b is measured for several values of V_{bias}, the CV curves of Fig. 4.9 on page 71 are obtained, being $\frac{1}{C_b^2}$ proportional to V_{bias}

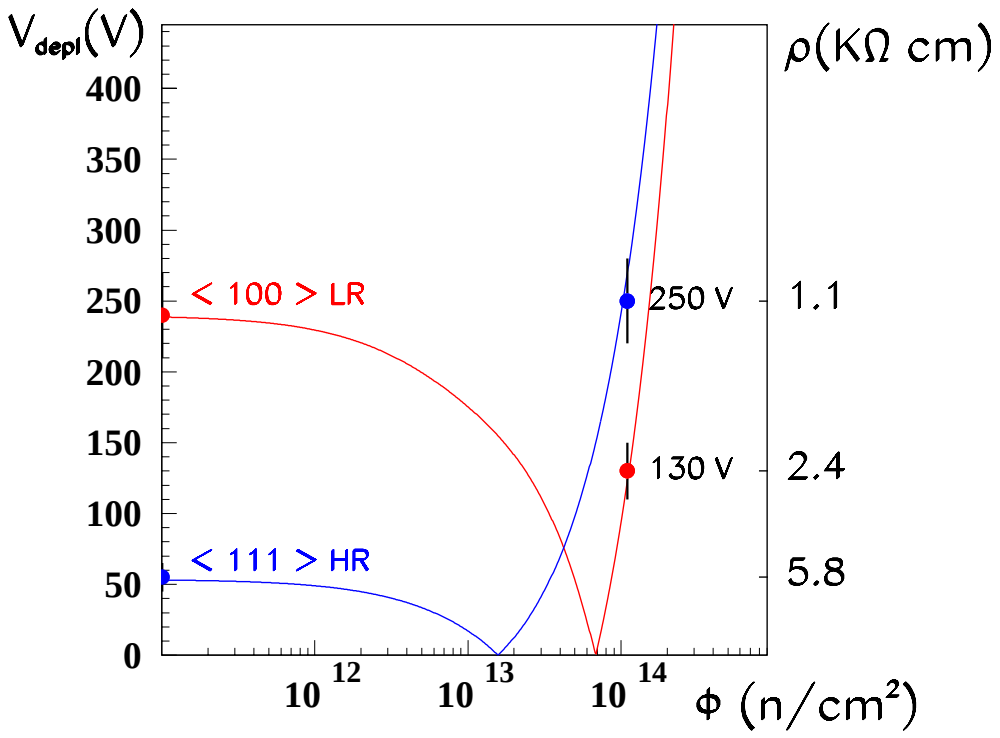

Figure 4.8: *Depletion voltage V_{depl} as a function of the neutron fluence ϕ for two kinds of silicon detectors, ⟨100⟩ "Low Resistivity" $\rho = 1.13 \pm 0.16$ kΩ cm and ⟨111⟩ "High Resistivity" $\rho = 5.8 \pm 1.1$ kΩ cm.*

until $V_{bias} < V_{depl}$ and then approaching a constant value. The knee of the CV curve defines the measured value of the depletion voltage V_{depl}. For the "High Resistivity" (HR, $\rho = 5.8$ kΩ cm) sensor the type inversion point is at lower fluence with respect to the "Low Resistivity" (LR, $\rho = 1.1$ kΩ cm) ones, therefore the depletion voltage is higher when increasing the radiation fluence ϕ (Fig. 4.8). For this reason, "Low Resistivity" sensors (in the range 1.5÷3.0 kΩ cm for thin sensors and 3.5÷7.5 kΩ cm for thick sensors) will be used for the CMS tracker, because the depletion voltage during LHC operations is kept within reasonable values, thus allowing to overdeplete the junction at lower bias voltage reducing the risk of electrical breakdown in the silicon.

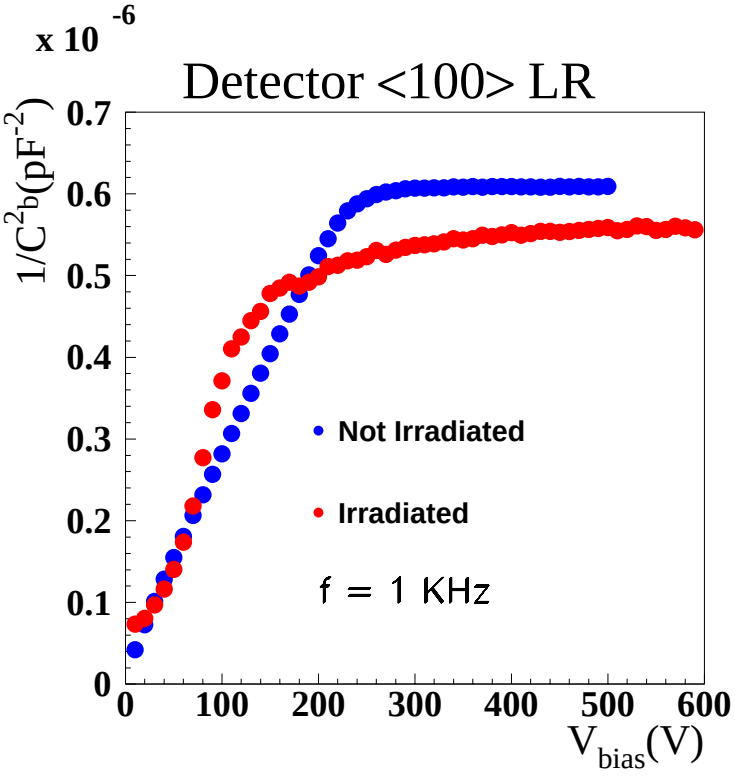

(a)

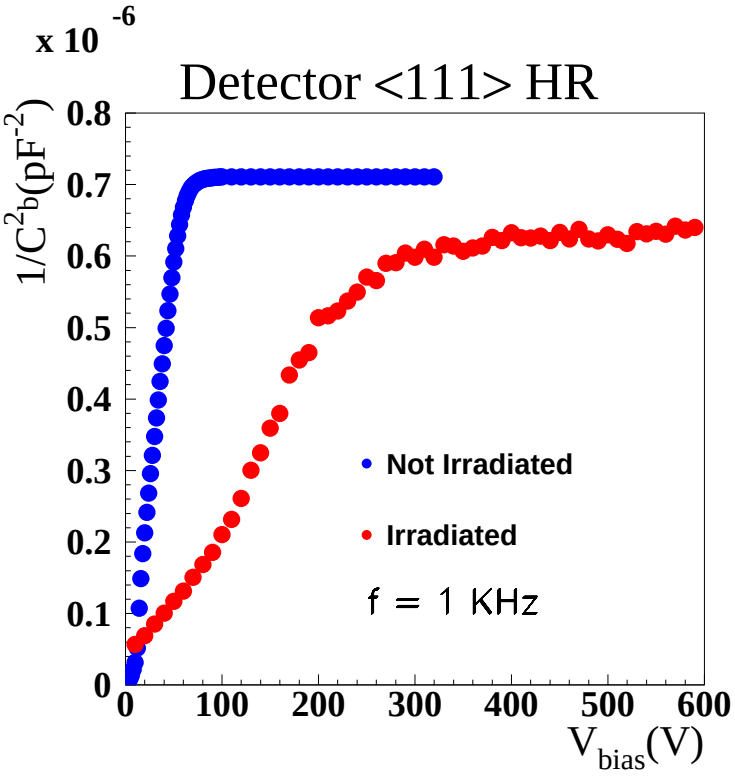

(b)

Figure 4.9: *Measurement at* 1 kHz *of the bulk capacitance* C_b *as a function of the bias voltage* V_{bias} *for* ⟨100⟩ LR *"Low Resistivity" (a) and* ⟨111⟩ HR *"High Resistivity" (b) sensors before and after irradiation with neutrons.*

4.5 Analysis of Test Beam on *Milestone 99* modules

Several sensors with different characteristics were produced during year 1999, equipped with APV6 readout chips [66] and called *Milestone 99* modules. Some of them were irradiated with neutrons to study in detail full size prototypes exposed to radiation fluences comparable with what foreseen for the experiment. Two different test beams were done during year 2000 at CERN: in July not irradiated modules were tested with *mip* (minimum ionizing particle) beams, while in August similar modules were tested after irradiating the sensors with 1 MeV equivalent neutron fluence of 1.1×10^{14} n cm^{-2}. The aim of these tests was to probe the long term behaviour of the detectors under LHC operating conditions to guarantee a satisfactory performance for the whole lifetime of the CMS experiment. In the innermost layer of the CMS silicon tracker the 1 MeV equivalent neutron fluence after ten years of LHC is expected to be 1.6×10^{14} n cm^{-2} [44].

The detectors assembled in Florence were wedge-shaped, as the one in Fig. 4.10, with 512 strips and characteristics summarized in Tab. 4.2.

Wedge detectors	Lattice	Resistivity	Depletion voltage [V]	
512 strips	orientation	[kΩ cm]	$\phi=0$ n cm^{-2}	$\phi=1.1\times10^{14}$ n cm^{-2}
⟨100⟩ LR	⟨100⟩	1.13±0.16	250	130*
⟨111⟩ HR	⟨111⟩	5.8±1.1	50	250*

* type inverted

Table 4.2: *Florence detector parameters. The strip pitch is between* 108.5 *and* 137.4 μm*, the total crystal length is* 127.32 cm*, the bulk thickness is* 300 μm.

The experimental setup was organized in a chain of aligned modules kept at low temperature for irradiated detectors to prevent thermal runaway. The irradiated detectors were also stored at low temperature to slow down the reverse annealing effect. Some detectors were aligned with strips perpendicular to the collimated pion beam, among which the two Florence detectors were placed. Two smaller silicon detectors (telescopes) closed the chain at both sides. Plastic scintillators for the trigger were also present. I have analysed the response of the Florence detectors when crossed by the 100 GeV pion *mip* beam provided by the CERN accelerating facility SPS at X5 West Hall. The results are given in terms of signal and noise as a function of the applied voltage to the module, read either in deconvolution or peak mode. Moreover, I have realized a simple tracking algorithm, which made possible to estimate the *hit* efficiency of the modules and for the first time to compute the rate of false *hits* (*Ghost Hit* rate) and extract some information about their origin.

4.5.1 Cluster finding

The raw output of each strip j of the module is the sum of three different contributions and it can be expressed in ADC channels with the following equation:

$$\mathrm{ADC}^j = \mathrm{S}^j + \mathrm{PED}^j + \mathrm{CMN} \tag{4.2}$$

where S^j is the signal, PED^j is the pedestal value and CMN the common mode noise [67].

The definition of a strip pedestal is the average value of the strip output level when no signal is present. It can be computed as the mean of the ADC counts of a single strip on several events without the presence of any signal. The common mode noise is the joint shift of the baseline in groups of adjacent strips belonging to the same readout chip and is calculated event by event as mean over a group of strips. It is a random effect and typically follows a gaussian distribution. The signal S^j is obtained by subtracting

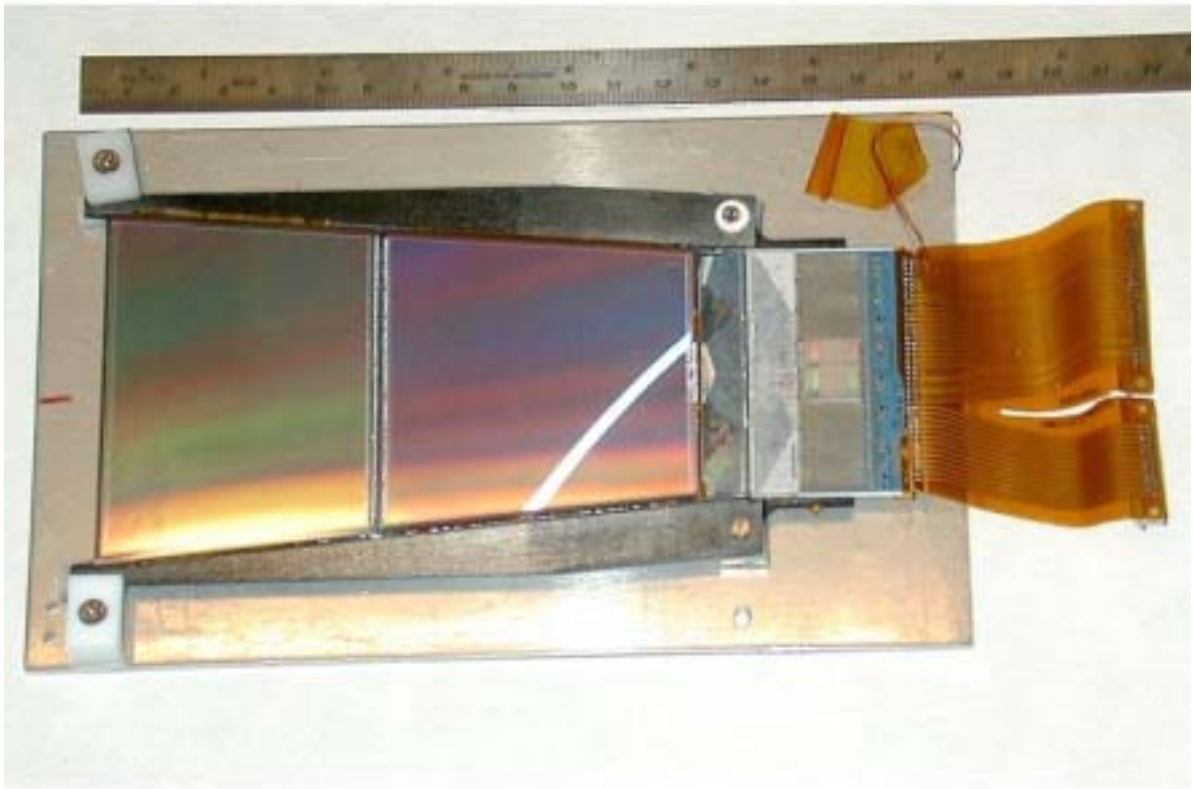

Figure 4.10: *A wedge-shaped* 300 µm *thick silicon microstrip sensor with readout electronics (on the right) from Milestone 99 production tested in Florence.*

to the raw ADC counts the pedestal and common noise contributions. The spread of the distribution of the signals S^j, collected during several triggers when the strip j is not fired by a particle, is the strip noise N^j.

Sets of contiguous strips that have a signal value compatible with the charge released by a *mip* passing through the detector are grouped into clusters following an iterative algorithm. At first all the strips are scanned looking for the ones with Signal-to-Noise ratio greater than a certain threshold T_S:

$$\left(\frac{S^j}{N^j}\right)_{seed} > T_S \tag{4.3}$$

When a strip obeying Eq. 4.3 is found, it is labelled as "*Cluster seed*". If two or more adjacent strips obey Eq. 4.3, the seed is assumed to be the strip with greater charge S^j. Once the cluster seed is fixed, neighbour strips are added to the cluster if their Signal-to-Noise ratio is greater than a given threshold T_a:

$$\left(\frac{S^j}{N^j}\right)_{neighbour} > T_a \tag{4.4}$$

The total number of strips forming a cluster is called cluster multiplicity. The total ADC counts $S_{cluster}$ corresponding to the charge of the particle passed through the detector is the sum of the cluster strip signals, whereas the cluster noise $N_{cluster}$ is given by the seed noise, since it is almost constant across a chip. To avoid clusters made by statistical fluctuations of the strip signals, a cluster is accepted only if its Signal-to-Noise ratio is greater than a final threshold T_c:

$$\left(\frac{S_{cluster}}{N_{cluster}}\right) > T_c \tag{4.5}$$

The cluster finding algorithm thresholds used in the analysis are summarized in the following scheme:

$$\begin{aligned} \left(\tfrac{S^j}{N^j}\right)_{seed} &> T_S = 4 \\ \left(\tfrac{S^j}{N^j}\right)_{neighbour} &> T_a = 2 \\ \left(\tfrac{S_{cluster}}{N_{cluster}}\right) &> T_c = 5 \end{aligned} \tag{4.6}$$

The most probable cluster charge value is reported in Fig. 4.11 as a function of the applied voltage V_{bias} for the not irradiated $\langle 100 \rangle$ LR module. The collected charge grows

rapidly with increasing bias voltage and continues to grow up even more slowly for V_{bias} greater than the measured depletion voltage, which amounts to 250 V. This is due to the higher electric field inside the overdepleted bulk, which reduces the probability for e/h pairs to recombine while drifting to the electrodes and possibly to a "ballistic" effect due to the combined operation of faster charge collection time on fast electronics. The mean value of the strip noise is around 4 ADC channels and reaches a constant when working with fully depleted modules.

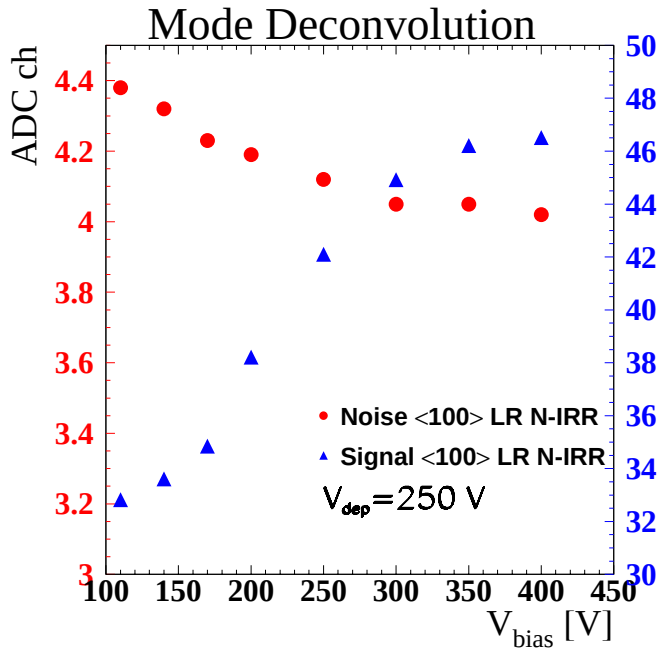

Figure 4.11: *Mean value of the strip noise (points, left axis) and most probable value of cluster charge (triangles, right axis) in ADC counts as a function of the applied voltage V_{bias} to ⟨100⟩ "Low Resistivity" modules (not irradiated), whose depletion voltage is 250* V.

The charge is best collected when working with overdepleted sensors ($V_{bias} \gtrsim 1.5 V_{depl}$) both for irradiated and not irradiated detectors, as shown in Fig. 4.12 on page 76, where the Signal-to-Noise ratio S/N (most probable value) of the clusters is reported as a function of the bias voltage in units of depletion voltage for the two Florence modules. If the module is overdepleted the charge collection, and hence the Signal-to-Noise ratio, reaches a constant value higher than 10, that is about 10% lower when irradiated modules are considered. The error assigned to the S/N value is about 0.3. It is mainly due to systematics and is estimated in comparing different sets of data taken at the same experimental conditions (bias voltage, temperature, APV parameters).

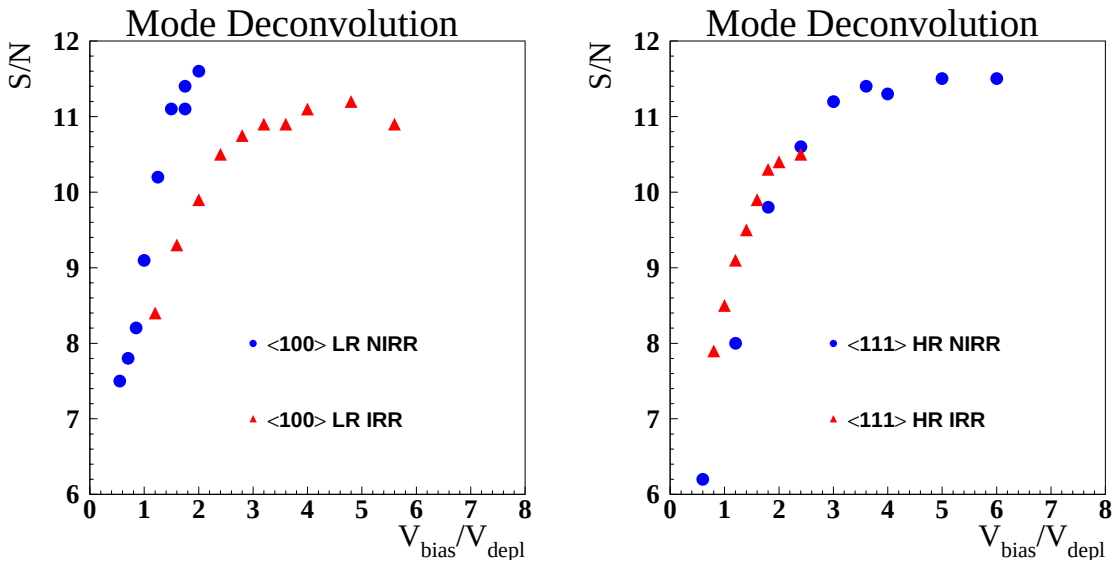

(a) (b)

Figure 4.12: *Signal-to-Noise ratio most probable value as a function of the applied voltage in units of depletion voltage for ⟨100⟩ "Low Resistivity" (a) and ⟨111⟩ "High Resistivity" (b) modules before (circles) and after (triangles) irradiation with neutrons. The higher V_{bias}/V_{dep} after irradiation is reached with "Low Resistivity" modules, thus allowing an efficient usage of these kind of modules after some years of LHC operation.*

4.5.2 Track finding

I have realized a simple tracking program by exploiting the information on the reconstructed clusters in the two telescopes and the two Florence detectors. Fixing three detectors, the two telescopes and one of the Florence modules, the position of the expected *hit* in the second Florence module is extrapolated and selected within a fiducial region. The *hit* efficiency is computed by counting the times a cluster, correlated with the ones of the other detectors, is found. Moreover, if some uncorrelated clusters are present, we have also a measure of the *Ghost Hit* rate (per strip per event).

The *hit* efficiency is greater than 99% if a working point is chosen to keep the Signal-to-Noise ratio greater than 9, both for irradiated and not irradiated detectors, as it is shown in Fig. 4.13. The number of *Ghost Hits* is divided by the number of detector strips and the number of triggered events to define the *Ghost Hit* rate shown in Fig. 4.14 on page 78 for all the modules as a function of the bias voltage. It does not depend on the applied voltage if the sensor is fully depleted and its value is about 2×10^{-4} *Ghost Hits* per strip per event. In a 512 strip detector, this *Ghost Hit* rate

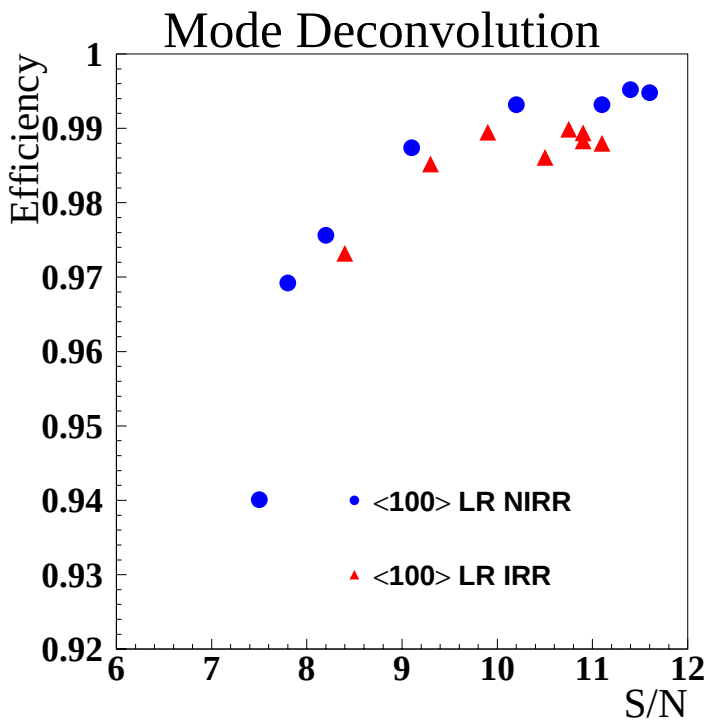

Figure 4.13: *Efficiency as a function of the Signal-to-Noise ratio for* ⟨100⟩ *"Low Resistivity" modules before (circles) and after (triangles) irradiation with neutrons.*

translates in one *Ghost Hit* every ten events on average.

The *Ghost Hits* are partly originated by statistical fluctuations and mostly by interactions of the *mip* beam with the crossed materials. The *Ghost Hit* position is mildly correlated with the position of the pion beam but anyway about 1 mm away from the expected track *hit* position. Therefore *Ghost Hits* could be interpreted as signals generated by δ-rays, which are electrons undergoing to a large enough momentum to leave their parent atoms in particularly close encounters with the incoming charged particles. This statement is confirmed by the charge distribution of the *Ghost Hit* clusters. Figure 4.15 on page 79 shows the track cluster charge distribution (in ADC channels) superimposed with that of *Ghost Hit* clusters (the coloured histogram). The energy release distribution of the *mip*s inside the silicon follows a Landau curve with the most probable value of the energy E_{track}=62.3 ADC channels (from the fit). The *Ghost Hit* charge distribution is composed by a noise component, pointed out by the narrow peak on the left, and by a distribution not dissimilar to the signal one, even if peaked at a different value. The *Ghost Hit* cluster multiplicity is 2.4 on average, while the *mip* charge is shared 70% of the times by only two strips.

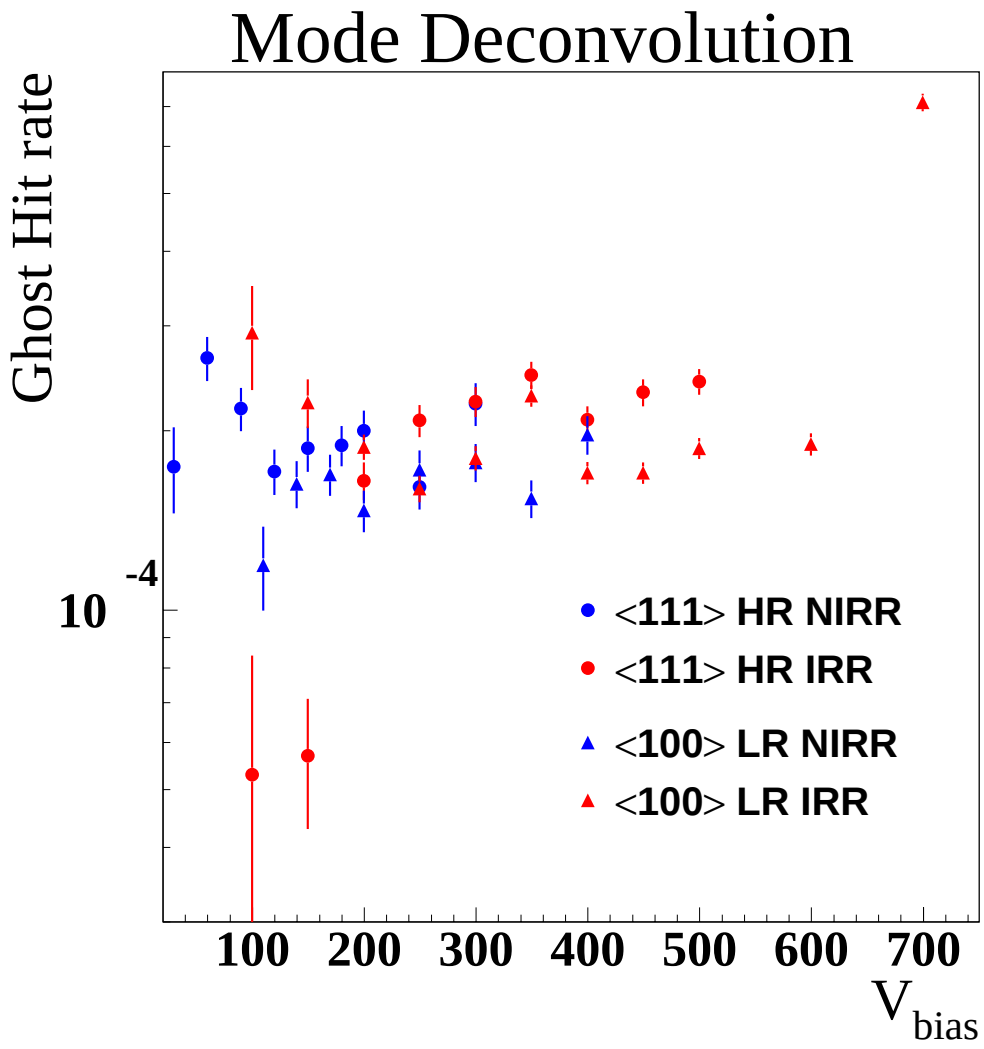

Figure 4.14: *Ghost Hit rate per strip per event as a function of the bias voltage V_{bias} for different Florence detectors, either not irradiated (points) or irradiated with neutrons (triangles).*

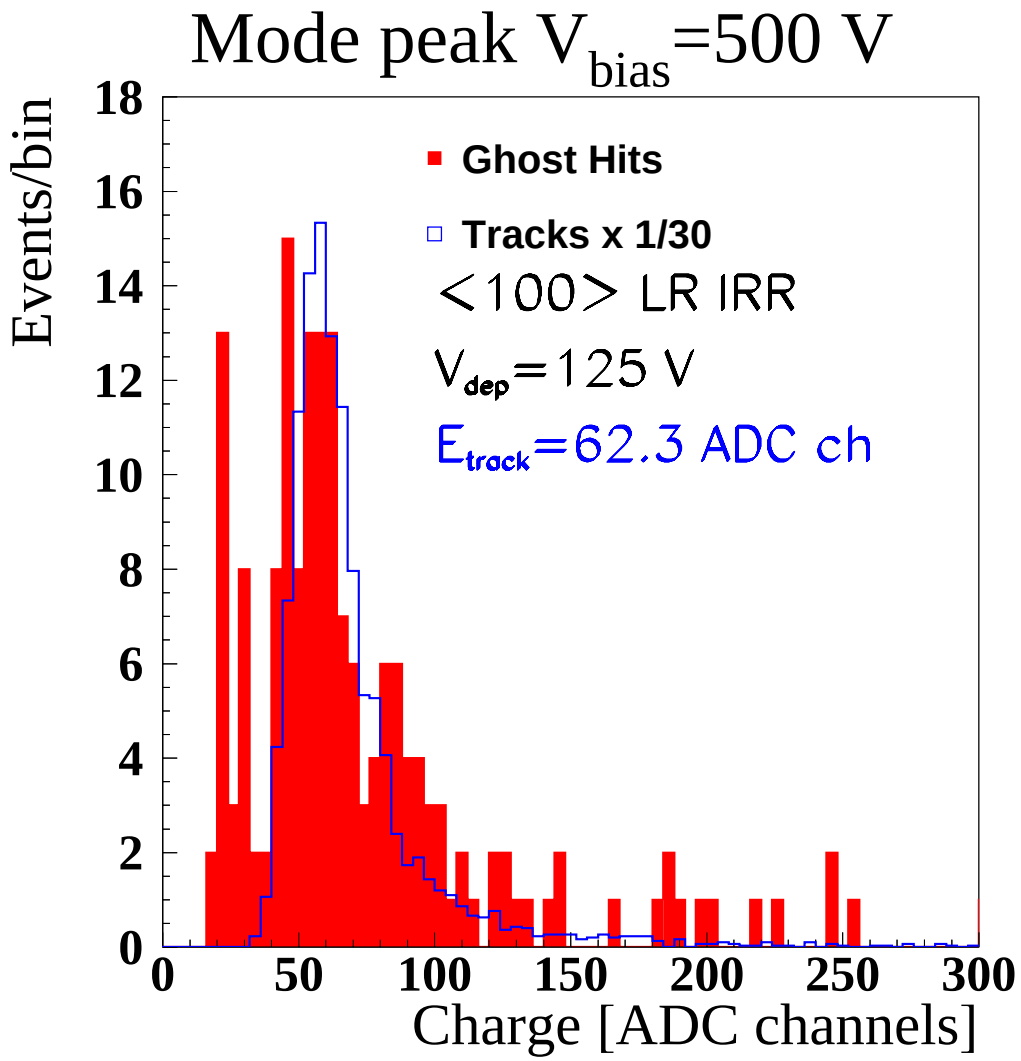

Figure 4.15: *Charge distribution (in ADC channels) for clusters originated by mips (open histogram) superimposed to that of Ghost Hit clusters (coloured histogram).*

4.5.3 Final results

The collection of the most important results from the analysis is reported in Tab. 4.3 for the Florence modules, whose main characteristics were summarized in Tab. 4.2. The better values of the Signal-to-Noise ratio S/N are reached when working with overdepleted sensors ($V_{bias} \gtrsim 1.5 V_{depl}$) and is above 10 both in deconvolution and peak readout mode. The *hit* efficiency is higher than 99% and the *Ghost Hit* rate per strip per event is about 2×10^{-4} independently from the bias voltage. Since a detector is fully efficient if the Signal-to-Noise ratio is above 9, the collected results of Tab. 4.3 give us confidence in the possibility to operate the silicon microstrip detector efficiently even after ten years of LHC running.

	Test Beam July 2000 (Not-Irradiated modules)				Test Beam August 2000 (Irradiated Modules)			
	⟨100⟩ LR		⟨111⟩ HR		⟨100⟩ LR		⟨111⟩ HR	
Temperature	10° C		10° C		-17° C		-17° C	
Depletion Voltage (V_{bias})	250 V		50 V		130 V		250 V	
Bias Voltage (V_{bias})	400 V		200 V		300 V		500 V	
Mode	peak	dec.	peak	dec.	peak	dec.	peak	dec.
S/N	17.2	11.6	18.0	11.3	14.8	10.5	15.0	10.4
Ghost Hit rate [$\times 10^{-4}$]	1.5	2.0	2.4	2.0	1.8	1.8	3.0	2.4

Table 4.3: *Performance of Milestone 99 Florence* 300 μm *thick silicon microstrip detectors. The error on the S/N ratio is about* 0.3 *and is due mainly to systematics. The error on the Ghost Hit rate is statistical, being of the order of* 0.3×10^{-4}.

Part II

Track Reconstruction and b-tagging

Chapter 5

Track Reconstruction

The software requirements and computing resources needed by LHC experiments exceed by far those of any currently existing high energy physics experiment. During 1995 the CMS software group has chosen new technologies of object-oriented programming language, object data base management service and flexible software architecture to solve the problem of rationally writing and maintaining the huge software system of the experiment. In this chapter the full CMS event production chain, from generation to reconstruction, is presented and the tracking algorithm developed by the CMS tracker group (the PRS-bτ group [68]) is introduced.

The CMS collaboration has decided to adopt the same software architecture both for online selection and offline analysis, but the complexity of track finding algorithms does not allow their blind usage during the High-Level trigger because they are too time-expensive. Some alternative strategies have been studied as, for example, the possibility to avoid the propagation of tracks through the whole tracker (*partial track reconstruction*). A detailed study has been done to test the expected performance of the track finding algorithm as a function of the number of points (*hits*) used to compute the parameters of a track. The performance of the tracker is already at a good level by stopping the track reconstruction after seven *hits* are added to a track, resulting in a saving of CPU time, which makes possible an efficient use of the tracker during High-Level trigger. Furthermore, tracks are reconstructed only around the triggered Level-1 objects (muons, jets). A detailed study at generator level has defined the most suitable regions around Level-1 jets to reconstruct tracks inside and for the first time it was demonstrated how the tracker can help in jet direction measurement to achieve a better resolution in η and φ.

I have tested the reliability of partial track reconstruction, at first by demonstrating that the CMS tracker can really be used during High-Level trigger and then by tuning

the track finder algorithm to reach the better HLT performance in terms of efficiency and timing. Finally, I have defined the recipe of HLT track finding around jets by writing the necessary software code, which was integrated into the CMS reconstruction and analysis program, and by connecting it with the pre-existent b-tag code to realize the b-trigger algorithm described in the next chapter.

5.1 Simulation and Reconstruction software

The study of the performance of the under-construction CMS experiment and its software is done in two independent ways. Algorithms and reconstruction software are tested with *ad hoc* simulated events, as "particle guns", for instance single muons propagating in the detector, or couples of back-to-back jets originated by b, c or lighter quarks. Specific physics channels are instead studied from the simulation of complete processes mixed up with pile-up of Minimum Bias collisions.

The pp interactions at $\sqrt{s}=14$ TeV are generated according to the parton distribution functions introduced in Sec. 3.1.2 by Monte Carlo simulation programs, PYTHIA [69] and ISAJET [70]. The relevant decay modes can be selected by the user to generate specific physics processes.

The generated final state particles are propagated into the CMS detector, whose geometry and response are simulated with the fortran [71] program CMSIM [72] based on the GEANT 3 [73] package to mimic the effects of the passage of particles through matter. The description of the CMS geometry is detailed and includes not only active subdetector volumes, but also cables and mechanical support structures.

The collision point is distributed around the CMS reference frame origin according to the composition of three independent gaussian distributions: along z axis with $\sigma_z=5.3$ cm and along bend plane x and y axes with $\sigma_x=\sigma_y=15$ μm. All the final particles produced at generator level are propagated through CMS taking into account multiple scattering, Compton scattering, pair production processes, showering in detector materials and hadronic interactions [74].

The information about energy deposition and location is stored into detector dependent entities, called *hits*, which contain all the details needed to simulate detector response. The simulated trajectories covered by the particles (*simulated tracks*) are also stored to be used in testing of the algorithms as "Monte Carlo truth". The average size of a simulated event file is 2 MB and the CPU time required to simulate one event ranges from 60 s for a pure Minimum Bias event to a maximum of 500 s for inclusive 1 TeV di-jet events, if using a 1 GHz Pentium III CPU.

The CMS reconstruction and analysis software is written in C^{++} [75] programming language. The results of intense computing simulated processes and, when the experiment will be running, real raw data have to be stored (*persistency*) in order to be used in several circumstances. This service is an issue of the "Coherent Object-Oriented Base for Simulation Reconstruction and Analysis" COBRA [76]. An "Object Data Base Management Service" (ODBMS) responds to the requirements of the collaboration and provides a coherent solution to the problem of persistent object management. The CMS software programs have run up to now under RedHat Linux 6.2.1.1 [77] platforms and Objectivity/DB 6.1.3 [78] has represented a valid solution. Anyway the CMS collaboration has planned to switch to RedHat Linux 7.3.1 [77] and a CERN internal solution has been searched for to replace the database commercial products.

The response of the detector is simulated taking into account the pile-up events of the actual and the contiguous bunch crossings. Pile-up events from the previous 5 and following 3 bunch crossings are superimposed to the "on-time" crossing in order to mimic the electronic readout behaviour and to take into account the energy pile-up in calorimeters. Pile-up events are randomly added from a Minimum Bias data base, which contains 200 000 events, separately for low and high luminosity, according to Poisson distributions around the central values calculated in Sec. 3.1.3, which are 3.5 and 17.3 respectively. The recycling of the same Minimum Bias events for pile-up is due to the limited available CPU resources used to massively produce them. The final products are the digitized *hits* (*digis*), which are used as input for the trigger simulation or the reconstruction programs. The *digis* are equivalent to the raw data collected by CMS when real data taking will be operational. Digitization is performed independently for low and high luminosity simulations.

The "Object-oriented Reconstruction for CMS Analysis" program ORCA [79] includes the code for reconstruction and also simulation of detector response, Level-1 and High-Level triggers and even the analysis code. The reconstruction software is based on COBRA [76], which provides basic services and utilities, as mathematical and statistical algorithms and routines, and implements the *implicit invocation* and the *action-on-demand*. These concepts imply that all the different modules (reconstruction, physics and utility modules) register themselves at creation time and are invoked only when required. In this way only the needed libraries are loaded and executed.

In the following the name of the C^{++} classes used in the CMS packages will be indicated `in this way`.

5.2 Reconstruction of tracks

The design of a reconstruction software system is sensibly dependent on the experimental apparatus, however several common issues can be found as general properties of track finding algorithms. The data provided by a simulated tracking device are of three types:

1. *hits* produced by charged tracks coming from primary or secondary vertices

2. *hits* produced by particles not relevant for physics analysis (Minimum Bias) or not belonging to the physics event (particles from beam pipe interactions, δ rays)

3. fake *hits* given by the intrinsic noise of the detectors

This classification is of course not available to the reconstruction program. The task of the track finding and reconstruction methods is first to divide the collected *hits* into groups of *track candidates* which should represent the trajectory of a charged particle and then to test their consistency with a fit to a given *track model*.

Actually the *hits* are the simulated *digis*, when the CMS experiment will start data taking they will be the raw data.

5.2.1 Track Model

The track models depend on the experimental configuration and design. In CMS the track model is derived from the equation of motion of a charged particle in a static magnetic field $\vec{B}$ given by the Lorentz force [80]

$$m\gamma\frac{d^2\vec{x}}{dt^2} = \kappa q\vec{v}\times\vec{B} \tag{5.1}$$

where $\vec{x}(t)$ is the position of the particle at time t, $\gamma=(1-\beta^2)^{-\frac{1}{2}}$ the relativistic factor, $\vec{v}$ the particle velocity, q the charge and m the mass of the particle, whereas κ is a constant related to the choice of the units. Since

$$\left(\frac{d^2\vec{x}}{dt^2}\right)\times\left(\frac{d\vec{x}}{dt}\right) = \vec{0} \tag{5.2}$$

the following relations are valid:

$$\left|\frac{d\vec{x}}{dt}\right| = constant = |\vec{v}| = \beta \mathrm{c}$$

$$\frac{d\vec{x}}{dt} = \frac{d\vec{x}}{ds} \cdot \frac{ds}{dt} = \frac{d\vec{x}}{ds}\beta \mathrm{c} \tag{5.3}$$

$$\frac{d^2\vec{x}}{dt^2} = \frac{d^2\vec{x}}{ds^2}\left(\beta \mathrm{c}\right)^2$$

where $s(t)$ is the curvilinear arc length or *path length*. The Eq. 5.1 can be rewritten in terms of geometrical quantities only by eliminating the parameter t:

$$\frac{d^2\vec{x}}{ds^2} = \frac{\kappa q}{|\vec{p}|} \cdot \frac{d\vec{x}}{ds} \times \vec{B} \tag{5.4}$$

with $\vec{p} = m\gamma\vec{v}$ momentum of the particle. The Eq. 5.4 is a system of three independent second order differential equations being $\vec{x} = (x, y, z)$, therefore six parameters are required to solve the problem in addition to the unknown constant $\frac{\kappa q}{|\vec{p}|}$. The identity

$$\left(\frac{dx}{ds}\right)^2 + \left(\frac{dy}{ds}\right)^2 + \left(\frac{dz}{ds}\right)^2 = 1 \tag{5.5}$$

and the arbitrary choice of one coordinate, the *reference surface*, limits the minimum number of parameters to individuate a trajectory to five. The curvilinear parameters [81]

$$\text{Track} \equiv \{c, \cot\theta, \varphi, d_0, z_{\mathrm{IP}}\} \tag{5.6}$$

are a useful set to define a track [44]. Their geometrical interpretation is:

$\boldsymbol{c = \frac{-qB_z}{\sqrt{p_x^2+p_y^2}} = -\frac{qB_z}{p_\mathrm{T}}}$ Track signed curvature, related to the magnitude of the transverse momentum $\vec{p}_\mathrm{T}$.

$\boldsymbol{\cot\theta = \frac{p_z}{p_\mathrm{T}}}$ Dip-Angle, the complementary of the angle between $\vec{p}$ and $\vec{p}_\mathrm{T}$, it represents the pointing direction of a track.

$\boldsymbol{\varphi = \arctan\left(\frac{p_y}{p_x}\right)}$ Azimuthal angle of the momentum vector at impact point.

$\boldsymbol{d_0, z_{\mathrm{IP}}}$ The impact point $(x_{imp}, y_{imp}, z_{imp})$ is the reference point of the track trajectory set at the distance of closest approach to the nominal vertex $(0, 0, 0)$.
The longitudinal impact parameter coincides with the z coordinate: $z_{\mathrm{IP}} = z_{imp}$.
The transverse impact parameter is defined as $d_0 = (y_{imp}\cos\varphi - x_{imp}\sin\varphi)$.

In a homogeneous magnetic field the solution of Eq. 5.4 is a helix with axis parallel to the magnetic field $\vec{B}$ direction, which is parallel to the CMS z axis.

Giving the trajectory of Eq. 5.4 with the parameters 5.6, some intrinsic limits on the measurement of a track can be individuated. First of all the minimum number of measurements required to estimate the unknown parameters can not be less than the number of parameters themselves. At minimum they could be a constraint on the transverse coordinates of the charged particle production vertex and the two innermost *hits* from the pixel detector.

The design of the CMS magnetic field and the architecture of the silicon tracker impose limits on the minimum and maximum measurable transverse momentum. Assuming the direction of the magnetic field $\vec{B}$ to be the z axis ($B_z = |\vec{B}| = B$) and according to Eq. 3.1, the relation between the transverse momentum p_{T} and the curvature radius R_c is expressed by

$$p_{\mathrm{T}}[\,\mathrm{GeV/c}] = 0.3 \cdot B_z[\mathrm{T}] \cdot R_c[\mathrm{m}] \tag{5.7}$$

and hence the minimum measurable p_{T} is given by the radius of the full circle that links the origin and the outermost layer at distance d from the origin, as shown in Fig. 5.1. The minimum measurable transverse momentum p_{T}^{min} is from Eq. 5.7:

$$p_{\mathrm{T}}^{min}[\,\mathrm{GeV/c}] = 0.3 \cdot B_z[\mathrm{T}] \cdot \frac{d}{2}[\mathrm{m}] \tag{5.8}$$

and assuming $B_z = 4$ T with the outermost layer distance from beam line as $d \simeq 1$ m, the resulting p_{T}^{min} value is about 0.6 GeV/c. Particles with transverse momentum lower than 0.6 GeV/c will never reach the outermost layer of the CMS tracker.

On the opposite, the maximum measurable transverse momentum is defined by the minimum sagitta s which can be measured to distinguish between the arc $\overset{\frown}{AB}$ from the straight line $\overline{AB}$ of Fig. 5.2. The curvature radius R_c can be expressed as

$$R_c = \frac{s^2 + \left(\frac{d}{2}\right)^2}{2s} \tag{5.9}$$

Assuming the distance d between the innermost pixel and the outermost silicon microstrip measurements to be of the order of 1 m and the minimum sagitta equal to the pitch between the strips of the middle layers $s \simeq 130$ μm, the result is $R_c \simeq 1$ km. Using Eq. 5.7 again, the maximum measurable p_{T} is estimated to be of the order of 1 TeV/c. More precisely, the sign of p_{T} and hence the charge of the particle can not be reliably measured if the error on the inverse transverse momentum is of the same order of $\frac{1}{p_{\mathrm{T}}}$, or equivalently the sagitta s measurement is compatible with zero.

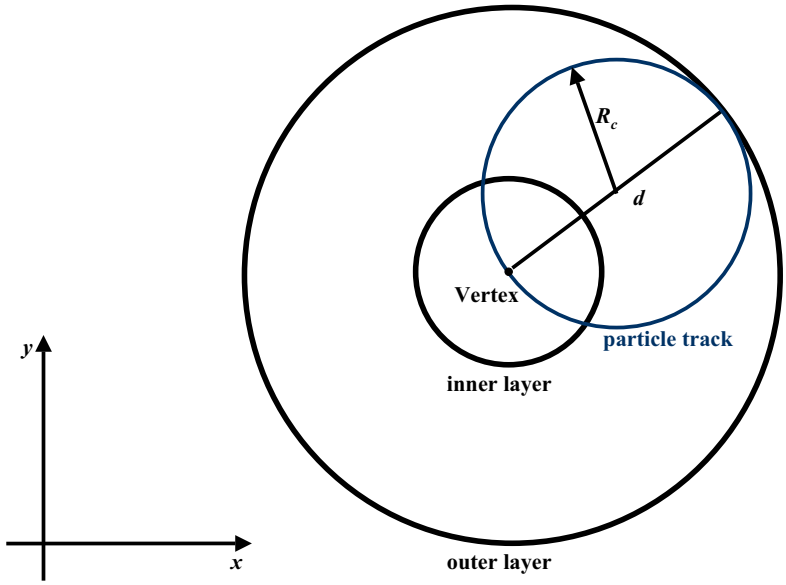

Figure 5.1: *Definition of the minimum measurable transverse momentum.*

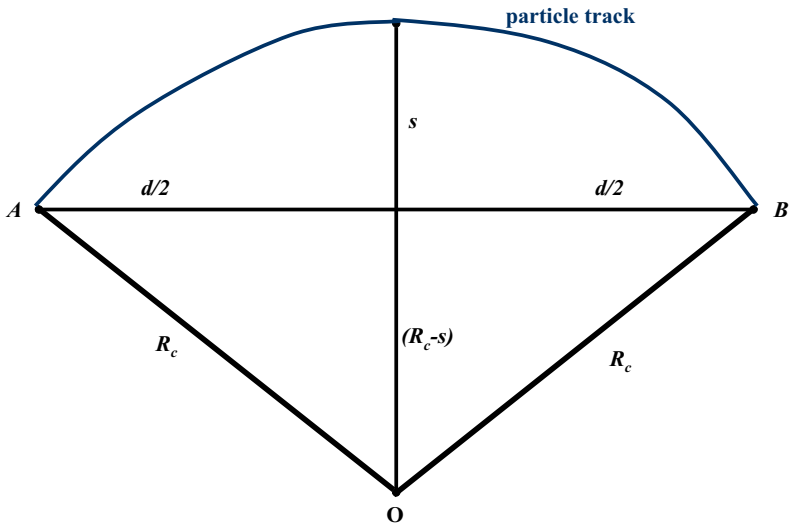

Figure 5.2: *Definition of the sagitta s as the distance of the mid-point of the arc to the chord defined by the points A and B of the circumference with radius R_c centered in O.*

5.3 The Kalman Filter

The basic object in the implementation of the track reconstruction in ORCA is the `RecHit`, which contains the information of the position of the *hit* and the corresponding errors expressed in different coordinate frames: the measurement frame (a strip, a pixel cell), the local frame (the surface of a detector) and the global CMS frame. The `RecHit`s are created from *digis* and in testing the performance of the reconstruction algorithms it is useful to associate them to the corresponding simulated *hits*, or `SimHit`s. This is done with some *hit* association criteria, based on information produced during digitization.

The basic object in track reconstruction is the `TrajectoryStateOnSurface`, usually referred to as `TSOS`, which contains the local and global position and direction of the track together with the curvature and the covariance matrix of track parameters. A reconstructed track (`RecTrack`) in the tracker is a sequence of `RecHit`s propagated from a surface to another reachable surface by updating the `TSOS` state with a geometrical extrapolation. The trajectory is fitted to the track model, depending on the shape of the magnetic field, taking into account the measurements and errors of the `RecHit`s and the stochastic model of material effects (multiple scattering, energy loss). Hence the track fitting requires the knowledge of the detector layout and resolution together with the model describing the trajectory of a particle. At this level the software is the same for reconstruction of either Monte Carlo tracks or true tracks, because they are reconstructed from `RecHit`s, which are *digis* in case of Monte Carlo events or the raw data when CMS will be turned on. Of course all the operations related to associations of reconstructed with simulated objects are excepted.

Any `RecTrack` can be associated with a set of compatible simulated tracks in the tracker (`TkSimTrack`s) by means of a track associator. A `TrackAssociatorByHits` associates a `RecTrack` to a `TkSimTrack` if the number of `RecHit`s associated to the `SimHit`s is greater than a given fraction of the total `RecHit`s. In the following analyses this threshold is set to 50%, hence a `RecTrack` is associated to a `TkSimTrack` if it shares more than 50% of its `RecHit`s with the simulated track `SimHit`s. This method is useful in studying track reconstruction efficiency and fake track[1] rate of the track finding algorithms.

One of the track reconstruction algorithms developed within ORCA is based on the Kalman Filter [82], a recursive procedure to estimate the states of a dynamic system, a stochastic model evolving in time. The Kalman Filter allows also to incorporate multiple scattering and energy loss during track propagation and performs track fitting in three

[1] A fake track is naturally defined as a `RecTrack` not associated to any `TkSimTrack` following a given association criterion.

steps:

Filtering in this phase the *state vector*, which describes the track in each intersection point with a measurement surface, is updated adding the information of a local measurement.

Prediction the *state vector* estimation in a future time is guessed.

Smoothing all the measurements collected up to the present time are used to better estimate the *state vector* in the past.

The design and implementation of the Kalman Filter in ORCA is modular [83], a `ModularKfReconstructor` being composed with four C^{++} classes dealing with different tasks, which interplay with each other. The four objects for track reconstruction in ORCA are:

`SeedGenerator` generator of *seeds*, the trajectory "starting values".

`TrajectoryBuilder` building of the trajectories starting from the *seeds*.

`TrajectoryCleaner` resolution of ambiguities among multiple reconstructed trajectories.

`TrajectorySmoother` smoothing of the trajectories, better estimation of the track parameters.

5.3.1 Seed Generation

A reduced set of data is investigated in order to define the starting values of potential track candidates, the trajectory *seeds*. The *seeds* can be extracted by measurements in muon chambers or calorimeters or by pixel *hits*. They are useful to reduce the search parameter space where to look for further *hits* to add to the trajectory candidates, because they allow a preliminary rough estimate of the track parameters.

The `CombinatorialSeedGeneratorFromPixel` is used to create *seeds* from the pixel detector layers. In Fig. 5.3 the principle of *seed* generation is sketched: all the pair of *hits* compatible from being generated by a track originated from the beam spot (a cylinder of 0.1 cm radius and 15 cm long centered in CMS reference frame origin) and with a minimum p_{T} of 0.9 GeV/c are selected to form the *seeds* to propagate from inside out through the tracker layers. Starting from each `RecHit` from the pixel outer layer, the inner `RecHits` compatible with the searched trajectory are linked with the starting one to form a *seed*. The pixel layers are optimal in seeding of tracks within hadron jets.

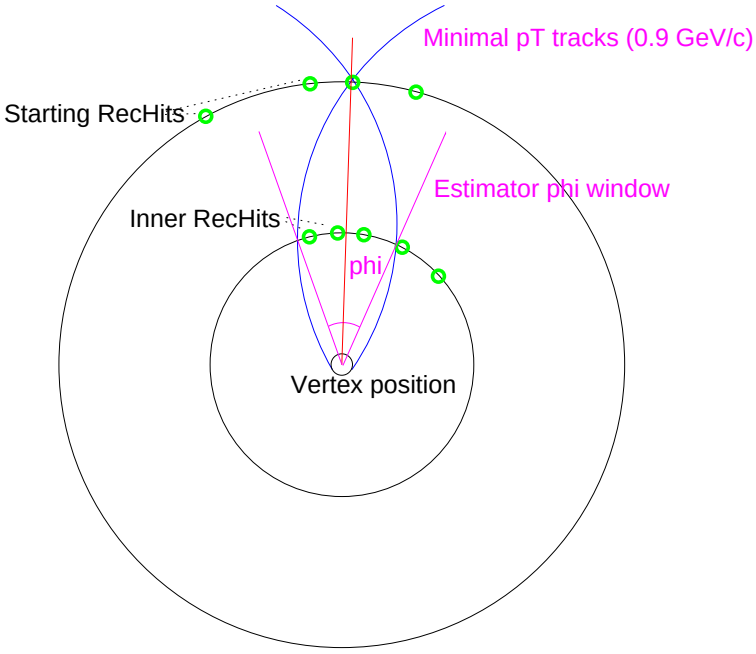

Figure 5.3: *Principle of operation of the* `CombinatorialSeedGeneratorFromPixel` *seed generator.*

5.3.2 Trajectory Building

Starting from each *seed*, measurements (*hits*) are added to form the trajectory candidates, which could be more than one per *seed*. The `CombinatorialTrajectoryBuilder` works it in two steps. At first the compatible layers for the propagation of a trajectory candidate are selected (*Navigation*) and then `RecHits` belonging to these layers are consistently added. A combinatorial search of compatible *hits* is performed. This part of the track reconstruction is the most expensive in terms of computing power. Even if the search for compatible `RecHits` is optimized for each layer, the combinatorial growth of the number of candidates has to be limited not to permit the `CombinatorialTrajectoryBuilder` to take an arbitrarily large computing time and memory. In propagating the trajectory candidates from layer to layer it is possible to split a single candidate into two or more candidates if two or more different `RecHits` can be accepted. In this way the number of the trajectories to propagate could grow rapidly for some complex events. To avoid the explosion of the algorithm, a maximum number of five trajectory candidates with $p_T > 0.9$ GeV/c is propagated in the following layer starting from the present one. This procedure goes on until the absence of compatible layers (for instance the tracker is ended) or compatible *hits* (typical for fake tracks) occurs. If two consecutive layers with no compatible *hits* are found, the propagation

is immediately stopped. Additional stopping conditions can be inserted, as the maximum number of `RecHits` to be added to each `RecTrack` to perform *conditional tracking* developed for High-Level trigger purposes.

5.3.3 Trajectory Cleaning

It is implicit in the combinatorial trajectory building the possibility to reconstruct trajectories sharing a certain number of `RecHits` or the same *seed*. The ambiguities of multiple reconstructed trajectories are solved by the trajectory cleaner.

The `TrajectoryCleanerBySharedHits` gathers together the mutually exclusive ones from the sample of all the reconstructed trajectories and discards for each set all but the *best* one, which is defined as the trajectory with the better value of χ^2 normalized to the degrees of freedom.

5.3.4 Trajectory Smoothing

The Kalman Filter smoother (`KFFittingSmoother`) performs two fits to the trajectory in opposite directions, from outside in and from inside out. The results are statistically combined to better define the trajectory and the track parameters at every surface crossed by the charged particle.

5.4 Partial Track Reconstruction

The possibility to use the combinatorial track reconstruction algorithm during the HLT has been explored first of all with studying the reconstruction of tracks with the tracker by applying some stopping conditions. The requirement of HLT track finding is to save CPU time together with the better measurement of the track parameters. The precision of the track impact parameter measurements is essential to recognize b-jet tracks and depends mainly on the innermost layer measurements. Going on in track reconstruction, the multiple scattering dominates and the impact parameter errors do not decrease resulting in a waste of CPU time from the High-Level trigger point of view.

In an "inside-out" Kalman Filter the track parameters are not known at the interaction point until the smoothing stage. Moreover, it would be too computationally expensive to smooth each track candidate after updating with a new *hit* only to check if a certain precision is reached. For this reason, it has been considered the possibility of breaking track reconstruction early, as soon as the track is composed with a maximum number of *hits*.

How many hits in the track do we like to have? To answer this question, I have studied in detail the performance of the tracker in estimating the track parameters as a function of the number of *hits* per track, in order to develop a reliable conditional track reconstruction for High-Level trigger [84].

The reconstruction performance is scanned in (η, p_{T}) plane, divided into 4×6 bins according to the following scheme:

- 4 $|\eta|$ bins corresponding to well defined tracker regions:

$\mathbf{0 \leqslant \lvert\eta\rvert \leqslant 0.9}$	barrel region (all the *hits* belong to TIB and TOB)
$\mathbf{0.9 < \lvert\eta\rvert \leqslant 1.3}$	overlap region till the end of TOB
$\mathbf{1.3 < \lvert\eta\rvert \leqslant 1.8}$	overlap region till the end of TIB
$\mathbf{1.8 < \lvert\eta\rvert \leqslant 2.4}$	forward region, all the *hits* belong to the disks (TID and TEC)

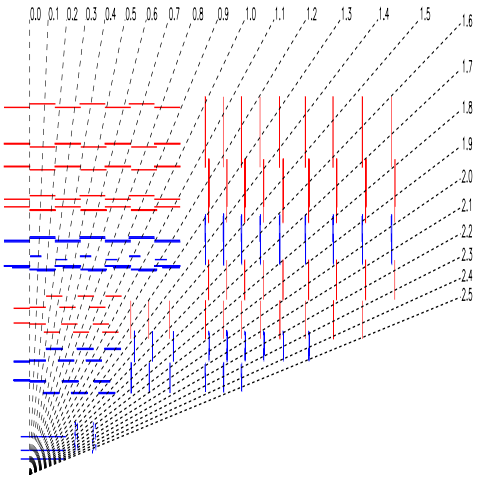

- 6 p_{T} bins in logarithmic sequence:

$$\mathbf{0.9 \leqslant p_T[GeV/c] \leqslant 1.3}$$
$$\mathbf{1.3 < p_T[GeV/c] \leqslant 1.8}$$
$$\mathbf{1.8 < p_T[GeV/c] \leqslant 2.5}$$
$$\mathbf{2.5 < p_T[GeV/c] \leqslant 5.0}$$
$$\mathbf{5.0 < p_T[GeV/c] \leqslant 10.0}$$
$$\mathbf{10.0 < p_T[GeV/c] < \infty}$$

Three simulated samples of back-to-back $\mathrm{b\bar{b}}$ jets with $E_{\mathrm{T}} = 200$ GeV, whose directions are in the regions $0 < |\eta| < 0.9$ (barrel), $1.2 < |\eta| < 1.6$ (overlap) and $2.0 < |\eta| < 2.4$ (forward) respectively, are studied. Tracks are reconstructed in the whole tracker acceptance with full pixel detector design (not staged). The version of the programs used for the generation and simulation chain are PYTHIA 6.158, CMSIM 122 and ORCA_5_2_0 for the digitization. The analysis is performed with ORCA_5_3_2.

	TkSimTrack	RecTrack
p_{T}[GeV/c]$\geqslant$	0.9	0.7
$0\leqslant\|\eta\|\leqslant$	2.5	2.6
d_0[cm]$\leqslant$	3.	120.
z_{IP}[cm]$\leqslant$	30.	170.
Number of *hits* $\geqslant$	0	8

Table 5.1: *Selection cuts to define the sample of* `TkSimTracks` *and* `RecTracks` *to compute track reconstruction global efficiency.*

The global efficiency of track reconstruction is defined by considering the subsamples of filtered reconstructed and simulated tracks according to Tab. 5.1. The value of the global efficiency is the ratio between the selected `RecTracks` associated to one of the selected `TkSimTrack` ($N_{REC}^{sel,ASS}$) and the total number of selected simulated tracks (N_{SIM}^{sel}):

$$\epsilon_{global} = \frac{N_{REC}^{sel,ASS}}{N_{SIM}^{sel}} \tag{5.10}$$

The value of ϵ_{global} is reported in Fig. 5.4 for the three samples of 200 GeV transverse energy $b\bar{b}$ jets.

The collection of all reconstructed tracks is analysed in detail. At first all the `RecHits` for each track are collected and ordered from the innermost to the outermost with respect to the pixel and silicon strip layer positions. The first three `RecHits` are selected, being the two *hits* forming the *seed* and the next `RecHit`[2], and subsequently the three measurements are smoothed. The result is the estimation of the `RecTrack` parameters with only the first three *hits*, provided only the correct *hits*, selected with the complete track reconstruction, are used. In this way there is no control on the efficiency and fake rate of partial track reconstruction, but only a useful estimation of the achievable performance is done. The *next* `RecHit` is then added to the array of `RecHits` and the new partial track (four `RecHits`) is smoothed and the result stored. This procedure goes on till eleven *hit* arrays are formed (when possible).

Each `RecTrack` associated to a `TkSimTrack` is assigned to one of the 24 (η, p_{T}) regions according to the value of the simulated track pseudorapidity and transverse momentum. For all the `RecTracks` of each region the resolution of the measured parameters are computed as a function of the number of *hits* used to smooth the trajectory. The most

[2]It could be in the pixel detector if at least three planes of pixels are crossed by the track or else be the first *hit* belonging to the silicon microstrip detectors.

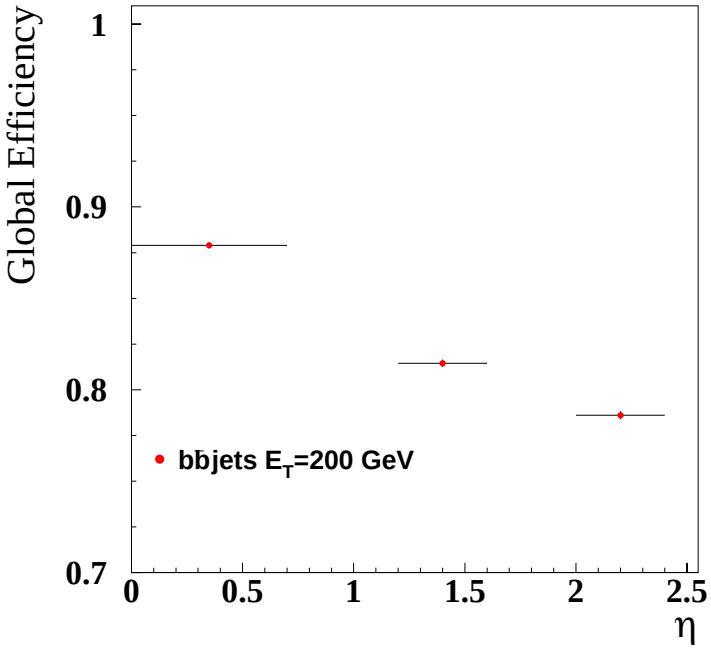

Figure 5.4: *Global efficiency of track reconstruction as defined by Eq. 5.10 and Tab. 5.1 for* 200 GeV E_{T} *back-to-back* $\mathrm{b\bar{b}}$ *jets directed along three different* $|\eta|$ *regions. Error bars (statistical) are almost fully comprised within the marker size.*

important parameters for b-physics are the transverse momentum p_{T} and the transverse (d_0) and longitudinal (z_{IP}) impact parameters. Also the angular measurements $\cot\theta$, φ and η are analysed as well.

For any given measurable track parameter x, the resolution is defined as the standard deviation of the distribution of the residuals between the measured value x^{rec} and the simulated x^{sim}:

$$Resolution = \sigma\left(x^{rec} - x^{sim}\right) \tag{5.11}$$

Hence for each `RecTrack`, for every fixed number of *hits* and for all the parameters a gaussian fit of the distribution of $(x^{rec} - x^{sim})$ was performed with the analysis program PAW [85] with great expense of computing time and memory. The $\sigma\left(x^{rec} - x^{sim}\right)$ together with the corresponding error is reported as a function of the number of `RecHits`, as shown for example in Fig. 5.5 for the transverse momentum (a) and the transverse impact parameter (b) of tracks in the barrel with different p_{T}. The points in correspondence of "0" `RecHits` are the values obtained from the complete reconstruction of all the tracks. The `RecTracks` are divided in two subsamples: reconstructed tracks with only two *hits* in the pixels (about 20% of the total) and with three or more pixel *hits*.

In this way it can be pointed out the effect of pixel staging, explained at the end of Sec. 4.1, in deteriorating the measurement of track parameters. This is especially evident for the impact parameter measurements (Fig. 5.5b), where the resolutions in the two subsamples are very different.

All the measurements approach the asymptotic value obtained with the full track reconstruction after only five or six *hits* are considered. This is true for a large range in transverse momentum and pseudorapidity, covering the physically interesting regions. This good result is the first step in the building of an efficient track finding algorithm relevant for application in High-Level trigger. Two further aspects of the track reconstruction has to be investigated: the performance of track reconstruction, for instance global efficiency and fake rate, when stopped at a fixed number of *hits* and the time spent by the algorithms, which is reduced if tracks are reconstructed only around the interesting objects, as jets or muons from the Level-1 trigger (regional reconstruction).

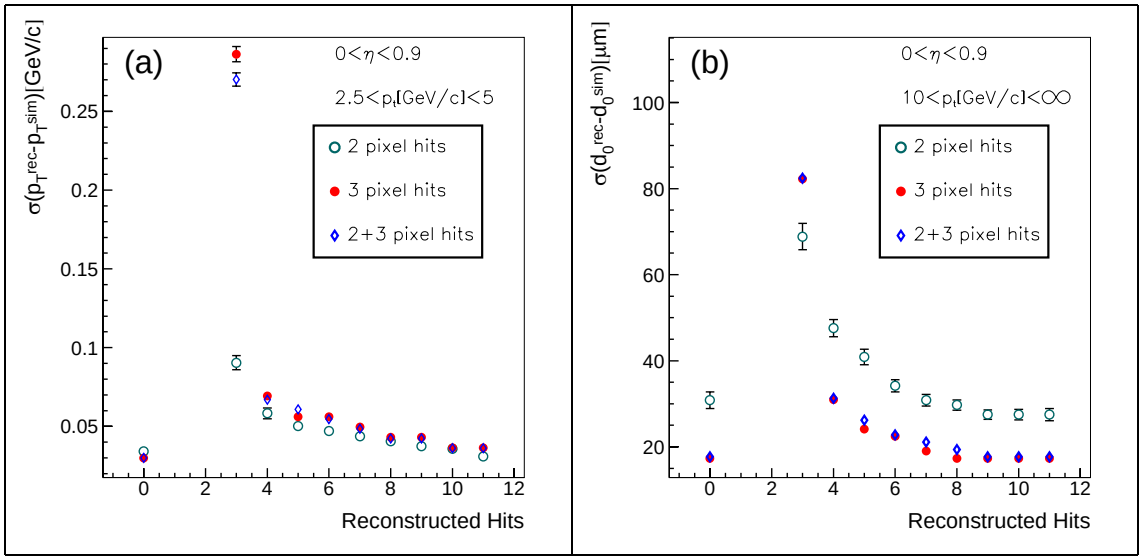

Figure 5.5: *Resolution of transverse momentum p_T (a) and transverse impact parameter d_0 (b) as a function of the number of smoothing steps for partial track reconstruction compared with full track reconstruction (leftmost point at 0) for tracks in the barrel region.*

5.4.1 Partial reconstruction performance

The partial track reconstruction performance is very close to the asymptotic value when at least five *hits* are added to the trajectory. The best choice for the trajectory building stopping condition (maximum number of *hits*) will be finally done according both to the tracking performance and to the CPU time required for partial track reconstruction at High-Level trigger stage.

Transverse Momentum

The measurement of the transverse momentum p_T depends on the extension of the lever arm, hence if one `RecHit` is in the silicon strip detectors the resolution reaches a value very close to the asymptotic one, either for soft tracks (Fig. 5.6a) or hard tracks (Fig. 5.6b). This behaviour is well betrayed by the curve originated from tracks with only two pixel *hits*. In this case the third *hit* is in the silicon microstrips while for tracks with three or more pixel *hits* it is still in the pixel detector layers. As soon as also these tracks reach the microstrip layers, the measurement of p_T is nearly independent from the number of pixel *hits* and does not change too much if smoothing after adding one more *hit*.

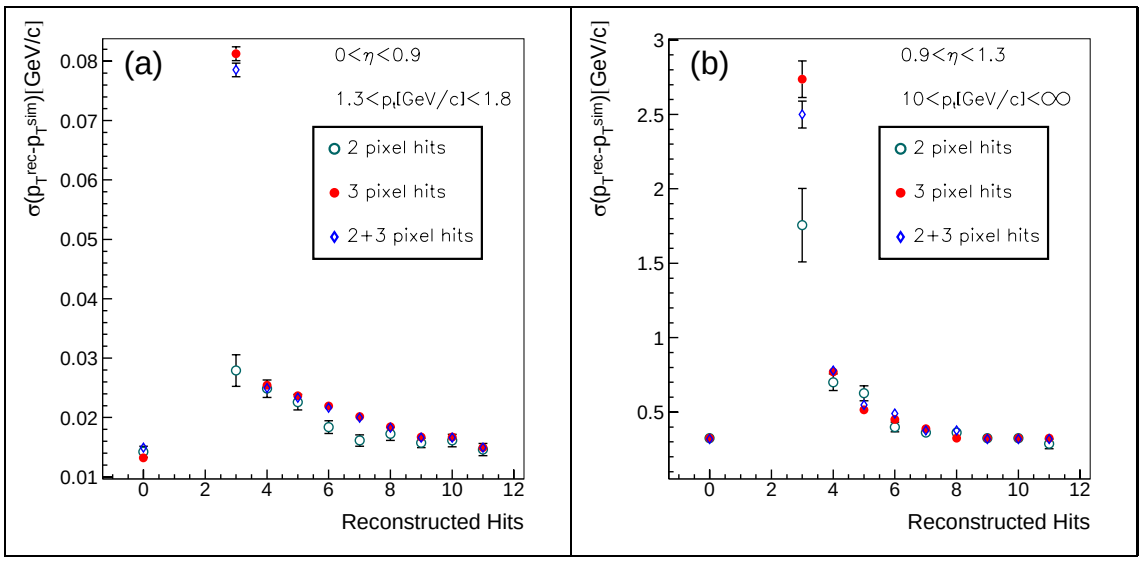

Figure 5.6: *Resolution of transverse momentum p_T as a function of the number of smoothing steps for partial track reconstruction compared with full track reconstruction (leftmost point at 0) for soft tracks in the barrel (a) and hard tracks in the overlap region (b).*

Transverse Impact Parameter

The larger lever arm affects the resolution of the transverse impact parameter measurement for higher p_T tracks, because once the track has reached the silicon strip layers the resolution drops down approaching the asymptotic value, as shown in Fig. 5.7a. The precision of d_0 measurement is dominated by pixel *hit* resolution and deteriorated by multiple scattering in the innermost pixel layers. Hence a track with less pixel *hits* has a worst resolution in d_0 and a higher asymptotic value of a factor two or more in all $|\eta|$ regions, as shown in Fig. 5.7.

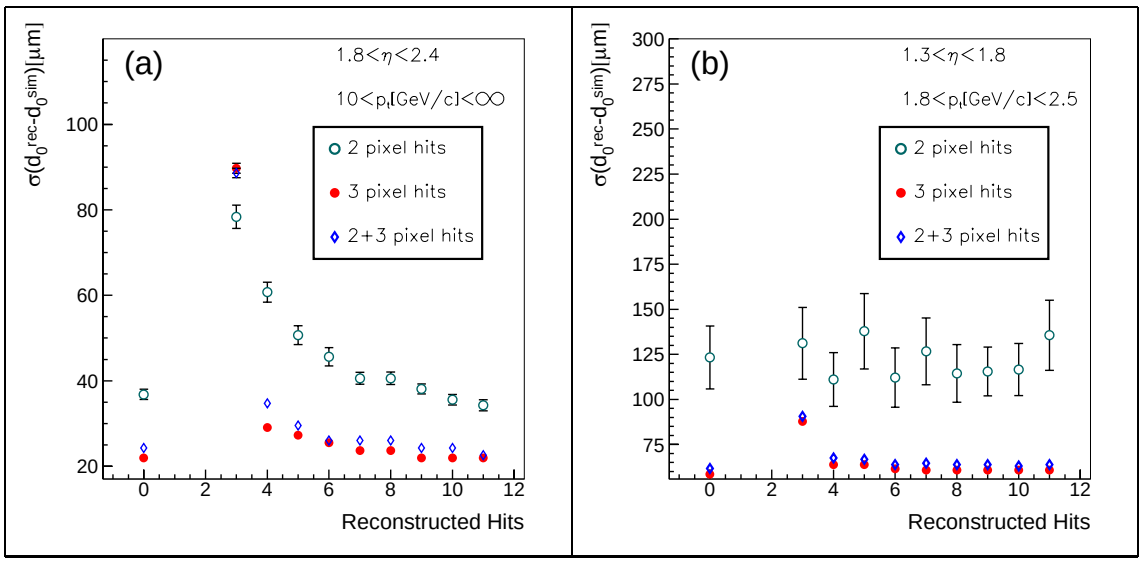

Figure 5.7: *Resolution of transverse impact parameter d_0 as a function of the number of smoothing steps for partial track reconstruction compared with full track reconstruction (leftmost point at 0) for hard tracks in the forward region (a) and soft tracks in the overlap region (b).*

Longitudinal Impact Parameter

The better resolution in z of the pixels dominates in estimating the longitudinal impact parameter, because in rz projection tracks are almost rectilinear, then the asymptotic value is given mainly by pixel measurements. The presence of measurements near the impact point is essential, hence for tracks with three or more pixel *hits* the resolution is better with respect to tracks with two pixel *hits* only. This effect is pointed out by the plots of Fig. 5.8 and is valid in all $|\eta|$ and p_{T} regions. At lower momenta the presence of multiple scattering effects degrades the resolution.

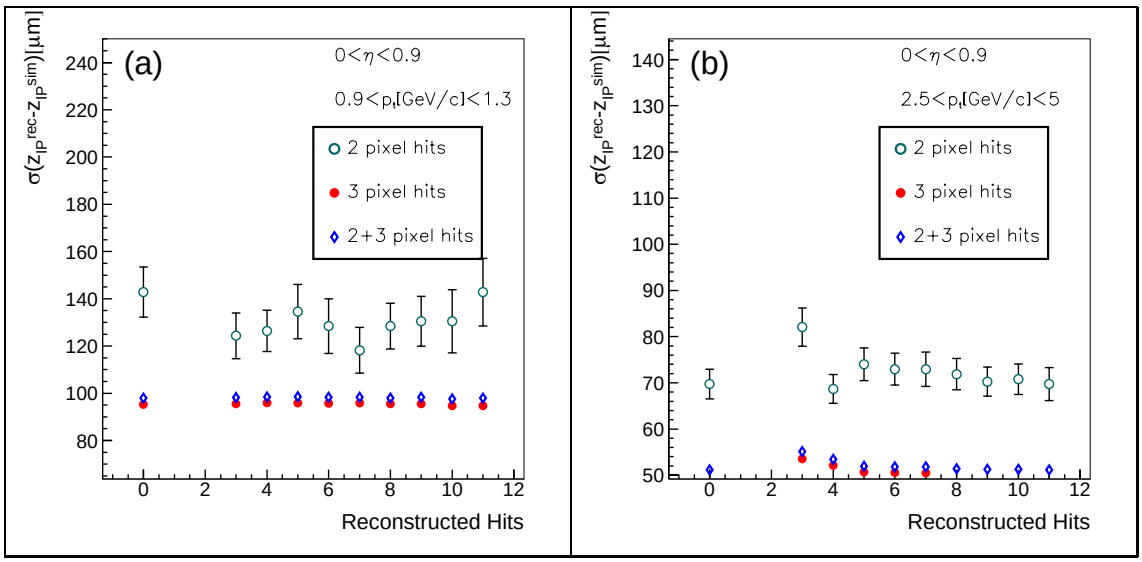

Figure 5.8: *Resolution of longitudinal impact parameter z_{IP} as a function of the number of smoothing steps for partial track reconstruction compared with full track reconstruction (leftmost point at 0) for softer tracks (a) and harder tracks (b) in the barrel.*

5.5 Regional Track Reconstruction

The High-Level trigger tracking has to address specific questions, such as verifying that the transverse momentum of a muon candidate is above a certain threshold or whether a lepton is isolated or a jet is a b-jet. The Level-1 triggered objects should be inputs for the HLT track reconstruction, which is not demanded to reconstruct the whole event, but only to define a minimum amount of objects with the maximum number of useful information.

To recognize if a jet is originated from the production and hadronization of b quarks it is enough to reconstruct the tracks belonging to the jet aggregate trying to have the higher efficiency in reconstructing tracks from displaced secondary vertices, characterized by the higher values of the transverse impact parameter. The goal is to define a *Region of Interest* for track reconstruction around b-jets in order to reduce the number of *seeds* to propagate with saving of CPU time, which could be spent in other operations.

With this goal in mind, a study has been done at generator level by simulating with PYTHIA 6.158 some $q\bar{q}, gg \rightarrow b\bar{b}$ events with production of two back-to-back jets in the central region with transverse energy of 100 GeV and a tolerance of 10 GeV. The jet direction is calculated by means of LUCELL [69] routine, which defines jets in the (η, φ) plane.

All the tracks of charged "stable" particles[3] are divided into *Primary* and *Secondary*. The first set is composed with tracks coming directly from the interaction vertex, or primary vertex, whereas the second set gathers up the tracks originated from the decay of b hadrons ($\tau \simeq 1.5$ ps) in displaced secondary vertices ($c\tau \simeq 480$ μm). These tracks are of course the more important for the tagging of b-jets. For each track the pseudo-angular distance from the jet axis

$$\Delta R = \sqrt{(\eta_{track} - \eta_{jet})^2 + (\varphi_{track} - \varphi_{jet})^2} = \sqrt{\Delta\eta^2 + \Delta\varphi^2} \tag{5.12}$$

is calculated. The number of tracks from both sets within several values of ΔR threshold is reported in Fig. 5.9.

The b-jet secondary tracks are selected with an efficiency of nearly 100% if the *Region of Interest* around the jet direction, referred to as "jet cone", is defined as $\Delta R < 0.4$. In Tab. 5.2 the number of the primary and secondary tracks for two amplitudes of the jet cone is listed together with the fraction f of selected tracks.

[3]Particles are defined "stable" if they do not decay within the detector.

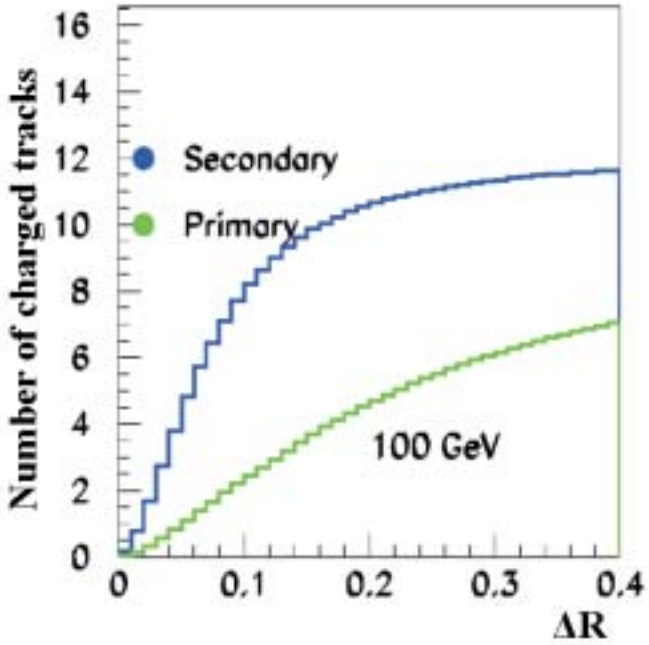

Figure 5.9: *Number of primary and secondary charged tracks in* $E_{\mathrm{T}} = 100$ GeV $\mathrm{b\bar{b}}$ *jet events as a function of the pseudo-angular distance* ΔR *from jet axis at generator level.*

		$\Delta R < 0.15$		$\Delta R < 0.4$	
	All	tracks	f	tracks	f
Primary	15	3.5	0.2	7	0.5
Secondary	12	10	0.8	12	1.0

Table 5.2: *Mean number of selected charged tracks and fraction to the total (*f*) in barrel* $E_{\mathrm{T}} = 100$ GeV *back-to-back* $\mathrm{b\bar{b}}$ *jet samples for different values of the Region of Interest* ΔR*.*

5.6 High-Level Trigger tracking

The definition of the track finding algorithm to be used during HLT is straightforward from the results of Sec. 5.4 and 5.5. Regional seeding and partial track reconstruction represent the most suitable solution to the puzzle of fast track reconstruction in HLT algorithms using the tracker.

Regional Seeding

Since the trajectories of charged tracks are represented by helixes and the helix curve is five-dimensional, the corresponding constraints can be put on the parameters collected in Eq. 5.6 and represented by:

2 positions transverse (d_0) and longitudinal (z_{IP}) impact parameters with respect to the nominal interaction point

2 directions pseudorapidity ($\eta = -\log\left(\tan\frac{\theta}{2}\right)$) and azimuthal angle ($\varphi$)

1 kinematics the transverse momentum p_{T}

Some constraints are imposed to limit the number of *seeds* by searching for $p_{\mathrm{T}} > 0.9$ GeV/c *seeds* coming from the primary vertex fiducial region ($d_0 < 0.1$ cm and $|z_{\mathrm{IP}}| < 15$ cm), as described in Sec. 5.3.1. According to the results of Sec. 5.5, the angular constraints η and φ are useful to restrict the *hits* on the seeding pixel layers to search for *seeds* compatible with being inside a well defined tracking region, for example around Level-1 jet directions. The detectors which are not compatible with the tracking region are never accessed for *hits* and also their *digis* (raw data) are never requested, according to the principle of the *action-on-demand* explained in Sec. 5.1, which ensures that only the minimal amount of raw data is loaded and clustered. For b-jet events it is important also to further limit the region around the interaction point (constraints on d_0 and z_{IP}) by determining the correct position of the primary vertex before generating the trajectory *seeds*.

Partial Track Reconstruction

If the trajectory *seed* is contained within the tracking region, the resulting track is very likely to be inside the five-dimensional region as well. The only constraint to apply to speed-up the trajectory building is on the transverse momentum by abandoning immediately the propagation of trajectory candidates below the p_{T} threshold. The CPU time is saved by stopping reconstruction at a fixed number of *hits* and then smoothing the trajectory to have a set of partially reconstructed tracks around some *Regions of Interest*, defined by the triggered Level-1 objects.

The feasibility of the HLT track reconstruction algorithm is demonstrated by the fact that using at least five *hits* the precision of track parameters is not so far from full reconstruction and by the limited width of the jet cones ($\Delta R < 0.4$) suitable for almost

complete b-jet track finding. In this paragraph the reliability of the HLT tracking is meticulously studied by looking at the quality of the reconstructed tracks. Two quantities are defined to test the skill of a track reconstruction algorithm: the global efficiency and the fake rate.

The global efficiency ϵ has been defined in Sec. 5.4 and here reported again for completeness:

$$\epsilon = \frac{N_{REC}^{sel,ASS}}{N_{SIM}^{sel}} \tag{5.13}$$

where $N_{REC}^{sel,ASS}$ is the number of selected `RecTrack`s associated to one of the selected `TkSimTracks` N_{SIM}^{sel}. The selection of reconstructed and simulated track serves to form unbiased subsamples of tracks to compute a realistic value of the global efficiency.

The fake rate R_{fake} is defined as the fraction of reconstructed tracks not associated to any simulated track:

$$R_{fake} = \frac{N_{REC}^{sel,nASS}}{N_{REC}^{sel}} \tag{5.14}$$

The selection of the subsamples of `RecTrack`s and `TkSimTracks` is generally different from what done for efficiency not to over-estimate the fake rate.

The values of efficiency and fake rate are computed by reconstructing tracks around back-to-back jets mixed up with low and high luminosity pile-up of Minimum Bias events, which make the track reconstruction harder. In case of low luminosity also the staged pixel scenario has been considered. Two $|\eta|$ regions have been defined in simulating the di-jet events, the central region $|\eta| < 1.4$ and the forward region $1.4 < |\eta| < 2.4$. The transverse energy of the jets is set to 50, 100 or 200 GeV to have the possibility of testing the reconstruction algorithm either for soft jet topologies or harder jet events.

The preliminary step before starting the HLT tracking is to identify the position of the primary vertex of the interesting interaction. Simplified tracks are reconstructed with pairs or triplets of pixel *hits* with p_{T} greater than 2 GeV/c and compatible with coming from a fiducial cylinder around the beam line. These tracks are called `PixelLine`s [86] and could be used also to define the trajectory *seeds*, even if with a lower seeding efficiency. The `PixelLine`s are grouped into clusters according to the longitudinal impact parameter distribution, as, for instance, shown in Fig. 5.10. The harder cluster, being the one with the greater sum of the constituting `PixelLine` p_{T} of Fig. 5.11, defines the longitudinal position z_{PV}^{rec} of the primary vertex. The transverse position of the primary vertex can be set to $x_{PV}^{rec} = y_{PV}^{rec} = 0$ without loss of tracking efficiency, being the spread of the interaction point below the resolution of the pixel detector measurements.

The seeding is performed within pixel detector constraining the *seeds* to have p_{T} greater than 2 GeV/c and maximum impact parameter of 2 cm in the radial direction

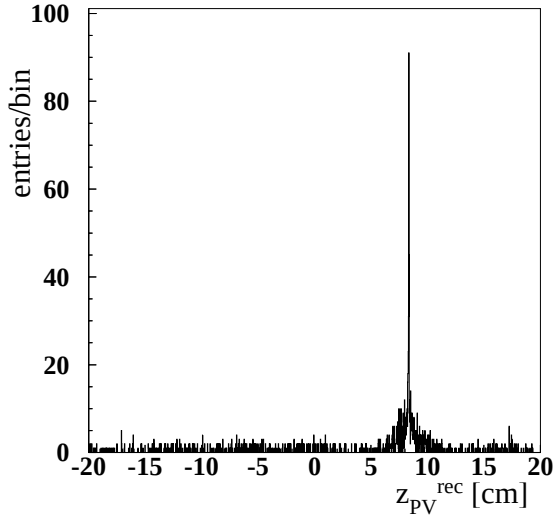

Figure 5.10: *Histogram of the extrapolated z_{PV}^{rec} values of the pixel hit pairs for a $E_{\mathrm{T}}=50$ GeV u$\bar{\mathrm{u}}$ event.*

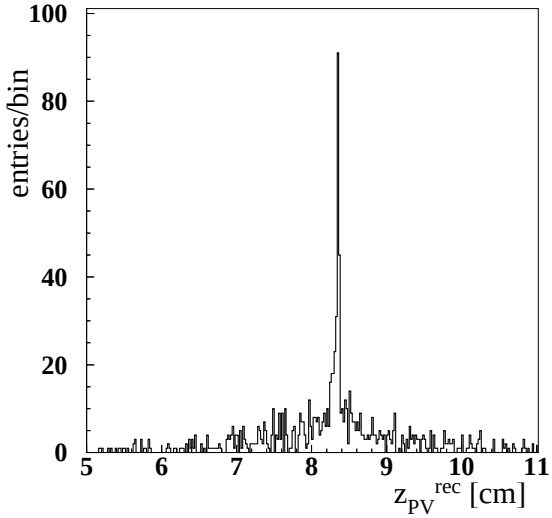

Figure 5.11: *A zoom view centered on the reconstructed primary vertex candidate.*

and 0.5 cm maximum distance from z_{PV}^{rec} along the z axis. Jet directions are reconstructed by calorimeters during Level-1 trigger and a rectangular tracking region in (η, φ) plane is opened around them with $\Delta\eta = \Delta\varphi = 0.2$. All the *seeds* formed with these prescriptions are propagated through the tracker layers and trajectory building is stopped at maximum number of *hits* ranging from four to ten.

The tracking efficiency ϵ is calculated from Eq. 5.13 by selecting the subsamples of `RecTrack`s and `TkSimTrack`s according to the following criteria:

Selection of reconstructed tracks (ϵ) `RecTrack`s with a minimum number of *hits* equal to the stopping condition (from 4 to 10) and being around the triggered Level-1 jets within a *Region of Interest* $\Delta R < 0.2$ (corresponding to the circle inscribed into the square region in (η, φ) plane) form the N_{REC}^{sel} subsample.

Selection of simulated tracks (ϵ) `TkSimTrack`s originated from the interaction vertex and not from pile-up are selected to calculate the tracking efficiency independently from the correct detection of the primary vertex position. No requirement on the number of simulated *hits* are made and cuts on the other track parameters equal to what used for seeding are applied. Moreover, each track has to be

within $\Delta R<0.2$ around one of the Level-1 jets. These simulated tracks compose the subsample N_{SIM}^{sel}.

The fake rate R_{fake} is calculated from Eq. 5.14 with a different selection on both the reconstructed and simulated tracks:

Selection of reconstructed tracks (R_{fake}) `RecTrack`s with a number of *hits* equal to the stopping condition (from 4 to 10) and well reconstructed ($p_{\mathrm{T}}>2.0$ GeV/c and $d_0<0.2$ cm) are selected if inside one of the Level-1 jets within $\Delta R<0.2\sqrt{2}$ (corresponding to the circle circumscribed out from the square-shaped tracking region in (η,φ) plane) are grouped to form the N_{REC}^{sel} subsample for fake rate calculation.

Selection of simulated tracks (R_{fake}) `TkSimTrack`s are selected if belong to one of the triggered jets ($\Delta R<0.2\sqrt{2}$) with no requirement on the number of *hits* and a larger acceptance on d_0 and z_{IP}. The constraint on coming from the interaction vertex must not be applied not to over-estimate the fake rate if the z position of the primary vertex z_{PV}^{rec} is not correctly reconstructed. These simulated tracks make up the subsample N_{SIM}^{sel} for fake rate calculation.

The constraints applied in HLT track reconstruction and the selection criteria for `TkSimTrack`s and `RecTrack`s to define the subsamples for ϵ and R_{fake} calculation, are summarized in Tab. 5.3.

	HLT Tracking	Efficiency Filters		Fake Rate Filters	
		`TkSimTrack`	`RecTrack`	`TkSimTrack`	`RecTrack`
p_{T}[GeV/c]$\geqslant$	*seed*: 2.0 *trajectory*: 0.9	2.0	0.7	0.7	0.9
PV	$(0,0,z_{PV}^{rec})$	$(x_{PV}^{sim},y_{PV}^{sim},z_{PV}^{sim})$	$(0,0,z_{PV}^{rec})$	$(0,0,0)$	$(0,0,z_{PV}^{rec})$
d_0[cm]$\leqslant$	0.2	0.2	120.	300.	0.2
z_{IP}[cm]$\leqslant$	0.5	0.5	170.	300.	30.
RoI	$\Delta\eta<0.2$ $\Delta\varphi<0.2$	$\Delta R<0.2$	$\Delta R<0.2$	$\Delta R<0.2\sqrt{2}$	$\Delta R<0.2\sqrt{2}$
hits$\geqslant$	$n=4,\ldots,10$	0	n	0	n

Table 5.3: *Selection cuts to define the filtered samples of* `TkSimTrack`*s and* `RecTrack`*s to compute HLT track reconstruction global efficiency and fake rate. Tracks are reconstructed around Level-1 jets with regional seeding constraints and trajectory building stopping conditions summarized in the first column.*

The comparison between the global efficiency and the fraction of fake tracks as a function of the number of *hits* along the track is shown in Fig. 5.12 for $E_{\mathrm{T}} = 100$ GeV $\mathrm{b\bar{b}}$ (a), $\mathrm{u\bar{u}}$ (b) and $\mathrm{c\bar{c}}$ (c) jets at low luminosity using full pixel design. The efficiency decreases slightly with the increasing number of *hits*, mainly due to nuclear interactions on the detector, which produce tracks more difficult, or even impossible, to reconstruct. The fake rate is below 1% for tracks with at least seven *hits* in the central region. In the case of staged pixel scenario during the low luminosity data taking, the fake rate increases considerably for the same number of *hits*.

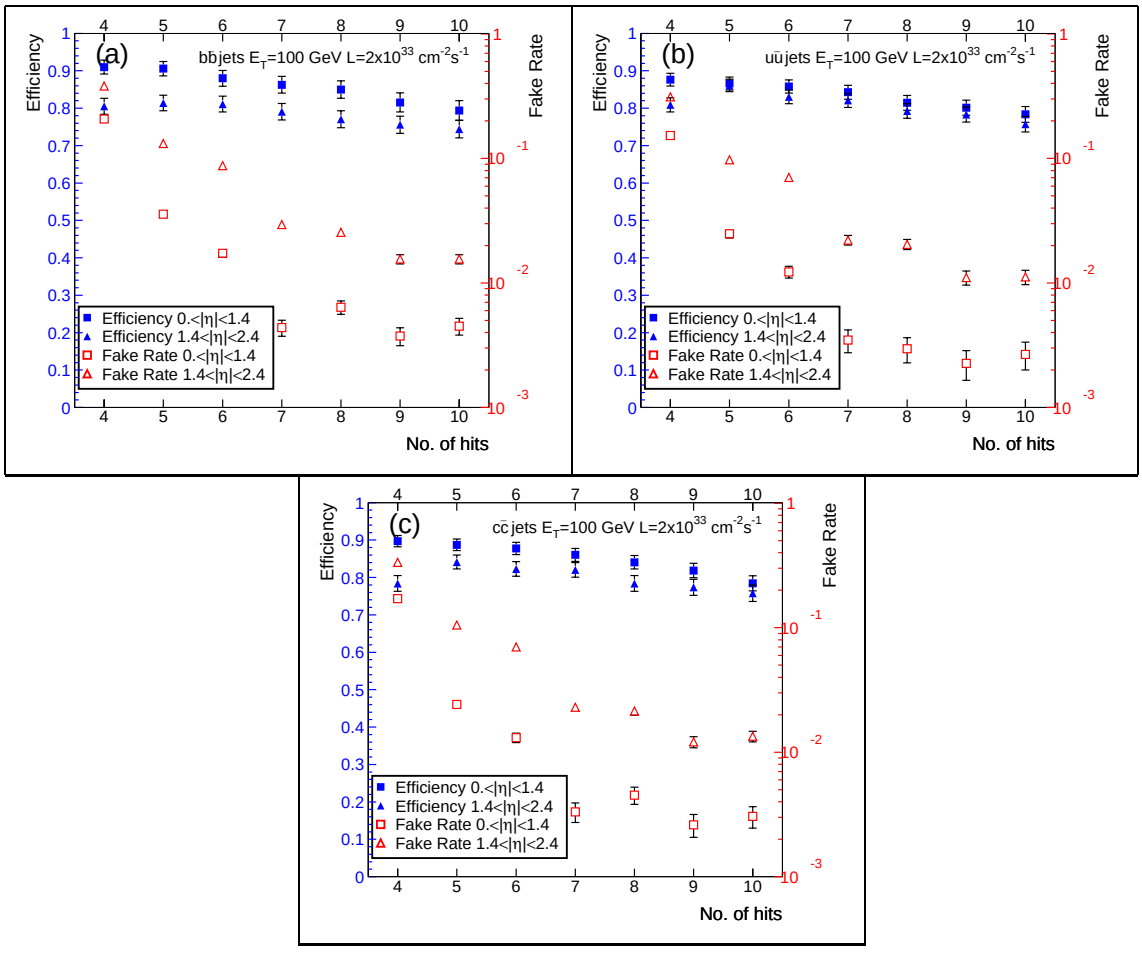

Figure 5.12: *Efficiency (left axis) and fake rate (right axis) for track reconstruction as a function of the number of hits along the track for* $E_{\mathrm{T}} = 100$ GeV $\mathrm{b\bar{b}}$ *(a),* $\mathrm{u\bar{u}}$ *(b) and* $\mathrm{c\bar{c}}$ *(c) jets at low luminosity.*

In Tab. 5.4 the value of efficiency and fake rate are compared for the three different scenarios, low luminosity with and without pixel staging and high luminosity, when the reconstruction is stopped at a maximum of seven *hits*. In general there is a loss in

efficiency in the overlap region between barrel and endcap layers $1.0 < |\eta| < 1.5$, where the track finding is more difficult due to the different geometry of the tracker layers and the larger amount of material budget. In the case of staged pixel scenario and harder jets the track reconstruction efficiency in the forward region is higher than for the central region, on account of the higher value of the fake rate.

5.7 Timing Analysis

The time spent in track finding is the limiting constraint on the operations made during HLT. The work described in the previous paragraph would be useless if we can not demonstrate that the CPU time needed to run the algorithms is affordable.

The fraction of the complete track reconstruction time is spent in the four parts of track finding with these proportions:

- Seed Generation <5%
- Trajectory Building >80%
- Trajectory Cleaning ∼1%
- Trajectory Smoothing <10%

The trajectory building is the most expensive part of track reconstruction, hence if CPU time have to be saved we should concentrate on track propagation optimization.

One of the most time consuming aspect of trajectory building is the splitting of a single trajectory candidate into at most five different candidates to propagate from a layer to the adjacent layers if compatible *hits* are found. If the maximum number of track candidates to propagate is decreased from five to three, the global efficiency of the track reconstruction is not lowered, but at least 20 ms/ev are gained in di-jet events. The CPU time is normalized to the speed of a 1 GHz Pentium III CPU (see Sec. 3.2.6). Figure 5.13 on page 110 shows the time spent in the HLT track algorithm for $b\bar{b}$ jets (left) and $u\bar{u}$ jets (right) with $E_T = 100$ GeV in both the central and the forward regions when no pile-up is added to the main interaction.

The lower part of the time bars (*"Vertex Reconstruction"*) represents the time taken by the vertex reconstruction with `PixelLine`s and is about 40 ms independently from the cut applied on the transverse momentum. The *"Track Reconstruction"* part is the one dominated by the trajectory building and the 20 ms gain when limiting the maximum number of candidates from five to three is estimated by comparing the right bars with the corresponding bars on the left. Moreover, also the contributions to the total time given

7 *hits*		$b\bar{b}$		$u\bar{u}$		$c\bar{c}$	
Low Luminosity (staged)		ϵ	$R_{fake}[\times 10^{-2}]$	ϵ	$R_{fake}[\times 10^{-2}]$	ϵ	$R_{fake}[\times 10^{-2}]$
$E_T = 50$ GeV	central	0.70 ± 0.04	0.4 ± 0.1	0.77 ± 0.02	0.09 ± 0.05	0.70 ± 0.03	0.15 ± 0.06
	forward	0.61 ± 0.04	2.1 ± 0.2	0.70 ± 0.04	0.8 ± 0.2	0.78 ± 0.03	1.2 ± 0.2
$E_T = 100$ GeV	central	0.82 ± 0.03	0.67 ± 0.09	0.68 ± 0.02	0.5 ± 0.1	0.73 ± 0.02	0.32 ± 0.06
	forward	0.73 ± 0.02	3.7 ± 0.2	0.78 ± 0.02	2.7 ± 0.2	0.74 ± 0.02	2.9 ± 0.2
$E_T = 200$ GeV	central	0.73 ± 0.02	1.8 ± 0.1	0.74 ± 0.02	1.3 ± 0.1	0.75 ± 0.02	1.4 ± 0.1
	forward	0.77 ± 0.02	10.9 ± 0.3	0.79 ± 0.02	7.4 ± 0.3	0.80 ± 0.02	8.0 ± 0.3
Low Luminosity		ϵ	$R_{fake}[\times 10^{-2}]$	ϵ	$R_{fake}[\times 10^{-2}]$	ϵ	$R_{fake}[\times 10^{-2}]$
$E_T = 50$ GeV	central	0.79 ± 0.03	0.39 ± 0.08	0.84 ± 0.02	0.07 ± 0.04	0.81 ± 0.02	0.22 ± 0.06
	forward	0.78 ± 0.04	1.8 ± 0.2	0.74 ± 0.04	0.8 ± 0.2	0.84 ± 0.02	1.1 ± 0.1
$E_T = 100$ GeV	central	0.86 ± 0.02	0.44 ± 0.06	0.84 ± 0.02	0.35 ± 0.07	0.86 ± 0.02	0.33 ± 0.06
	forward	0.79 ± 0.02	2.9 ± 0.2	0.82 ± 0.02	2.2 ± 0.2	0.82 ± 0.02	2.3 ± 0.2
$E_T = 200$ GeV	central	0.90 ± 0.01	1.01 ± 0.08	0.89 ± 0.01	0.55 ± 0.08	0.89 ± 0.01	0.74 ± 0.08
	forward	0.82 ± 0.02	7.4 ± 0.2	0.84 ± 0.02	5.5 ± 0.2	0.86 ± 0.01	6.6 ± 0.2
High Luminosity		ϵ	$R_{fake}[\times 10^{-2}]$	ϵ	$R_{fake}[\times 10^{-2}]$	ϵ	$R_{fake}[\times 10^{-2}]$
$E_T = 50$ GeV	central	0.66 ± 0.04	0.45 ± 0.09	0.66 ± 0.03	0.22 ± 0.07	0.58 ± 0.03	0.18 ± 0.06
	forward	0.62 ± 0.04	2.1 ± 0.2	0.64 ± 0.03	1.3 ± 0.2	0.65 ± 0.03	0.16 ± 0.02
$E_T = 100$ GeV	central	0.84 ± 0.02	0.44 ± 0.07	0.74 ± 0.02	0.29 ± 0.06	0.84 ± 0.02	0.47 ± 0.07
	forward	0.75 ± 0.03	3.8 ± 0.2	0.76 ± 0.02	2.6 ± 0.2	0.79 ± 0.02	2.9 ± 0.2
$E_T = 200$ GeV	central	0.79 ± 0.02	1.14 ± 0.09	0.84 ± 0.01	0.74 ± 0.08	0.83 ± 0.02	0.88 ± 0.09
	forward	0.83 ± 0.02	11.0 ± 0.3	0.86 ± 0.01	7.0 ± 0.2	0.81 ± 0.02	8.7 ± 0.3

Table 5.4: *Global efficiency ϵ and fake rate R_{fake} for HLT track reconstruction around Level-1 jets with different energies and pseudorapidity ranges (central: $0 < |\eta| < 1.4$, forward: $1.4 < |\eta| < 2.4$). The track reconstruction is stopped and trajectories smoothed when at maximum 7 hits are added. Quoted errors are statistical.*

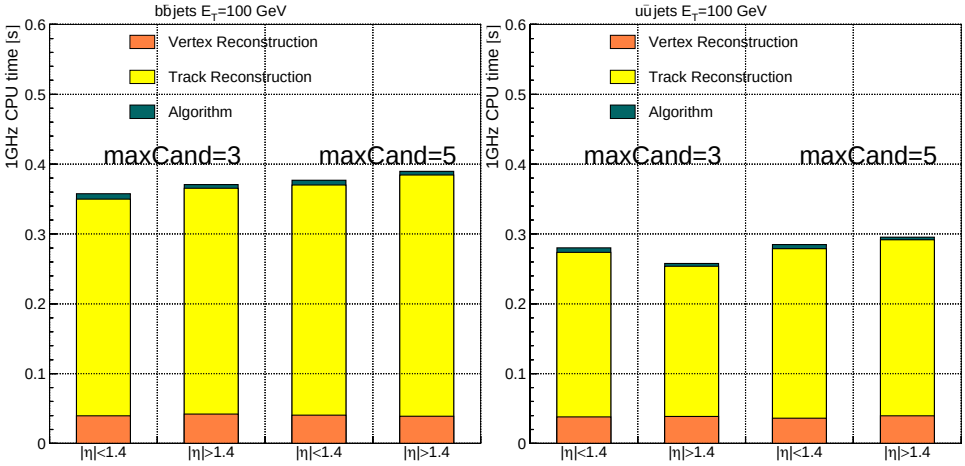

Figure 5.13: *Execution time for 7 hit track reconstruction around* $E_{\mathrm{T}} = 100$ GeV $\mathrm{b\bar{b}}$ *(left) and* $\mathrm{u\bar{u}}$ *(right) di-jet events in the central* ($|\eta| < 1.4$) *and forward* ($|\eta| > 1.4$) *regions. No pile-up is added. The gain in the total time when limiting the maximum number of candidates to propagate (*`maxCand`*) from 5 to 3 is* 20 ms/ev. *The three components shown with different colours are described in the text. Time is normalized to the clock tick of a common 1 GHz* Pentium III *CPU.*

by the b-tagging *"Algorithm"* explained in Ch. 6 is indicated and it is clear that this part takes a negligible fraction of time with respect to the vertex and track reconstruction.

A more important progress in the timing of the trajectory building is related to the optimization of the Kalman Filter algorithm, which has been done once the CMS collaboration realized the feasibility of the HLT tracking. The situation is improved with a more detailed description of the geometry of each specific type of tracker layer (TIB, TOB, TEC, TID and pixel barrel and disks). At the moment this optimization is implemented in ORCA only for the barrel layers of either the pixel and the tracker (TIB and TOB). The new TOB layer description allows to make the trajectory builder three times faster in this region, all other things being equal.

The time for track reconstruction around $\mathrm{b\bar{b}}$ (left) and $\mathrm{u\bar{u}}$ jets (right) in the central region using the default Kalman Filter or the `FastBarrel` propagation is shown in Fig. 5.14. The improvement is about 60 ms/ev with no loss on the track efficiency.

The HLT tracking algorithm is then changed according to these two results; from now on it will be implicit the use of the configuration described above.

The total time is computed for the two sets of $\mathrm{b\bar{b}}$ and $\mathrm{u\bar{u}}$ jets with low luminosity pile-up as a function of the number of *hits* at which track reconstruction is stopped. The time for $\mathrm{b\bar{b}}$ and $\mathrm{u\bar{u}}$ jets is shown in Fig. 5.15.

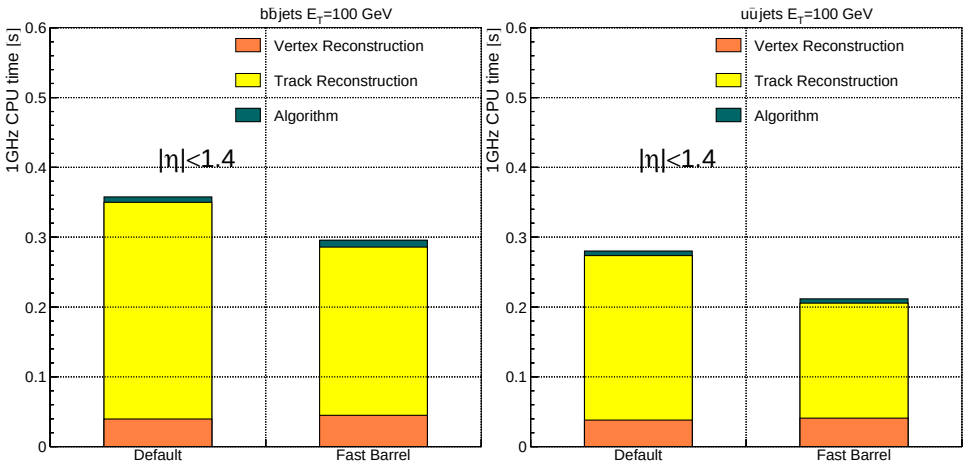

Figure 5.14: *Execution time for 7 hit track reconstruction around* $E_{\mathrm{T}} = 100$ GeV $\mathrm{b\bar{b}}$ *(left) and* $\mathrm{u\bar{u}}$ *(right) di-jet events in the central region* $|\eta| < 1.4$. *No pile-up is added. The gain in the total time using the* `FastBarrel` *Kalman Filter instead of the default algorithm is* 60 ms/ev. *The three components shown with different colours are described in the text. Time is normalized to the clock tick of a common 1 GHz* Pentium III *CPU.*

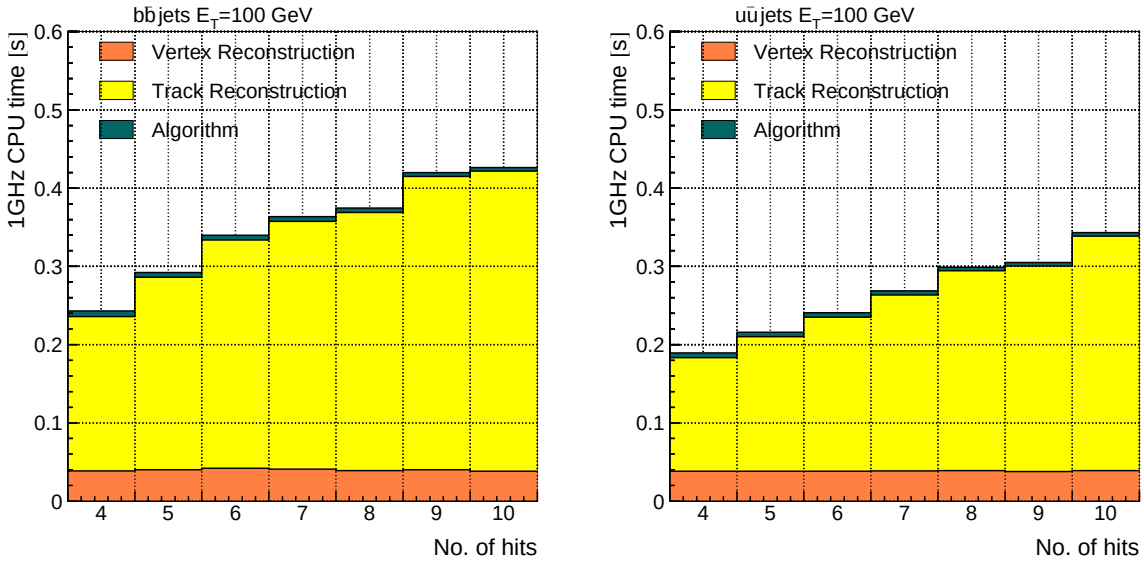

Figure 5.15: *Execution time, at low luminosity, as a function of the number of track hits used for* $E_{\mathrm{T}} = 100$ GeV $\mathrm{b\bar{b}}$ *(left) or* $\mathrm{u\bar{u}}$ *(right) jet events in the region* $|\eta| < 2.4$. *The mean tracking time is greater than the one shown in fig. 5.14, because* `FastBarrel` *Kalman Filter operates only in the region* $|\eta| < 1.4$. *The three components shown with different colours are described in the text. Time is normalized to the clock tick of a common 1 GHz* Pentium III *CPU.*

Most of the time is due to track reconstruction and increases almost linearly with increasing number of *hits*. An average of 30 ms is spent per each added *hit* from five to seven. The time spent in reconstructing tracks around $b\bar{b}$ jets with seven *hits* is 317 ms/ev, whereas it is lower, about 225 ms/ev, for $u\bar{u}$ jets. This difference is due to the mean number of reconstructed tracks per jet, which is 7 for $b\bar{b}$ and 6 for $u\bar{u}$ jets. An average of two more tracks are propagated in $b\bar{b}$ events resulting in an additional tracking time of about 100 ms.

At least seven *hits* have to be considered to reach either a good track parameter resolution (Sec. 5.4) and efficient track finding performance (Sec. 5.6). According to the above results, a safe margin on the 500 ms per event CPU time benchmark exists and track reconstruction can really be stopped when a maximum number of seven *hits* is added to each track.

The HLT track reconstruction with the timing optimization discussed above has been tested also in a more "realistic" situation. An inclusive QCD sample has been simulated requiring the transverse momentum of the parton interaction $\hat{p}_{\mathrm{T}}$ to range between 50 GeV/c and 170 GeV/c. A total of about 150 000 events were analysed. The reconstruction is stopped at seven *hits* around $\Delta R < 0.4$ Level-1 jet cones with the apex centered in the primary vertex reconstructed with `PixelLine`s. The center of the time distribution together with the spread is shown in Fig. 5.16 as a function of the measured jet transverse energy when only one jet (a,c) or two jets (b,d) are within the tracker acceptance in low luminosity conditions, at full design (a,b) or with staged pixel detector (c,d). The execution time per jet is independent from the jet transverse energy, if it is less than 100 GeV, and it is however less than 200 ms. This result is very important, because it demonstrates that a b-trigger algorithm to select events with a couple of b-tagged central jets should run at HLT. The reconstruction time does not change in passing from full pixel detector to staged pixel scenario. Events with more than one jet within the tracker acceptance are produced by the harder interactions with higher track multiplicity. For this reason the tracking time per jet, when two central jets are present, is nearly twice the time to perform HLT track reconstruction in events with only one central jet.

For the same jet transverse energy and pseudorapidity region, the number of *seeds* to be considered increases from 7 to 44 on average in going from low to high luminosity, causing the growth of the reconstruction time by a factor four. The execution time shown in Fig. 5.17 on page 114 (a,b) does not depend on jet energy, but the time spent per jet is nearly 1 s when using the `CombinatorialSeedGeneratorFromPixel`. Therefore an alternative option should be looked for, for example `PixelLine`s can be

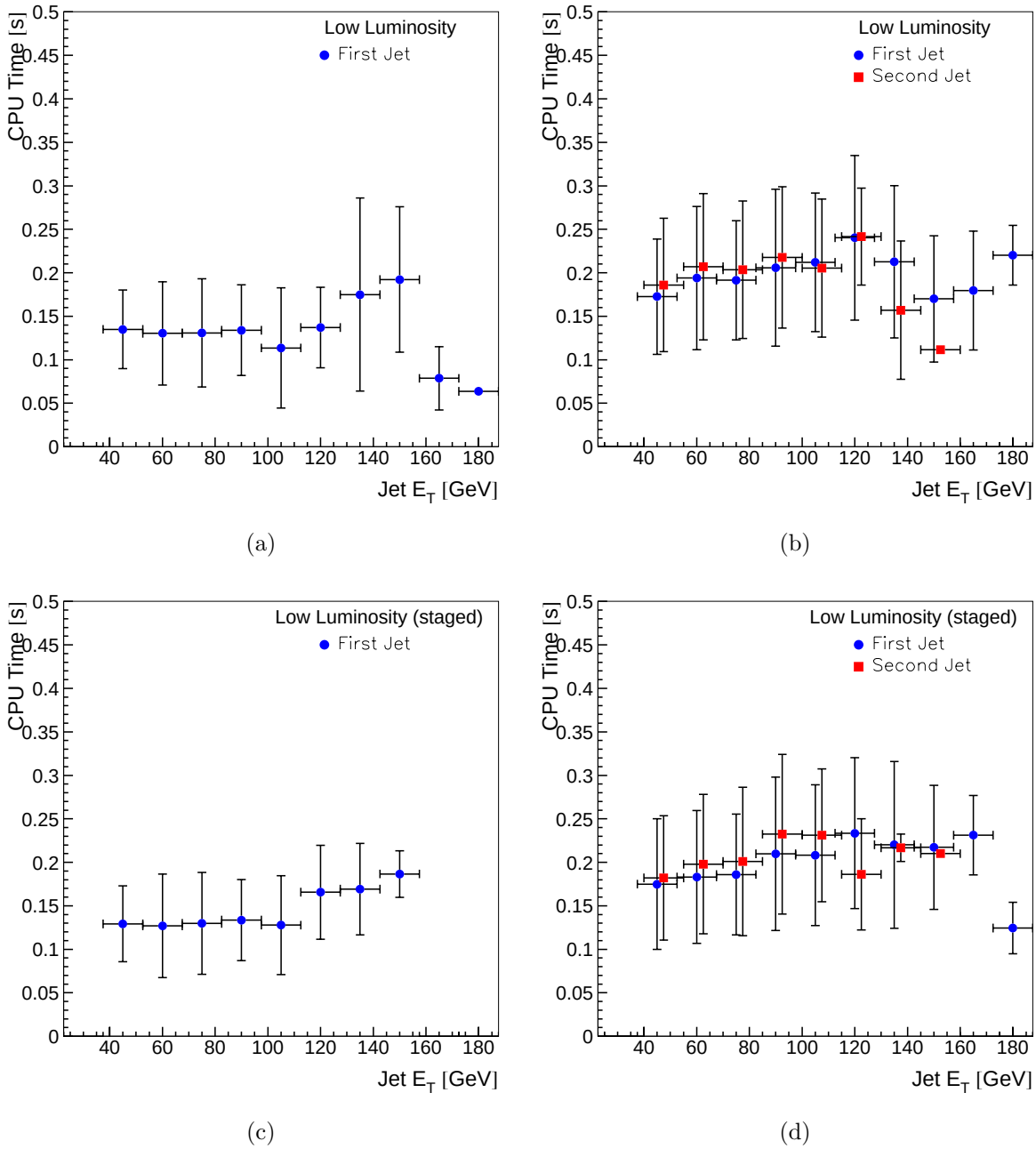

Figure 5.16: *Execution time at low luminosity with full pixel detector (a,b) or staged pixel scenario (c,d) for the HLT track finding for different jet transverse energies. The left plots (a,c) refer to events with only one jet within tracker acceptance, while right plots (b,d) show the timing for the leading (*First Jet*) and next-to-leading (*Second Jet*) jet in events where two jets are within the tracker acceptance. The error bars represent the spread in the time distributions. Time is normalized to the clock tick of a common 1 GHz* Pentium III *CPU.*

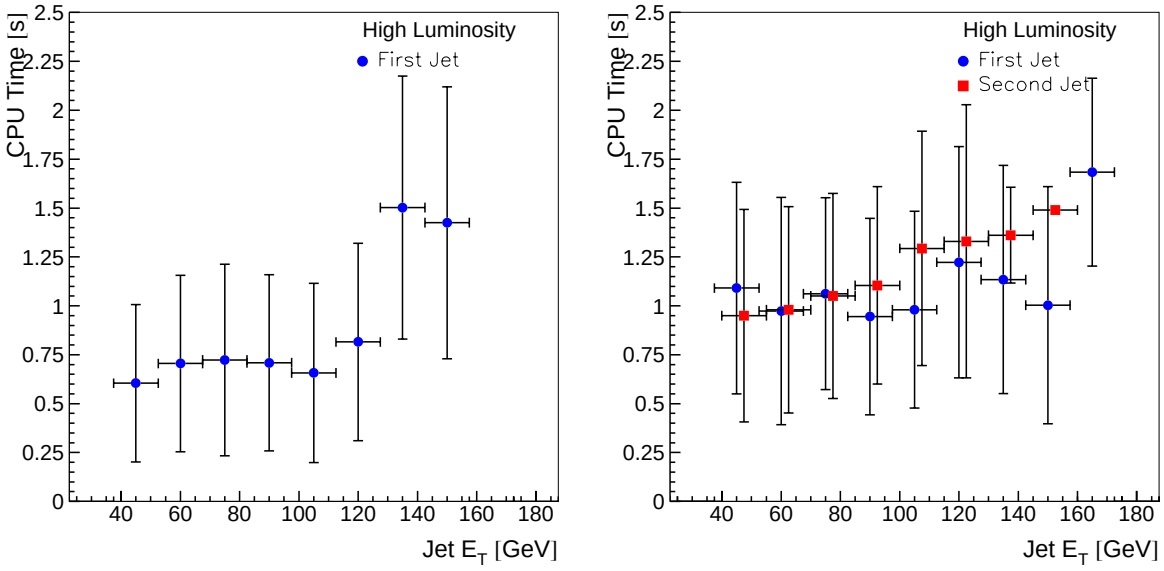

(a)

(b)

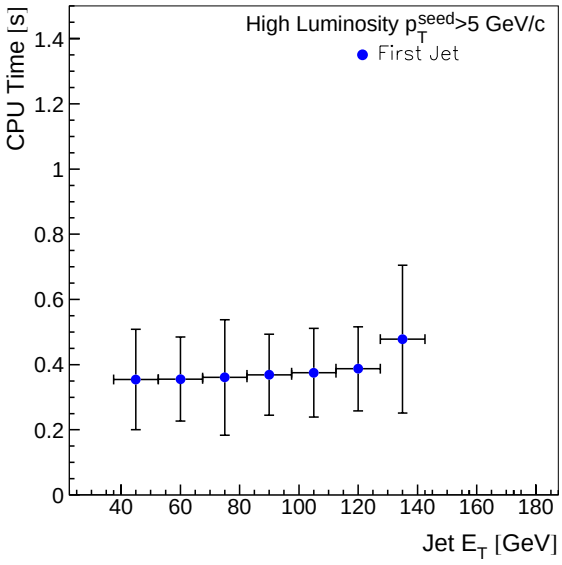

(c)

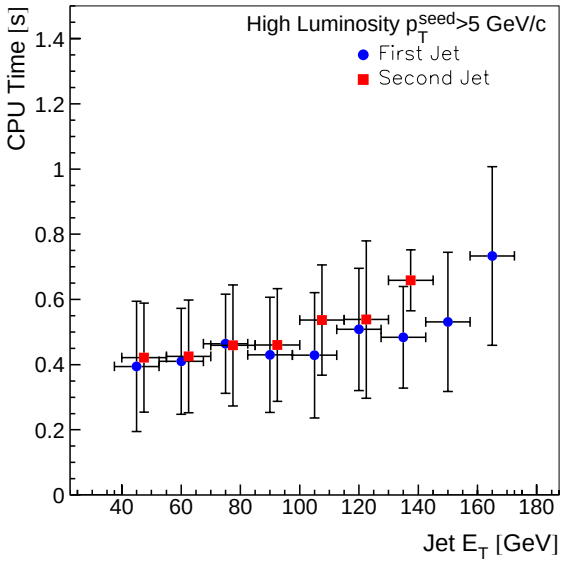

(d)

Figure 5.17: *Execution time at high luminosity for the HLT track finding (a,b) and when the regional seeding is replaced by seeding from* $p_T > 5$ GeV/c `PixelLines` *within jet cones (c,d) for different jet transverse energies. The left plots (a,c) refer to events with only one jet within tracker acceptance, while right plots (b,d) show the timing for the leading (*First Jet*) and next-to-leading (*Second Jet*) jet in events where two jets are within the tracker acceptance. The error bars represent the spread in the time distributions. Time is normalized to the clock tick of a common 1 GHz* Pentium III *CPU.*

used to define both the trajectory *seeds* constructing only the ones with $p_T > 5$ GeV/c for vertexing and selecting only the ones around the Level-1 jet axis for seeding. In this case the time is reduced by a factor two with respect to the combinatorial regional seeding, as demonstrated by comparing Fig. 5.17a with c and 5.17b with d. Using this simple seeding mechanism we are confident that this algorithm can be used also at high luminosity. The higher threshold on *seed* p_T contributes also to lower the number of trajectory candidates to propagate. Only the stiffer tracks from the harder interaction are reconstructed, hence the reconstruction time per jet is independent from the number of central jets in the event (Fig. 5.17c and d).

The vertex is reconstructed in 80% of the events within 100 µm from the simulated position z_{PV}^{sim}, as shown in Fig. 5.18. The drop in efficiency at lower `PixelLine` p_T threshold is due to the incorrect vertexing, which occurs when the vertex of one of the Minimum Bias pile-up interactions is reconstructed. Tracks from Minimum Bias events are softer than the ones from the primary interaction, hence when the *seed* p_T threshold is above 3 GeV/c, the asymptotic value for the efficiency is reached and more than 95% of the times the primary vertex longitudinal coordinate is individuated less than 300 µm away from the simulated position.

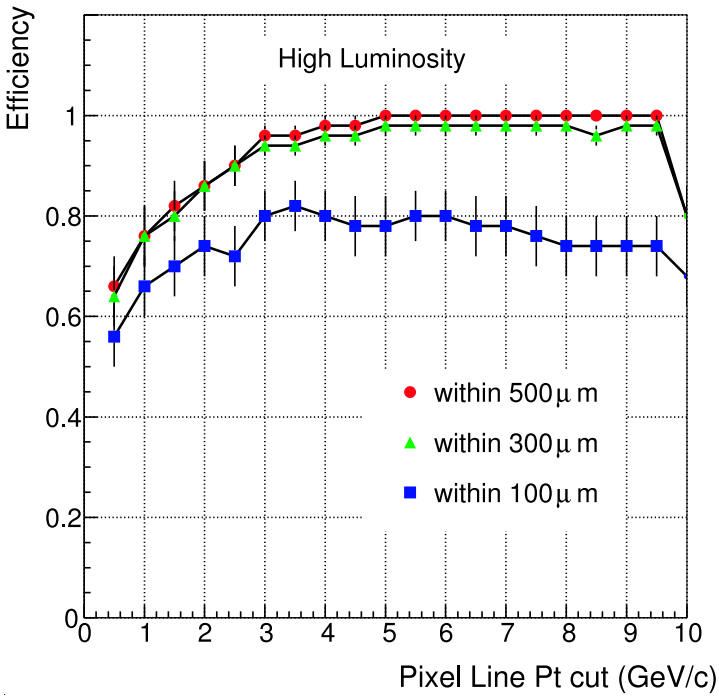

Figure 5.18: *Efficiency of the pixel algorithm to correctly determine the primary vertex position of the event along the beam axis within* 100, 300 *and* 500 µm, *at high luminosity, as a function of the minimum* p_T *cut on the* `PixelLines`.

In this chapter we have demonstrated that the CMS tracker data can be used at HLT providing we perform a fast and partial regional tracking around Level-1 jets. In this way a High-Level trigger algorithm to select b quark physics can be built with including a fast b-tag technique as explained in the next chapter. This result is very important, because before this study the CMS tracker was not thought to be efficiently used at High-Level trigger stage.

Chapter 6

The b-tagging

Many interesting physics channels contain b-jets in the final state, which are hidden by the most copious production of light flavoured background jets. Several methods for identification of hadron jets produced from b quark fragmentation have been developed and are collected under the generic name of b-tagging. In the past experiments inclusive b-tagging played an important rôle in the measurement of the branching ratio of the decay $Z \rightarrow b\bar{b}$ [87] or in the discovery of top quark through $t \rightarrow bW$ decay at TeVatron [17]. The Higgs boson via $H \rightarrow b\bar{b}$ decay and the supersymmetric particle decays [88] are searched for following similar approaches.

The algorithms used for b-tagging rely on the large value of beauty hadron lifetime ($c\tau \simeq 450$ μm), which allows to extract some information to recognize a b-jet. Lifetime information can be extracted following different methods. Some of them are based on the track impact parameters, because, according to Fig. 6.1, tracks coming from b hadron decays are originated from a well detectable secondary vertex (*decay point*) and therefore have a large impact parameter with respect to the nominal primary interaction point. Tracks coming from the primary vertex (jet origin) have impact parameters compatible with zero within the tracking resolution.

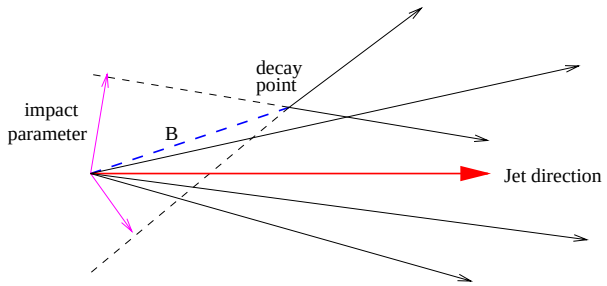

Figure 6.1: *Representation of a hadron jet from a* b *quark (not to scale) [89].*

Complementary methods are based on the capability of detector to individuate secondary vertices, which would be the clearest evidence of a long-lived hadron decay. Both methods need a powerful microvertex detector and are limited either by the efficiency of vertex and track reconstruction or by the experimental resolution on the track parameters. Some different approaches exist, as the lepton tag from $b \to c\ell\nu_\ell$ and $c \to (d, s)\ell\nu_\ell$ decays or as the invariant mass tag, which relies on the reconstruction of the b hadron mass. It is obvious to notice that the best performance in b-tagging is reached combining different methods, since a larger number of information on b hadron decays is used.

The tagging algorithms, which will run at the HLT stage, should be robust and fast with a limited number of operations. The chosen tag relies upon the track impact parameter, because it is a simple algorithm since it is based on the selection of good quality tracks around the jet direction already available after HLT tracking.

This chapter is dedicated to the description of the b-tag based on the track impact parameter counting method and the study of the performance, which should be achieved during the HLT. The application of the High-Level trigger algorithm for b-jet identification to a simulated sample of QCD jets demonstrates the feasibility and the power of the developed method in selecting b physics events and discarding the most abundant jet background.

6.1 Track Impact Parameter

The track impact parameter, distance of closest approach to a nominal primary vertex point, can be calculated either in the transverse plane (*two-dimensional impact parameter*) or in three dimensions (*three-dimensional impact parameter*). In both cases the measurement heavily relies on the precision of the innermost pixel *hits*.

Two-dimensional Impact Parameter

The two-dimensional impact parameter is estimated by an analytical calculation, because in the transverse view the trajectory projection is a circumference. It is the distance of closest approach d_0 between the trajectory and the primary vertex position in the transverse plane, as defined in Sec. 5.2.1. The primary vertex transverse coordinates are measured with the pixel detector.

Three-dimensional Impact Parameter

The three-dimensional impact parameter allows to extract a larger set of information on b hadron production, but the error is spoiled by the precision on the measured longitudinal coordinate of the primary vertex z_{PV}^{rec}. The determination of the value of the three-dimensional impact parameter is performed in steps, which can be summarized referring to Fig. 6.2 [89] as:

1. The point S of closest approach of the trajectory to the jet direction, the *minimum distance* $\overline{SQ}$, is extracted: this point approximates the decay point of the b hadron.

2. The track is linearised near the point S and the distance from the primary vertex V is computed: the distance defines the value of the three-dimensional impact parameter (*i.p.*).

3. The distance $\overline{VQ}$ approximates the flight path of the b hadron and is referred to as *decay length*.

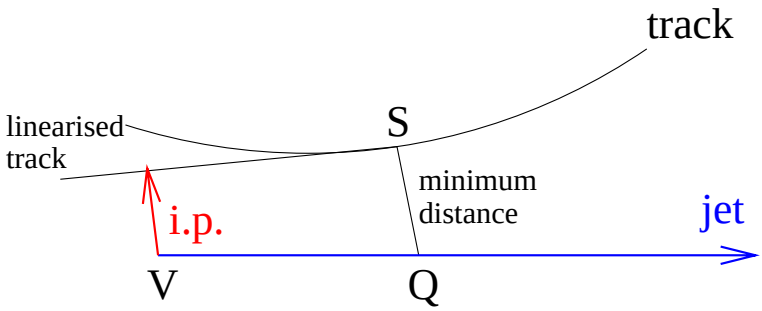

Figure 6.2: *Representation of the definition of the track three-dimensional impact parameter i.p. (not to scale) [89].*

Sign of the Impact Parameter

A sign is assigned to the value of the impact parameter. Referring to Fig. 6.2, the *i.p.* sign is defined to be positive if the point Q is upstream of V in the jet direction and negative otherwise, or equivalently the scalar product of the *i.p.* vector and the jet direction vector is positive (or negative). A similar definition is made to the assignment of the two-dimensional impact parameter sign. Tracks from b decay secondary vertices should have positive large values of the impact parameter, whereas tracks from the primary vertex should have values comparable to the experimental resolution and equally distributed between negative and positive values.

The tagger method makes use of the track impact parameter significance, which is defined as the ratio between the impact parameter value IP and its estimated error σ_{IP}

$$S_{IP} = \frac{IP}{\sigma_{IP}} \tag{6.1}$$

to take into account the experimental resolution, which influences the measurement of IP. In the b-tag track counting method a jet is defined to be tagged as a b-jet if there exists a minimum number of tracks exceeding a given threshold on S_{IP}. In fact, the distribution of the two-dimensional impact parameter significance of Fig. 6.3 is different for tracks coming from b or light-flavoured jets. The b-jet track significance is asymmetrically distributed with a long tail on the large positive values of S_{IP}, which is a hint of lifetime. The u-jet distribution is symmetric and should follow a gaussian function centered in zero with unitary standard deviation, because the value of the impact parameter is compatible with zero within the error. The broader gaussian component is due to pattern recognition mistakes and large angle multiple scattering effects.

A similar behaviour is present in the three-dimensional impact parameter significance distribution of Fig. 6.4 with the long tail of positive values for b-jets . In this case both distributions show a hole around zero due to the three-dimensional phase space [90].

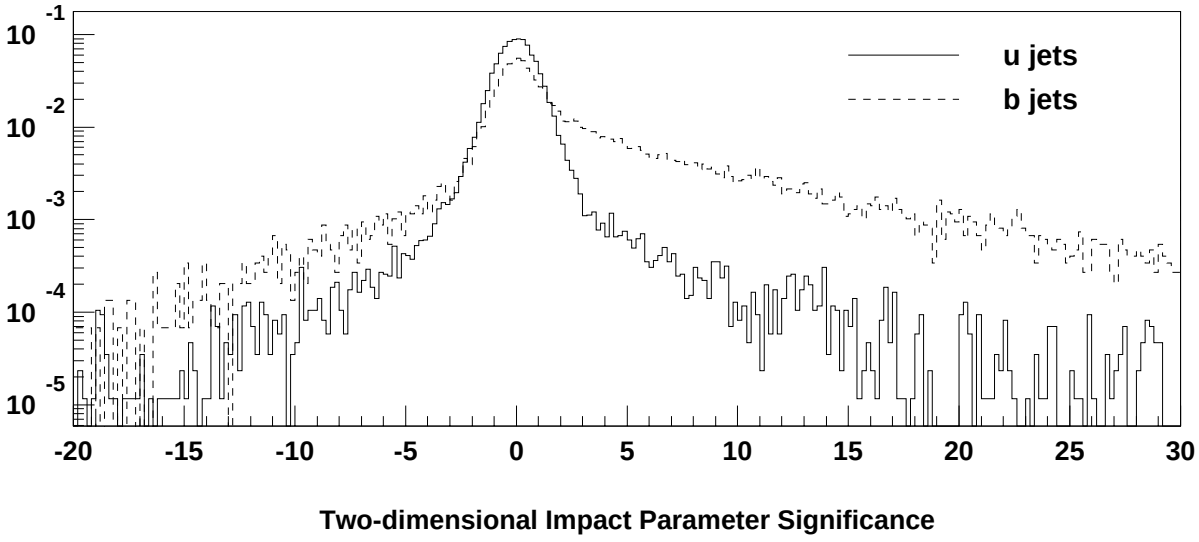

Figure 6.3: *Two-dimensional impact parameter significance distributions for* $E_{\mathrm{T}} = 100$ GeV *and* $|\eta| < 0.7$ $\mathrm{b\bar{b}}$ *(dashed line) and* $\mathrm{u\bar{u}}$ *jets (solid line) [89]. Units on the vertical axis are arbitrary.*

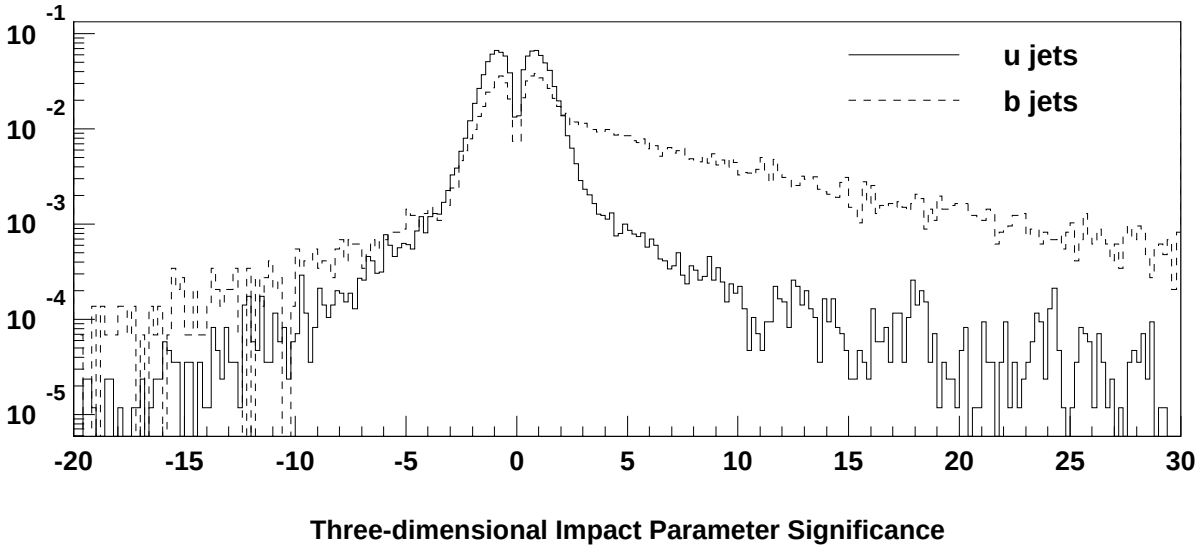

Figure 6.4: *Three-dimensional impact parameter significance distributions for* $E_{\mathrm{T}} = 100$ GeV *and* $|\eta| < 0.7$ $\mathrm{b\bar{b}}$ *(dashed line) and* $\mathrm{u\bar{u}}$ *jets (solid line) [89]. Units on the vertical axis are arbitrary.*

6.2 Refinement of jet direction using tracks

The performance of the tagger depends crucially on the track quality and on the measurement of the jet direction. The effect due to badly reconstructed jet direction or primary vertex can affect the precision on the measurement of the track parameters, causing the sign flip of the impact parameter. In Fig. 6.5 it is sketched how the measurement of the true b-jet direction B resulting in the wrong reconstructed *Jet Axis* is responsible of the incorrect assignment of the impact parameter sign, from positive to negative, for the tracks whose directions are within the shaded area. The jet axis resolution is worst for jets too close-by or very large rapidity b-jets, but also a badly reconstructed primary vertex contributes to the sign flip for short-lived or low momentum b hadrons. This effect shows up in the left tails of Fig. 6.3 and 6.4, where the b-jet component is larger than the u-jet one because a fraction of large and positive track impact parameters are sign flipped.

The HLT track finder algorithm reconstructs tracks around Level-1 jets, whose resolution both in η and φ is greater than 0.1, hence very poor. This is due to the coarse granularity of the calorimetric trigger cells and unfortunately deteriorates the b-tagging performance using the track counting method alone. A way to improve the resolution in η and φ for the jets is to wait for HLT jet reconstruction, which produce more accurate measurements of direction and energy of the jets, referred to as Level-2 jets. The Level-2

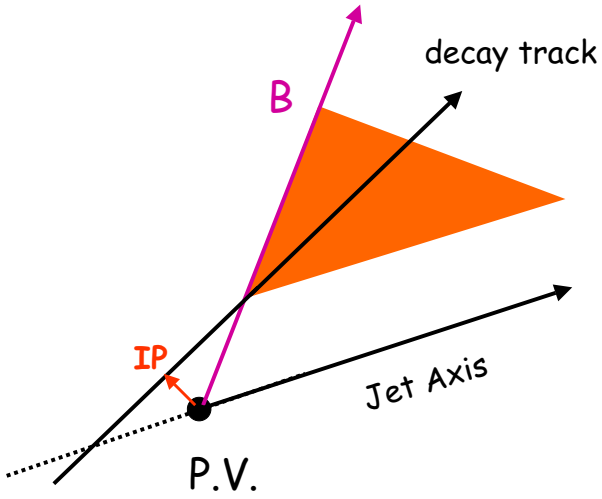

Figure 6.5: *Sign flip of track impact parameter IP. If the true jet direction B is badly reconstructed into Jet Axis, the definition of the sign of the impact parameter for tracks inside the shaded area turn to be negative instead of positive.*

jet reconstruction takes a time of about 40 ms per jet; this means that almost 10% of the time allocated for the b-trigger algorithm should be dedicated to reconstruct jets before track finding. A valid alternative to the Level-2 jet reconstruction is to use the already reconstructed tracks around the Level-1 jets to refine the jet direction measurements (L1Tk jets).

Figure 6.6 shows the resolution of the refined value of jet direction (η and φ) as a function of the jet cone size ΔR used to select reconstructed tracks within. In the upper plot the jet η and φ are simply defined as the mean value of the η and φ of the selected tracks within the chosen ΔR. Both resolution values reach a minimum around $\Delta R = 0.4$ and then start to grow with increasing jet cone size. This effect is due to the lower p_{T} tracks, which are coming mainly from the primary vertex and are added to the jet if a wider region around the jet axis is considered. To avoid this effect, the jet η and φ can be calculated by weighting with the track p_{T} to define the L1Tk jets:

$$\begin{cases} \eta_{new} = \sum_i \eta^i p_{\mathrm{T}}^i / \sum_i p_{\mathrm{T}}^i \\ \varphi_{new} = \sum_i \varphi^i p_{\mathrm{T}}^i / \sum_i p_{\mathrm{T}}^i \\ \Delta R_i < \Delta R \end{cases} \tag{6.2}$$

and in this case once the plateau is reached the resolution does not change with increasing ΔR, as demonstrated by the lower plot of Fig. 6.6. This method fails if two jets are too close to each other.

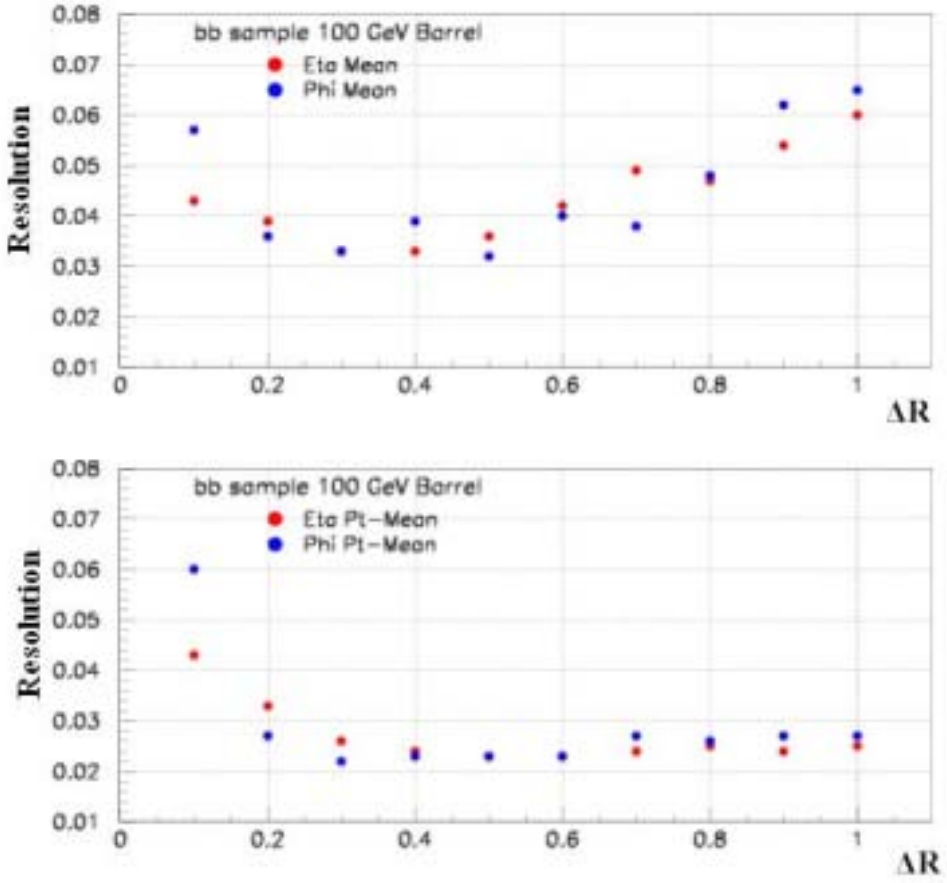

Figure 6.6: *Resolution on the measurement of refined jet direction (η and φ) using the tracks within jet cones as a function of the cone size ΔR. In the upper plot a simple mean on the η and φ of the tracks is performed, while in the lower plot the mean is weighted on track transverse momentum p_{T}.*

The new direction of the Level-1 jet calculated with tracks is more accurate than Level-2 calorimetric measurement and the jet refinement algorithm is absolutely faster than Level-2 calorimetric reconstruction, because it takes less than 3 ms per jet once tracks have been reconstructed. The jet η and φ resolutions are shown in Fig. 6.7 after calorimetric Level-1 and Level-2 and after jet direction refinement using the tracks reconstructed by HLT track finder (L1Tk jets).

6.3 The track counting method

The track counting method is based on the requirement of a minimum number of tracks with impact parameter significance S_{IP} exceeding some threshold [44]. An average of

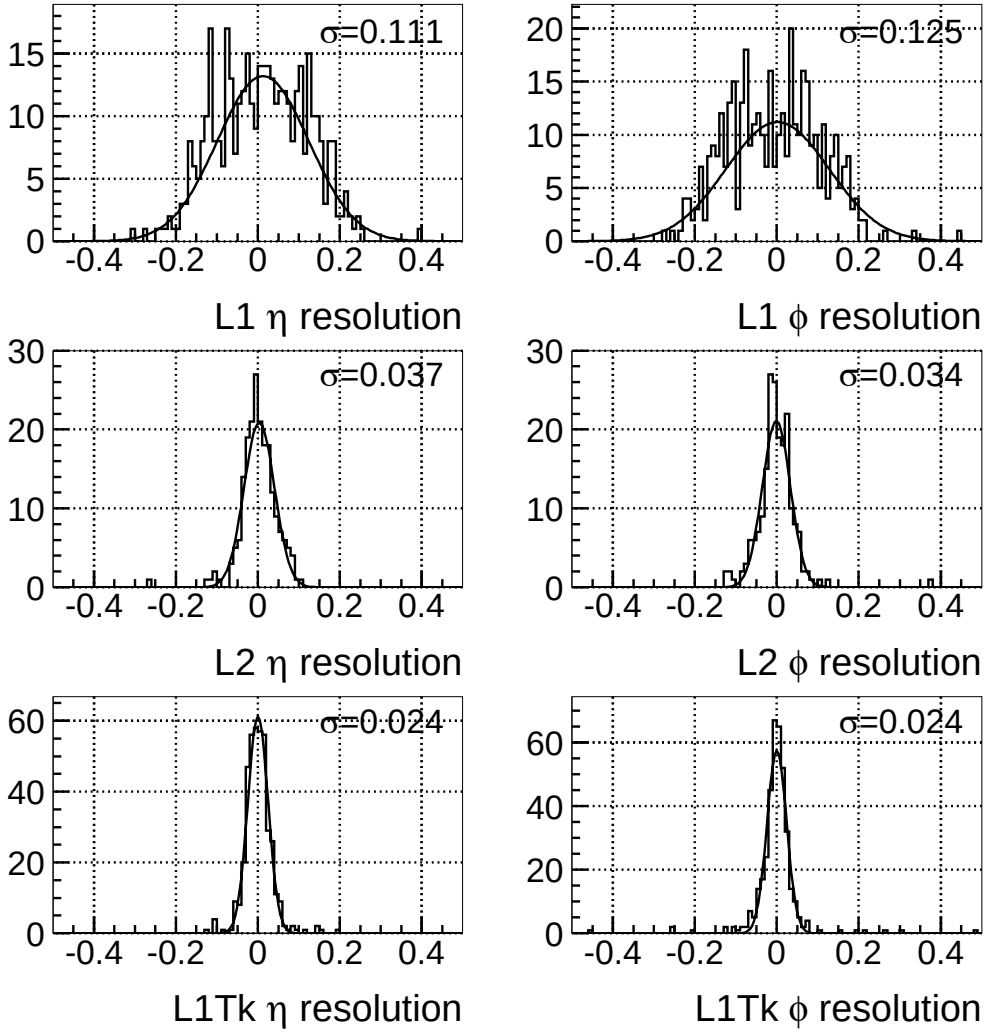

Figure 6.7: *Jet angular resolution with respect to the generator information using Level-1 calorimetric jet reconstruction (L1), High-Level trigger calorimetric jet reconstruction (L2) and by adding tracking information to refine Level-1 jet measurement (L1Tk).*

five particles per b hadron decay chain are expected, hence, depending on the topology of the process under study, a fine tuning of the number of tracks and of the choice of the appropriate S_{IP} threshold is necessary.

The performance of the tagger is given in terms of the b-tag efficiency ϵ_b and mistagging rate ϵ_u. Both variables are related to the single jet: ϵ_b is defined as the fraction of jets tagged as "b" in $b\bar{b}$ jet samples, while ϵ_u is the fraction of $u\bar{u}$ jets wrongly tagged as "b". Each point on the (ϵ_u, ϵ_b) plane is the result of a different set of cut parameters,

namely the minimum number of tracks n_{tracks} and the threshold on the lower value of the impact parameter significance S_{IP}^{min}. The most performant algorithm is the one with the higher ϵ_b at fixed ϵ_u, which is chosen to be 10% in HLT studies.

The results of the b-tag selection are shown both for online and offline algorithms. In the former case, jet reconstruction is performed by combining Level-1 calorimetric information with partial reconstructed tracks to define the L1Tk jets; in the latter case it is assumed an almost ideal evaluation of the jet direction achieved by the most sophisticated and time consuming offline algorithms. In the last case, jets are defined by the PYTHIA routine PYCELL [69] at generator level. In this way the degradation of the performance due to calorimeters is decoupled from the one due to the tracker [91].

For the offline performance studies tracks are reconstructed in the whole tracker layers around jets, while for the online the HLT track reconstruction is used. The primary vertex longitudinal position z_{PV} is reconstructed with `PixelLine`s with a p_{T} cut of 1 GeV/c (5 GeV/c) and the regional seeding around jet directions is performed with a minimum p_{T} value of 1 GeV/c (2 GeV/c) for the *seeds* at low (high) luminosity [51]. A jet is tagged if it has two tracks within $\Delta R < 0.4$ jet cone with S_{IP} greater than a variable threshold ranging from 0.5 to 5.0 in steps of 0.5 units. A set of points in the (ϵ_u, ϵ_b) plane is thus collected. Tracks are required to have at least 3 (2) pixel *hits* for the full (staged) pixel detector configuration.

The mistagging rate ϵ_u is raised by secondary interactions within the tracker material, which can produce secondary vertices, thus tracks with large impact parameters. In addition, $\mathrm{K}_{\mathrm{s}}^0$, Λ^0 or c hadrons can provide real decay vertices and constitute a physical irreducible background. To reduce the effects of these processes, a cut on the maximum impact parameter of 2 mm is applied [91].

The performance of the b-tag algorithm for $E_{\mathrm{T}} = 100$ GeV di-jet events in two different $|\eta|$ regions, central and forward, is reported in Fig. 6.8 (6.9) for low (high) luminosity using the two-dimensional impact parameter. The first thing to notice is that fixing the luminosity there is no degradation between the online b-tag with respect to full reconstruction followed by offline b-tag. The online selection does not result in a reduced performance and represent the best that can be done by using the track counting method alone. If the low luminosity plot of Fig. 6.8 is compared with the corresponding one obtained at high luminosity of Fig. 6.9, the different performance is explained by two concurring causes: the different cut on track *seed* transverse momentum and the increased pixel inefficiency at high luminosity [92].

The b-tag efficiency ϵ_b for a fixed mistagging rate $\epsilon_u = 0.10$ is reported in Tab. 6.1 both for low and high luminosity. If during the low luminosity period the configuration

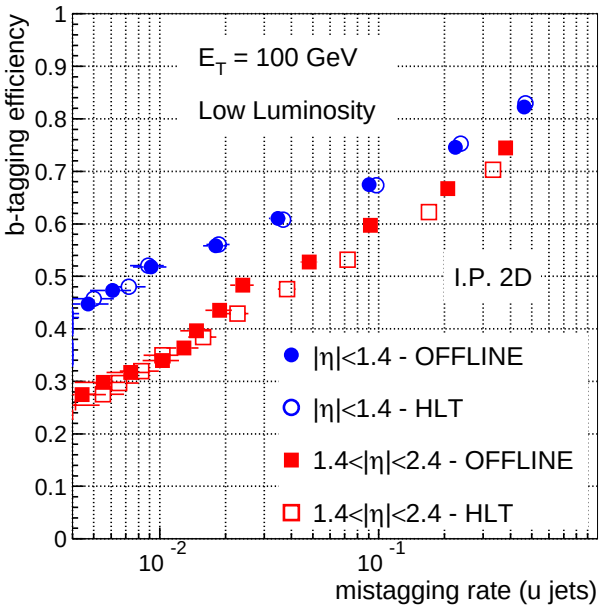

Figure 6.8: *Comparison between offline and High-Level trigger* b*-tag efficiency versus mistagging rate for jets with* $E_{\mathrm{T}} = 100$ GeV *in the low luminosity scenario using the track two-dimensional impact parameter counting* b*-tag.*

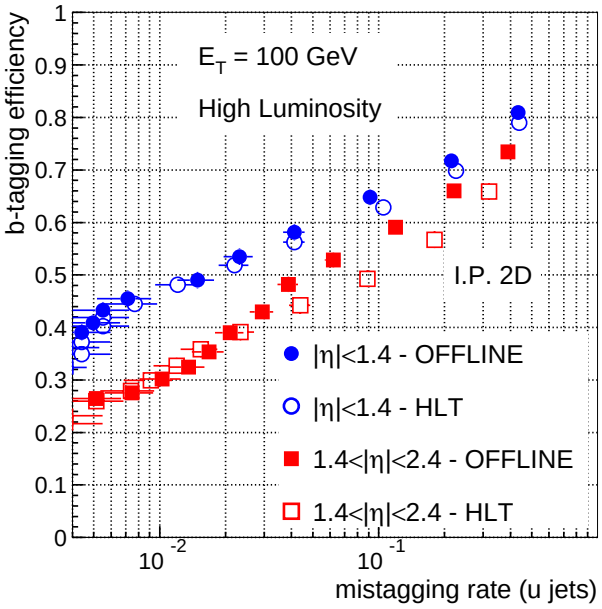

Figure 6.9: *Comparison between offline and High-Level trigger* b*-tag efficiency versus mistagging rate for jets with* $E_{\mathrm{T}} = 100$ GeV *in the high luminosity scenario using the track two-dimensional impact parameter counting* b*-tag.*

of the pixel detector is staged, a loss of ϵ_b ranging from 5% to 10% results at fixed values of ϵ_u both for online and offline methods. The comparison between the staged and the no-staged scenarios for HLT is shown in Fig. 6.10; as already stated, the microvertex detector plays a fundamental rôle in b-tagging.

$\epsilon_u = 0.10$	Central $\lvert\eta\rvert < 1.4$		Forward $1.4 < \lvert\eta\rvert < 2.4$	
ϵ_b	HLT	OFFLINE	HLT	OFFLINE
Low Luminosity	0.67	0.67	0.56	0.59
High Luminosity	0.63	0.65	0.51	0.56

Table 6.1: *Efficiency of* b*-jet tag* ϵ_b *for fixed mistagging rate* $\epsilon_u = 0.10$.

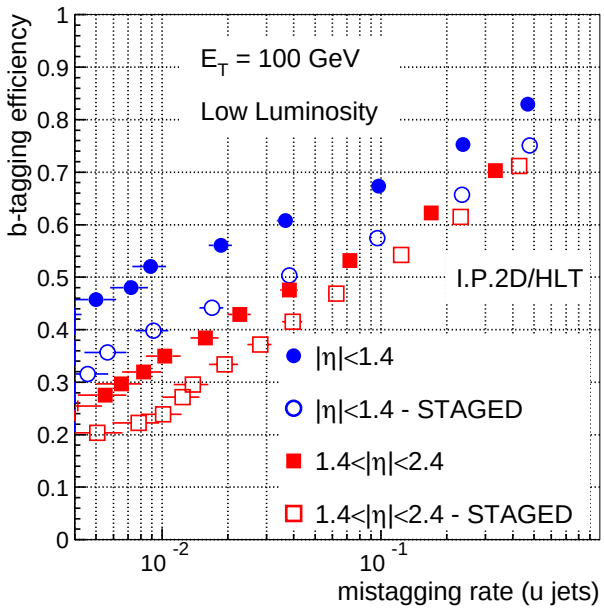

Figure 6.10: *Comparison of* b*-tag performance between staged and full pixel detector configurations, at low luminosity, for the High-Level trigger algorithm, using the track two-dimensional impact parameter counting* b*-tag.*

In Fig. 6.11 the b-tag performance for different jet E_{T} is reported. The better performance of $E_{\mathrm{T}} = 100$ GeV jets is due to the reduced multiple scattering component of the error σ_{IP} on the extrapolation of the impact parameter. The multiple scattering is the main limiting factor on the performance of $E_{\mathrm{T}} = 50$ GeV jets. On the other hand, the $E_{\mathrm{T}} = 200$ GeV jets have a higher value of ϵ_u because of increased primary track multiplicity.

A better performance can be reached if instead of the two-dimensional impact parameter the three-dimensional is used; a gain of 10% in ϵ_b, as it is shown in Fig. 6.12, is obtained. The CPU time does not change, hence in the next development of the analysis the three-dimensional impact parameter b-tag will be used.

6.4 QCD jet rate

The HLT algorithm for b-trigger has been extensively tested in reconstructing and reducing the rate of inclusive QCD jet events, which are expected to be the major background component in selecting H→b$\bar{\text{b}}$ decays. This test is very important since it would validate the use of the CMS tracker in the HLT and the possibility to select interesting b-physics events. The sample used for this study consists of Minimum Bias events with jets in three different ranges of the parton interaction transverse momentum to cover the $\hat{p}_{\mathrm{T}}$ region between 50 and 170 GeV/c. A total of about 50 000 events have been analysed per each $\hat{p}_{\mathrm{T}}$ bin, whose corresponding cross sections [93] are summarized in Tab. 6.2. Regional seeding and partial reconstruction of tracks around triggered Level-1 jets is performed together with the b-tag track counting algorithm with two-dimensional impact parameter [94], which takes a negligible time, less than 10 ms per event, in carrying out its task.

Monte Carlo sample		Cross Section [mb]
Minimum Bias + Jets	$50<\hat{p}_{\mathrm{T}}$[GeV/c]<80	2.4×10^{-2}
Minimum Bias + Jets	$80<\hat{p}_{\mathrm{T}}$[GeV/c]<120	3.4×10^{-3}
Minimum Bias + Jets	$120<\hat{p}_{\mathrm{T}}$[GeV/c]<170	5.7×10^{-4}

Table 6.2: *Cross sections [93] and kinematic cuts applied at generator level of the inclusive QCD jet simulated samples.*

The impact of the b-tag algorithm on the inclusive jet rate after Level-1 trigger has been investigated by studying the reduction of the QCD background when requiring the presence of one or two tagged jets within the tracker acceptance $|\eta|<2.4$. A jet is tagged as a b-jet if it contains within the $\Delta R<0.4$ jet cone at least two reconstructed tracks with two-dimensional impact parameter significance greater than 2.

The Level-1 trigger rate obtained when one to four jets are inside the tracker acceptance is reported as a function of the less energetic jet energy in Fig. 6.13 for the low luminosity scenario. Looking at the picture, when two central jets are required with at

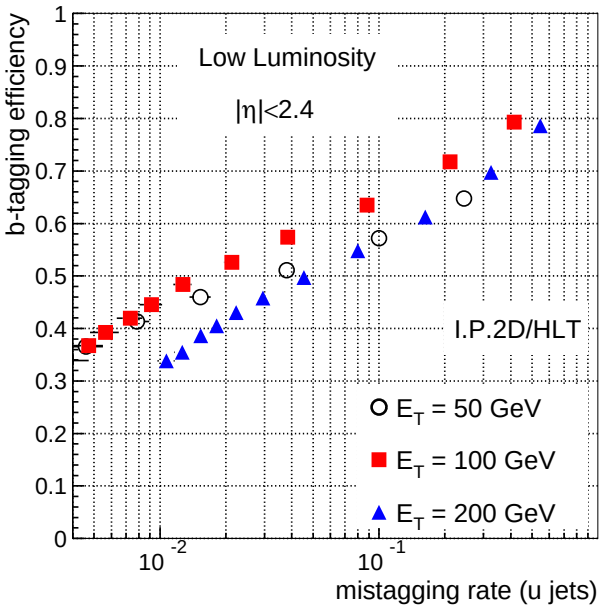

Figure 6.11: *Efficiency for* b*-tagging versus mistagging rate for different jet transverse energies at low luminosity in the High-Level trigger case using the track two-dimensional impact parameter counting* b*-tag.*

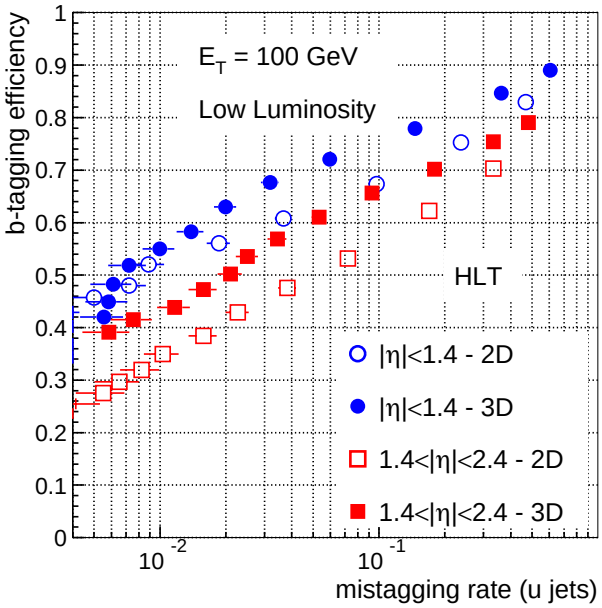

Figure 6.12: *Efficiency for* b*-tagging versus mistagging rate for three-dimensional* (3D) *or two-dimensional* (2D) *impact parameter counting* b*-tag in the HLT case.*

least $E_{\mathrm{T}} = 120$ GeV, the Level-1 trigger rate is about 500 Hz. A similar Level-1 output is obtained if only one jet with $E_{\mathrm{T}} > 150$ GeV is required to be inside tracker acceptance. The inclusive trigger should be efficient in selecting b-jets originated by resonant decays, such as $\mathrm{H} \rightarrow \mathrm{b\bar{b}}$, hence the presence of one or two (central) b-tagged jets is an additional requirement which is made to reduce the trigger rate. In Fig. 6.14 on page 131 the Level-1 calorimetric trigger rate is reported as a function of the leading jet E_{T} (upper figure) or the next-to-leading jet transverse energy (lower figure) as measured during calorimetric Level-1 trigger. In the upper (lower) plot the curve labelled as "no bTag" corresponds to the "1st Jet" ("2nd Jet") curve of Fig. 6.13, hence the Level-1 output rate. If the online b-tag algorithm is used to tag the leading (next-to-leading) jet, the QCD rate is reduced by a factor 10 in passing from Level-1 input to High-Level trigger output. Moreover, if both jets are tagged and have a transverse energy greater than 120 GeV, the HLT output rate is of the order of 5 Hz. If only one jet with $E_{\mathrm{T}} > 200$ GeV, corresponding to the 237 GeV threshold at 95% of Tab. 3.6 on page 55, is required to be central and tagged, the same output rate is obtained. The effect on a possible $\mathrm{H} \rightarrow \mathrm{b\bar{b}}$ signal is a reduction of the order of $\epsilon_b^2 \simeq 0.4$, a more accurate estimation will be reported in Sec. 9.6.

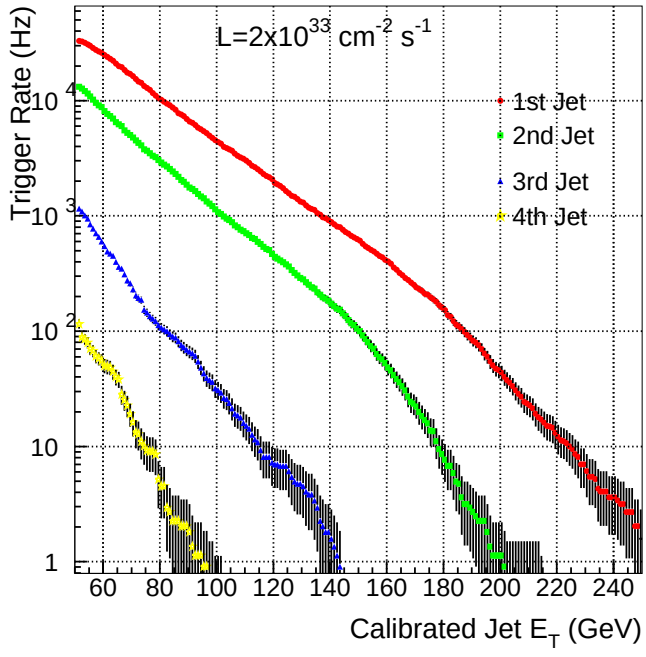

Figure 6.13: *Low luminosity trigger rate after Level-1 calorimetric selection when one to four jets are within the tracker acceptance as a function of the transverse energy of the less energetic jet.*

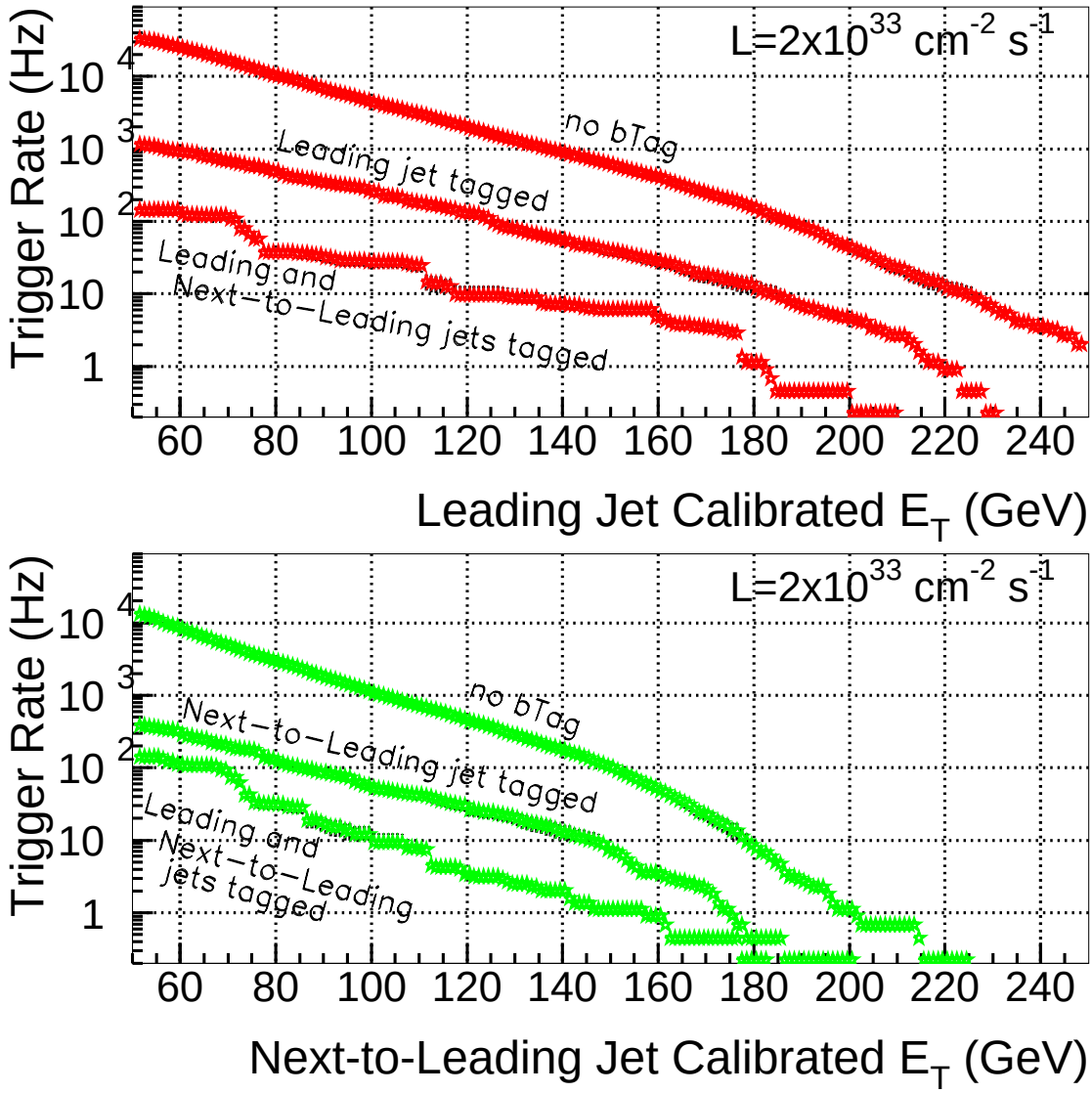

Figure 6.14: *Rate after the HLT* b*-tag selection for low luminosity for the leading (top) and next-to-leading (bottom) jets within the tracker acceptance, ordered in decreasing transverse energy* E_{T}*. In each plot the upper curves labelled as "no bTag" indicate the trigger rate after Level-1. The middle curves refer to the case when only one jet is tagged (the leading or the next-to-leading), while the lower curves refer to the case when both the leading and next-to-leading jets are tagged as* b*-jets.*

The same study has been done also for high luminosity, where the Level-1 trigger rate is estimated to be the one shown in Fig. 6.15. Even in this case the HLT b-tag capability to reduce the rate is of the order of a factor 10 per tagged jet. If two jets are required to be within the tracker acceptance with E_{T} greater than 130 GeV, the Level-1 1 kHz trigger rate is pushed down to 10 Hz at HLT requesting both the leading and next-to-leading jets to be tagged as b-jets.

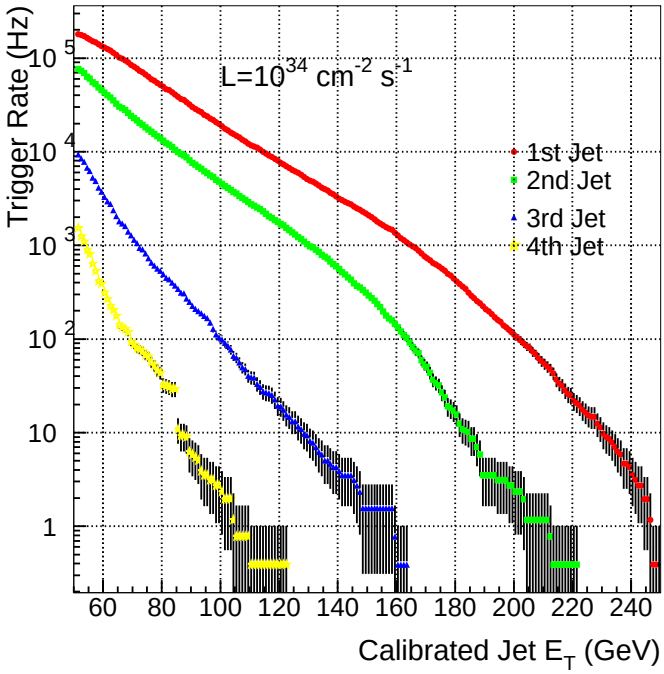

Figure 6.15: *High luminosity trigger rate after Level-1 calorimetric selection when one to four jets are within the tracker acceptance as a function of the transverse energy of the less energetic jet.*

This study has demonstrated the possibility to extensively use the tracker during HLT phase with an efficient track reconstruction and b-tagging at low and high luminosity. The HLT algorithm execution time should be sustained by the processor farm running after Level-1 trigger. The comparison with offline tagging performance indicates that almost no information is lost in the online tagging and a reduction factor on the QCD jet rate of almost 100 is obtained if the two most energetic jets are tagged.

In the last part of this work these results will be used to realize an algorithm dedicated to the HLT selection of events containing b-jets and a muon to select such events as $\mathrm{W}(\rightarrow \mu\nu_{\mu})\mathrm{H}(\rightarrow \mathrm{b\bar{b}})$, otherwise largely discarded by the original CMS low luminosity High-Level trigger table proposal (Tab. 3.6 on page 55).

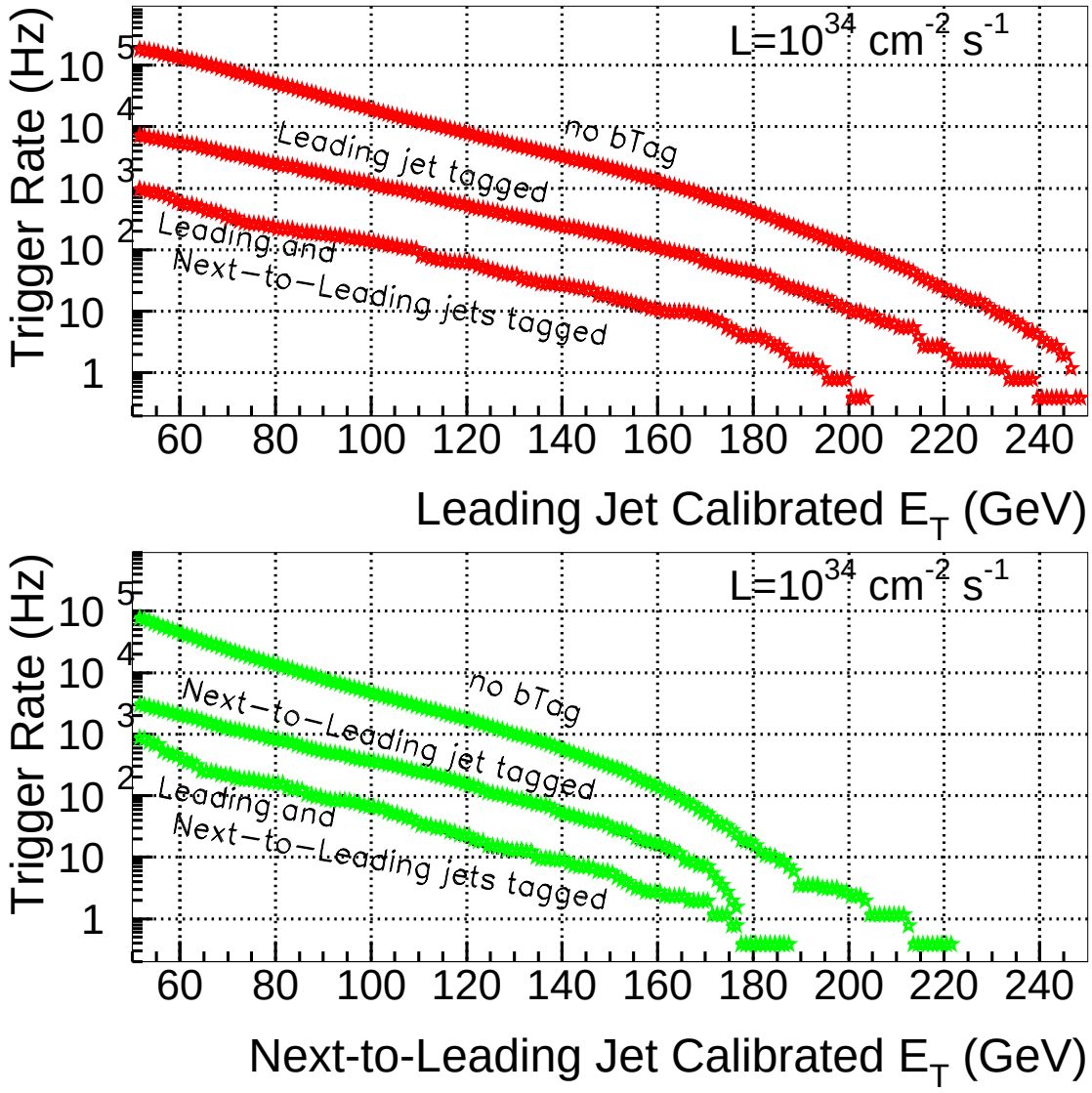

Figure 6.16: *Rate after the HLT* b-tag *selection for high luminosity for the leading (top) and next-to-leading (bottom) jets within the tracker acceptance, ordered in decreasing transverse energy* E_{T}*. In each plot the upper curves labelled as "no bTag" indicate the trigger rate after Level-1. The middle curves refer to the case when only one jet is tagged (the leading or the next-to-leading), while the lower curves refer to the case when both the leading and next-to-leading jets are tagged as* b-*jets.*

Part III

High Level Trigger Algorithm with CMS Tracker

Introduction

This part describes the use of the CMS Tracker to select Higgs boson decays into b-jet pairs. It represents my original contribution to the CMS collaboration. The channel under study is the associate production of a Higgs and a W boson, followed by the decays $W \rightarrow \mu\nu$ and $H \rightarrow b\bar{b}$, which can be triggered on low luminosity conditions.

I have realized a fast HLT algorithm using all the elements I have studied and developed in Part II. Starting from muon and calorimetric hardware-based Level-1 trigger, events with at least one muon with $p_T > 10$ GeV/c and two jets with $E_T > 20$ GeV are selected in the central pseudorapidity region. Tracks are partially reconstructed within the Tracker using a regional approach. An isolated muon is then searched for using the Tracker alone. The initial Level-1 trigger rate (560±20 Hz) can be lowered to 1.4±0.2 Hz by applying b-tagging criteria to the jets in the event. The signal selection efficiency for a 115 GeV/c^2 Higgs boson mass is 13%, corresponding to 351±24 events per year at 2×10^{33} $cm^{-2}s^{-1}$ luminosity. The response time of the software described here allows to use the algorithm at High-Level trigger stage [95]. In this way at LHC startup, the CMS detector will be able to cover the search for the Higgs boson in the low mass region by complementing the $H \rightarrow \gamma\gamma$ decay channel with the $W(\rightarrow\mu\nu)H(\rightarrow b\bar{b})$ and $t\bar{t}H$ associated production.

Chapter 7

Monte Carlo Samples for WH search

The samples used to compute the trigger rates were produced during the so called "Spring 2002" production [96]. They were all generated with PYTHIA 6.158 [69] and the CMS detector response was simulated with CMSIM 125 [72]. The background samples are divided into processes involving vector bosons (W, Z) and $t\bar{t}$ pair production containing muons in the final state and Minimum Bias events. An average of 3.5 soft pp interactions per bunch crossing are superimposed, as expected at LHC during the low luminosity period. Pile-up events from the previous 5 and following 3 bunch crossings are also superimposed to the "on-time" crossing to mimic the Tracker readout electronics behaviour and to take into account the energy pile-up in the calorimeters, relevant in the present analysis for jet reconstruction and muon isolation. As a result, an average of 30 soft interactions are superimposed to each hard process, making the track reconstruction more difficult. Digitization and reconstruction of the events have been completely performed with the object-oriented program for CMS analysis ORCA 6_2_3 [79]. All the subdetectors are fully simulated.

7.1 The signal $W(\rightarrow \mu\nu)H(\rightarrow b\bar{b})$

In the sample used for this study the Higgs boson mass is set to 115 GeV/c^2. The W boson is forced to decay into muon and neutrino, the Higgs boson into $b\bar{b}$. No requirements on the muons and jets at generator level were made. The cross section value of 0.131 pb is provided by PYTHIA [69] and corresponds to more than 2 500 events per year, assuming to collect 20 fb^{-1} in one year at low luminosity. The number of analysed events corresponds to 60% of the total amount of one year statistics.

In Fig. 7.1 the cross section multiplied by the decay branching fractions is reported as a function of the Higgs boson mass. The upper curve is obtained with the leading order calculation of WH associated production, the lower curve includes the higher order corrections [33]. The branching ratio of Higgs boson decay into $b\bar{b}$ is calculated with HDECAY [13] and for $m_H = 115$ GeV/c^2 is equal to 73%. The branching ratio of $W \to \mu\nu_\mu$ decay is measured to be 0.1057(22) [1]. The value of the cross section for the signal obtained from Fig. 7.1 is between 0.14 and 0.16 pb and is in agreement with the PYTHIA generator value.

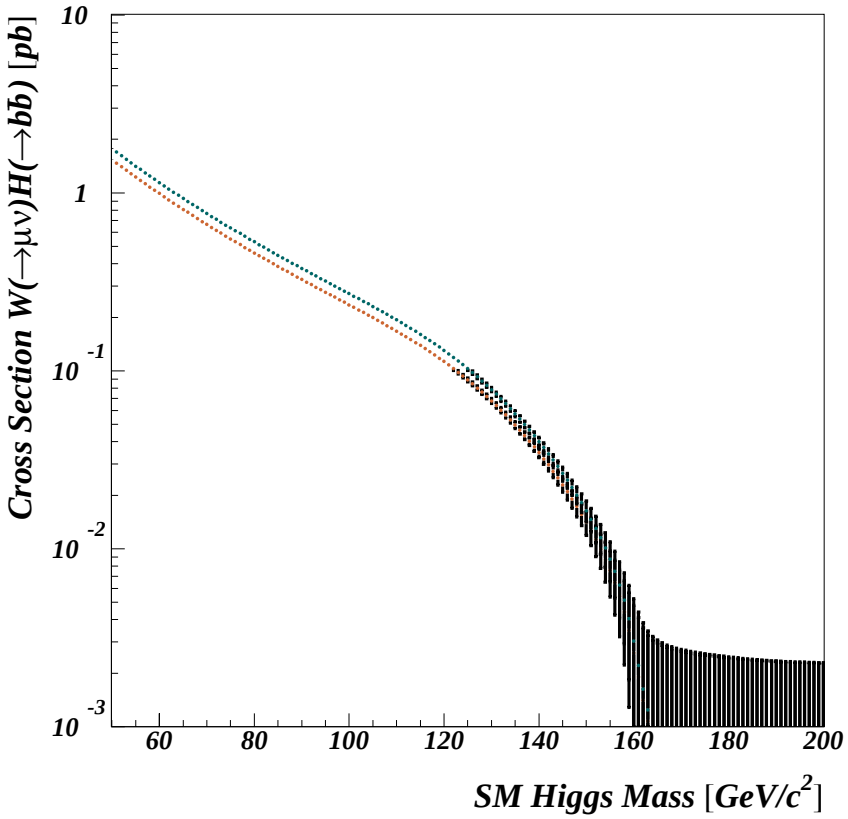

Figure 7.1: *Cross section for the associated production* $pp \to WH$ *[33] multiplied by the decay branching ratios* $H \to b\bar{b}$ *[13] and* $W \to \mu\nu_\mu$ *[1]. Upper curve: leading order calculation of* WH *production. Lower curve: higher order corrections to* WH *associated production cross section.*

7.2 Minimum Bias

Three samples of Minimum Bias events with muons in the final state have been simulated. The full simulation of all the possible LHC events which could lead to potentially triggered muons in the final state is very demanding, both in terms of the data volume to be stored and the CPU time needed to produce and process them. Therefore an event weighting procedure has been developed to account for the different processes which lead to the production of unstable particles decaying into muons [97]. In the first sample a cut depending on pseudorapidity is applied to cope with the different minimum momenta for a muon to reach the muon chambers in three regions of the detector ($p_{\mathrm{T}} > 3$ GeV/c in $|\eta| < 1.2$, $p_{\mathrm{T}} > 1.8$ GeV/c in $1.2 < |\eta| < 1.7$, and $p > 3.5$ GeV/c in $|\eta| > 1.7$). This sample will be referred to as "Low p_{T}^{μ}" for simplicity. In the other two samples at least one generated muon within $|\eta| < 2.5$ is required, with different transverse momentum thresholds: 4 and 10 GeV/c. To avoid double counting, in the first (second) sample only the events with generated muon p_{T} less than 4 GeV/c (between 4 and 10 GeV/c) have been used. In Fig. 7.2 on page 142 the integrated rate of single muons obtained at generator level is shown as a function of the muon p_{T} threshold for a luminosity of 2×10^{33} cm^{-2}s^{-1}. Charged kaons and pions contribute as a source of muons as much as b and c quarks at low p_{T}, whereas at higher p_{T} the W boson decay into $\mu\nu$ dominates.

The rate R corresponding to n_{sel} selected events can be calculated as

$$R = \frac{\left(\sum_{i=1}^{n_{sel}} w_i\right)}{\left(\sum_{i=1}^{N_{tot}} w_i\right)} \cdot \frac{\overline{\sigma}\left(\sum_{i=1}^{N_{tot}} w_i\right)}{N'_{gen}} \cdot \mathcal{L} = \epsilon \cdot \sigma \cdot \mathcal{L} \tag{7.1}$$

where $\overline{\sigma}$ is the cross section of the generated process, $\left(\sum_{i=1}^{N_{tot}} w_i\right)$ the sum of the weights w_i of the N_{tot} processed events and N'_{gen} the normalized number of generated events, summarized in Tab. 7.1 for the various analysed datasets. A more detailed description of the N'_{gen} calculation and technicalities related to the production process of these events is given in Appendix B. A weighted cross section

$$\sigma = \frac{\overline{\sigma}\left(\sum_{i=1}^{N_{tot}} w_i\right)}{N'_{gen}} \tag{7.2}$$

can be defined for each sample. In this way the rate R is simply the product of the ratio ϵ between the sum of the selected event weight and the total weight (the selection efficiency), the weighted cross section σ and the luminosity $\mathcal{L} = 2 \times 10^{33}$ cm^{-2}s^{-1} ($= 2 \times 10^{6}$ mb^{-1}s^{-1}). The sum of the weights, equal to N_{tot} if events have unitary weights, are reported together with the weighted cross section σ in the last two columns

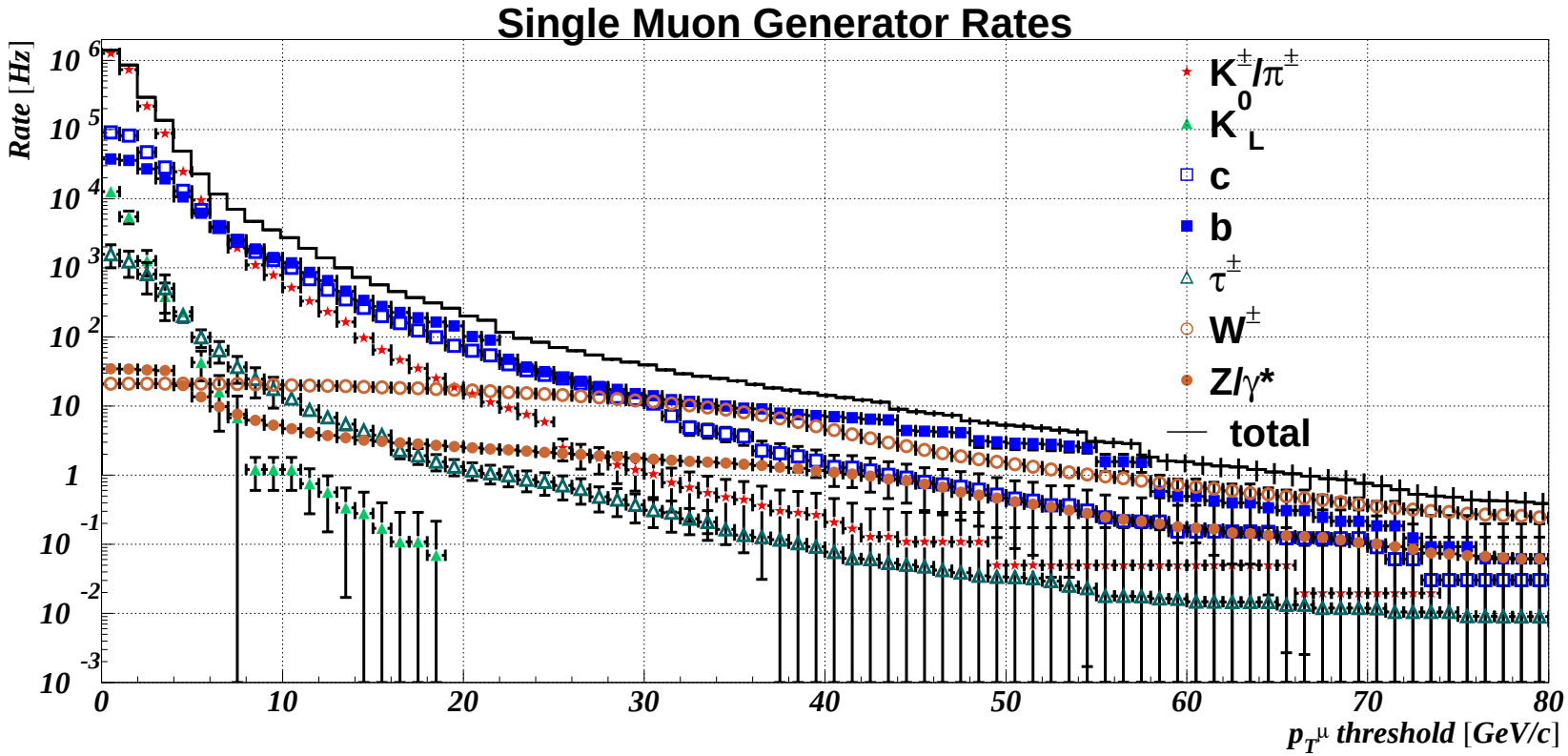

Figure 7.2: *Total rate of single muon production from PYTHIA [69] as a function of the muon p_{T} threshold for a luminosity of 2×10^{33} cm^{-2}s^{-1}.*

of Tab. 7.1. To save the CPU time and speed-up the production of the Minimum Bias sample with at least one muon with $p_{\mathrm{T}} > 10$ GeV/c, a minimum $\hat{p}_{\mathrm{T}}$ of 10 GeV/c was also required.

Monte Carlo	Kinematic cuts		Cross Section	Analysis Parameters		
sample	p_{T}^{μ} [GeV/c]	$\lvert\eta^{\mu}\rvert$	$\overline{\sigma}$ [mb]	N'_{gen}	$\left(\sum_{i=1}^{N_{tot}} w_i\right)$	σ [mb]
$\mathrm{W} \to \mu + X$	>3	<2.5	1.85×10^{-4}	284 809	25 000	1.62×10^{-5}
$\mathrm{Z}/\gamma^* \to \mu + X$	>3	<2.5	1.00×10^{-3}	1 134 278	25 000	2.20×10^{-5}
$\mathrm{t\bar{t}} \to \mu + X$	>3	<2.5	6.24×10^{-7}	34 669	14 996	2.70×10^{-7}
MB Low p_{T}^{μ}	see text	<2.5	55.22	1 346 472	1 692.57	0.069
MB $p_{\mathrm{T}}^{\mu} > 4$ GeV/c	>4	<2.5	55.22	11 703 428	4 870.97	0.023
MB $p_{\mathrm{T}}^{\mu} > 10$ GeV/c	$>10^*$	<2.5	2.66	17 474 234	4 626.03	0.00070

* also $\hat{p}_{\mathrm{T}}$

Table 7.1: *Generated Monte Carlo datasets. Muons with $p_{\mathrm{T}} > p_{\mathrm{T}}^{min}$ are selected within $|\eta^{\mu}| < 2.5$. The cross section $\overline{\sigma}$ is referred to the generated events before selection and weighting. The number of normalized generated events N'_{gen} and the sum of the weights w_i of the N_{tot} analysed events allow to define the weighted cross section σ.*

7.3 Decays with one muon in the final state

The inclusive production of W and Z bosons and $\mathrm{t\bar{t}}$ pairs were generated requiring a muon from the particle decay chains within the muon chamber acceptance ($|\eta| < 2.5$), with a minimum p_{T} of 3 GeV/c. The production cross sections ($\overline{\sigma}$) multiplied by the decay branching fractions and the kinematic factors σ are summarized in Tab. 7.1.

The differential cross sections $d\sigma/dp_{\mathrm{T}}^{\mu}$ as a function of the generated muon transverse momentum p_{T}^{μ} is shown in Fig. 7.3 on page 144 separately for the different processes. The three Minimum Bias samples are merged together to cover the whole generated muon transverse momentum spectrum.

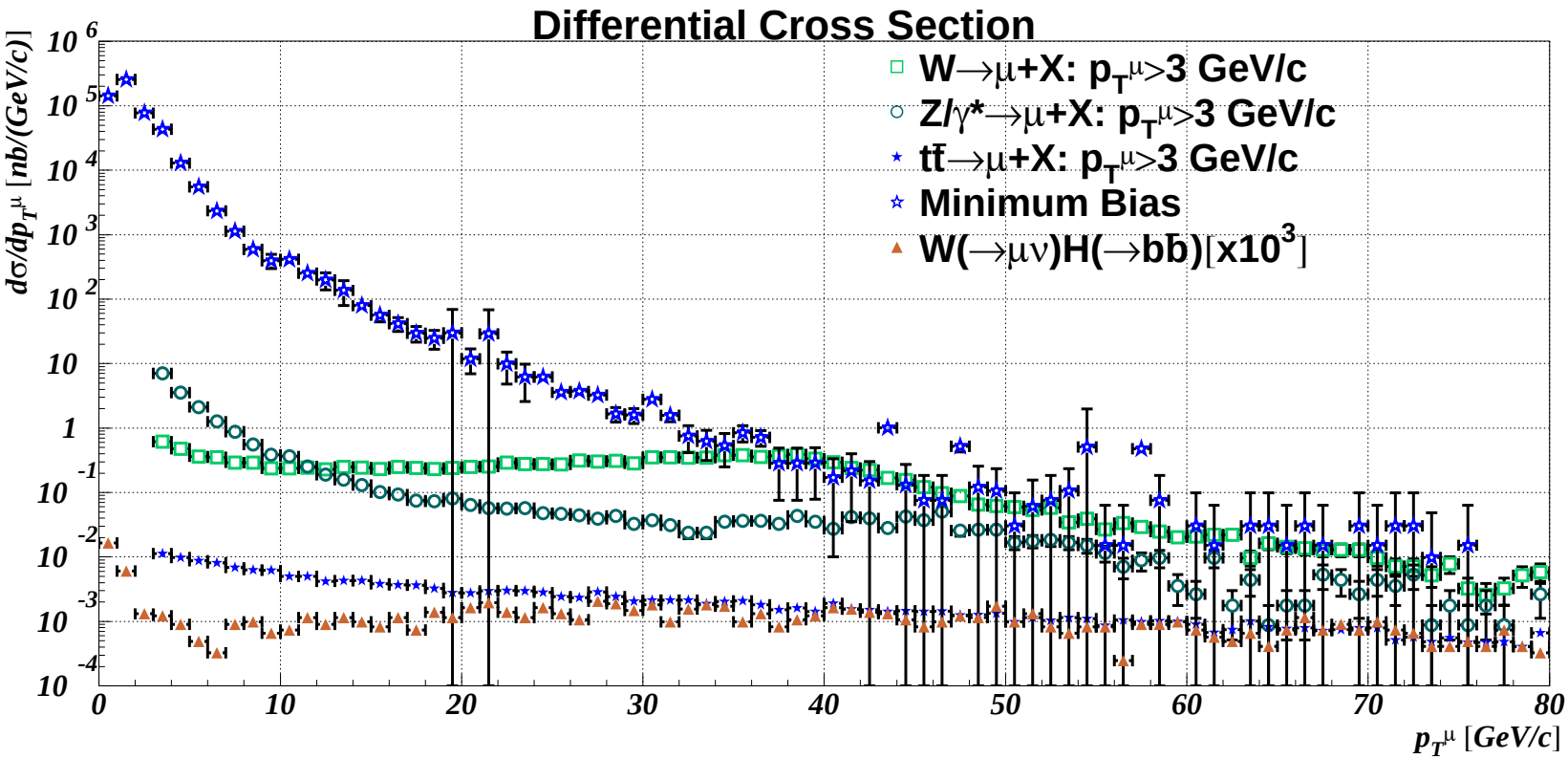

Figure 7.3: *Differential cross section as a function of generated muon transverse momentum within* $|\eta|<2.1$ *acceptance. Decays of* W (Z/γ^*, $t\bar{t}$) *with at least one true muon with* $p_T>3$ GeV/c *are represented by open squares (open circles, filled stars). The differential cross section for the Minimum Bias (open star symbols) is obtained merging together different samples following the prescriptions described in the text. The cross section for the signal (filled triangles) is multiplied by* 10^3.

Chapter 8

Level-1 Trigger

The CMS Level-1 trigger is based on the identification of muons, electrons, photons, jets and missing transverse energy [50]. A combined Level-1 trigger between muon chamber segments and energy deposition on calorimeters is required to select events with muons and jets.

8.1 Level-1 Muon Trigger

Level-1 muons are defined by the Global Muon Trigger (GMT) [50]. All the muon subdetectors contribute to the muon trigger with complementary characteristics: good spatial resolution for the Drift Tubes (DT) and Cathode Strips Chambers (CSC) and excellent time resolution for the Resistive Plate Chamber (RPC) system. The redundancy of the muon system ensures a robust trigger. However a reduction of the trigger electronics, which will not be installed in the forward Cathode Strip Chamber station, limits the muon trigger acceptance to $|\eta| < 2.1$.

The GMT sends to the Global Trigger (GT) at most the four highest p_{T} candidates obtained by matching the segments delivered by the subsystems. The distribution of the number of Level-1 muon candidates per event is shown in Fig. 8.1.

The GMT accepts also candidates reconstructed by only one subsystem, hence a quality code has been defined for the Level-1 muon candidates. The quality flag of the Level-1 muon candidates coming from GMT is shown in Fig. 8.2; a larger value of the flag corresponds to a better reconstructed muon. In the present Level-1 muon trigger strategy low quality muons (quality flag=1) are ignored in any trigger selection (single muon, double muon or combined triggers). These muons are badly reconstructed by both muon systems, RPC and DT+CSC. The higher quality flags correspond to muons reconstructed by only one system (quality flag equal to 2 if unmatched RPC and 3 if

unmatched DT+CSC) or by both systems. In the latter case the minimum p_{T} value measured by the two systems (RPC for quality flag 6 or DT+CSC for quality flag 7) is assigned to the Level-1 muon. The quality flag values 4 and 5 are actually not assigned, they will be used to indicate halo and cosmic muons.

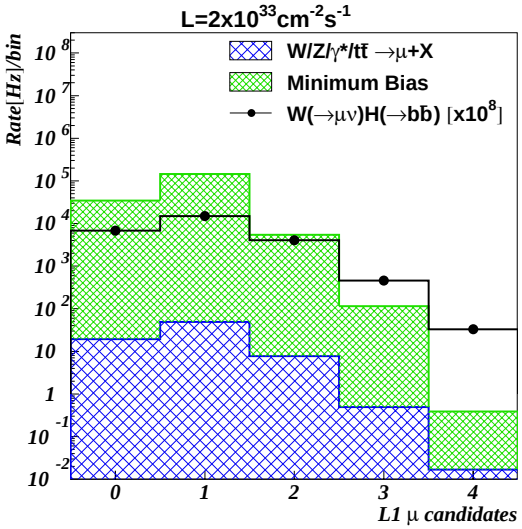

Figure 8.1: *Number of Level-1 muon candidates given by the Global Muon Trigger.*

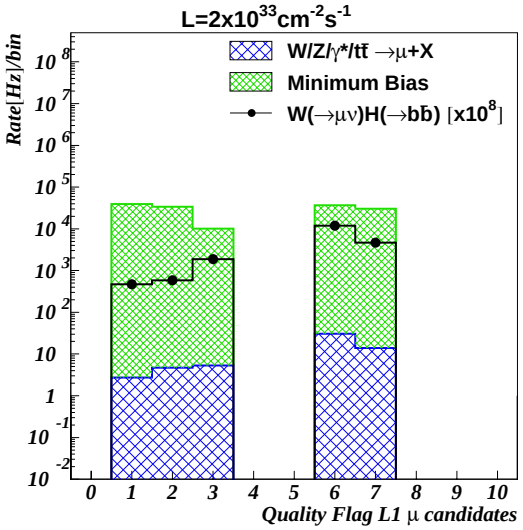

Figure 8.2: *Quality flag of the Level-1 muon candidates. The lower value (1) corresponds to muons badly reconstructed by both the muon systems (RPC and DT+CSC). To reduce Level-1 rate, these candidates are discarded.*

A combined measurement of RPC and DT+CSC signals also provides the information about the bunch crossing a triggered muon belongs to. During the Level-1 trigger selection the muon candidate is also required to come from the interaction originated by the "on-time" bunch crossing. The following Level-1 muon trigger selection is applied:

- $p_{\mathrm{T}}^{\mu} > 10$ GeV/c
- $|\eta^{\mu}| < 2.1$
- quality flag>1
- "on-time" bunch crossing

8.2 Level-1 Jet Trigger

Jets are reconstructed with low granularity by Level-1 Global Calorimeter Trigger [50, 45, 47]. The calorimeters are subdivided into towers with a size $\Delta\eta \times \Delta\varphi$=0.087×0.087 up to $|\eta|<2$, at higher pseudorapidity values the $\Delta\eta$ size increases up to 0.35. The calorimeter towers of Fig. 8.3 are organized in regions made by 4×4 towers. In the forward calorimeters a single tower defines a region by itself due to the higher size.

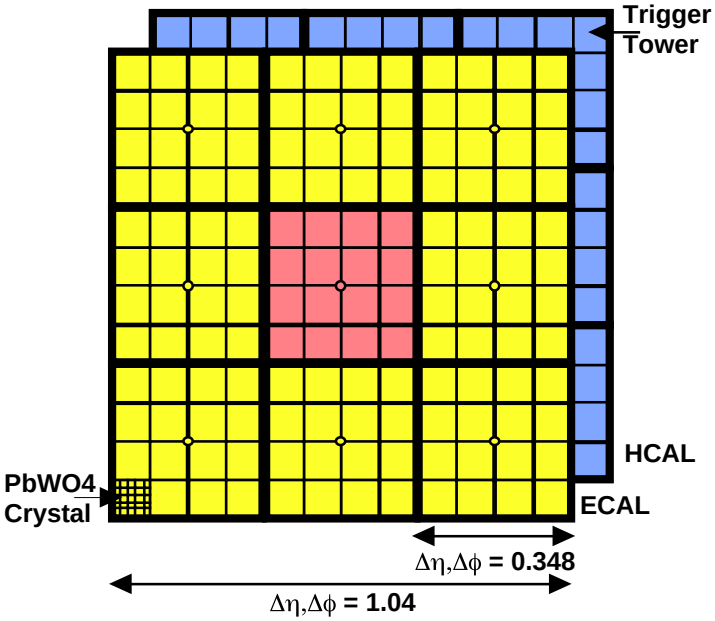

Figure 8.3: *Definition of calorimeter towers for Level-1 trigger.*

The jet trigger is based on the sum of ECAL and HCAL transverse energy. The Level-1 candidates are defined by the trigger towers with energy deposit higher than the neighbouring eight. The measured jet transverse energy E_{T} is corrected online depending both on measured pseudorapidity and transverse energy values, according to a second degree polynomial, whose coefficients are listed in some calibration tables [98]. The corrected value E_{T}^{cor} will be used in the following whenever thresholds on jet transverse energy are applied.

Sometimes low E_{T} jets from hard scattering can be mismeasured as high E_{T} jets. This could happen when either particles or a small jet from a pile-up interaction impact the calorimeter near one of the low E_{T} jets, creating a "fake jet" with higher E_{T}. Fake jets are also created when particles from different interactions impact the calorimeters too close-by. The rapidity distribution of central Level-1 jets with transverse energy above a certain threshold is shown in Fig. 8.4 with a solid line. The distribution of

the jets with a good matching in (η, φ) plane with jets made at generator level are superimposed with dashed lines. Above $E_{\mathrm{T}} = 30$ GeV (Fig. 8.4c) the number of fake jets is very small, while at lower energies the pile-up contribution is significant.

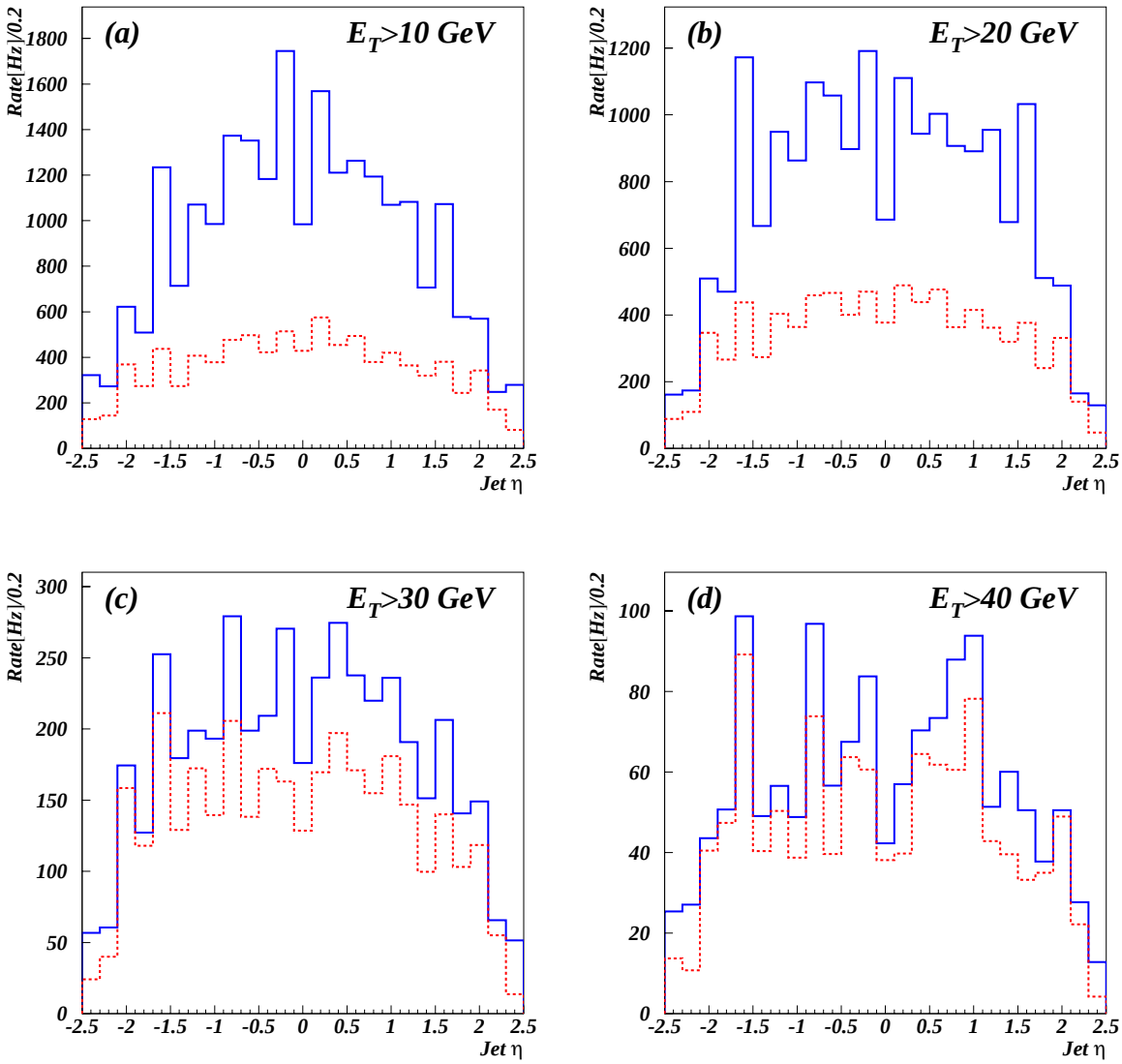

Figure 8.4: *Pseudorapidity distribution of reconstructed jets at low luminosity for different thresholds on jet transverse energy E_{T}. Solid line: all reconstructed jets. Dashed line: only jets with a good match to a generator level jet from hard scattering.*

8.3 Combined Level-1 Trigger thresholds between muon and jets

The trigger rate for combined Level-1 muon and Level-1 jet triggers (one, two or three jets respectively) are shown in Fig. 8.5, 8.6 and 8.7 for several thresholds of muon transverse momentum and jet transverse energies. No pseudorapidity requirements are made on jets coming from the calorimeters, which have $|\eta| < 5$ acceptance.

To select $W(\rightarrow \mu\nu)H(\rightarrow b\bar{b})$ events, at least one muon and two jets have to be triggered at Level-1. If a Level-1 muon with $|\eta| < 2.1$ and $p_T > 10$ GeV/c is required together with a pair of jets with transverse energy greater than 20 GeV, a total Level-1 output of 1880±50 Hz is obtained, according to Fig. 8.6 on page 151. This Level-1 rate is too high to be dedicated to the WH event selection. If the jet pair is required to be central, with $|\eta| < 3$ at Level-1, the output is reduced to an acceptable level, 560±20 Hz. The Level-1 trigger WH signal efficiency is about 36%. Hence the HLT algorithm will analyse Level-1 triggered events with these properties:

- 1 Muon: $|\eta^{\mu}| < 2.1$; $p_T^{\mu} > 10$ GeV/c
- 2 Jets: $|\eta^{j_1,j_2}| < 3.0$; $E_T^{j_1,j_2} > 20$ GeV

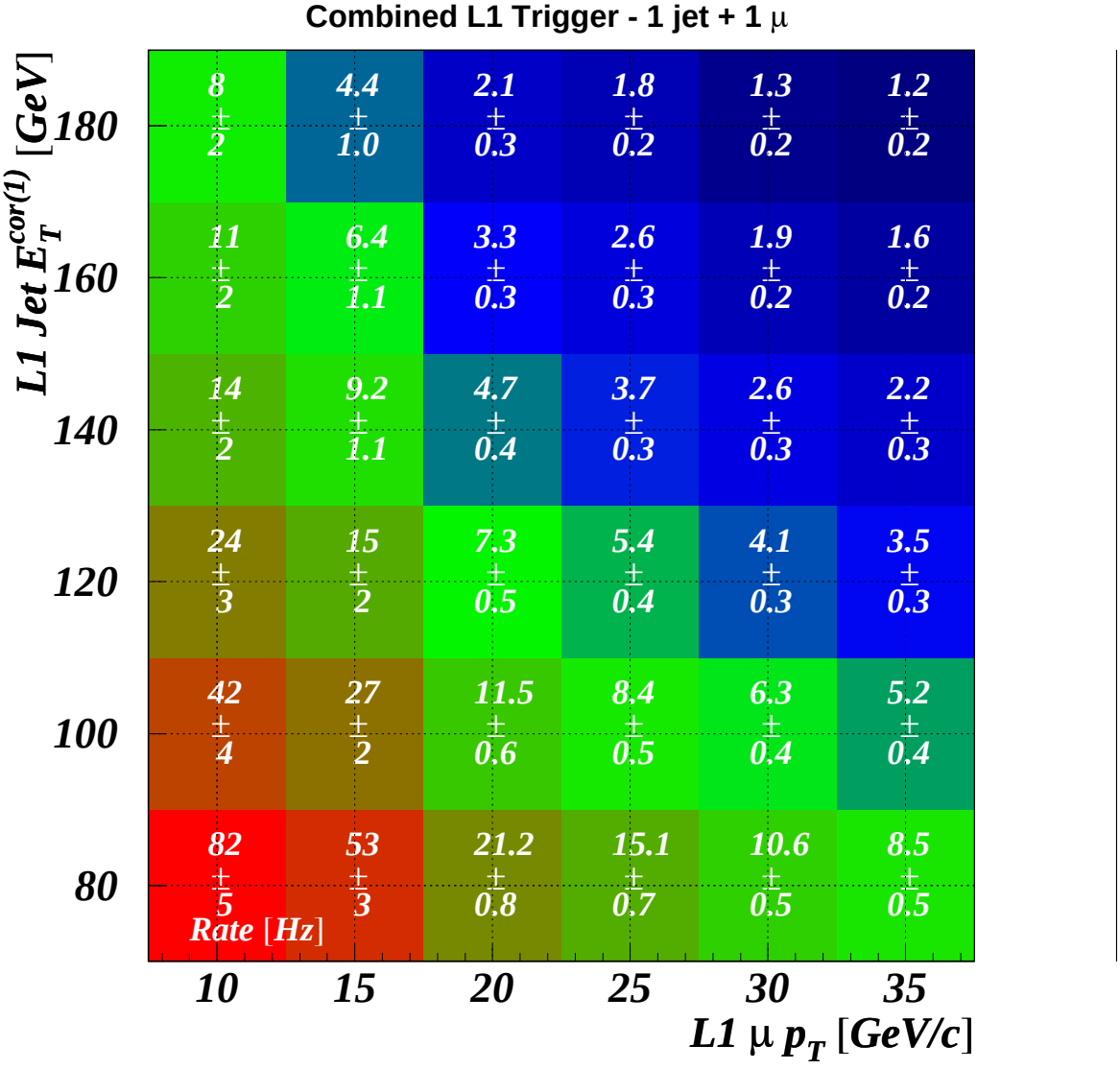

Figure 8.5: *Combined trigger rate requiring 1 Level-1 muon in $|\eta|<2.1$ + 1 Level-1 jet in $|\eta|<5$ for several Level-1 muon transverse momentum thresholds (abscissa) and corrected transverse energy thresholds of the Level-1 jet (ordinate).*

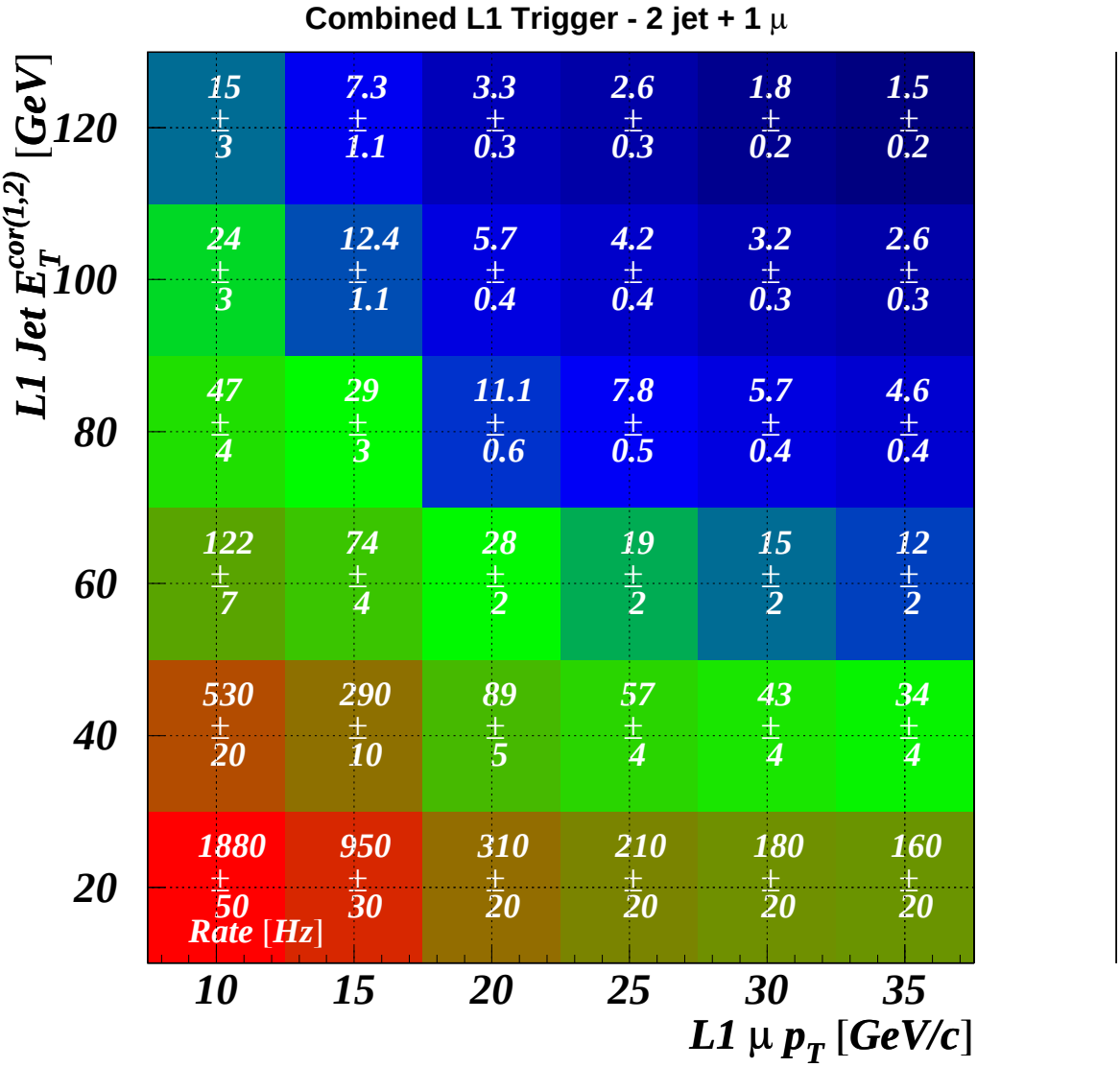

Figure 8.6: *Combined trigger rate requiring 1 Level-1 muon in $|\eta| < 2.1$ + 2 Level-1 jets in $|\eta| < 5$ for several Level-1 muon transverse momentum thresholds (abscissa) and corrected transverse energy thresholds of the Level-1 jets (ordinate).*

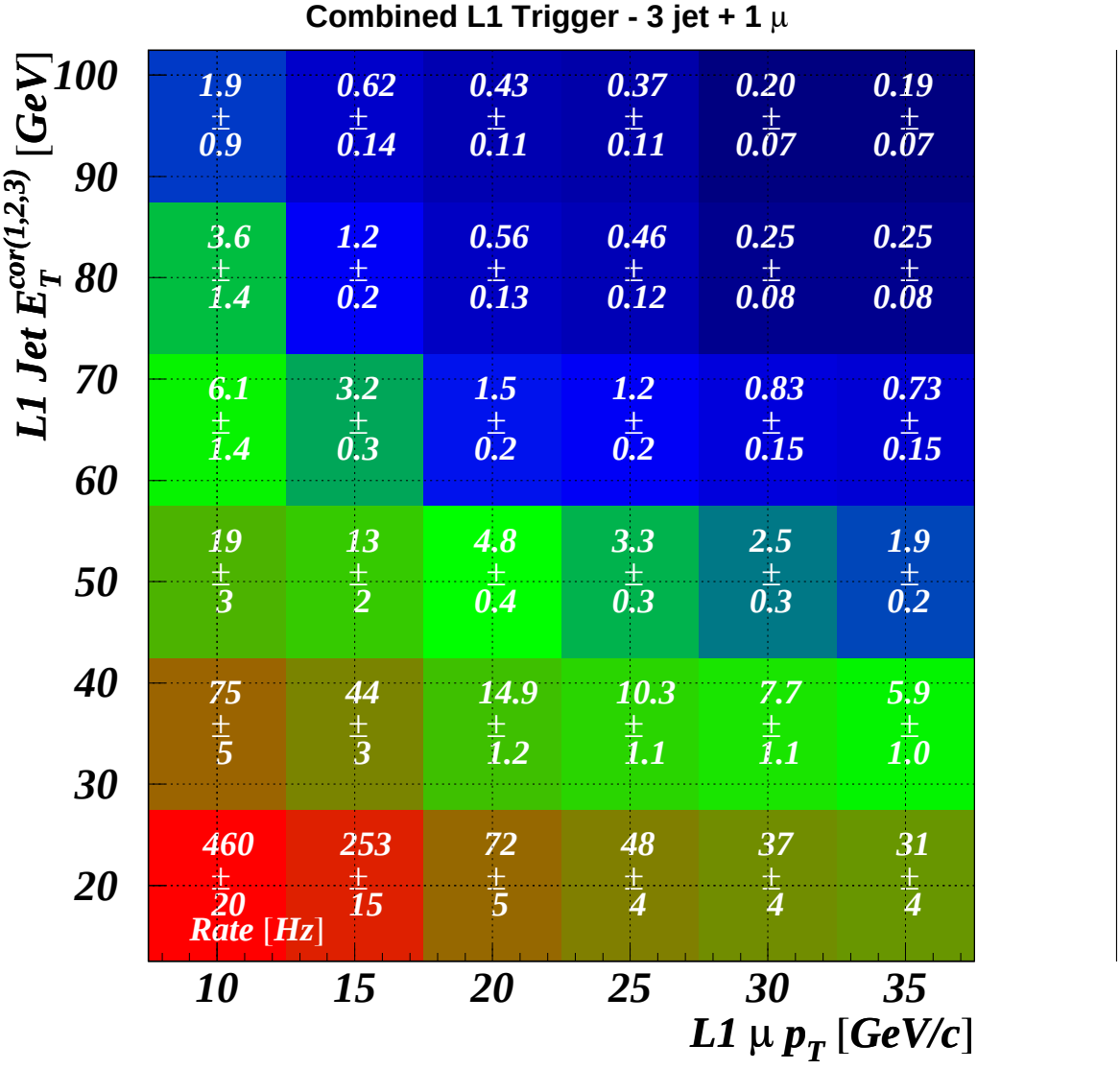

Figure 8.7: *Combined trigger rate requiring 1 Level-1 muon in $|\eta| < 2.1$ + 3 Level-1 jets in $|\eta| < 5$ for several Level-1 muon transverse momentum thresholds (abscissa) and corrected transverse energy thresholds of the Level-1 jets (ordinate).*

Chapter 9

High-Level Trigger Selection of $WH \rightarrow \mu\nu b\bar{b}$

The High-Level Trigger (HLT) in CMS will rely upon commercial processors. Events passing Level-1 trigger are forwarded to HLT and filtered by fast software algorithms running on a personal computer farm. A fast and efficient algorithm to trigger on events with one isolated muon and b-jets has been developed using CMS Tracker, reconstructing charged particle tracks online, to select an event sample possibly containing the searched WH signal. The use of the Tracker is very important because it allows not only to individuate the muon track and check it for isolation, but also to apply a simple b-tag on jets. The number of operations made by the algorithm running at HLT is limited by the time that can be spent to select events. This time depends on the Level-1 trigger output rate together with the number of processing units of the PC farm and the CPU clock of the processors. Therefore the timing performances of the algorithm developed for trigger purposes are monitored and the measurement of time is normalized to the clock tick of a common 1 GHz Pentium III CPU [55].

9.1 Level-2 Muon Reconstruction with Tracker

A track corresponding to the triggered muon is searched for in the Tracker using a regional approach. A region centered in the origin point, with a tolerance of 15 cm along the z direction (beam axis) and a maximum transverse impact parameter of 100 μm is defined around the Level-1 muon direction, with $\Delta\eta < 0.1$ and $\Delta\varphi < 0.3$, for regional track reconstruction. Track *seeds* are built up by combining pixel *hits* contained in the region. Only the *seeds* satisfying the requirement $p_T > 10$ GeV/c are propagated to reconstruct Level-2 muon candidates (L2Tk). The Level-2 muon trigger efficiencies in

the Tracker, when the most energetic Level-1 candidates are considered, are listed in Tab. 9.1. The efficiency of reconstructing a Level-1 muon in the Tracker is 86% and the number of track candidates is nearly always only one for WH events.

Monte Carlo sample	L2Tk Muon track efficiency
$W/Z/\gamma^*/t\bar{t} \rightarrow \mu + X$	0.88±0.08
Minimum Bias	0.75±0.05
$W(\rightarrow \mu\nu_\mu)H(\rightarrow b\bar{b})$	0.86±0.06

Table 9.1: *Efficiency of Level-1 muon candidate track reconstruction with tracker (L2Tk muon).*

The L2Tk muon track reconstruction efficiency is lower for low p_T muons and is above 90% if the generated muon transverse momentum is greater than 30 GeV/c, as shown in Fig. 9.1.

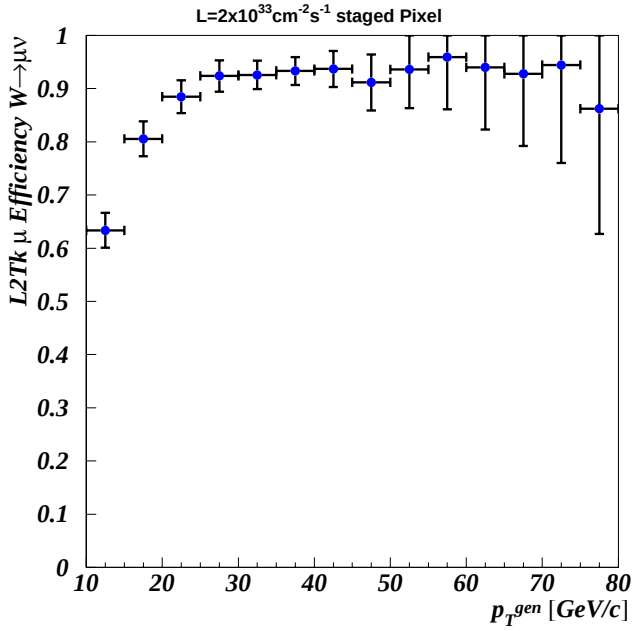

Figure 9.1: *L2Tk muon track reconstruction efficiency as a function of the generated muon transverse momentum in* $W \rightarrow \mu\nu$ *decays.*

The resolution on the measurement of the muon inverse transverse momentum, defined as the standard deviation of the fitted gaussian to the $\frac{1/p_{\mathrm{T}}^{rec}-1/p_{\mathrm{T}}^{gen}}{1/p_{\mathrm{T}}^{gen}}$ distribution, is reported in Tab. 9.2. The resolution of the Level-1 muon is poor, whereas L2Tk muon measurement is similar to the one obtained with the time consuming standard HLT muon reconstruction (Level-3 muon), which is performed by matching the muon trajectories, propagated inside muon chambers within a not uniform realistic magnetic field, to the pixel *hits*. For example, the Level-3 muon resolution is 1.0% in the barrel region for Minimum Bias events [51], well in agreement with the L2Tk resolution of 0.9%.

	Level-1 Muon			L2Tk Muon		
	barrel	overlap	endcap	barrel	overlap	endcap
$\mathrm{W}\rightarrow\mu+X$	26%	55%	41%	1.0%	1.3%	1.8%
$\mathrm{Z}/\gamma^{*}\rightarrow\mu+X$	13%	61%	18%	1.0%	1.3%	1.6%
$\mathrm{t\bar{t}}\rightarrow\mu+X$	14%	28%	21%	1.2%	1.5%	1.9%
Minimum Bias	12%	18%	14%	0.9%	1.4%	1.6%
$\mathrm{W}(\rightarrow\mu\nu_{\mu})\mathrm{H}(\rightarrow\mathrm{b\bar{b}})$	26%	55%	41%	1.4%	1.5%	2.1%

Table 9.2: *Gaussian standard deviation of the distribution of* $\frac{1/p_{\mathrm{T}}^{rec}-1/p_{\mathrm{T}}^{gen}}{1/p_{\mathrm{T}}^{gen}}$*, where* p_{T}^{gen} *and* p_{T}^{rec} *are the generated and reconstructed (at Level-1 or with Tracker L2Tk) transverse momenta of the muon in the indicated pseudorapidity intervals: barrel (*$|\eta|<0.8$*), overlap (*$0.8<|\eta|<1.2$*) and endcap (*$1.2<|\eta|<2.1$*).*

The muon reconstruction in the Tracker is very fast, most of the time being spent in clearing the fake *seeds* during the first propagation steps. Once it is identified, the muon track is propagated fully to the outermost Tracker layers. The distribution of time spent by the algorithm to single out and reconstruct the muon track is shown in Fig. 9.2 on page 156. The average time is between 50 and 70 ms for the background and 80 ms for signal events.

Reconstructing the muon in the Tracker allows the measurement of the primary vertex longitudinal position z_{PV} using the longitudinal impact parameter z_{IP} of the muon track. This is very important because it allows to determine the muon isolation in the Tracker as described in Sec. 9.2. In Fig. 9.3 on page 157 the distribution of the difference between reconstructed (z_{PV}^{rec}) and simulated (z_{PV}^{sim}) primary vertex z coordinate is shown. The resolution on z_{PV} is about 50 μm both for the signal and the $\mathrm{W/Z}/\gamma^{*}/\mathrm{t\bar{t}}$ decays and is obviously equal to the resolution of the measurement of the longitudinal

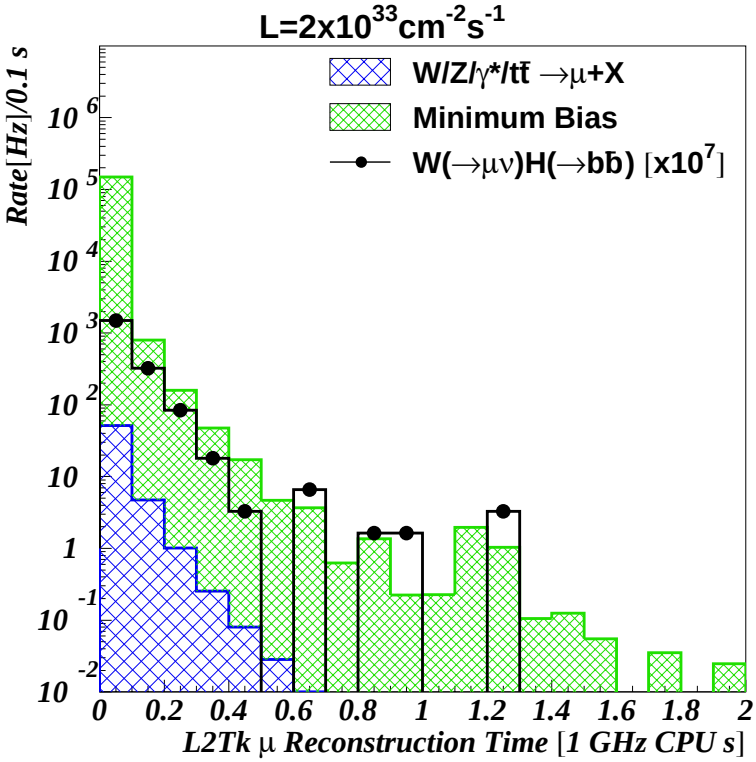

Figure 9.2: *Time distribution of Level-2 muon reconstruction within Tracker (L2Tk muon track). Time is normalized to the clock tick of a common 1 GHz* Pentium III *CPU.*

impact parameter for a reconstructed high p_{T} track. The worse resolution for Minimum Bias events, 114 μm, is caused by muons not coming from the primary vertex, originating from b or c quark fragmentation and decay or from other long-living particles (pions, Kaons), as shown in Fig. 9.4. In these cases, nearly half of the events are 500 μm away from the simulated z_{PV} value. For the signal sample, only 2.2% of the events are above 500 μm from the simulated z position of the primary vertex of pp interaction. The primary vertex transverse coordinates are taken to be the origin $(0, 0)$, because the transverse size of the LHC beam is small ($\sigma_x = \sigma_y = 15$ μm) if compared to the pixel resolution. In this phase when the strategy of physics selection is being developed, the simulated primary vertex position is smeared with three independent gaussian distributions around the nominal position $(0, 0, 0)$. When LHC will begin to operate the primary vertex transverse position will be corrected by continuously monitoring the tracks from collected calibration events to measure the possible time dependent primary vertex displacement.

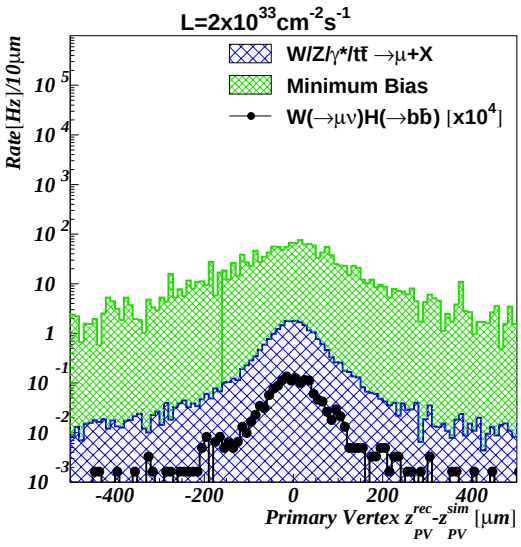

Figure 9.3: *Difference between reconstructed (z_{PV}^{rec}) and simulated (z_{PV}^{sim}) primary vertex z coordinate.*

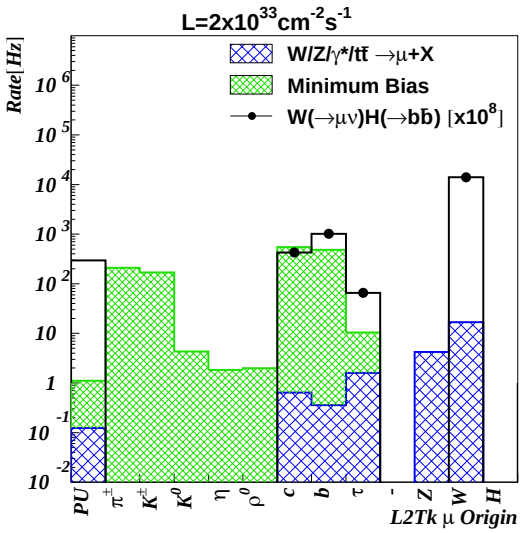

Figure 9.4: *Origin of the reconstructed L2Tk muon at generator level. In the first column PU stands for muons coming from pile-up events.*

9.2 Muon Isolation

Starting from the measured position of the primary vertex along the beam axis z_{PV} and the L2Tk muon track, a new regional search for pixel *seeds* is performed. Since now the primary vertex position and the direction of the muon are well known, more strict constraints for track reconstruction are imposed. The maximum distance for a track from the primary vertex position is set to 1 mm both in z and $r\varphi$ directions. A cone pointing to the reconstructed primary vertex, $\Delta\eta < 0.2$ and $\Delta\varphi < 0.2$ wide, is opened around the L2Tk muon track direction and *seeds* with p_{T} down to 0.8 GeV/c are propagated toward silicon microstrip layers. The p_{T} threshold for track candidates during the propagation is 0.9 GeV/c and reconstruction is stopped when a maximum of seven *hits* are added to a track. This number of *hits* is enough to reach a sufficient resolution in the measurement of track transverse momentum and impact parameter keeping the computational time at affordable level, as discussed in detail in Ch. 5.

The sum of the track transverse momenta, excluding the muon, is evaluated. An upper cut on the value of this sum gives the isolation criterion. Fig. 9.5 shows the value of this quantity for the reconstructed tracks around the L2Tk muon candidate.

An upper cut at 3 GeV/c is a good compromise between signal selection efficiency and background rejection; nearly a factor two of the Minimum Bias interactions is rejected and more than 90% of the signal is selected.

The time needed by the isolation algorithm is of the order of 60 ms per event for the signal and non Minimum Bias background events. For Minimum Bias this time is increased to 80 ms per event due to muons coming mainly from b or c hadrons decay chains embedded into high multiplicity jets. The time distribution for the isolation algorithm is shown in Fig. 9.6.

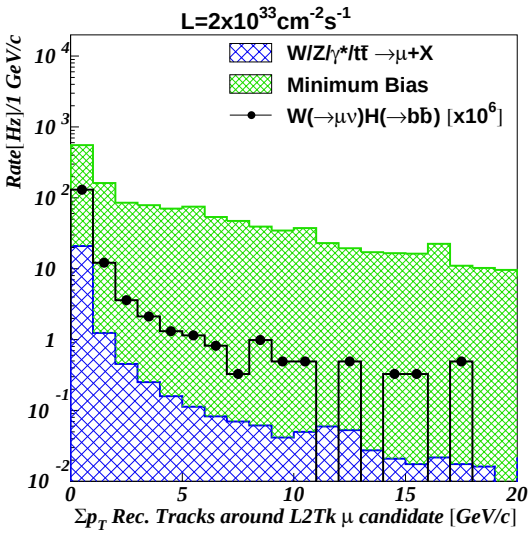

Figure 9.5: *Sum of p_T of the reconstructed tracks around the L2Tk muon track. Isolation cut at 3 GeV/c is applied to select isolated muons from W→μν decay.*

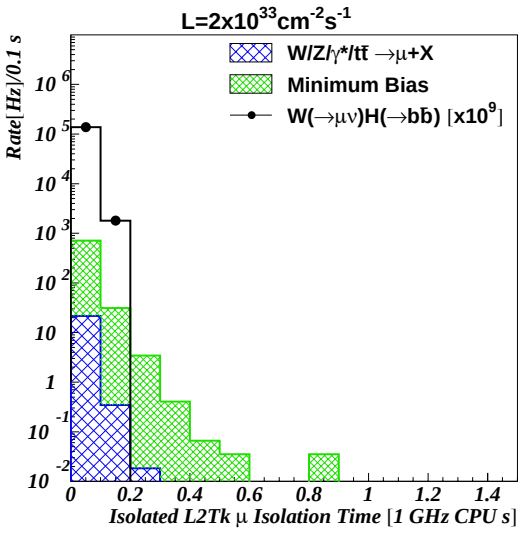

Figure 9.6: *Distribution of time to perform track reconstruction around L2Tk muon direction. Time is normalized to the clock tick of a common 1 GHz* Pentium III *CPU.*

9.3 Track reconstruction around Level-1 jets

Around each jet a cone is opened with both $\Delta\eta$ and $\Delta\varphi$ equal to 0.4 and centered in the reconstructed primary vertex. Tracks with $p_T > 2$ GeV/c and compatible with coming from a cylinder of 3 mm diameter and 3 mm height along beam axis, centered in the primary vertex, are partially reconstructed with no more than seven *hits*. If the pseudo-angular distance $\Delta R = \sqrt{\Delta\eta^2 + \Delta\varphi^2}$ between two jets is smaller than 0.4, track reconstruction is performed only around the most energetic jet in order to avoid track double counting. For background events, this algorithm requires on average 65 ms per jet. For signal events the time required is a bit longer, 120 ms per jet, but this does not affect the overall speed. The time distribution is shown in fig. 9.7.

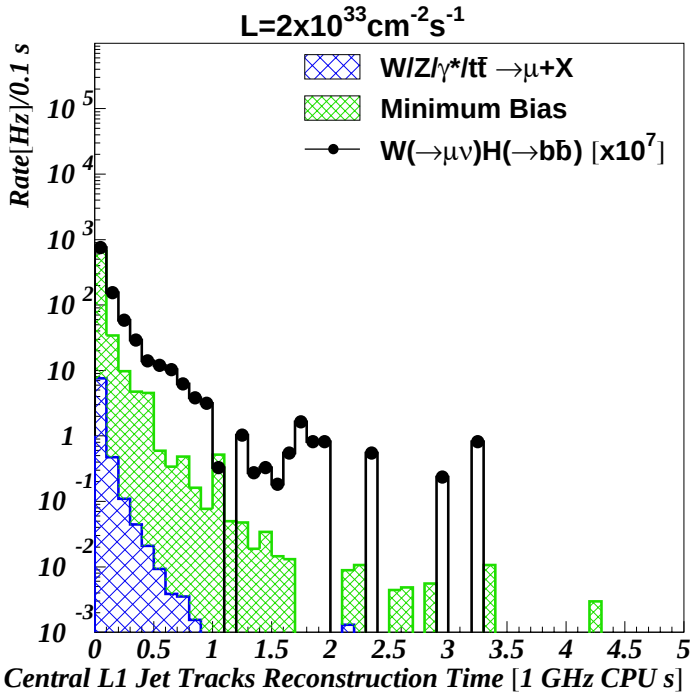

Figure 9.7: *Distribution of time to perform partial track reconstruction around Level-1 jet direction. Time is normalized to the clock tick of a common 1 GHz* Pentium III *CPU.*

If there are at least two reconstructed tracks within the cone $\Delta R < 0.4$ around jet direction, jet η and φ are recalculated with a mean over the tracks, weighted by the track p_T, as described in Sec. 6.2. The direction resolution achieved for 100 GeV transverse energy jets is 0.025 both for η and φ; this resolution is much better than the calorimetric Level-1 jet resolution of about 0.120 on the same jets.

After jet refinement, central jets are retained only if $|\eta| < 2.4$. For the Level-1 jets a different cut, $|\eta| < 3$, was applied because of the lower granularity in η of the forward and backward calorimeter regions. The corrected E_{T} distribution of the first and second more energetic central jet is shown in Fig. 9.8a and 9.8b respectively. Central jets coming from Higgs boson decay have a transverse energy between 40 and 80 GeV.

9.4 Online b-tag

With the more precise knowledge of the jet position in the space, it is possible to compute track impact parameters with respect to the jet direction [89]. A simple online b-tag algorithm is performed to select events with at least one central b-jet, requiring at least two tracks with two-dimensional impact parameter significance S_{IP} greater than 2. In this way it is possible to enrich the sample with b-jet content and to reject most of the background consisting of light flavoured jets. The performance of the track counting b-tag algorithm has been widely discussed in Ch. 6.

9.5 High-Level Trigger selection

In the previous sections the trigger algorithm has been explained in detail, nevertheless it is useful to summarize the steps of the WH$\rightarrow\mu\nu$b$\bar{\text{b}}$ online selection:

Muons and jets from Level-1 hardware-based trigger

Apply trigger thresholds on muon p_{T} and jet corrected E_{T}

Muon sector

1 L2Tk Muon = Level-2 Muon track reconstruction within the Tracker

2 Primary Vertex reconstruction with L2Tk muon track

3 Muon Isolation with Tracker

Jet sector

4 Reconstruction of tracks around Level-1 jets

5 L1Tk Jet = Jet η and φ refined measurements with tracks

6 online b-tag

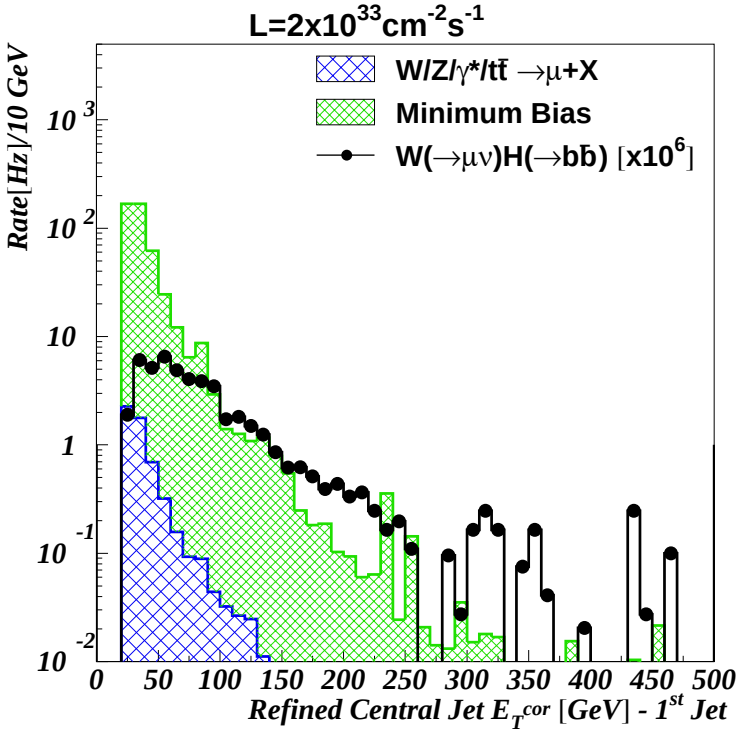

(a)

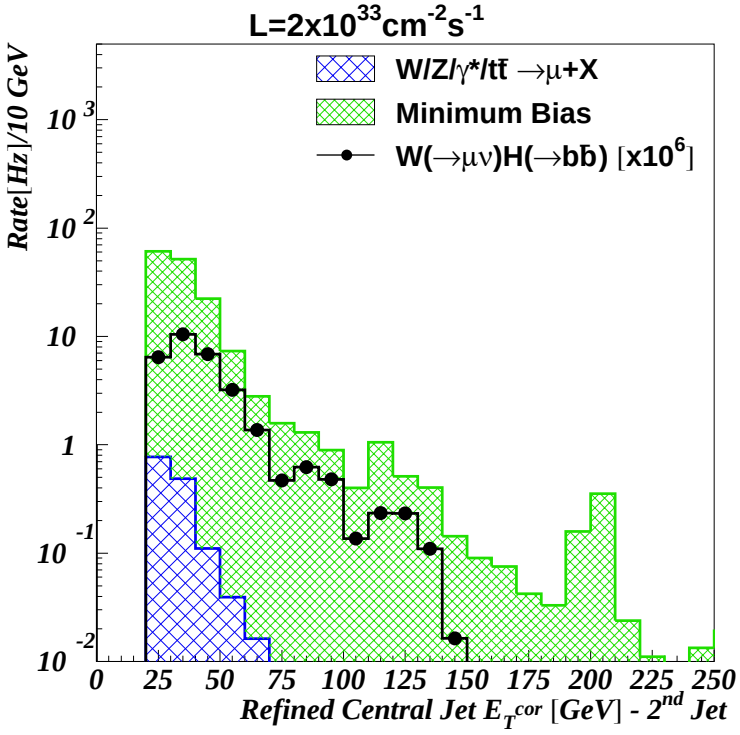

(b)

Figure 9.8: *Distribution of the corrected transverse energy for the most energetic (a) and the second most energetic (b) central jet ($|\eta|<2.4$) after calorimetric Level-1 reconstruction and refinement of η and φ measurement with Tracker.*

The complete online algorithm for WH selection is very fast. The average time spent for the signal events passing the trigger thresholds is 380 ms, with 15% of the events exceeding the 500 ms benchmark. For background events the algorithm is faster, mainly due to the jet sector of the analysis. The average time is 270 ms and 11% of the events are above 500 ms. The execution time distribution is shown in Fig. 9.9. The b-tagging algorithm takes negligible extra-time, less than 10 ms per jet pair, so it is suitable for online selection.

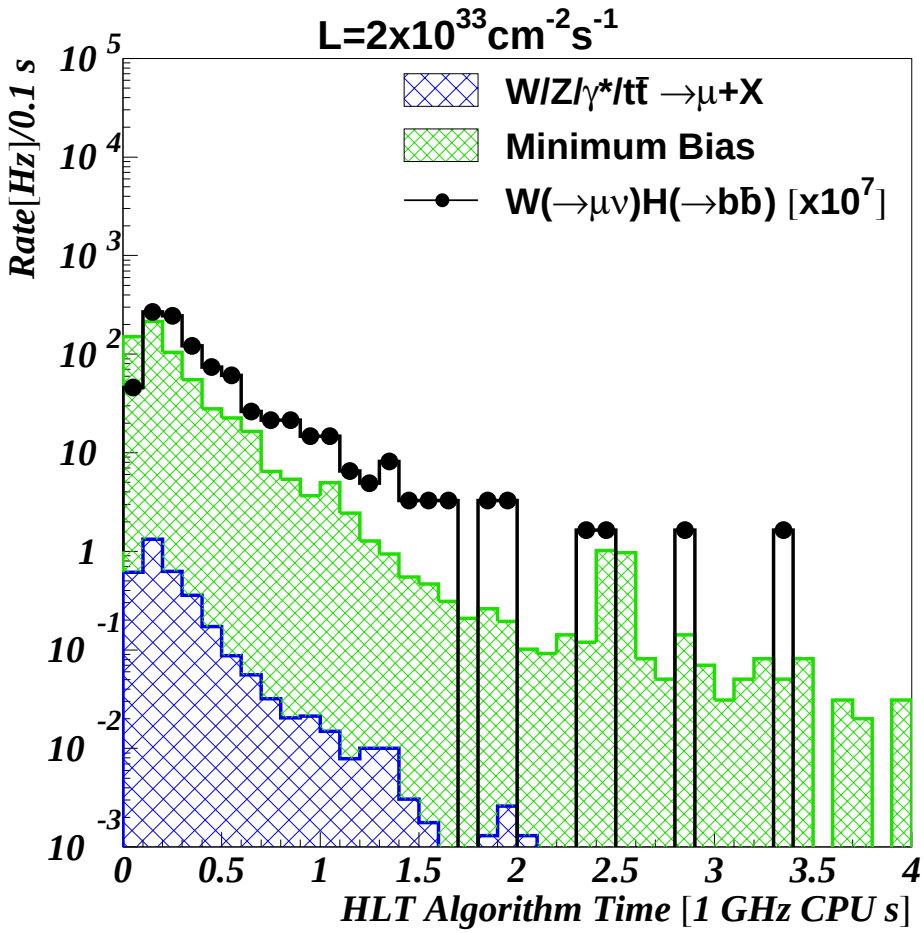

Figure 9.9: *Distribution of time to perform the High-Level trigger selection algorithm using a 1 GHz* Pentium III *CPU. Time is computed for the events that have one triggered Level-1 muon with* $p_T > 10$ GeV/c *and two central jets with* $E_T > 20$ GeV. *Time to perform track reconstruction inside the two leading jets is also included. The average value for the signal (background) is* 380 ms (270 ms) *per event. Additional time to perform* b*-tag is negligible and is not included.*

A detailed report on the time spent by the whole trigger algorithm is shown in Tab. 9.3.

	L2Tk Muon Reconstruction	L2Tk Muon Isolation	Level-1 Jet Tracking (per jet)	HLT Algorithm (2 jets + b-tag)
$W \rightarrow \mu + X$	72 ms	54 ms	55 ms	241 ms
$Z/\gamma^* \rightarrow \mu + X$	57 ms	58 ms	61 ms	254 ms
$t\bar{t} \rightarrow \mu + X$	92 ms	92 ms	145 ms	488 ms
Minimum Bias	51 ms	83 ms	65 ms	269 ms
$W(\rightarrow \mu\nu_\mu)H(\rightarrow b\bar{b})$	84 ms	61 ms	116 ms	379 ms

Table 9.3: *Time spent in the different parts of the High-Level Trigger algorithm for* WH *selection: reconstruction of L2Tk muon track with Tracker around Level-1 muon chamber candidates (first column), muon isolation with tracks reconstructed around L2Tk muon direction (second column) and reconstruction of tracks around Level-1 jets with jet η and φ refinement (third column, time is given per jet). The last column indicates the total time spent for events that pass muon isolation criteria and have two central jets at which* b*-tag is applied. Time is normalized to the clock tick of a common 1 GHz* Pentium III *CPU.*

9.6 High-Level Trigger performance

The last part of this work is the optimization of the combined trigger thresholds between the muon and the jets in order to choose the best working point keeping the selection efficiency high and reduce the background rate to few Hz. The total rate as a function of the Level-1 muon p_T threshold for several cuts applied in sequence is shown in Fig. 9.10. The initial requirement is at least one muon after Level-1 trigger together with two central calorimetric Level-1 jets with more than 20 GeV transverse energy. If a Level-1 threshold $p_T > 10$ GeV/c is applied on the muon, the output rate is 560±20 Hz. The efficiency for the signal $WH \rightarrow \mu\nu b\bar{b}$ is (35.5±1.2)%, as can be seen in Fig. 9.11.

The second selection regarding the L2Tk muon reconstruction and isolation is shown with triangles. The rate is reduced by a factor 10 and the WH selection efficiency is 80% with respect to the Level-1 trigger output.

To further reduce the background a b-tag can be applied to the two leading jets. One jet is b-tagged if at least two tracks in a cone $\Delta R < 0.4$ are found with an impact

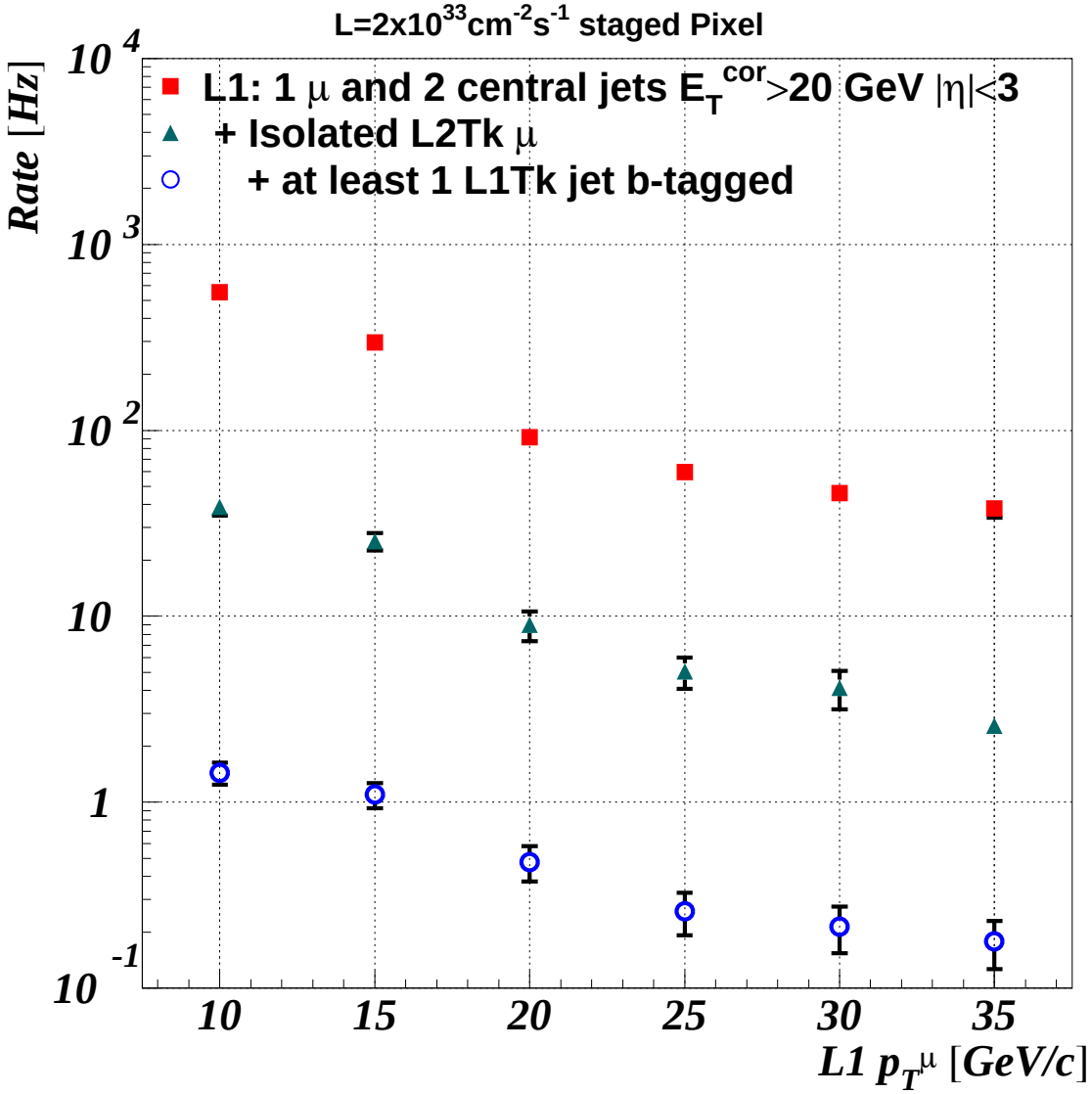

Figure 9.10: *Rate for background events as a function of the single muon p_T threshold as measured by Level-1 muon trigger.*

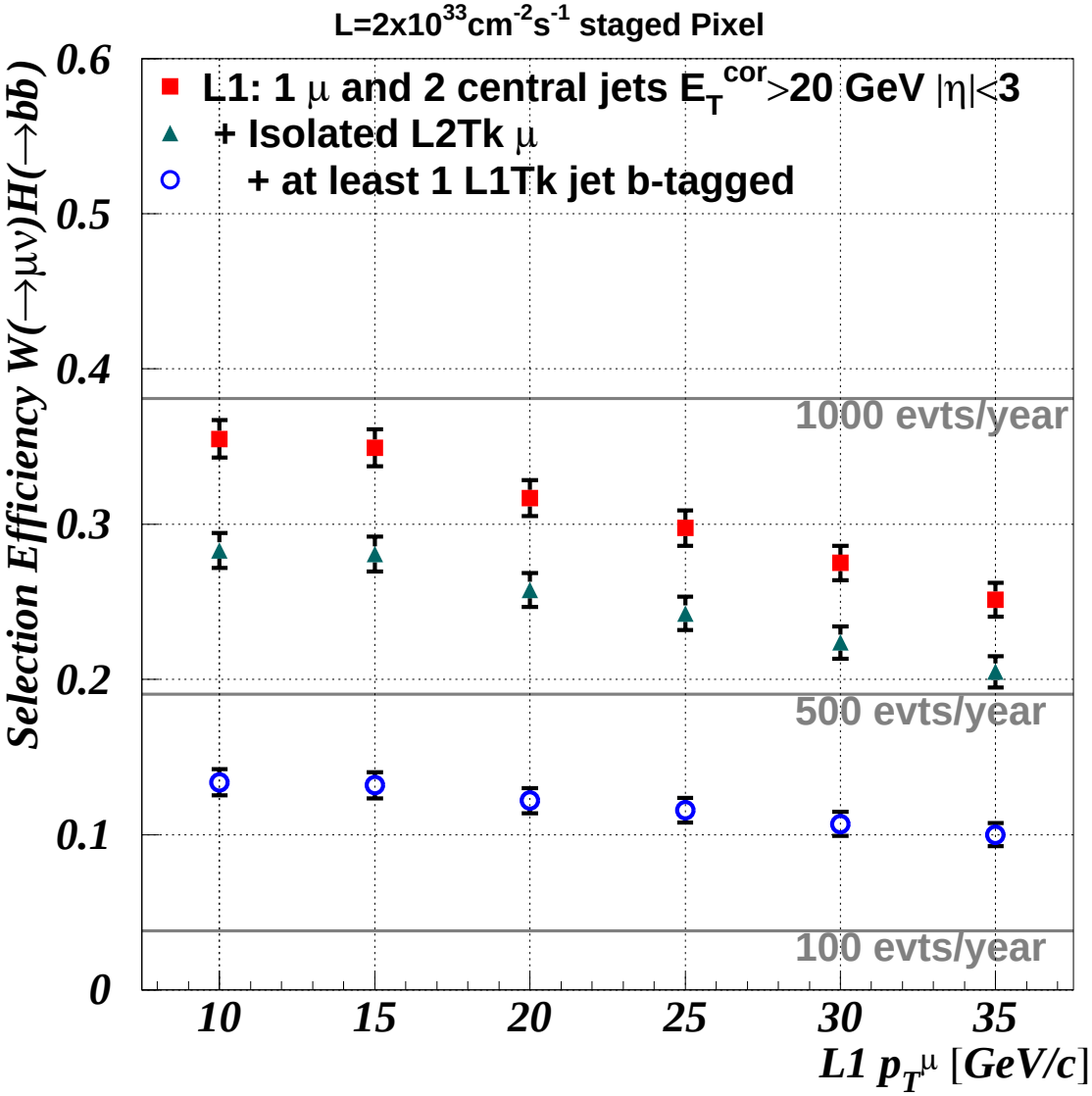

Figure 9.11: *Efficiency for the signal* $\mathrm{W}(\rightarrow \mu\nu)\mathrm{H}(\rightarrow \mathrm{b\bar{b}})$ *as a function of the single muon* p_{T} *threshold as measured by Level-1 muon trigger.*

parameter significance S_{IP} greater than 2. The measurement of track impact parameter is made in two dimensions. The background rate is drastically reduced if one of the two leading jets is b-tagged: for a Level-1 muon p_{T} threshold of 10 GeV/c the rate is 1.4±0.2 Hz, nearly 30 times less than before b-tag was applied (see Fig. 9.10). The efficiency for the signal WH is reduced by a factor two, its value being (13.4±0.9)% (see Fig. 9.11). At $\mathcal{L} = 2 \times 10^{33}$ cm^{-2}s^{-1} this corresponds to 351±24 signal events per year. During the offline analysis, background can be further reduced with dedicated studies based on the application of more sophisticated b-tag techniques and a better quality of data obtained using full reconstruction and calibrated detector information.

The background rates and signal efficiencies after each selection are summarized in Tab. 9.4 for the proposed Level-1 trigger thresholds together with two alternative options.

If the Level-1 muon p_{T} threshold is raised to 15 GeV/c, the Level-1 trigger output for events with one muon and two jets with $E_{\mathrm{T}} > 20$ GeV is 950±30 Hz (see Fig. 8.6 on page 151). For two central leading jets the rate is lowered to 300±10 Hz. After the muon isolation and jet b-tag, a HLT output of 1.1±0.2 Hz results (Fig. 9.10) with (13.2±0.8)% signal efficiency (Fig. 9.11). The number of signal events collected in one year of LHC low luminosity run is 345±21.

If the Level-1 muon p_{T} threshold is left at 10 GeV/c, but the Level-1 jet E_{T} threshold is raised to 40 GeV, the Level-1 output rate is about 530 Hz and down to 198±9 Hz if the two jets are central. The HLT final output rate is 0.61±0.12 Hz with 233±18 collected signal events per year at low luminosity.

In both cases the only gain is on the lower rate of events triggered at Level-1. Detailed studies on the Signal-to-Background optimization should be done offline to decide the more favourable working point from the final selection point of view.

9.6.1 Selection of $t\bar{t}(\rightarrow bW(\rightarrow \mu\nu))$

The events containing a pair of top quarks are also efficiently selected with this HLT algorithm. For events with one top quark decaying into bW and the W boson decaying into $\mu\nu$ (with $p_{\mathrm{T}}^{\mu} > 3$ GeV/c and $|\eta^{\mu}| < 2.1$ at generator level), a selection efficiency of (28.2±0.6)% is achieved requiring two central jets with $E_{\mathrm{T}} > 20$ GeV and one isolated muon with $p_{\mathrm{T}} > 10$ GeV/c at Level-1. Assuming the production cross section to be of the order of 100 pb, including the kinematic cuts, the correspondent number of triggered events is about 500 000 per year, as it is shown in Fig. 9.12, with a total of 10^7 background events. Any other HLT stream has lower efficiency in selecting this process. This data set is of particular importance for the top quark physics and can be used also to select

	Level-1 Trigger: 1 Muon $p_T^\mu > 10$ GeV/c $\lvert\eta^\mu\rvert < 2.1$ 2 Jets $E_T^{j_1,j_2} > 20$ GeV $\lvert\eta^{j_1,j_2}\rvert < 3$			Level-1 Trigger: 1 Muon $p_T^\mu > 15$ GeV/c $\lvert\eta^\mu\rvert < 2.1$ 2 Jets $E_T^{j_1,j_2} > 20$ GeV $\lvert\eta^{j_1,j_2}\rvert < 3$			Level-1 Trigger: 1 Muon $p_T^\mu > 10$ GeV/c $\lvert\eta^\mu\rvert < 2.1$ 2 Jets $E_T^{j_1,j_2} > 40$ GeV $\lvert\eta^{j_1,j_2}\rvert < 3$		
$\frac{Rate\ [\mathrm{Hz}]}{Efficiency}$	Level-1	Isolation	b-tag	Level-1	Isolation	b-tag	Level-1	Isolation	b-tag
$W \rightarrow \mu + X$	2.46(5)	1.61(4)	0.043(7)	2.19(5)	1.55(4)	0.043(7)	0.68(3)	0.37(2)	0.019(5)
$Z/\gamma^* \rightarrow \mu + X$	0.92(4)	0.40(3)	0.019(6)	0.72(4)	0.37(3)	0.019(6)	0.30(2)	0.096(13)	0.011(4)
$t\bar{t} \rightarrow \mu + X$	0.312(2)	0.141(2)	0.0673(14)	0.277(2)	0.138(2)	0.0658(14)	0.297(2)	0.131(2)	0.0636(14)
Minimum Bias	551(16)	37(4)	1.3(2)	295(10)	23(3)	1.0(2)	197(9)	5.0(1.3)	0.52(12)
Total Rate [Hz]	560±20	39±4	1.4±0.2	300±10	25±3	1.1±0.2	198±9	5.6±1.3	0.61±0.12
$W(\rightarrow \mu\nu_\mu)H(\rightarrow b\bar{b})$	35.5±1.2%	28.3±1.1%	13.4±0.9%	34.8±1.2%	28.1±1.1%	13.2±0.8%	21.0±1.0%	16.7±0.9%	8.9±0.7%
$W \rightarrow \mu\nu_\mu$	9.0±0.2%	7.0±0.2%	0.18±0.03%	8.7±0.2%	6.8±0.2%	0.18±0.03%	2.21±0.12%	1.6±0.1%	0.08±0.02%
$t\bar{t}(\rightarrow bW(\rightarrow \mu\nu_\mu))$	77.9±0.5%	58.7±0.6%	28.2±0.6%	76.1±0.5%	58.0±0.6%	27.9±0.6%	72.4±0.6%	54.1±0.6%	26.6±0.6%

Table 9.4: *Background rates (in* Hz*) and selection efficiencies for the signal* WH*, the* $W \rightarrow \mu\nu$ *and* $t\bar{t}(\rightarrow bW(\rightarrow \mu\nu))$ *processes after the Level-1 and High-Level trigger selections. "Level-1" refers to the Level-1 trigger data output to analyse at HLT, "Isolation" to the additional requirement of muon reconstruction in the Tracker (L2Tk Muon) and isolation, "*b*-tag" to the selection of events with at least one* b*-tagged jet of the two central jets within the Tracker (L1Tk Jets).*

$t\bar{t}(\rightarrow bW(\rightarrow \mu\nu))H(\rightarrow b\bar{b})$ associated production allowing to explore the Higgs boson low mass region even at the starting of LHC.

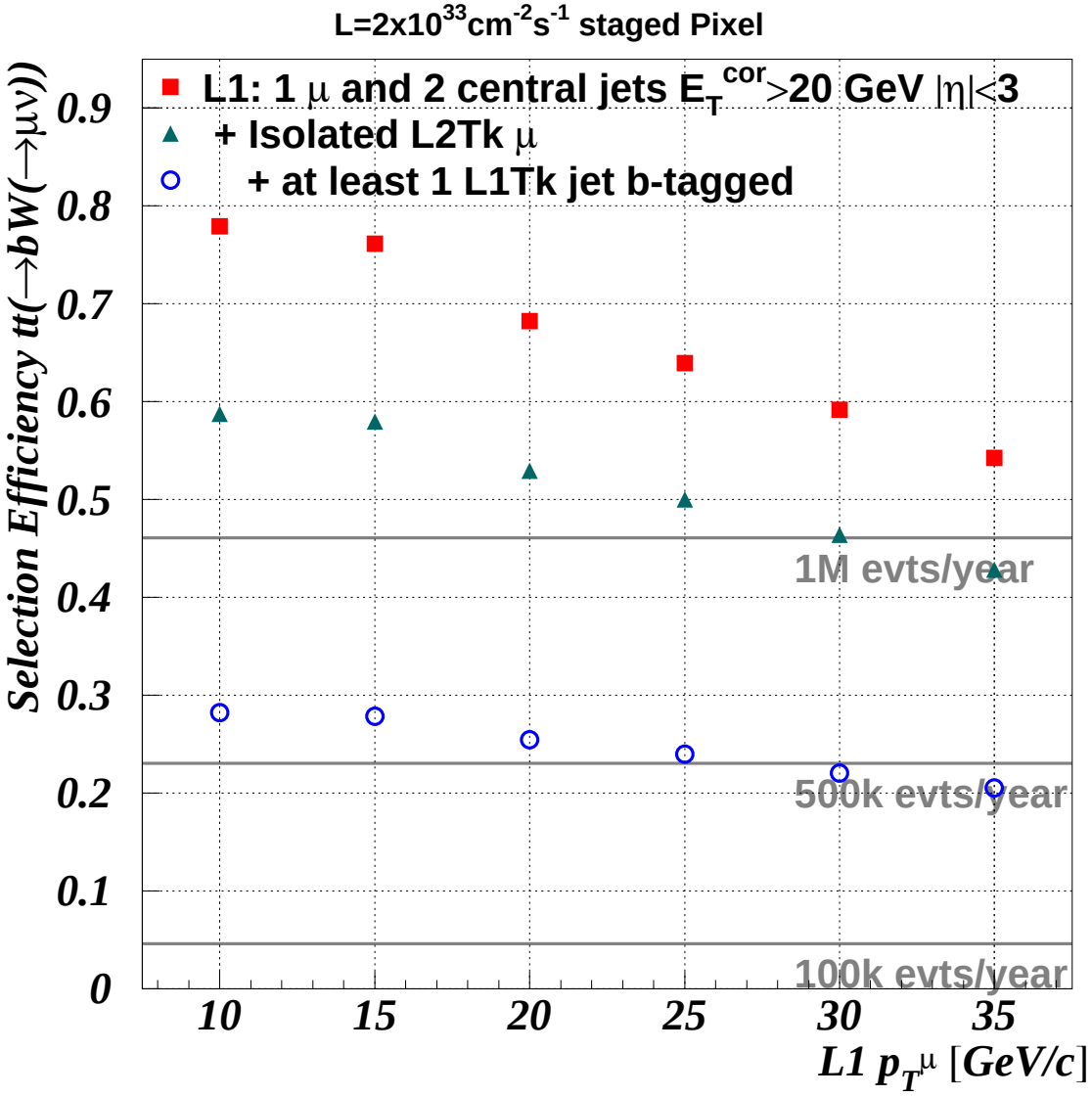

Figure 9.12: *Efficiency for the* $t\bar{t}$ *production, with one top quark decaying* $t \rightarrow bW(\rightarrow \mu\nu)$*, as a function of the single muon* p_T *threshold as measured by Level-1 muon trigger. The muon from* W *decay has* $p_T^\mu > 3$ *GeV/c and* $|\eta^\mu| < 2.1$ *at generator level.*

9.6.2 High-Level Trigger Timing

The time to process each event with the HLT stream is also computed. The total time is obtained by adding the single contributions until one event is accepted or discarded. The time distribution is shown in Fig. 9.13 and the average value per event is reported in Tab. 9.5. The average value for Minimum Bias events is 143 ms with only 5% of the events above the 500 ms benchmark, while for $t\bar{t}$ and WH processes the mean time is around 300 ms with 13% of the events out of 500 ms limit. This performance, together with the 1.4 Hz final output rate, confirms the feasibility of the High-Level trigger implementation of the described algorithm.

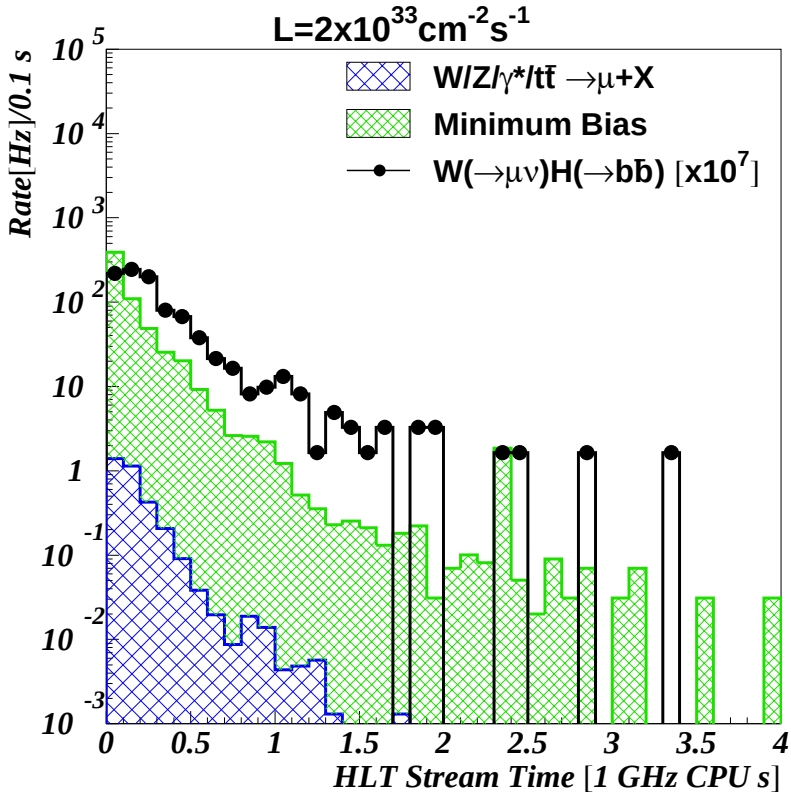

Figure 9.13: *Distribution of time to perform the trigger algorithm using a 1 GHz* Pentium III *CPU. Time is computed as resulting from the High-Level Trigger stream. Starting from Level-1 output (1 muon* $p_{\mathrm{T}}^{\mu} > 10$ GeV/c *and* $|\eta^{\mu}| < 2.1$ *+ 2 jets* $E_{\mathrm{T}}^{jet} > 20$ GeV *and* $|\eta^{jet}| < 3$*) the total time per each event is obtained by adding the time of the sequential HLT steps until the event is discarded (or accepted): L2Tk muon reconstruction + L2Tk muon isolation + tracks around the first jet, L1Tk jet refinement and* b*-tag + (if first jet is not* b*-tagged) tracks around the second jet, L1Tk jet refinement and* b*-tag .*

Process	HLT stream
$W \rightarrow \mu + X$	161 ms
$Z/\gamma^* \rightarrow \mu + X$	160 ms
$t\bar{t} \rightarrow \mu + X$	288 ms
Minimum Bias	143 ms
$W(\rightarrow \mu\nu_\mu)H(\rightarrow b\bar{b})$	306 ms

Table 9.5: *High-Level Trigger stream mean time per event, normalized to the clock tick of a common 1 GHz* Pentium III *CPU.*

9.7 Conclusions

The WH channel is important to help in the discovery of a light Higgs boson [99] at low luminosity. It was demonstrated that with offline selections based on more sophisticated b-tag techniques and b-jet pair invariant mass peak identification, the most copious background can be rejected and a 3.5σ discovery significance can be reached in three years at low luminosity [100] allowing to discovery a Higgs boson signal if combined with other channels, as $t\bar{t}H$ and $H \rightarrow \gamma\gamma$, which is the most important at high luminosity.

This analysis is also the starting point of future offline analyses, which will involve also associated $t\bar{t}H$ production, because this algorithm is also efficient (almost 30%) in selecting $t\bar{t}$ events, with one top quark decaying in $t \rightarrow bW(\rightarrow \mu\nu)$.

The initial Level-1 output rate of about 560 Hz can be reduced to less than 2 Hz HLT output rate by triggering on events with one Level-1 muon with $p_T > 10$ GeV/c and two jets with $E_T > 20$ GeV within the Tracker acceptance. Performing regional track reconstruction in a limited region of space around Level-1 muon, the muon track can be efficiently reconstructed and checked for isolation. Moreover, with tracks partially reconstructed around the jet directions, a better resolution on the measurement of jet η and φ can be achieved and a simple b-tag algorithm can be applied online. A possible application of this algorithm to a discovery channel, the associated production of a 115 GeV/c^2 mass Standard Model Higgs boson with a W boson, decaying via $H \rightarrow b\bar{b}$ and $W \rightarrow \mu\nu$, has given promising results: about 350 events can be triggered per year at CMS at low luminosity, $\mathcal{L} = 2 \times 10^{33}$ cm^{-2}s^{-1}.

This study has shown the feasibility of a High-Level trigger selection of WH using the CMS Tracker. With the HLT algorithm described in this part, event topologies with

an isolated muon and two central jets can be triggered in an average time shorter than 150 ms on a 1 GHz Pentium III CPU, well within the HLT time benchmark of Tab. 3.8 on page 56. Furthermore, the signal events are reconstructed and selected in less than 400 ms without exceeding the maximum allowed CPU time for HLT operations.

Conclusions

The work presented in this thesis has demonstrated that the CMS silicon Tracker can be extensively used in the High-Level Trigger (HLT) to select events otherwise discarded by the calorimeters and muon chambers trigger alone.

The High-Level trigger algorithms play a fundamental rôle at hadronic colliders as LHC, since they allow to select hardly recognizable topologies, as in the case of the channel $W(\rightarrow\mu\nu)H(\rightarrow b\bar{b})$ embedded into the hadronic background. During the initial low luminosity period at LHC the associated production channels WH and $t\bar{t}H$ could help in the search for the Higgs boson with mass around 115 GeV/c^2 in addition to the cleaner $H\rightarrow\gamma\gamma$ decay, which has a lower cross section and needs more statistics. To realize the HLT algorithm and efficiently select such events, I have studied and developed a special fast track reconstruction that allows to use the CMS tracker information online.

Fast track reconstruction is performed in a limited spatial region around the Level-1 calorimetric jet directions with tracks propagating up to a maximum number of tracker layers, such as to reach a reasonable resolution on track parameters while at the same time not exceeding the maximum CPU time allocated to the High-Level trigger selection. The online track finding efficiency is high and the fraction of fake tracks is kept below the percent level, thus allowing a better measurement of the jet parameters with respect to the calorimeter trigger information and a reliable b-tagging algorithm based on track impact parameter.

In this context a fast algorithm to trigger on events with b-jets has been implemented exploiting the online track finding to enrich the b content of the selected sample at HLT stage without affecting too much the Level-1 trigger bandwidth. The 0.5 kHz Level-1 output rate, obtained with requiring one jet in the central pseudorapidity region $|\eta|<3$ with transverse energy greater than 200 GeV, is reduced to 5 Hz by applying b-tag selection after online track reconstruction around the jet. Thank to this work, a portion of the CMS High-Level trigger bandwidth will be dedicated to the selection of inclusive b-jet events.

Furthermore, the algorithm I have completely implemented for WH trigger selection analyses events with at least one muon with transverse momentum $p_T>10$ GeV/c and two jets with $|\eta|<3$ and $E_T>20$ GeV from the Level-1 trigger, corresponding to a 560 ± 20 Hz rate. The muon track is reconstructed with tracker and checked for isolation, while online b-tag criterion is applied to single out b-jets from the Higgs boson decay. The HLT output rate is reduced to 1.4 ± 0.2 Hz with more than 350 collected signal events per year at low luminosity (20 fb^{-1} and in the hypothesis of $m_H=115$ GeV/c^2) to be stored for more refined offline analyses. This result is very important, because

for the first time it has been shown that the CMS silicon tracker data can be used online to select at trigger level some interesting events hard to single out without the tracking system signals. In the future similar algorithms will be implemented to select also associated $t\bar{t}H$ production thus allowing the CMS detector to cover the Higgs boson searches, even with low luminosity, in the low mass region, which is the most probable for Higgs boson discovery according to recent hints from LEP experiments.

Appendix A

Spontaneous breaking of a local SU(2) gauge theory

The most general renormalizable lagrangian for a two-component complex scalar field [101] is given by Eq. A.1

$$\mathcal{L} = T - V = \left(\partial_\mu \phi\right)^\dagger \left(\partial^\mu \phi\right) - \mu^2 \left(\phi^\dagger \phi\right) - \lambda \left(\phi^\dagger \phi\right)^2 \tag{A.1}$$

where

$$\phi = \begin{pmatrix} \phi_\alpha \\ \phi_\beta \end{pmatrix} = \frac{1}{\sqrt{2}} \begin{pmatrix} \phi_1 + i\phi_2 \\ \phi_3 + i\phi_4 \end{pmatrix} \tag{A.2}$$

is the complex doublet of scalar fields ϕ_1, ϕ_2, ϕ_3 and ϕ_4. The expression A.1 is manifestly invariant under a global SU(2) transformation

$$\phi' = U(\vec{\alpha})\phi = e^{i\vec{\alpha}\cdot\frac{\vec{\tau}}{2}}\phi \tag{A.3}$$

where $\vec{\tau}$ indicates a three-component vector made up with Pauli matrices τ_1, τ_2 and τ_3:

$$\tau_1 = \begin{pmatrix} 0 & 1 \\ 1 & 0 \end{pmatrix}$$

$$\tau_2 = \begin{pmatrix} 0 & -i \\ i & 0 \end{pmatrix} \tag{A.4}$$

$$\tau_3 = \begin{pmatrix} 1 & 0 \\ 0 & -1 \end{pmatrix}$$

Under a local SU(2) transformation

$$\phi'(x) = U(\vec{\alpha}(x))\phi(x) = e^{i\vec{\alpha}(x)\cdot\frac{\vec{\tau}}{2}}\phi(x) \tag{A.5}$$

with the three-component $\vec{\alpha}$ parameter dependent on the same x coordinates as ϕ, the invariance of Eq. A.1 is preserved if the minimal substitution between the usual derivative ∂_μ and the covariant derivative $\mathcal{D}_\mu$ of Eq. A.6 is performed:

$$\mathcal{D}_\mu = \partial_\mu + ig\frac{\vec{\tau}}{2} \cdot \vec{W}_\mu \tag{A.6}$$

The gauge field $\vec{W}_\mu$ transformation is ruled by Eq. A.7

$$\vec{W}_\mu \rightarrow \vec{W}_\mu - \frac{1}{g}\left(\partial_\mu \vec{\alpha}\right) - \vec{\alpha} \times \vec{W}_\mu \tag{A.7}$$

and the invariant lagrangian together with the gauge field kinetic term is

$$\mathcal{L} = \left(\mathcal{D}_\mu \phi\right)^\dagger \left(\mathcal{D}^\mu \phi\right) - V(\phi) - \frac{1}{4}\vec{W}_{\mu\nu} \cdot \vec{W}^{\mu\nu} \tag{A.8}$$

The potential

$$V(\phi) = \mu^2\left(\phi^\dagger \phi\right) + \lambda\left(\phi^\dagger \phi\right)^2 \tag{A.9}$$

is fundamental to prosecute this brief account and it is important to analyse it in detail. The mathematical properties of A.9 are different in case of positive or negative sign of μ^2. The sign of λ is assumed to be positive: $\lambda > 0$. The graph of potential V as a function of $|\phi|$ is shown in Fig. A.1.

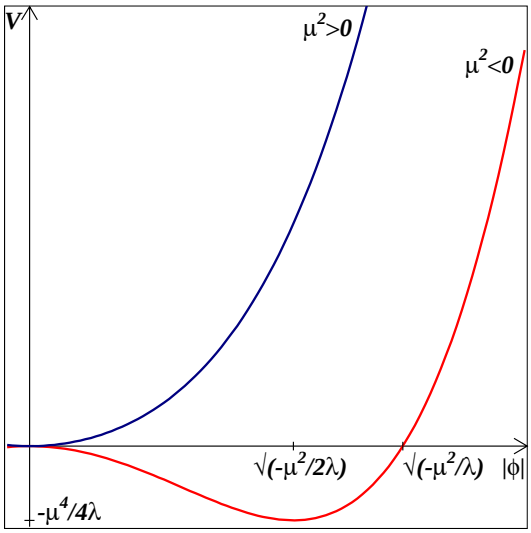

Figure A.1: *Higgs potential V as a function of $|\phi|$ in the two cases $\mu^2 > 0$ and $\mu^2 < 0$.*

$\mu^2 > 0$

The potential of Fig. A.2 describes the dynamics of four scalar fields with mass μ. The quartic term $\left(\phi^\dagger\phi\right)^2 = |\phi|^4$ represents the interaction between four fields ϕ_i through four-legged vertex diagrams with coupling constant λ.

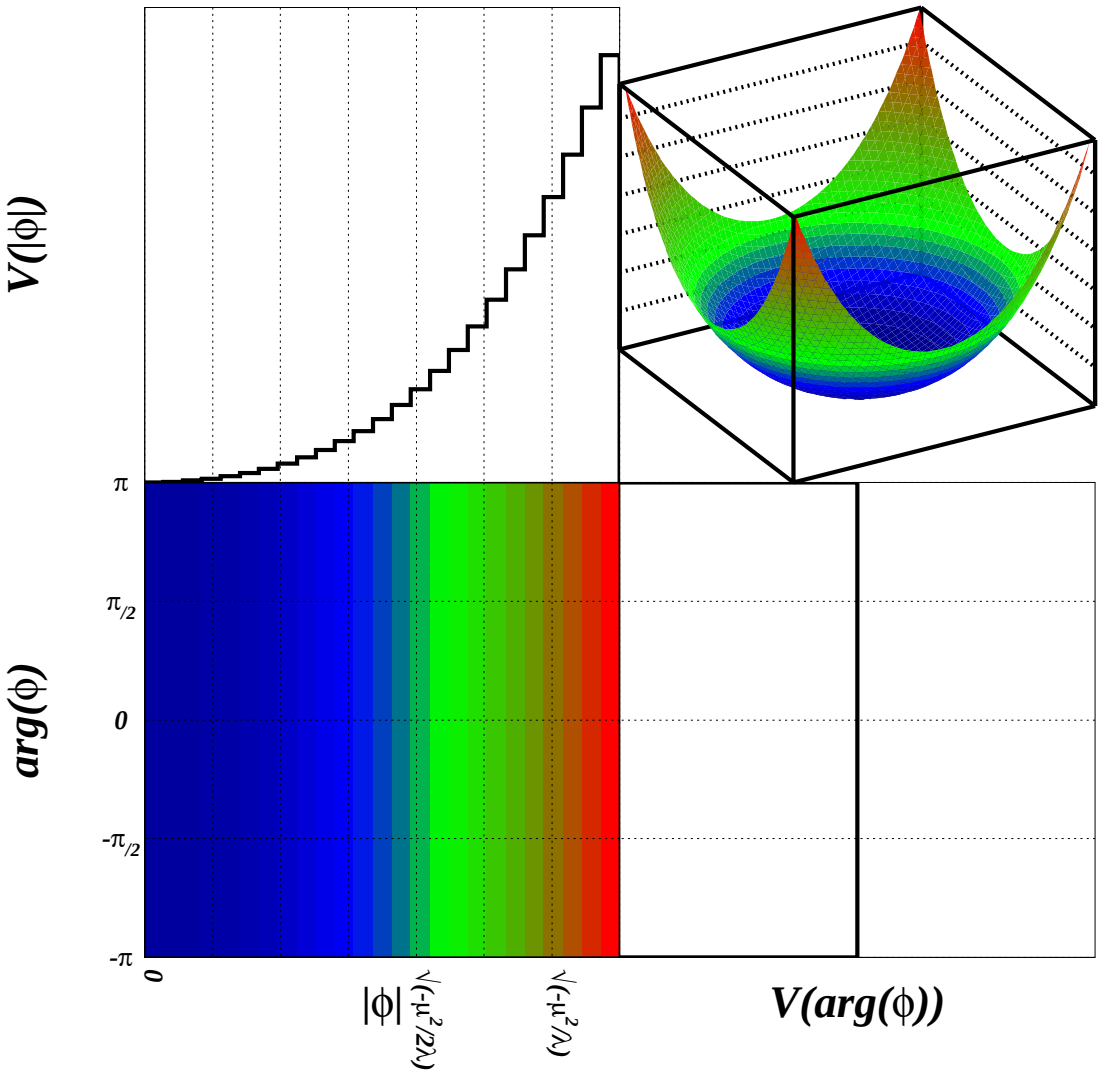

Figure A.2: *Two-dimensional representation of Higgs potential V as a function of ϕ in the case $\mu^2 > 0$.*

$\mu^2 < 0$

In this case the potential of Fig. A.3 has a "wrong" mass term and there are two stationary $|\phi|$ points corresponding to the solutions of $\frac{\partial V}{\partial |\phi|} = 0$.

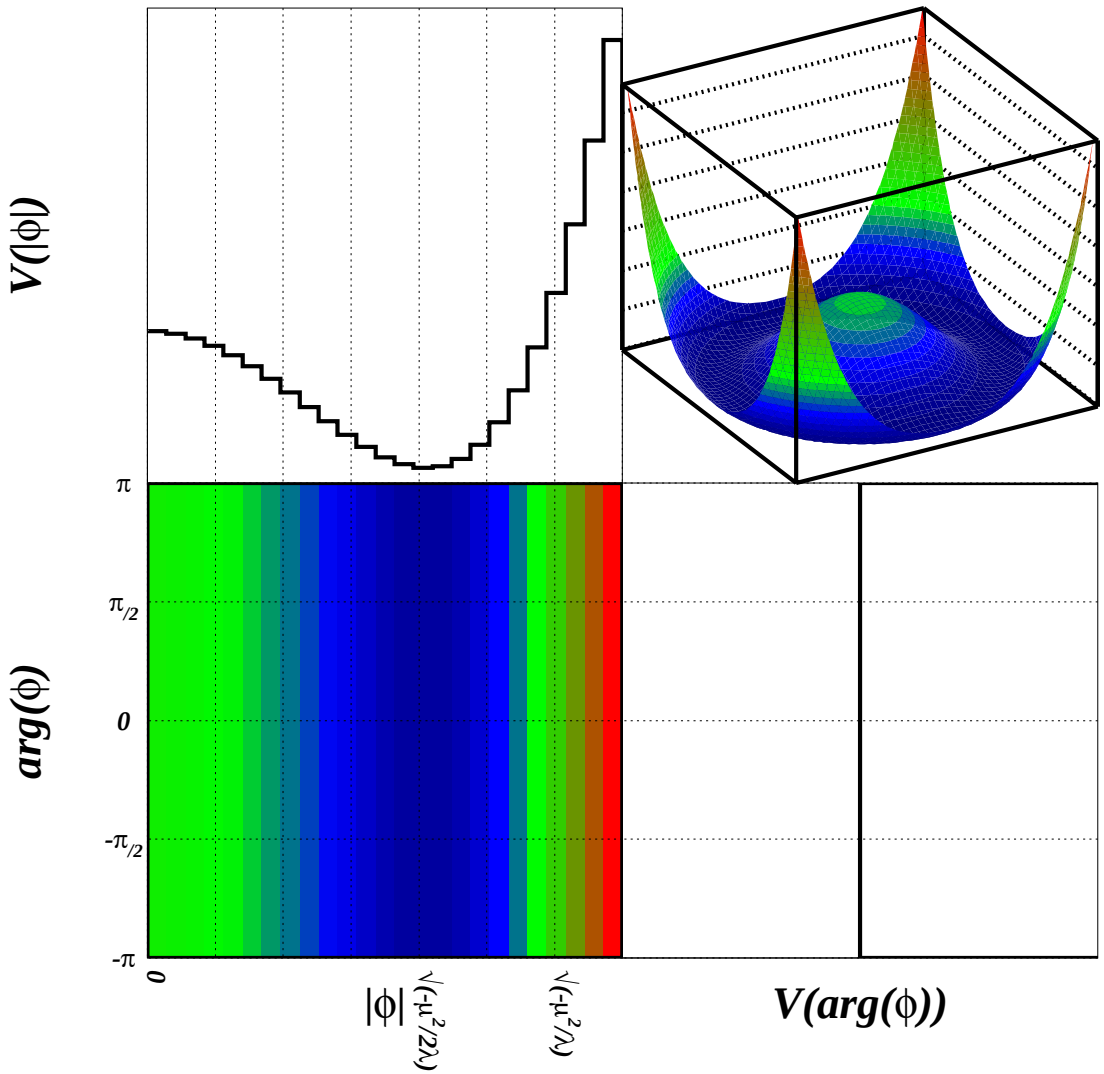

Figure A.3: *Two-dimensional representation of Higgs potential V as a function of ϕ in the case $\mu^2 < 0$.*

The local minimum is located in correspondence of the value of $|\phi|$ of Eq. A.10

$$|\phi|^2 = -\frac{\mu^2}{2\lambda} = \frac{1}{2}\left(\phi_1^2 + \phi_2^2 + \phi_3^2 + \phi_4^2\right) \tag{A.10}$$

and its value is

$$V_{min} = -\frac{1}{4}\frac{\mu^4}{\lambda} \tag{A.11}$$

The four-dimensional surface of Eq. A.10 is SU(2) invariant, hence $V(\phi)$ can be expanded near a particular value, thus defining the vacuum expectation value ϕ_0 of the field $\phi(x)$. The following values can be chosen:

$$\begin{cases} \phi_1 = \phi_2 = \phi_4 = 0 \\ \\ \phi_3^2 = -\frac{\mu^2}{\lambda} \equiv v^2 \end{cases} \tag{A.12}$$

therefore the vacuum expectation value ϕ_0 is

$$\phi_0 = \frac{1}{\sqrt{2}} \begin{pmatrix} 0 \\ v \end{pmatrix} \tag{A.13}$$

The expansion of $\phi(x)$ near ϕ_0 can be parameterized as

$$\phi(x) = e^{i\vec{\tau}\cdot\frac{\vec{\theta}(x)}{v}} \begin{pmatrix} 0 \\ \frac{v+h(x)}{\sqrt{2}} \end{pmatrix} \tag{A.14}$$

(with $\vec{\theta}(x) \in \mathbb{R}^3$, $h(x) \in \mathbb{R}$ and τ_i (i=1,2,3) the Pauli matrices of Eq. A.4) without loss of generality, since

$$\begin{aligned} \phi(x) &\simeq \left(1 + i\vec{\tau}\cdot\frac{\vec{\theta}(x)}{v}\right) \frac{1}{\sqrt{2}} \begin{pmatrix} 0 \\ v + h(x) \end{pmatrix} \simeq \frac{1}{\sqrt{2}} \begin{pmatrix} \theta_2 + i\theta_1 \\ v + h - i\theta_3 \end{pmatrix} \\ &= \phi_0 + \begin{pmatrix} \theta_2 + i\theta_1 \\ h - i\theta_3 \end{pmatrix} = \phi_0 + \delta\phi \end{aligned} \tag{A.15}$$

The expression A.15 is the definition of a SU(2) gauge transformation for the field

$$\tilde{\phi}(x) = \begin{pmatrix} 0 \\ \frac{v+h(x)}{\sqrt{2}} \end{pmatrix} \tag{A.16}$$

defined in the following way:

$$\tilde{\phi}'(x) = e^{i\vec{\tau}\cdot\frac{\vec{\theta}(x)}{v}} \begin{pmatrix} 0 \\ \frac{v+h(x)}{\sqrt{2}} \end{pmatrix} = U\left(\frac{2\vec{\theta}(x)}{v}\right)\tilde{\phi}(x) \tag{A.17}$$

Therefore, because of lagrangian A.8 gauge invariance, the only field that does not disappear between $\theta_1(x)$, $\theta_2(x)$, $\theta_3(x)$ and $h(x)$ is the latter. Lagrangian A.8 will not have tracks of the three fields $\vec{\theta}(x)$ anymore. The massless fields $\theta_1(x)$, $\theta_2(x)$ and $\theta_3(x)$ are called Goldstone bosons.

The potential A.9 expansion at lower order in $h(x)$ powers is

$$V_{Higgs} = -\frac{\lambda v^4}{4} + \frac{1}{2}(2\lambda v^2)h^2(x) + o\left(h(x)^2\right) \tag{A.18}$$

with $m_{\theta_1} = m_{\theta_2} = m_{\theta_3} = 0$ and

$$m_h = \sqrt{2\lambda v^2} = \sqrt{-2\mu^2} \tag{A.19}$$

Performing explicit calculations for the mass term

$$\mathcal{L}_{mass} = \left(ig\frac{\vec{\tau}}{2} \cdot \vec{W}_\mu \tilde{\phi}\right)^\dagger \left(ig\frac{\vec{\tau}}{2} \cdot \vec{W}^\mu \tilde{\phi}\right) \tag{A.20}$$

Eq. A.21 is obtained[1]

$$\mathcal{L}_{mass} = \frac{g^2 v^2}{8}\left[\left(W_\mu^1\right)^2 + \left(W_\mu^2\right)^2 + \left(W_\mu^3\right)^2\right] \tag{A.21}$$

from which the boson mass

$$M_W = \frac{1}{2}gv \tag{A.22}$$

is of immediate[2] identification.

Lagrangian A.8 actually describes three massive gauge fields $\vec{W}_\mu$ and one massive scalar field $h(x)$. The gauge fields have "eaten" the Goldstone bosons thus acquiring mass, the three scalar degrees of freedom becoming the longitudinal polarizations. This is a simple example of Higgs mechanism of spontaneous symmetry breaking, whose evolution is sketched in the scheme of Fig. A.4.

[1]The notation $\left(W_\mu\right)^2$ is a shortcut for $W_\mu W^\mu$.

[2]The mass term for a boson B_μ is $\frac{1}{2}M^2\left(B_\mu\right)^2$.

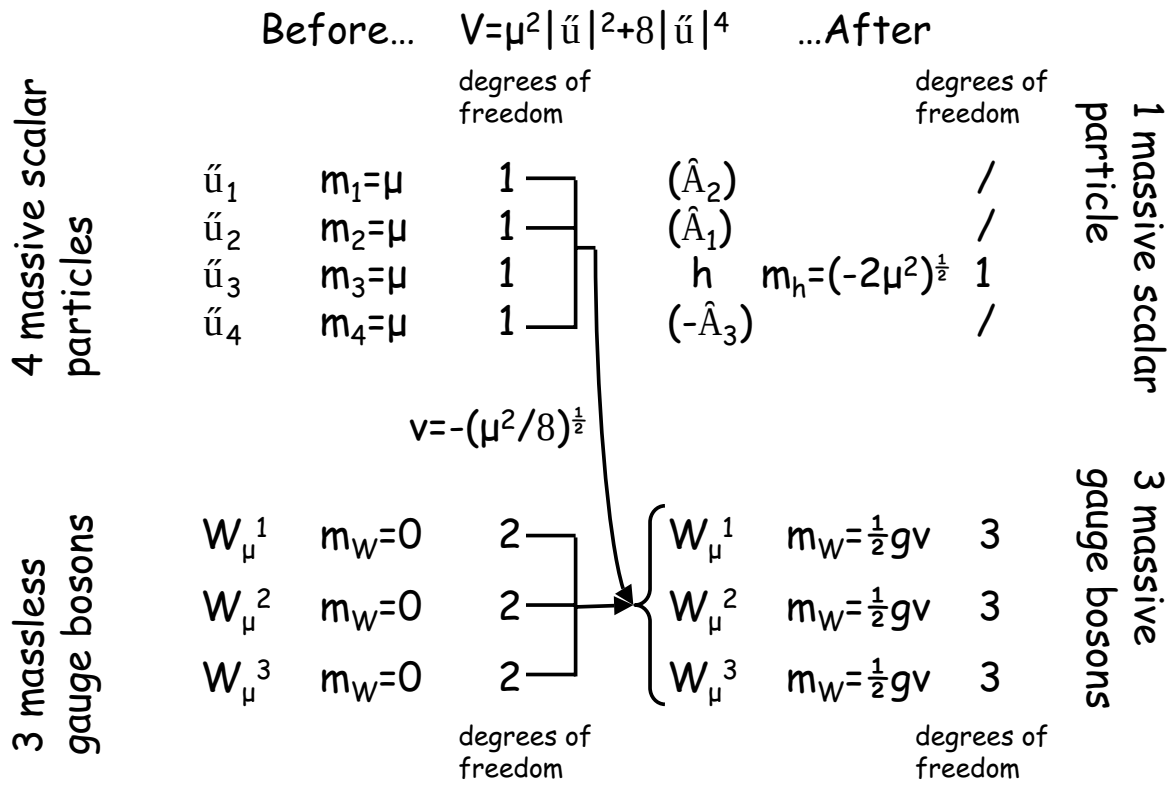

Figure A.4: *Spontaneous symmetry breaking mechanism.*

Appendix B

Simulated event normalization

A sample of generated events with total cross section $\overline{\sigma}$ can be filtered to select only a subsample of events satisfying some kinematic or physics requirements.

The corresponding rate R can be calculated as

$$R = \epsilon_{MC} \cdot \overline{\sigma} \cdot \mathcal{L} \tag{B.1}$$

where $\mathcal{L}$ is the luminosity and ϵ_{MC} the fraction of generated events, which have the required properties.

The selections made at generation and simulation level for the Minimum Bias events enriched with muons produced during the "Spring 2002" production [96] are two [97].

A first selection is based on the number of events with at least one muon in the final state according to the kinematic cuts of Tab. 7.1 on page 143, which reduce to N_{hit} simulated events the generated N_{gen}. The calorimeter and muon chambers response is digitized and a sample made with N_{digi} events is obtained, with $N_{digi} \leqslant N_{hit}$ due to incidental crashes during the digitization process. A filter to select events which certainly have muon candidates after Level-1 trigger reduce the number of events to N_{filter}. For these events also the Tracker response has been fully simulated (zero suppression, cluster finding). The ϵ_{MC} efficiency is factorized into two contributions: $\epsilon_{pres} = \frac{N_{hit}}{N_{gen}}$ is the preselection efficiency and $\epsilon_{L1} = \frac{N_{filter}}{N_{digi}}$ the Level-1 filter efficiency. If a subset with N_{tot} events is analysed from the total N_{filter} amount, the total rate R of Eq. B.1 can be rewritten as:

$$R = \epsilon_{L1}\epsilon_{pres} \cdot \overline{\sigma} \cdot \mathcal{L} = \frac{N_{tot}}{N'_{gen}} \cdot \overline{\sigma} \cdot \mathcal{L} \tag{B.2}$$

The normalized number of generated events N'_{gen} is calculated taking into account the various selections made at generator level and the number of analysed events N_{tot}:

$$N'_{gen} = \left(\frac{N_{digi}}{N_{hit}}\right) \cdot \left(\frac{N_{tot}}{N_{filter}}\right) \cdot N_{gen} \tag{B.3}$$

In presence of weighted events, in Eq. B.2 the number of processed events N_{tot} has to be replaced by the sum of the w_i event weights $\sum_{i=1}^{N_{tot}} w_i$.

The number of the production parameters and the total number of analysed events N_{tot} used to calculate the N'_{gen} of Tab. 7.1 on page 143 are reported in Tab. B.1.

Monte Carlo sample	Production Parameters				Analysed events
	N_{gen}	N_{hit}	N_{digi}	N_{filter}	N_{tot}
$W \rightarrow \mu + X$	569 618	50 000	49 995	49 995	25 000
$Z/\gamma^* \rightarrow \mu + X$	2 268 510	49 999	49 989	49 989	25 000
$t\bar{t} \rightarrow \mu + X$	46 229	20 000	20 000	19 996	14 996
MB Low p_T^μ	1 357 640	150 483	150 453	14 573	14 456
MB $p_T^\mu > 4$ GeV/c	54 709 859	255 732	255 665	228 336	48 858
MB $p_T^\mu > 10$ GeV/c	30 375 111	86 914	86 897	86 897	50 000

Table B.1: *Production parameters [97] and number of analysed events of the Monte Carlo datasets used to calculate the normalized number of generated events N'_{gen} of Tab. 7.1.*

Minimum Bias samples enriched with muons

Each event is generated taking over the decay of the particles that can potentially produce a muon. For this purpose, all potential muon parents are declared stable at event generation. Then all the possible final states are simulated according to the branching fractions of the particles, which can decay directly or indirectly into muons. From all the possible final states, only the ones with a muon satisfying the kinematic requirements are selected and assigned a probability. One of these configurations is randomly chosen according to the relative probability, which is taken into account to define the event weight w_i. The selected event is fully simulated and pile-up interactions from the Minimum Bias database are added as expected at high or low luminosity. However, since the events in the Minimum Bias samples used for the determination of the muon trigger rates are forced to contain muons, no muon should be present in the pile-up events to avoid an artificial increase of the di-muon rates and a bias due to the multiple occurrence of few triggering pile-up events. The pile-up sample was therefore filtered to remove all events containing potentially triggering muons [97].

Bibliography

[1] Particle Data Group, *Phys. Rev.*, **D66** (2002) 010001, *"Review of Particle Physics"*.

[2] S.L. Glashow, *Nucl. Phys.*, **22** (1961) 579-588, *"Partial Symmetries of Weak Interactions"*.

[3] A. Salam, *"Elementary Particle Theory"*, N. Svartholm, Stockholm, Almquist and Wiksells (1968), 367.

[4] S. Weinberg, *Phys. Rev. Lett.*, **19** (1967) 1264-1266, *"A Model of Leptons"*.

[5] M. Goldhaber, L. Grodzins and A.W. Sunyar, *Phys. Rev.*, **109** (1958) 1015-1017, *"Helicity of Neutrinos"*.

[6] N. Cabibbo, *Phys. Rev. Lett.*, **10** (1963) 531-532, *"Unitary Symmetry and Leptonic Decays"*;
M. Kobayashi and T. Maskawa, *Prog. Theor. Phys.*, **49** (1973) 652-657, *"CP Violation in the Renormalizable Theory of Weak Interaction"*;
L. Wolfenstein, *Phys. Rev. Lett.*, **51** (1983) 1945, *"Parametrization of the Kobayashi-Maskawa Matrix"*.

[7] R.K. Ellis, W.J. Stirling and B.R. Webber, *"QCD and Collider Physics"*, Cambridge University Press (1996).

[8] R.P. Feynman, R.B. Leighton and M. Sands, *"The Feynman Lectures on Physics"*.

[9] P.W. Higgs, *Phys. Lett.*, **12** (1964) 132-133, *"Broken Symmetries, Massless Particles and Gauge Fields"*; *Phys. Rev. Lett.*, **13** (1964) 508-509, *"Broken Symmetries and the Masses of Gauge Bosons"*; *Phys. Rev.*, **145** (1966) 1156-1163, *"Spontaneous Symmetries Breakdown Without Massless Bosons"*;
F. Englert and R. Brout, *Phys. Rev. Lett.*, **13** (1964) 321-322, *"Broken Symmetry and the Mass of Gauge Vector Mesons"*;

G.S. Guralnik, C.R. Hagen and T.W.B. Kibble, *Phys. Rev. Lett.*, **13** (1964) 585-587, *"Global Conservation Laws and Massless Particles"*.

[10] G. 'tHooft, *Nucl. Phys.* **B33** (1971) 173-199, *"Renormalization of Massless Yang-Mills Fields"*;
G. 'tHooft, *Nucl. Phys.* **B35** (1971) 167-188, *"Renormalizable Lagrangians for Massive Yang-Mills Fields"*, Reprinted in: *"Developments in the Quark Theory of Hadrons. A Reprint Collection."* Vol. I, 1964-1978. Eds.: D.B. Lichtenberg and S.P. Rosen, Hadronic Press, Inc. Nonantum, Mass. 02195, U.S.A. 1980, 171-192;
G. 'tHooft and M.J.G. Veltman, *Nucl. Phys.* **B44** (1972) 189-213, *"Regularization and Renormalization of Gauge Fields"*;
G. 'tHooft and M.J.G. Veltman, *Nucl. Phys.* **B50** (1972) 318-353, *"Combinatorics of Gauge Fields"*.
G. 'tHooft and M.J.G. Veltman were awarded Nobel Prizes in Physics 1999 *"for elucidating the quantum structure of electroweak interactions in physics"*.

[11] J.F. Gunion, H.E. Haber, G. Kane and S. Dawson, *"The Higgs Hunter's Guide"*, Addison Wesley, Menlo Park, 1990; Perseus Publishing, Cambridge, Massachussets, 2000.

[12] W.-Y. Keung and W.J. Marciano, *Phys. Rev.*, **D30** (1984) 248, *"Higgs Scalar Decays:* $\mathrm{H} \to \mathrm{W}^{\pm} X$*"*;
R.N. Cahn, M.S. Chanowitz and N. Fleishon, *Phys. Lett.*, **B82** (1979) 113, *"Higgs Particle Production by* $\mathrm{Z} \to \mathrm{H}\gamma$*"*;
L. Bergström and C. Hulth, *Nucl. Phys*, **B259** (1985) 137, *"Induced Higgs Couplings to Neutral Bosons in* $\mathrm{e}^{+}\mathrm{e}^{-}$ *Collisions"*;
M.A. Shifman, A.I. Vainshtein, M.B. Voloshin and V.I. Zakharov, *Sov. J. Nucl. Phys.*, **30** (1979) 711-716, *"Low-Energy Theorems for Higgs Boson Couplings to Photons"*.

[13] A. Djouadi, J. Kalinowski and M. Spira, DESY 97-079, IFT-96-29, PM-97/04, hep-ph/9704448, *"HDECAY: a Program for Higgs Boson Decays in the Standard Model and its Supersymmetric Extension"*.

[14] K. Riesselmann, DESY-97-222 (1997), hep-ph/9711456, *"Limitations of a Standard Model Higgs Boson"*.

[15] T. Appelquist and C.W Bernard, *Phys. Rev.*, **D22** (1980) 200, *"Strongly Interacting Higgs Bosons"*,

A. Longhitano, *Nucl. Phys.*, **B188** (1981) 118, *"Low-Energy Impact of a Heavy Higgs Boson Sector"*,
T. Appelquist and G.-H. Wu, *Phys. Rev.*, **D51** (1995) 240-250, hep-ph/9406416, *"The Electroweak Chiral Lagrangian and CP Violating Effects in Technicolor Theories"*.

[16] M.J.G. Veltman, *Acta. Phys. Polon.*, **B8** (1977) 475, *"Second Threshold in Weak Interactions"*.

[17] The CDF Collaboration, *Phys. Rev.*, **D50** (1194) 2966-3026, *Phys. Rev. Lett.*, **73** (1994) 225-231, hep-ex/9405005, *"Evidence for top quark production in* $\bar{\mathrm{p}}\mathrm{p}$ *collisions at* $\sqrt{s}=1.8$ TeV *"*.

[18] The LEP Collaborations ALEPH, DELPHI, L3, OPAL, the LEP Electroweak Working Group and the SLD Heavy Flavour Group, CERN-EP/2002-091, LEPEWWG/2002-02, ALEPH 2002-042 PHYSIC 2002-018, DELPHI 2002-098 PHYS 927, L3 Note 2788, OPAL PR 370, hep-ex/0212036, *"A Combination of Preliminary Electroweak Measurements and Constraints on the Standard Model"* (Prepared from Contributions of the LEP and SLD Experiments to the 2002 Summer Conferences).

[19] G. Montagna, O. Nicrosini, F. Piccinini and G. Passarino, *Comput. Phys. Commun.*, **117** (1999) 278-289, hep-ph/9804211, *"TOPAZ0 4.0: a New Version of a Computer Program for Evaluation of Deconvoluted and Realistic Observables at LEP-1 and LEP-2"*.

[20] D.Y. Bardin, P. Christova, M. Jack, L. Kalinovskaya, A. Olchevski, S. Riemann and T. Riemann, *Comput. Phys. Commun.*, **133** (2001) 229-395, DESY-99-070, hep-ph/9908433, *"ZFITTER V.6.21: a Semianalytical Program for Fermion Pair Production in* $\mathrm{e}^+\mathrm{e}^-$ *Annihilation"*.

[21] F. James and M. Roos, *Comput. Phys. Commun.*, **10** (1975) 343-367, CERN-DD-75-20, *"'MINUIT' a System for Function Minimization and Analysis of the Parameter Errors and Correlations"*.

[22] Lep Injector Study Group, CERN-LEP-TH-83-29, CERN-PS-DL-83-31, CERN-SPS-83-26, LAL-RT-83-09, *"LEP Design Report Vol.1: The LEP Injector Chain"* (1983),
CERN-LEP/84-01, *"LEP Design Report Vol.2: The LEP Main Ring"* (1984),
CERN-AC-96-01-LEP-2, *"LEP Design Report, Vol.3: LEP2"* (1996).

[23] ALEPH, DELPHI, L3 and OPAL Collaborations, The LEP Working Group for Higgs Boson Searches, ALEPH 2002-024 CONF 2002-013, DELPHI 2002-088 CONF 621, L3 Note 2766, OPAL Technical Note TN721, LHWG Note/2002-01, *"Search for the Standard Model Higgs Boson at LEP"*.

[24] ALEPH Collaboration, *"The ALEPH Detector (Apparatus for LEp PHysics) Technical Report"*, CERN-LEPC-83-2, LEPC-P-1 - Geneva: CERN, 1983;
ALEPH Collaboration, *"Proposal for the new vertex detector for ALEPH"*, CERN-LEPC-93-8, LEPC-P-1-Add-1 - Geneva: CERN, 1993.

[25] DELPHI Collaboration, *"DELPHI: The DELPHI Detector (DEtector with Lepton Photon and Hadron Identification) Technical Proposal"*, CERN-LEPC-83-3, DELPHI-83-66, LEPC-P-2 - Geneva: CERN, 1983;
DELPHI Collaboration, *"Proposal for the replacement of the small angle calorimeter of DELPHI"*, CERN-LEPC-92-6, LEPC-P-2-Add-1 - Geneva: CERN, 1992;
DELPHI Collaboration, *"Proposal for the upgrade of DELPHI in the forward region"*, CERN-LEPC-92-13, LEPC-P-2-Add-2 - Geneva: CERN, 1992;
DELPHI Collaboration, *"Proposal for the DELPHI very forward tracker"*, CERN-LEPC-93-6, LEPC-P-2-Add-3 - Geneva: CERN, 1993.

[26] L3 Collaboration, *"L3 Technical Proposal"*, CERN-LEPC-83-5, LEPC-P-4 - Geneva: CERN, 1983;
L3 Collaboration, *"Some improvements to the L3 detector for LEP 200"*, CERN-LEPC-94-5, LEPC-P-4-ADD-2-INS - Geneva: CERN, 1994;
L3 Collaboration, *"A very small angle tagger for L3"*, CERN-LEPC-95-1, LEPC-P-4-ADD-3-INS - Geneva: CERN, 1995.

[27] OPAL Collaboration, *"OPAL: The OPAL Detector (an Omni Purpose Apparatus for Lep) Technical Proposal"*, CERN-LEPC-83-4, LEPC-P-3 - Geneva: CERN, 1983;
OPAL Collaboration, *"Proposal for a new silicon microvertex detector for OPAL"*, CERN-LEPC-93-13, LEPC-P-3-add-1 - Geneva: CERN, 1993;
OPAL Collaboration, *"Proposal for a new silicon microvertex detector for OPAL"*, CERN-LEPC-93-13, LEPC-P-3-add-2 - Geneva: CERN, 1993;
OPAL Collaboration, *"Proposal to install scintillating tiles in the OPAL endcap"*, CERN-LEPC-94-09, LEPC-P-3-Add-3 - Geneva: CERN, 1994.

[28] ALEPH Collaboration, *Phys. Lett.*, **B495** (2000) 1-17, hep-ex/0011045, *"Observation of an Excess in the Search for the Standard Model Higgs Boson at Aleph"*.

[29] The LHC Study Group, CERN/AC/95-05 (1995), *"The Large Hadron Collider Conceptual Design Report"*.

[30] F. Wilczek, *Phys. Rev. Lett.*, **39** (1977) 1304, *"Decays of Heavy Vector Mesons into Higgs Particles"*,
H.M. Georgi, S.L. Glashow, M.E. Machacek and D.V. Nanopoulos, *Phys. Rev. Lett.*, **40** (1978) 692, *"Higgs Bosons from Two Gluon Annihilation in Proton-Proton Collisions"*,
J. Ellis, M.K. Gaillard, D.V. Nanopoulos and C.T. Sachrajda, *Phys. Lett.*, **B83** (1979) 339, *"Is the Mass of The Higgs Boson about* 10 GeV *?"*,
T.G. Rizzo, *Phys. Rev.*, **D22** (1980) 178, *Addendum-ibid.*, **D22** (1980) 1824-1825, *"Gluon Final States in Higgs Boson Decays"*.

[31] M. Spira, DESY T-95-05, hep-ph/9510347, *"HIGLU: A Program for the Calculation of The Total Higgs Production Cross Sections at Hadron Colliders via Gluon Fusion Including QCD Corrections"*.

[32] T. Han, G. Valencia and S. Willenbrock, *Phys. Rev. Lett.*, **69** (1992) 3274-3277, hep-ph/9206246, *"Structure Function Approach to Vector Boson Scattering in* pp *Collisions"*.

[33] T. Han and S. Willenbrock, *Phys. Lett.*, **B273** (1991) 167-172, *"QCD Correction to the* pp$\to$WH *and* ZH *Total Cross-Sections"*.

[34] Z. Kunszt, *Nucl. Phys.*, **B247** (1984) 339, *"Associated Production of Heavy Higgs Boson with Top Quarks"*,
D.A. Dicus and S. Willenbrock, *Phys. Rev.*, **D39** (1989) 751, *"Higgs Boson Production from Heavy Quark Fusion"*,
J.F. Gunion, *Phys. Lett.*, **B261** (1991) 510-517, *"Associated* $\mathrm{t\bar{t}}$ *Higgs Production as a Large Source of* WH *Events: Implications for Higgs Detection in the Lepton Neutrino Gamma Gamma Final State"*,
W.J. Marciano and F.E. Paige, *Phys. Rev. Lett.*, **66** (1991) 2433-2435, *"Associated Production of Higgs Bosons with* $\mathrm{t\bar{t}}$ *Pairs"*,
M. Spira, *Fortschr. Phys.*, hep-ph/9705337, **46** (1998) 203-284, *"QCD Effects in Higgs Physics"*;
S. Dawson, L.H. Orr, L. Reina and D. Wackeroth, hep-ph/0211438, *"Associated Top Quark-Higgs Boson Production at the LHC"*;
W. Beenakker, S. Dittmaier, M. Krämer, B. Plumper, M. Spira and P.M. Zerwas,

Phys. Rev. Lett., **87** (2001) 201805, DESY-01-077, EDINBURGH-2001-08, PSI-PR-01-10, hep-ph/0107081, *"Higgs Radiation Off Top Quarks at the TeVatron and the LHC"*,
W. Beenakker, S. Dittmaier, M. Krämer, B. Plumper, M. Spira and P.M. Zerwas, *Nucl. Phys.*, **B653** (2003) 151-203, DESY 02-177, Edinburgh 2002/18, MPI-PhT/2002-70, PSI-PR-02-22, hep-ph/0211352, *"NLO QCD corrections to* $t\bar{t}H$ *production in hadron collisions"*.

[35] ATLAS Collaboration, ATLAS TDR 14, CERN/LHCC 99-14, *"Atlas Detector and Physics Performance - Technical Design Report Vol. I"*

[36] ATLAS Collaboration, *"ATLAS: A Toroidal LHC ApparatuS Technical Proposal"*, CERN/LHCC-94-43, LHCC/P2.

[37] CMS Collaboration, *"The Compact Muon Solenoid Technical Proposal"*, CERN/LHCC 94-38, LHCC/P1, 15 December 1994.

[38] ALICE Collaboration, *"A Large Ion Collider Experiment Technical Report Design"*, CERN/LHCC 95-71, LHCC/P3.

[39] LHCb Collaboration, *"A Large Hadron Collider Beauty Experiment for Precision Measurements of CP-Violation and Rare Decays LHCb Technical Proposal"*, CERN/LHCC 98-04, LHCC/P4.

[40] ATLAS Collaboration, ATLAS TDR 15, CERN/LHCC 99-15, *"Atlas Detector and Physics Performance - Technical Design Report Vol. II"*

[41] J. Pumplin, D.R. Stump, J. Huston, H.L. Lai, P. Nadolsky and W.K. Tung, *JHEP*, **0207**, (2002) 012, hep-ph/0010017, *"New Generation of Parton Distributions with Uncertainties from Global QCD Analysis"*,
D. Stump, J. Huston, J. Pumplin, W.K. Tung, H.L. Lai, S. Kuhlmann and J. Owens, hep-ph/0303013, *"Inclusive Jet Production, Parton Distributions, and the Search for New Physics"*.

[42] CMS Collaboration, *"The Compact Muon Solenoid Letter of Intent"*, CERN/LHCC 92-3, LHCC/I1, 1 October 1992.

[43] CMS Collaboration, CMS Design Team, *"CMS: The Magnet Project Technical Design Report"*, CERN/LHCC 97-10, CMS TDR 1, 2 May 1997.

[44] CMS Collaboration, *"CMS: The Tracker Project Technical Design Report"*, CERN/LHCC 98-06, CMS TDR 5, 15 April 1998,
CMS Collaboration, *"Addendum to the CMS Tracker TDR"*, CERN/LHCC 2000-016, CMS TDR 5 Addendum 1, 21 February 2000.

[45] CMS Collaboration, *"CMS: The Electromagnetic Calorimeter Project Technical Design Report"*, CERN/LHCC 97-33, CMS TDR 4, 15 December 1997.

[46] D. Green, P. Hidas, K. Maeshima, R. Vidal, W. Wu and S. Kunori, CMS IN-2002/062, *"Dijet Mass Resolution With or Without the Endcap Ecal at CMS"*.

[47] CMS Collaboration, *"CMS: The Hadron Calorimeter Project Technical Design Report"*, CERN/LHCC 97-31, CMS TDR 2, 20 June 1997.

[48] CMS Collaboration, *"CMS: The Muon Project Technical Design Report"*, CERN/LHCC 97-32, CMS TDR 3, 15 December 1997.

[49] RD5 Collaboration, *Nucl. Instrum. Meth.*, **A336** (1993) 91-97, *"Bunch Crossing Identification at LHC Using a Mean Timer Technique"*.

[50] CMS Collaboration, *"CMS: The Trigger and Data Acquisition Project, Volume I: The Level-1 Trigger Technical Design Report"*, CERN/LHCC 2000-038, CMS TDR 6.1, 15 December 2000.

[51] CMS Collaboration, *"CMS: The Trigger and Data Acquisition Project, Volume II: Data Acquisition and High-Level Trigger Technical Design Report"*, CERN/LHCC 02-26, CMS TDR 6.2, 15 December 2002.

[52] A. Giassi, F. Palla and A. Starodumov, CMS NOTE-2002/045, *"Study for a High Level Trigger for the Decay Channel* $\mathrm{B_s} \to \mathrm{D_s}\pi \to \phi\pi\pi \to \mathrm{KK}\pi\pi$*"*.

[53] R. Ranieri, *Proceedings of the* 5^{th} *International Conference on Hyperons, Charm and Beauty Hadrons*, BEACH 2002, Vancouver, British Columbia (Canada) 25-29 June 2002, *Nucl. Phys. (Proc. Suppl.)*, **B115** (2003), CMS CR-2002/019, *"Study of channel* $\mathrm{B_s} \to \mathrm{J}/\psi\ \phi$ *at CMS"*, based on a work by N. Stepanov.

[54] Standard Performance Evaluation Corporation http://www.spec.org. The Intel Pentium III figures can be found at http://www.spec.org/osg/cpu95/results/cpu95.html.

[55] http://www.intel.com/design/pentiumiii.

[56] The Jargon Dictionary, http://info.astrian.net/jargon.

[57] M. Lozano, E. Cabruja, A. Collado, J. Santander and M. Ullan, *Nucl. Instrum. Meth.*, **A473** (2001) 95-101, *"Bump Bonding of Pixel Systems"*.

[58] L.L. Jones, M.J. French, Q. Morrissey, A. Neviani, M. Raymond, G. Hall, P Moreira and G. Cervelli, CERN/LHCC 99-09 162-166, *"The APV25 Deep Submicron Readout Chip for CMS Detector"*,
L.L. Jones, *"APV25-S1 User Guide Version 2.2"*, 5th September 2001, available at http://www.te.rl.ac.uk/med.

[59] C. Civinini, *Proceedings of the International Conference on High Energy Physics*, hep2001, Budapest (Hungary) 12-18 July 2001, *"The CMS Silicon strip sensors"*.

[60] S. Gadomski, G. Hall, T. Hogh, P. Jalocha, E. Nygard and P. Weilhammer, *Nucl. Instrum. Meth.*, **A320** (1992) 217-227, CERN-PPE-92-024, Jan 1992, *"The Deconvolution Method of Fast Pulse Shaping at Hadron Colliders"*.

[61] R. Wunstorf, T. Rohe and A. Rolf, *Nucl. Instrum. Meth.*, **A388** (1997) 308-313, *"Simulation of Irradiation-Induced Surface Effects in Silicon Detectors"*.

[62] S. Braibant, N. Demaria, L. Feld, A. Frey, A. Furtjes, W. Glessing, R. Hammarstrom, A. Honma, M. Mannelli, C. Mariotti, P. Mattig, E. Migliore, S. Piperov, O. Runolfsson, B. Schmitt and B. Surrow, CMS NOTE-2000/011, *"Investigation of Design Parameters and Choice of Substrate Resistivity and Crystal Orientation for the CMS Silicon Microstrip Detector"*.

[63] B.C. MacEvoy, G. Hall and K. Gill, *Nucl. Instrum. Meth.*, **A374** (1996) 12-26, *"Defect Evolution in Irradiated Silicon Detector Material"*.

[64] H. Feick, E. Fretwurst, G. Lindstroem and M. Moll, *Nucl. Instrum. Meth.*, **A377** (1996) 217-223, *"Long Term Damage Studies Using Silicon Detectors Fabricated from Different Starting Materials and Irradiated with Neutrons, Protons and Pions"*;
J.A.J. Matthews, P. Berdusis, M. Frautschi, J. Schuler, H. Sadrozinski, K. O'Shaughnessy, L. Spiegel, A. Palounek, H. Ziock, N. Bacchetta, D. Bisello and A. Giraldo, *Nucl. Instrum. Meth.*, **A381** (1996) 338-348, *"Bulk Radiation Damage in Silicon Detectors and Implications for LHC Experiments"*.

[65] R. Wunstorf, PhD Thesis, *"Systematische Untersuchungen zur Strahlenresistenz von Silizum-Detektoren für die Verwendung in Hochenergiephysik-Experimenten"*, University of Hamburg, October 1992.

[66] M. Raymond and G. Hall, CERN/LHCC 97-60, *"The APV6 Readout Chip for CMS Microstrip Detectors"*.

[67] M. Lenzi, PhD Thesis, *"Performance and optimization of the forward sensors in the CMS Silicon Tracker for LHC"*, University of Florence, December 1999.

[68] http://cmsdoc.cern.ch/cms/Physics/btau/management/top/btau.html.

[69] T. Sjöstrand, P. Edén, C. Friberg, L. Lönnblad, G. Miu, S. Mrenna and E. Norrbin, *Comput.Phys.Commun.*, **135** (2001) 238-259, hep-ph/0010017, *"High-Energy-Physics Event Generation with PYTHIA 6.1"*;
S. Mrenna, *Comput.Phys.Commun.*, **101** (1997) 232-240, hep-ph/9609630, *"SPYTHIA, A Supersymmetric Extension of PYTHIA 5.7"*.

[70] H. Baer, F.E. Paige, S.D. Protopopescu and X. Tata, hep-ph/0001086, *"ISAJET 7.48: A Monte Carlo Event Generator for* pp, $\bar{\text{p}}$p, *and* e^+e^- *Interactions"*.

[71] D.H. Ford and J. Rue, *"Standard FORTRAN Programming"*, (1982), 4^{th} edition, Homewood, IL: Richard D. Irwin Incorporated;
D.V. Griffiths and I.M. Smith, *"Numerical Methods for Engineers"*, (1991), Oxford, England, UK: Blackwell Scientific Publications;
M Metcalf, *"Effective FORTRAN 77"*, (1985), Oxford, England, UK: Oxford University Press;
L.R. Nyhoff and S.C. Leestma, *"Fortran 90 for Engineers"*, (1997), Upper Saddle River, New Jersey: Prentice-Hall Inc.

[72] CMS simulation package CMSIM, http://cmsdoc.cern.ch/cmsim/cmsim.html.

[73] GEANT 3 version 3.21/13 (release 15111999), *"Detector Description and Simulation Tool"*, CERN Program Library Long Writeup W513.

[74] C. Zeitnitz and T.A. Gabriel, *Nucl. Instrum. Meth.*, **A349** (1994) 106-111, *"The GEANT-CALOR Interface and Benchmark Calculations of ZEUS Test Calorimeters"*.

[75] B. Stroustrup, *"The C++ Programming Language (Third Edition and Special Edition)"*, Addison-Wesley, ISBN 0-201-88954-4 and 0-201-70073-5;
B. Stroustrup, *"The Design and Evolution of C++"*, Addison-Wesley, ISBN 0-201-54330-3.

[76] V. Innocente, L. Silvestris and D. Stickland, *Comput. Phys. Commun.*, **140** (2001) 31-44, *"CMS Software Architecture - Software Framework, Services and Persistency in High Level Trigger, Reconstruction and Analysis"*; http://cobra.web.cern.ch/cobra.

[77] http://www.redhat.com.

[78] http://www.objectivity.com.

[79] CMS Software and Computing Group, CMS IN-1999/001, *"Object Oriented Reconstruction for CMS Analysis"*;
http://cmsdoc.cern.ch/orca/orca.html, *"ORCA 6_3_0 User Guide"*.

[80] R.K. Boch, H. Grote, D. Notz and M. Regler, *"Data Analysis Techniques for High-Energy Physics Experiments"*, 2nd Edition, Cambridge University Press, 1990;
J.D. Jackson, *"Classical Electrodynamics"*, John Wiley & Sons, 1998.

[81] P. Billoir and S. Qian, *Nucl. Instrum. Meth.*, **A311**, (1992) 132-150, *"Fast Vertex Fitting with a Local Parametrization of Tracks"*;
T. Speer, K. Prokofiev and R. Frühwirth, CMS IN-2003/008, *"Vertex Fitting with the Kalman Filter Formalism in the ORCA Reconstruction Program"*.

[82] R. Frühwirth, *Nucl. Instrum. Meth.*, **A262** (1997) 444-456, HEPHY-PUB-87-503, *"Application of Kalman Filtering to Track and Vertex Fitting"*;
R. Frühwirth, P. Kubinec, W. Mitaroff, M. Regler *Comput. Phys. Commun.*, **96** (1996) 189-208, *"Vertex Reconstruction and Track Bundling at the LEP Collider Using Robust Algorithms"*.

[83] T. Todorov, *Proceedings of the International Conference on Computing in High Energy and Nuclear Physics* , CHEP 2000, Padova (Italy) 7-11 February 2000, *"An Object Framework for Track Reconstruction and its Implementation for the CMS Tracker"*.

[84] R. Ranieri, CMS NOTE-2003/xxx, in preparation.

[85] CERN Information Technology Division, *"PAW Physics Analysis Workstation User's Guide"*, CERN Program Library Long Writeup Q121;
CERN Computing and Networks Division, *"HBOOK – Statistical Analysis and Histogramming"*, CERN Program Library Long Writeup Y250.

[86] D. Kotlinski, CMS IN-2000/022, *"Track Reconstruction and Primary Vertex Finding using the Pixel Detector Data"*.

[87] The LEP Collaborations ALEPH, DELPHI, L3 and OPAL and the Line Shape Sub-group of the LEP Electroweak Working Group, CERN-EP/2000-153, hep-ex/0101027, *"Combination Procedure for the Precise Determination of Z Boson Parameters from Results of the LEP Experiments"*.

[88] S.P. Martin, hep-ph/9709356, *"A Supersymmetry Primer"*.

[89] F. Palla and G. Segneri, CMS NOTE-2002/046, *"Lifetime based* b*-tagging with CMS"*.

[90] D. Brown and M. Frank, ALEPH Note 92-135, PHYSIC 92-124, *"Tagging* B *Hadrons using Impact Parameters"*.

[91] G. Segneri, PhD Thesis, *"Scalar Top Quark Search at LHC with the CMS Detector"*, University of Pisa, October 2002.

[92] D. Kotlinski, *Proceedings of the 8^{th} International Conference on B-Physics at Hadron machines*, BEAUTY 2002, Santiago de Compostela, Galicia (Spain) 17-21 June 2002, *"CMS Pixel Detector"*.

[93] J.G. Branson and E. Trepagnier, CMS IN-2000/038, *"Weighting Bunch Crossing to Calculate Rates in the Presence of Pileup"*;
http://home.fnal.gov/∼hidaspal/xsec/mb_pythia_6_152.sigma.

[94] G. Segneri, CMS IN-2002/067, *"Object Oriented Library for* b*-tagging "*.

[95] R. Ranieri, CMS NOTE-2002/048, *"A High Level Trigger Selection of* $\mathrm{WH}\to\mu\nu\mathrm{b\bar{b}}$ *using the Tracker and* b*-jets "*.

[96] The CMS Production Team, CMS NOTE-2002/034, *"The Spring 2002 DAQ TDR Production"*.

[97] N. Amapane, S. Arcelli, D. Bonacorsi, A. Fanfani, U. Gasparini, M. Konecki, S. Lacaprara, S. Maggi, N. Neumeister, H. Rick and H. Sakulin, CMS NOTE-2002/041, *"Monte Carlo Simulation of Inclusive Single- and Di-Muon Samples"*.

[98] http://computing.fnal.gov/cms/jpg/spring2002.

[99] V. Drollinger, Th. Müller and D. Denegri, CMS NOTE-2002/006, IEKP-KA/2001-28, *"Prospect for Higgs Boson Searches in the channel* $\mathrm{W^{\pm}H^0}\to\ell^{\pm}\nu\mathrm{b\bar{b}}$*"*.

[100] E. Richter-Was, *Acta. Phys. Polon.*, **B31** (2000) 1931-1972, *"Revisiting the Observability of the* WH *and* ZH*,* $H \rightarrow b\bar{b}$ *Channel in* 14 TeV pp *and* 2 TeV $p\bar{p}$ *Collisions (*$\ell b\bar{b}$ *and* $\ell\ell b\bar{b}$ *Final States)".*

[101] F. Halzen and A.D. Martin, *"Quarks and Leptons"*, John Wiley & and Sons, New York, NY, 1984.

Acknowledgements

Il ringraziamento principale va a Elisabetta e alla mia famiglia, mamma, babbo e Save, gli zii Giovanni e Gina, la mia cugina Patrizia, senza i quali non sarei mai arrivato fino a questo punto.

Poi desidero ringraziare di cuore le persone che hanno sempre creduto in me, i professori delle superiori G. Betti e G. Giovacchini, che mi hanno insegnato moltissimo.

I am grateful to the CMS people I have worked with and who helped me in several ways: Fabrizio and Gabriele (sometimes I spent working week-ends with them), Teddy, Michela, the people from the muon group Nicola, Norbert, Giacomo.

Un ringraziamento speciale a Carlo, che mi ha permesso di realizzare questo lavoro e lo ha letto e commentato molto attentamente, e a Vitaliano per i validi consigli.

E un abbraccio va a tutti i componenti del Gruppo 1 della sezione INFN di Firenze, ad iniziare dalle gentilissime signore Guglielma e Gabriella.